No Smoke Without Fire: Cosmic Dust Emission as a Tracer of Star Formation in Galaxies

Nathan Bourne

The University of Nottingham

Thesis submitted to the University of Nottingham
for the degree of Doctor of Philosophy

July 2013

"In wonder all philosophy began, in wonder it ends, and admiration fill up the interspace; but the first wonder is the offspring of ignorance, the last is the parent of adoration."

– Samuel Taylor Coleridge

"All you really need to know for the moment is that the universe is a lot more complicated than you might think, even if you start from a position of thinking it's pretty damn complicated in the first place."

– Douglas Noel Adams

Supervisors: Dr. Loretta Dunne
Dr. Omar Almaini
Prof. Michael Merrifield

Examiners: Prof. Seb Oliver
Prof. Christopher Conselice

Abstract

Studies of the history of the Universe are for a large part concerned with mapping the evolution of galaxies over cosmic time. Beginning from the seeds of density perturbations in the early Universe, and building up through gravitational and astrophysical interactions to form the wide diversity seen in the present day, galaxies allow us to observe the distribution of luminous (and dark) matter over a wide range of look-back times.

A key process in galaxy evolution is the formation of stars, an activity which is readily observed by indirect means, although the detailed mechanism is not fully understood. One of the most successful methods for tracing star formation is to observe the emission from dust in galaxies. These tiny particles of carbon- and silicon-based solids resemble smoke, pervading the interstellar medium in many (if not all) galaxies, and blocking the short-wavelength radiation from hot, newly-formed stars. They re-radiate this energy as far-infrared radiation ($\lambda \sim 10 - 1000\,\mu\mathrm{m}$), which can be detected from sources throughout the Universe by telescopes such as the *Spitzer* and *Herschel* space observatories. The spectral form of this radiation varies from one galaxy to another, depending on many factors such as the activity within the galaxy, the amount of dust, and the sources heating the dust. Hence, with careful interpretation, we can use these observations to trace the star-forming activity and dust mass in different types of galaxies from early times through to the present day.

In this thesis I describe three projects, each of which utilises multi-wavelength datasets from large surveys to probe the dust emission from samples of galaxies at different cosmic epochs, and explore the relationship between dust emission and other galaxy properties. The first project samples the most massive galaxies at a range of redshifts spanning the peak era of star formation, and investigates the correlation between far-

infrared and radio emission. I use a ‘stacking’ methodology to avoid bias towards the brightest star-forming galaxies, and show that the far-infrared and radio tracers of star formation agree up to high redshifts in typical massive galaxies. In the second project I apply the stacking method to a large sample of low-redshift galaxies selected from a major optical survey spanning the last four billion years of evolution. I make use of the largest ever sub-millimetre imaging survey to produce a detailed and unbiased census of the dust mass in ordinary galaxies as a function of optical brightness, colour and look-back time. I show that the luminosity and temperature of dust is a strong function of galaxy mass and colour, while the dust masses of all galaxy types have decreased rapidly over the time span probed. The final project focuses on a small sample of nearby galaxies and utilises data obtained and reduced by myself to probe the molecular-gas content of galaxies selected to have large dust masses. This study addresses questions about how well the cold dust, traced by the sub-millimetre wavebands of *Herschel*, is correlated with the cold gas, which provides the fuel for ongoing star formation.

The thesis demonstrates the utility of statistical techniques for large surveys, and also contains aspects of data reduction and extensive discussion of the astrophysical interpretation of results. Through these various analyses I show that dust emission can provide a valuable window on the growth of galaxies through star formation. The work contained herein represents significant progress in the field of observational extragalactic astronomy, including work recently published in the scientific literature in two collaborative research papers led by myself, in addition to a third paper that I am currently preparing.

Acknowledgements

I have a great many people to thank for their part in creating this thesis. First of all, my deep appreciation and gratitude go to my wife Emma, for her support, understanding, and wonderful cooking – and also for undertaking the proof-reading. I also wish to thank my parents and my family (in which I include Emma's family) for their support, encouragement, and the inspiration to study astronomy and follow my dreams.

I am indebted to my supervisors, Loretta, Omar and Mike, as well as Steve Maddox who acted as my informal supervisor for a large portion of the work in the thesis. This would never have been possible without their advice and guidance, and I am especially grateful to Loretta and Steve for continuing this support throughout their emigration to New Zealand; I have no idea how they managed it. I cannot possibly list the many others for whose direct help and collaboration I am indebted – Rob Ivison, Edo Ibar, Emma Rigby, Dan Smith, Kate Rowlands, Carlos Hoyos, Simon Dye, Baerbel Koribalski, George Bendo, Matt Smith, Haley Gomez, Stephen Serjeant, Steve Eales, Joaquin González-Nuevo, Enzo Pascale – to name just a few. All of the work presented here is the product of collaborations, and I therefore gratefully acknowledge all of my colleagues and co-authors for providing data and all kinds of support that have made this work possible. Many thanks also go to my examiners for the time and effort they spent on assessing the thesis.

I would also like to acknowledge the astronomy community at large, for the indirect support which is always forthcoming, but often taken for granted. The availability of data, open-source software and codes, and general and technical advice in the public domain is overwhelming; and all free of charge. This only happens because individuals are willing to make available the products of their own hard work for the greater benefit of the community, and the value of this open attitude cannot be overstated. There have

been many times when I needed to ask for help from others who have never met me or worked with me, and I cannot think of a single time when anyone has not been keen to offer their time and expertise. In particular, I have made extensive use of the following public databases and software libraries: the NASA/IPAC Extragalactic Database, the Strasbourg Astronomical Data Center (CDS), the HyperLEDA database, `arXiv.org` (hosted by Cornell University Library), The SAO/NASA Astrophysics Data System (ADS), the Starlink software packages (provided by the Joint Astronomy Centre, Hawaii), the Topcat catalogue tool, the NASA IDL library and David Fanning's Coyote IDL Library.

I believe that the last four years in Nottingham have been the happiest of my life, and this is entirely due to the amazing friends that I have made here, both past and present. I do not need to list all of your names because you know who you are, but I will mention the significant contributions that Daniele and Fernando's Coffee Club, and Cafe Alice (with all her regulars), have made to my quality of life and the quality of the work in this document. The astronomy department at the University is an incredible place to work as a result of the people here, and I hope to stay in contact with the friends I have made here, wherever we all end up.

Finally, I know that some people will not be happy unless I include a particularly relevant quote:

"Dust... anybody, no?"

– Margerie Dawes

Contents

List of Figures

List of Tables

Glossary of Terms and Conventions

α	Spectral index of a power-law SED, i.e. $S_\nu \propto \nu^\alpha$
AGN	Active Galactic Nucleus
β	Spectral index of dust emissivity, i.e. $\kappa(\nu) = \kappa_0 \nu^\beta$
γ	Power-law index of evolutionary trend, i.e. $f(z) = (1+z)^\gamma$
CIB	Cosmic infrared background
CO	Carbon monoxide
CRE	Cosmic-ray electron
FIR	Far-infrared ($20 \lesssim \lambda \lesssim 200\,\mu$m)
FRC	Far-infrared–radio correlation
H I	Neutral atomic hydrogen
H II	Ionised hydrogen
H_2	Diatomic molecular hydrogen
IR	Infrared ($1 < \lambda < 1000\,\mu$m)
IMF	Initial stellar mass function
ISM	Interstellar medium
L	A monochromatic luminosity $\equiv L_\nu$ (W Hz^{-1})
$L_{\rm FIR}$	Integrated FIR luminosity ($40 - 120\,\mu$m) ($L_\odot$)
$L_{\rm TIR}$	Integrated total IR luminosity ($8 - 1000\,\mu$m) ($L_\odot$)
$L^\star$	Knee of the luminosity function, i.e. $\Phi(L)dL = \Phi^\star (L/L^\star)^\alpha e^{-(L/L^\star)} d(L/L^\star)$
$M^\star$	Absolute magnitude corresponding to $L^\star$
$M_\star$	Total stellar mass of a galaxy ($M_\odot$)
$M_{\rm dust}$	Total dust mass of a galaxy ($M_\odot$)
$M_{\rm star}$	Mass of a star ($M_\odot$)
MIR	Mid-infrared ($8 \lesssim \lambda \lesssim 20\,\mu$m)
NIR	Near-infrared ($1 \lesssim \lambda \lesssim 8\,\mu$m)
q	Logarithmic IR/radio ratio, e.g. $q_{TIR} = \log_{10}(L_{\rm TIR}/L_{1.4\rm GHz})$
S	A monochromatic flux $\equiv S_\nu$ (Jy)
SED	Spectral energy distribution
SNR	Supernova remnant / signal–to–noise ratio
SFG	Star-forming galaxy
SFR	Star-formation rate ($M_\odot$ yr^{-1})
SSFR	Specific star-formation rate, SFR/$M_\star$
Sub-mm	Sub-millimetre ($200 \lesssim \lambda < 1000\,\mu$m)
$T_{\rm dust}$	Dust temperature (K)
UV	Ultraviolet
z	Redshift

Non-SI Units and Constants

Ångstrom	$\text{Å} = 10^{-10}\,\text{m}$
Jansky	$\text{Jy} = 10^{-26}\,\text{W}\,\text{m}^{-2}\,\text{Hz}^{-1}$
Parsec	$\text{pc} = 3.086 \times 10^{16}\,\text{m}$
Solar mass	$\text{M}_\odot = 1.988 \times 10^{30}\,\text{kg}$
Solar luminosity	$\text{L}_\odot = 3.843 \times 10^{26}\,\text{W}$
AB magnitude	$m_{AB} = -2.5 \log_{10}(S_\nu/\text{Jy}) + 8.90$
Speed of light in vacuum	$c = 2.998 \times 10^{8}\,\text{m}\,\text{s}^{-1}$
Planck's constant	$h = 6.626 \times 10^{-34}\,\text{J}\,\text{s}$
Boltzmann's constant	$k_B = 1.381 \times 10^{-23}\,\text{J}\,\text{K}^{-1}$

Concordance Cosmology

Hubble's constant	$H_0 = 71\,\text{km}\,\text{s}^{-1}\,\text{Mpc}^{-1}$
Cosmological constant	$\Omega_\Lambda = 0.73$
Matter density	$\Omega_\text{M} = 0.27$

No Smoke Without Fire:
Cosmic Dust Emission as a Tracer of Star Formation in Galaxies

Chapter 1

Introduction

This thesis addresses questions about the history of star formation in the Universe and the role that dust can play in helping to answer them. The main body is composed of three self-contained chapters, which cover diverse projects but are linked by core themes: all of the work concerns the study of galaxy evolution by observing dust emission; it utilises multi-wavelength datasets from large surveys; and it focuses on statistical analysis of flux-limited samples. The central theme throughout the thesis is the notion of dust emission providing a window on the growth of galaxies through star formation. In this chapter I will begin by reviewing the relevant history and current status of extragalactic astronomy. I will explain why we should want to observe dust in the Universe and summarise what we have learned about galaxies by doing so. I will conclude this chapter with a plan for the projects described in the rest of the thesis.

1.1 The Origin of Galaxies in the Universe

1.1.1 The Nature of the Universe

Ever since Hubble (1925) first proved the extragalactic nature of the spiral nebulae, observational astronomers have been fascinated by the question of how the galaxies in the Universe came into being. The modern view of galaxies as “island universes” can be traced back to Kant (1755) and Wright (1750), and the term itself was first coined by Descartes (1636), but most of what we understand about the Universe today is thanks

to the rapid explosion of astronomical research that began with Hubble. One of the most fundamental discoveries was the expansion of the Universe, inferred from the radial velocities of galaxies (Hubble 1929; Hubble & Humason 1931). This constituted direct evidence for the Universe having a definite beginning – a singularity from which the Universe itself and everything in it originated – a theory known as the Big Bang (Lemaître 1931). The Big Bang is extremely well proven, from arguments relating to helium and isotopic abundances (Alpher, Bethe & Gamow 1948; Hoyle & Tayler 1964; Wagoner, Fowler & Hoyle 1967) and the temperature and isotropy of the cosmic microwave background (CMB; Alpher & Herman 1948; Penzias & Wilson 1965; Dicke *et al.* 1965; and see Figure 1.1). The question of whether the Universe was fated to continue expanding, or contract back to a final singularity, remained unanswered until observations of distant supernovae finally proved that the expansion of the Universe is accelerating (Riess *et al.* 1998; Schmidt *et al.* 1998; Perlmutter *et al.* 1999; and see also Efstathiou, Sutherland & Maddox 1990). The unknown source of this acceleration is known as dark energy, which some models attribute to the cosmological constant Λ in Einstein's (1917) field equations (see e.g. Longair 1994).

Another fundamental discovery of the 20th century is dark matter (e.g. Ostriker & Peebles 1973), which is inferred from several independent observational results. These include the velocity dispersion of galaxies in clusters (Zwicky 1933), which are related to the total cluster mass by the virial theorem (under dynamical equilibrium; Eddington 1916). The subsequent discovery of hot, X-ray emitting gas reservoirs in clusters (Forman *et al.* 1972; Gursky *et al.* 1972; Kellogg *et al.* 1973) accounted for some of this missing mass, but most still remains unaccounted for. The flat rotation curves of galaxies provided independent evidence for additional invisible mass (Babcock 1939; Bosma 1978; Rubin, Ford & Thonnard 1980), as did the vertical motions of stars in the Galactic disk (Oort 1932). Modified theories of gravity (e.g. Milgrom 1983) may also explain these observations; however they cannot explain gravitational lensing (a prediction of general relativity; Einstein 1916), in which light from distant galaxies and quasars is magnified by a large foreground mass that exceeds the mass of visible matter in the line of sight. This is elegantly demonstrated by the case of the bullet cluster, in which the mass responsible for lensing must reside in between two galaxy clusters, as if they have undergone a dissipational collision (Clowe *et al.* 2006; Angus

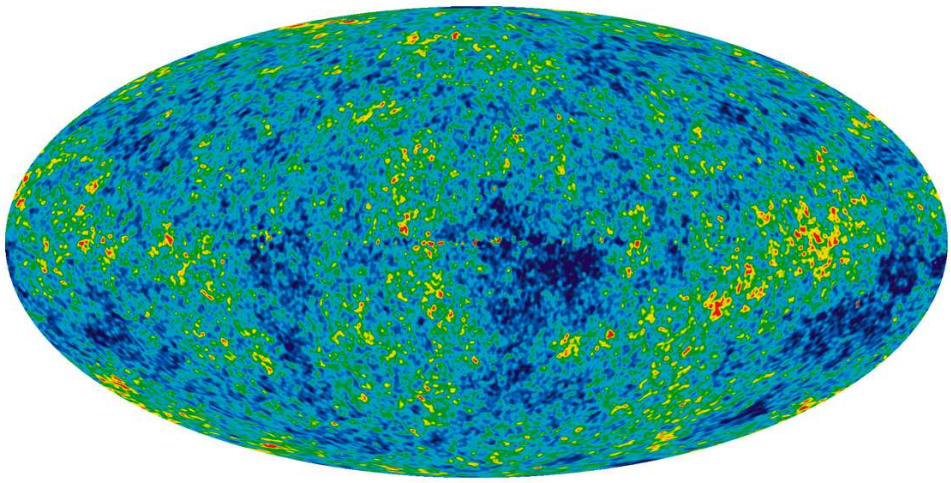

Figure 1.1: Temperature fluctuations in the whole-sky CMB from the Wilkinson Microwave Anisotropy Probe (WMAP) 7-year data (Jarosik *et al.* 2011), after removal of Galactic emission and the primary dipole caused by the motion of the Earth. The discovery of the CMB by Penzias & Wilson (1965) was one of the most significant observations in the history of astronomy: its very existence, its blackbody spectrum, temperature and isotropy, confirm the predictions of the big bang theory (Dicke *et al.* 1965); and subsequent measurements of the power spectrum of temperature anisotropies provide stringent tests of cosmological models, confirming the "concordance model" of ΛCDM. Furthermore, since the CMB radiation was emitted at the epoch of last scattering, when matter and radiation decoupled, this is the first light that it is possible to detect. The deviations from a perfect isotropic blackbody are tiny: temperature anisotropies are shown here on a scale of $\pm 200\,\mu$K around the average temperature of 2.73 K. These result from quantum fluctuations in the early Universe, which were the seeds for the dark matter over-densities and the eventual growth of large-scale structure. Credit: NASA / WMAP Science Team.

et al. 2007). The fact that dark matter does not appear to interact with visible matter or radiation (except via gravity) implies that it is non-baryonic in nature, and consists of some yet unidentified fundamental particle. The currently favoured candidate is a weakly interacting massive particle (WIMP; Peebles 1982; see a recent review by Bertone 2010).

The overarching cosmological paradigm which combines these theories is Lambda–Cold Dark Matter (ΛCDM; Ostriker & Steinhardt 1995). This model describes a spatially flat universe with energy density dominated by approximately 73 per cent dark energy, interpreted as the cosmological constant, and 23 per cent cold dark matter (CDM), with baryonic matter making up most of the remainder. ΛCDM is extremely well tested by independent observations including supernova-calibrated dis-

tances (Riess *et al.* 1998; Schmidt *et al.* 1998; Perlmutter *et al.* 1999), CMB fluctuations (Komatsu *et al.* 2011; Planck Collaboration *et al.* 2011c), baryonic acoustic oscillations (BAOs; Eisenstein *et al.* 2005; Blake *et al.* 2011; Anderson *et al.* 2012), the power spectrum of galaxy clustering in large optical surveys (Tegmark *et al.* 2004; Cole *et al.* 2005; etc) and that of dark matter from weak lensing (Refregier 2003; and references therein). A detailed, up-to-date review of the techniques may be found in Mo, van den Bosch & White (2010).

1.1.2 The Era of Galaxies

Once the expanding Universe had cooled sufficiently, atoms began to form out of the primordial plasma. This "recombination" occurred a few 10^5 years after the Big Bang ($z \sim 1100$), at a time when perturbations in the dark matter distribution had already grown large enough for the baryonic matter to collect in gravitational potential wells (see e.g. Rowan-Robinson 2004; Mo, van den Bosch & White 2010). These overdensities grew into the seeds for the galaxies and large-scale structure which were assembled over the ensuing 13.7 billion years (Figures 1.2, 1.3; Press & Schechter 1974; White & Rees 1978). In the first proto-galaxies, small clumps of gas became dense and cool enough for gravity to overcome the stabilising forces and for nuclear fusion to begin in the collapsing cores (Toomre 1977; White & Rees 1978). Thus stars were born, beginning a cycle that uses elemental hydrogen and helium to manufacture heavier elements ("metals"), and returns the metal-enriched gas to the interstellar medium (ISM). The first stars are likely to have been predominantly large and hot, and were probably responsible for the gradual reionisation of the intergalactic gas (occurring between $z \sim 6 - 15$), which finally made the Universe transparent to optical light (Rowan-Robinson 2004; Appleton *et al.* 2009).

Numerical N-body simulations (Figure 1.4) show that gravitationally-interacting dark matter develops structures hierarchically, with small haloes coalescing to assemble larger structures, culminating in the cosmic web of clusters, filaments and voids seen in the present-day Universe (Figure 1.5; Davis *et al.* 1985; Colberg *et al.* 2000; Evrard *et al.* 2002; Springel *et al.* 2005). However, luminous (baryonic) matter interacts in more complicated ways that are impossible to model precisely, and a class of mod-

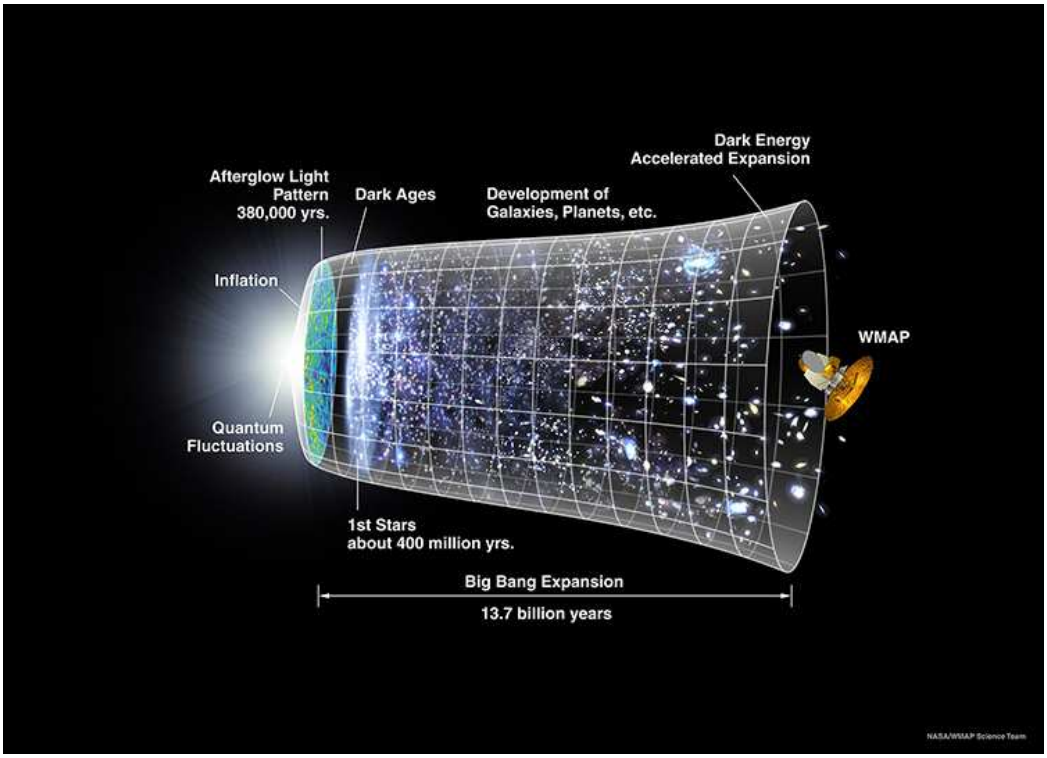

Figure 1.2: Schematic representation of the growth of structure in the Universe, from quantum fluctuations following the big bang (far left), being magnified through Inflation (Guth 1981) resulting in the CMB emitted from the last scattering surface; the first stars which reionised the Universe, and the evolution of galaxies stretching through to the present day. Image credit: NASA/WMAP Science Team.

els known as semi-analytical models (SAMs) has arisen in an attempt to address this shortfall (e.g. Cole *et al.* 1994, 2000; Baugh, Cole & Frenk 1996; de Lucia *et al.* 2006).

An example of the complex evolution of baryons is that galaxies appear to have assembled anti-hierarchically. This is evident from the simple observation that the most massive galaxies in the present day contain the oldest stars (Heavens *et al.* 2004; Gallazzi *et al.* 2005; Panter *et al.* 2007), and from high-redshift observations showing that the massive galaxy population was largely in place by $z \sim 1$, about six billion years after the Big Bang (Dickinson *et al.* 2003; Bundy, Ellis & Conselice 2005; Conselice *et al.* 2007; Pérez-González *et al.* 2008). Such a top-down formation scenario is also supported by observations of star-formation rates (SFRs) peaking at earlier times in more massive galaxies (Cowie *et al.* 1996; Kodama *et al.* 2004; Bauer *et al.* 2005; Feulner *et al.* 2005; Bundy *et al.* 2006; Chen *et al.* 2009). Analogies in the relationship between metallicity[1] and stellar mass in elliptical galaxies have been cited as

[1] i.e. the relative abundance of heavy elements, measured from the spectral features of N, O, Mg, Fe,

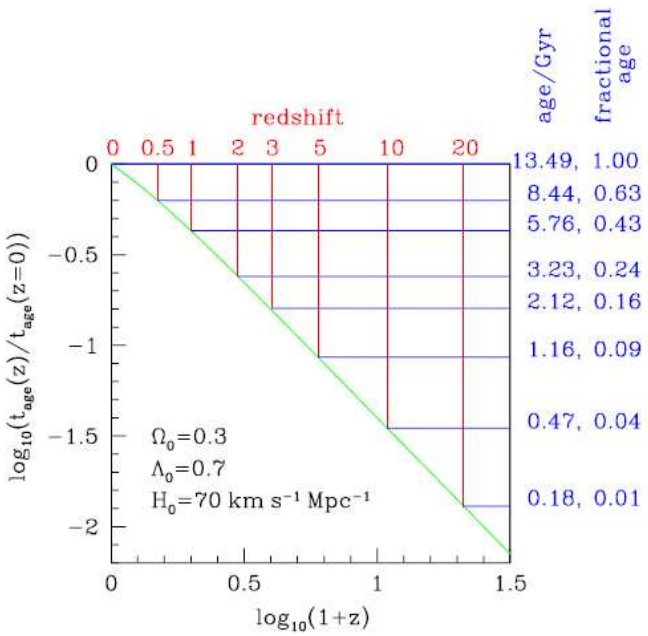

Figure 1.3: Observations of distant sources probe the Universe at earlier times, due to the finite and constant speed of light. The light we detect has undergone cosmological redshifting due to the expansion of the Universe since it was emitted. This diagram shows the relationship between the redshift and the age of the Universe when the light was emitted, under the concordance cosmology approximated by the parameters shown. According to this cosmology, the redshift range $0 < z < 1$ spans almost 60 per cent of the history of the Universe (the last six billion years). Reionisation is thought to have occurred around $6 < z < 15$ (in the first billion years), while the peak epoch of star formation occurred at $z \sim 2$, when the Universe was around three billion years old. Figure taken from Baugh (2006; Figure 2).

additional evidence for earlier formation times for more massive galaxies (Worthey, Faber & Gonzalez 1992; Matteucci 1994; Thomas *et al.* 2005), while the differential evolution of metallicity with redshift in galaxies of different masses corroborates such an interpretation (Savaglio *et al.* 2005; Erb *et al.* 2006; Maiolino *et al.* 2008). These various pieces of evidence for anti-hierarchical galaxy formation are known by the umbrella term of "downsizing" (Cowie *et al.* 1996); a comprehensive review is given by Fontanot *et al.* (2009).

The diversity of galaxy morphologies, from elliptical to spiral and irregular types (see below), and particularly the abundance of thin spiral disks, is difficult to reconcile with models, in which galaxies undergo major mergers which destroy thin disks and transform galaxies into ellipticals (Toomre 1977; Navarro & White 1994; Steinmetz & Navarro 2002; Puech *et al.* 2012). Another problem is that N-body simulations predict a far greater number of low-mass haloes that should contain galaxies, compared

etc. either in the atmospheres of stars (as absorption lines) or in interstellar gas (as emission lines).

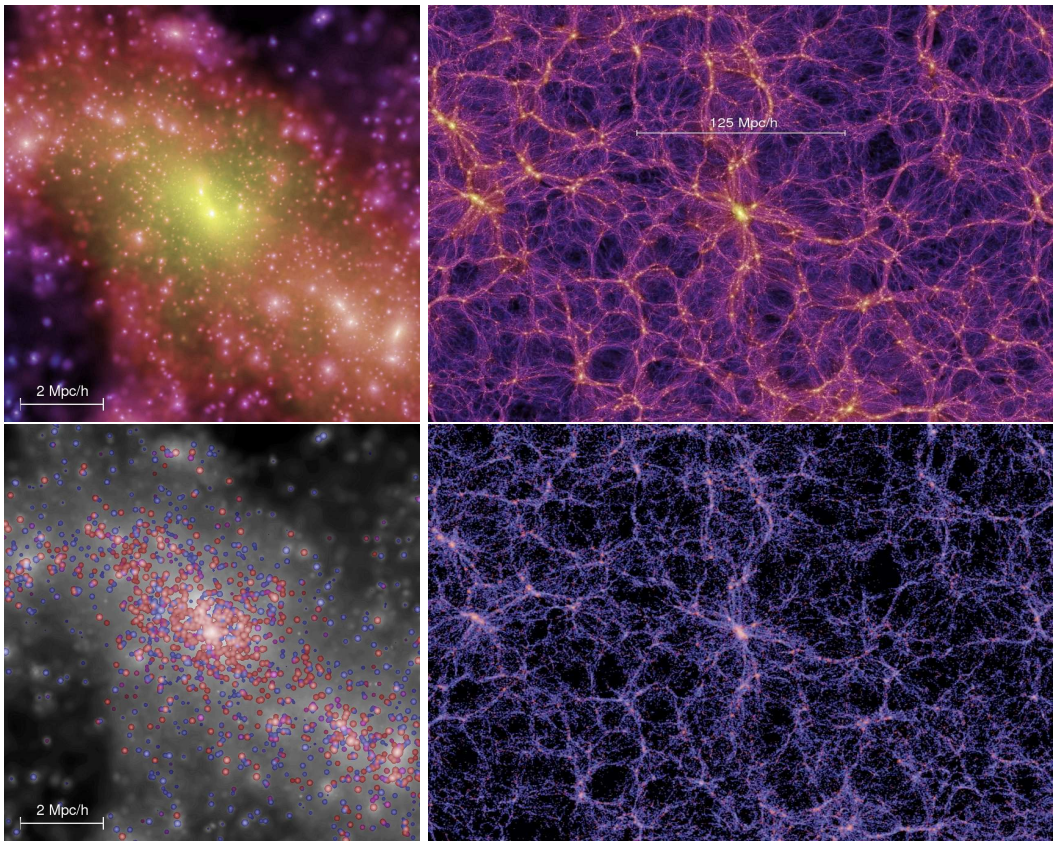

Figure 1.4: Snapshots from the Millennium Simulation (Springel *et al.* 2005) at $z = 0$. The upper two images show the dark matter distribution on the scale of an individual galaxy cluster (left) and a larger volume encompassing the large-scale structure of filaments and voids (right). Intensity represents surface density and colour represents local velocity dispersion. The lower two images show the galaxy light distribution in the same volumes from the SAM of Croton *et al.* (2006). Intensity and colour represent that of the optical light, with redder galaxies being more concentrated in the denser regions. Credit: Volker Springel and the Max-Planck-Institute for Astrophysics.

to the number of low-mass galaxies actually observed (Figure 1.6; White & Frenk 1991; Kauffmann, Guiderdoni & White 1994; Baugh 2006). This problem is manifested in the relatively small number of satellite galaxies observed in the local group, compared with the substructure seen in simulated galactic haloes (Moore *et al.* 1999; Kuhlen *et al.* 2008; Springel *et al.* 2008). The models also tend to predict too many extremely high-mass galaxies, due to overly efficient cooling of the gas (see e.g. Benson *et al.* 2003; Baugh 2006). Stars can only form from cold gas, so in order to reconcile the simulations with observations, modellers have proposed negative feedback scenarios which stifle star formation either by heating or by expelling the in-falling gas (White & Frenk 1991; Cole *et al.* 1994; Benson *et al.* 2003). The leading candidate for the quenching of star formation in high-mass galaxies is feedback from active galactic nuclei (AGN), powered by an accreting supermassive black hole (SMBH) in the

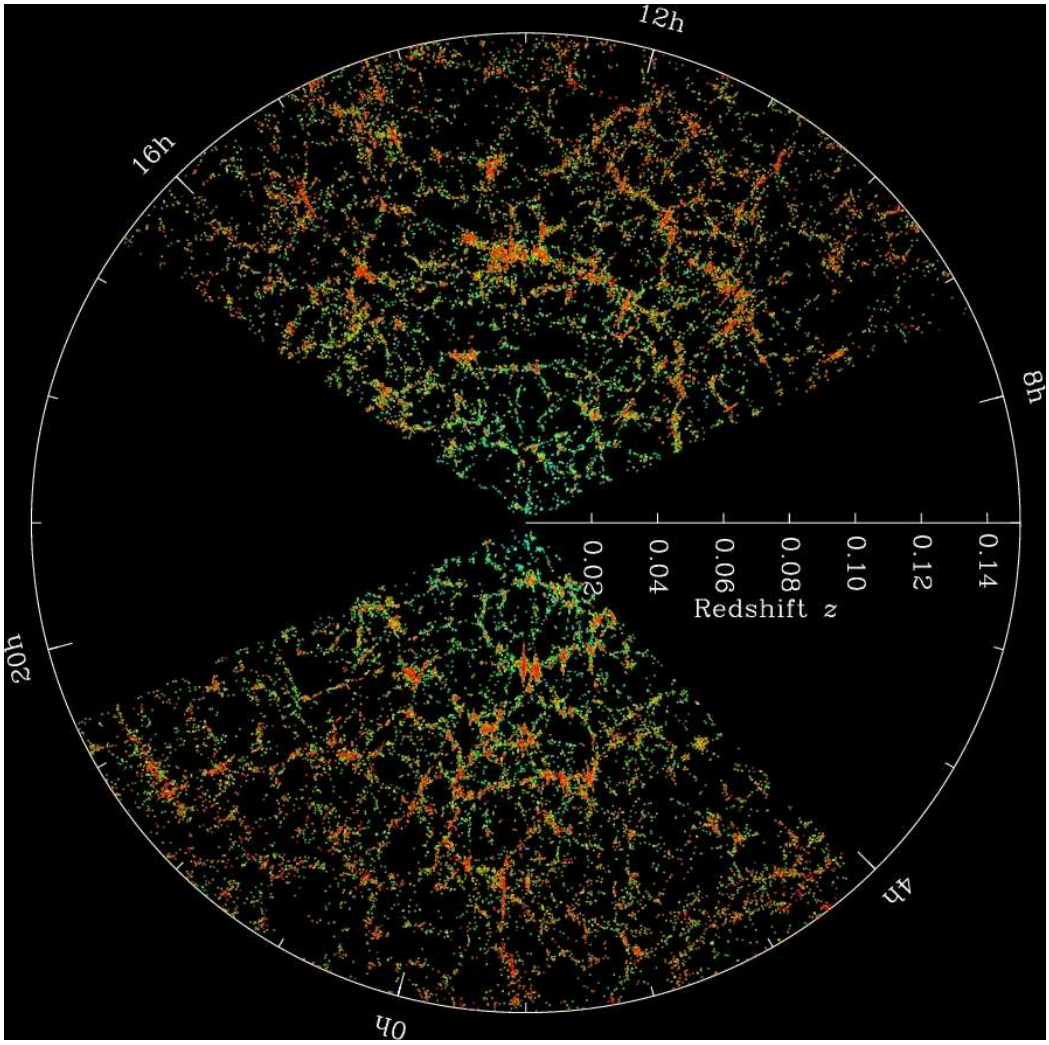

Figure 1.5: A slice ($-1.25 <$ Dec. < 1.25) through the Universe as mapped by the latest release of the Sloan Digital Sky Survey, SDSS-III (Aihara *et al.* 2011), showing how the distribution of galaxies at low redshifts ($z < 0.14$) probes the large-scale structure of dark matter (c.f. Figure 1.4). Galaxies are coloured according to their stellar mass, and the most massive (red) galaxies are seen to cluster most strongly around the density peaks. Credit: M. Blanton and the Sloan Digital Sky Survey.

centre of each galaxy, which drive off the inflowing cold gas in galactic super-winds ("quasar-mode feedback"; Di Matteo, Springel & Hernquist 2005) or by mechanical heating ("radio-mode" feedback; Croton *et al.* 2006). Such a scenario is not possible in the lower mass galaxies, whose AGN would not be powerful enough, but their numbers can be suppressed by supernova-driven feedback and the removal of gas via ram-pressure and tidal stripping (Bullock, Kravtsov & Weinberg 2000; Benson *et al.* 2002; Somerville 2002). With the addition of feedback prescriptions of this kind, the distribution of galaxy properties predicted by SAMs can reproduce the observations with high fidelity (e.g. Bower *et al.* 2006; de Lucia *et al.* 2006).

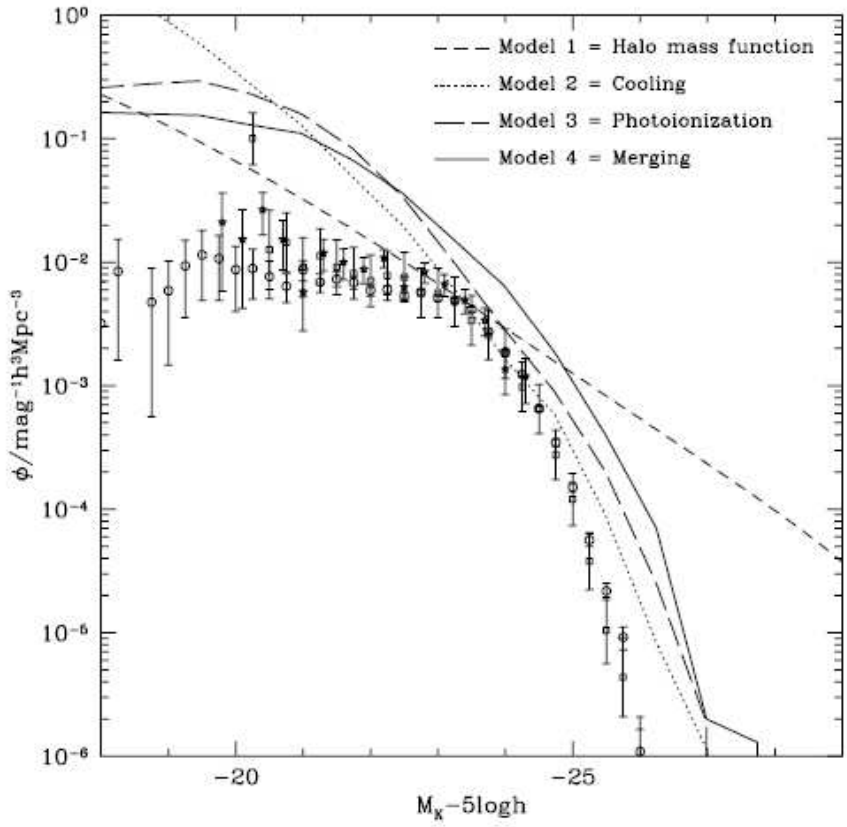

Figure 1.6: K-band luminosity functions of galaxies (number per unit magnitude per unit volume as a function of absolute magnitude) comparing data with models (Figure taken from Benson *et al.* 2003; Figure 1). Data are from Cole *et al.* (2001; circles); Kochanek *et al.* (2001; squares); Huang *et al.* (2003; stars). Lines show the results of the GALFORM SAM: (Model 1) with fixed halo mass-to-light ratio; (Model 2) including a gas cooling prescription; (Model 3) adding in photo-ionisation to suppress low-mass galaxy formation; and (Model 4) accounting for merging. Notice that the halo mass function (short-dashed line) drastically over-estimates the numbers of low-mass (far-left) and high-mass (far-right) galaxies, and that the addition of extra physical prescriptions shown here is not sufficient to reproduce the observed luminosity function.

1.1.3 The Rich Diversity of Galaxies

Clues to the processes of galaxy evolution can be obtained by examining the global properties of populations of galaxies, which is the focus of this thesis. A fundamental observation regarding the nature of galaxies is the bimodality of the population, which is noticeable in many different properties. One of the most obvious of these is the visual morphologies, which break down into two broad categories – spirals and ellipticals – encompassing many sub-catagories, most notably the division into barred and non-barred spirals. This was first formalised by Hubble (1926) into a sequence of classifications ranging from “early-type” ellipticals to “late-type” spirals, famously depicted in the “tuning fork” diagram (Hubble 1936). Hubble chose the terms “early” and “late”

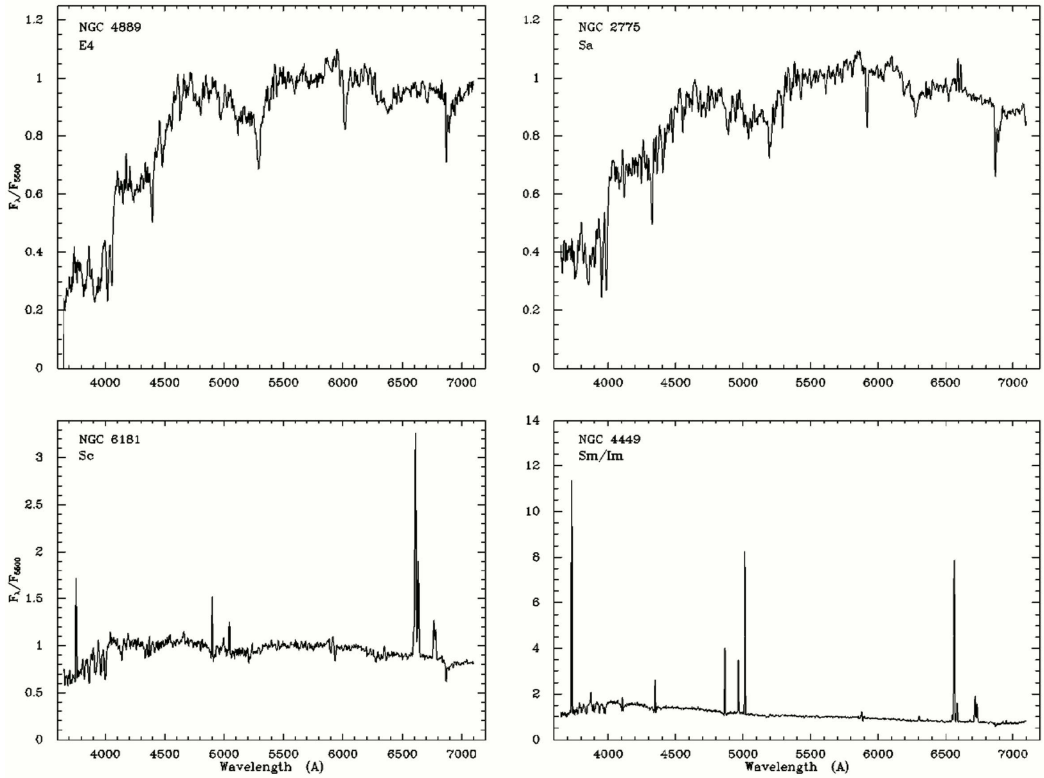

Figure 1.7: Optical spectra ($3600 < \lambda < 7200$ Å) of typical nearby galaxies of various morphological types (from left-right, top-bottom: elliptical, early-type spiral, late-type spiral, irregular) from Kennicutt (1992). The early-type galaxies have generally redder spectra, with a strong 4000 Å break and no emission lines, indicating an evolved stellar population. The late-type galaxies have bluer spectra due to the presence of hot, young stars, and strong nebular emission lines resulting from photo-ionised gas in the vicinity of star-forming regions. The strongest four lines seen in both of the bottom two panels are [OII]λ3727, Hβ λ4861, [OIII]λ5007, and Hα λ6563 (blended with [NII]λ6583), all of which are indicators of ongoing star-formation. Figure taken from Kennicutt (1998a; Figure 1).

to emphasise a continuous trend of increasing complexity (see Hubble 1926), and they bear no relation to any evolutionary sequence. Various alternatives, extensions and revisions to Hubble's scheme have emerged over the years to account for the increasing diversity of galaxies revealed by improved observations (Morgan 1958; de Vaucouleurs 1959, 1977; van den Bergh 1976; Kormendy & Bender 1996, 2012; Cappellari *et al.* 2011). Yet all of these schemes retain the fundamental essence of Hubble's tuning fork, especially the two broad classes which encompass the vast majority of bright galaxies.

The optical spectra of late-type galaxies (LTGs; types Sa/SBa and later) usually show the signatures of hot ionised gas heated by young stars (Figure 1.7), and they have blue broadband colours due to their light being dominated by emission from young stars (Figure 1.8. This contrasts with the red colours and lack of emission lines in early-type

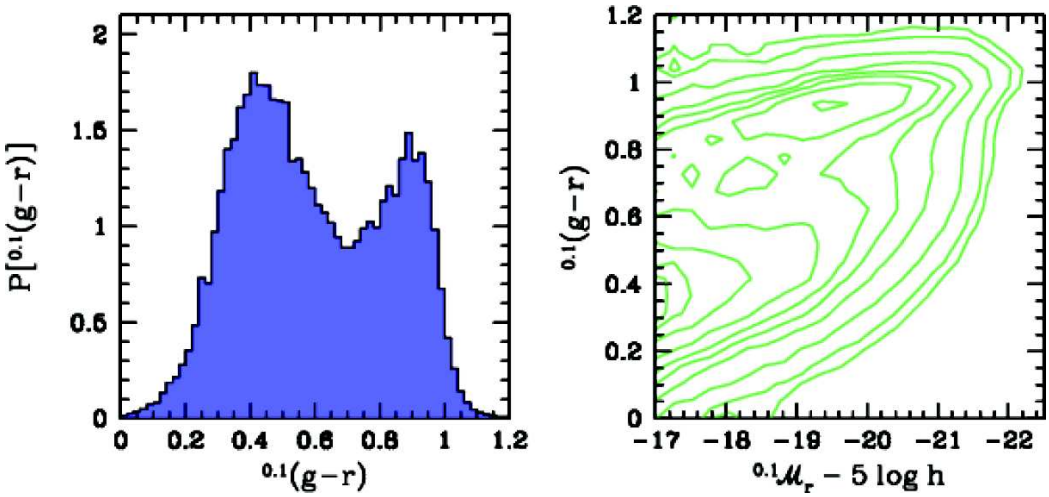

Figure 1.8: The bimodality in galaxy colours is shown in the probability density histogram of $g-r$ colours in $\sim 365,000$ galaxies from SDSS (left), and by the colour-magnitude diagram (CMD) of the same galaxies (weighted to account for Malmquist bias;[2] right). In the CMD, red galaxies (at the top) with little or no ongoing star-formation tend to lie along a tight linear locus known as the red sequence, while blue galaxies inhabit a more diffuse locus at generally higher absolute magnitudes (lower luminosities) known as the blue cloud. Note that the two populations are not distinct, and a significant number of galaxies fall in the intermediate region known as the green valley. This can include galaxies transitioning from a blue star-forming phase to a red quiscent phase, as well as blue SFGs which are reddened by dust (see Section 1.3). Figure taken from Mo, van den Bosch & White (2010; Figure 2.27).

galaxies (ETGs; types E+S0), which indicate a more quiescent population devoid of young stars or any trace of recent star-forming activity (Roberts 1963; Kennicutt & Kent 1983; Sandage 1986). Spiral galaxies are also generally richer in interstellar gas and dust compared to ellipticals, supporting the idea that the evolved ellipticals have exhausted (or expelled) their gas supply, and the formation of new stars to produce dust has dried up (see reviews by Soifer *et al.* 1987; Roberts & Haynes 1994; Kennicutt 1998a).

Galaxies grow as they gradually turn gas into stars, but the fact that many massive galaxies are passive shows that the star formation does not continue unabated forever. Furthermore, the huge reservoirs of hot gas surrounding giant ellipticals in clusters reveal that the galaxies do not simply run out of gas, in which case there must be some process to stop it cooling and accreting (Fukugita, Hogan & Peebles 1998; see also discussion in Section 1.1.2). Likewise it is clear that galaxies which do contain cold

[2]Malmquist bias is the tendency for a flux-limited sample to be increasingly dominated by more luminous sources with increasing distance (Malmquist 1922). To correct for this, galaxies in a sample can be weighted according to the volume within which they are detectable in the survey (Schmidt 1968; see Section 3.2.2 for more details).

gas do not convert it into stars with maximal efficiency, implying that some regulation must occur (e.g. Kennicutt 1998b).

The bimodality seems to imply that blue, star-forming spirals might evolve into red and dead ellipticals once their star formation has ceased. But what controls whether a galaxy is forming stars or not; what initiates star formation and what quenches it? A common dichotomy discussed in the literature is the notion of "nature versus nurture". Galaxy evolution might be controlled by external processes, merging and interaction, which is supported by observed correlations between galaxy environment and colour (Butcher & Oemler 1984; Pimbblet *et al.* 2002), morphology (Dressler 1980; Postman & Geller 1984), and SFR (Lewis *et al.* 2002). On the other hand, galaxy evolution could depend on secular galaxy properties or processes, and this is supported by observations of general correlations or scaling relations which are independent of environment. Examples include the Tully-Fisher relation between disk luminosity and rotational velocity (Tully & Fisher 1977); the Fundamental Plane relating the velocity dispersion, central surface brightness, and effective radius of elliptical galaxies (Faber & Jackson 1976; Djorgovski & Davis 1987; Dressler *et al.* 1987); and the Schmidt-Kennicutt (SK) law relating SFR surface density to gas surface density (Schmidt 1959; Kennicutt 1998b; see Chapter 4). Tight correlations exist between the mass of the central SMBH and the mass or velocity dispersion of the bulge of a galaxy (Magorrian *et al.* 1998; Gebhardt *et al.* 2000), indicating a link between galaxy formation and the growth of the SMBH. On the other hand, the Fundamental Metallicity Relation linking stellar mass, gas-phase metallicity and SFR in star-forming galaxies (SFGs; Tremonti *et al.* 2004; Mannucci *et al.* 2010), has been shown in recent work to vary between the centres and outskirts of clusters (Petropoulou, Vilchez & Iglesias-Paramo 2012).

The feedback scenarios described in earlier paragraphs provide possible means by which star formation can be either limited or halted outright by internal processes. Mechanisms for direct environmental feedback on galaxies include tidal interactions between galaxies and the cluster environment (White & Rees 1978; Mamon 1992), and "strangulation" or "stripping" of gas from in-falling spiral galaxies in clusters (Gunn & Gott 1972; Butcher & Oemler 1978; Larson, Tinsley & Caldwell 1980). These are supported by observational evidence that spirals are transformed into lenticulars (type S0)

in clusters (Dressler *et al.* 1997; Fasano *et al.* 2000; Moran *et al.* 2007). In addition, both tidal interactions and mergers between individual galaxies can certainly have a significant impact on the galaxies involved (e.g. Larson & Tinsley 1978; Condon *et al.* 1982; Keel *et al.* 1985) – the question therefore is whether such strong interactions (and their effects) are common enough to be important for the population as a whole, in clusters and in the field (e.g. Perez *et al.* 2009; de Ravel *et al.* 2011; Draper & Ballantyne 2012; Tonnesen & Cen 2012). Overall, it appears that both nature and nurture have some influence on galaxy evolution, but the competing factors are complex and hard to disentangle. In this thesis I will investigate the relationships between the ISM, stellar populations and star formation in samples of galaxies at various redshifts, in order to cast light on some of the factors determining galaxy evolution.

1.2 Observing Star Formation in Galaxies

The study of galaxy evolution is for a large part concerned with the history of star formation, since stars constitute perhaps the most important component of a galaxy. They are not just the most readily observed component, but they drive some of the most complex chemical and physical processes, and their formation and evolution impacts on the galaxy as a whole, including the gas and dust in the ISM.

1.2.1 Direct Observations: Unobscured Star Formation

There are many different approaches to measuring the SFRs of galaxies. One of the most direct methods is to measure the ultraviolet (UV) continuum luminosity, since this light is emitted mostly by hot, young stars (spectral types O and B; see e.g. Carroll & Ostlie 1996) with lifetimes $< 10^8$ years (Kennicutt 1998a), hence they trace the SFR averaged over that period of time. An alternative is to measure nebular emission lines in optical spectra: the Balmer lines of hydrogen (Hα, Hβ, etc), as well as ionised metal lines such as [OII]λ3727, [OIII]λ5007 (see Figure 1.7) are used to trace gas in H II regions, the bubbles of photo-ionised gas that form around the hottest OB stars (Stromgren 1939). These trace a slightly more instantaneous SFR because the stars that emit ionising radiation have lifetimes of $< 2 \times 10^7$ years (Kennicutt 1998a). Strictly

speaking, all methods linked to OB stars trace only the formation rate of massive stars. More massive stars burn hotter (effective temperatures $> 10,000$ K for O and B types), so emit more ionising radiation; but they are much rarer (e.g. Carroll & Ostlie 1996). Ultraviolet-emitting OB stars on the Main Sequence have mass $M_{\rm star} > 3\,{\rm M}_{\odot}$, although only stars with $M_{\rm star} > 10\,{\rm M}_{\odot}$ contribute significant ionising flux.

The conversion from these tracers to the total SFR therefore depends on the relative number of massive stars that form, which is determined by the distribution of initial masses. The initial mass function (IMF) is generally believed to be fairly constant among different galaxies and galactic star-forming regions (see review by Bastian, Covey & Meyer 2010), although understanding what controls it and how much it can vary is a topic of active research (Covey, Bastian & Meyer 2011). Evidence has recently begun to emerge that the IMF may vary as a function of mass-to-light ratio (Cappellari *et al.* 2012) or central velocity dispersion (Ferreras *et al.* 2012) in elliptical galaxies (see also van Dokkum & Conroy 2010), while some studies have claimed evidence of a variable IMF in globular clusters and ultra-compact dwarfs around the Milky Way (Kroupa *et al.* 2011; Dabringhausen *et al.* 2012; Marks *et al.* 2012). Clearly the popular concept of a universal IMF remains a contentious issue.

One further issue with emission line tracers is that young stars are not the only source of ionising radiation. Thermal emission from AGN accretion disks peaks in the UV or soft X-ray regime, so these will create H II regions of their own, leading to emission lines such as Hα when the electrons and protons recombine. The excitation levels are generally higher than in stellar H II regions, due to the hotter thermal spectrum of the accretion disk, so it is possible to distinguish AGN from star formation using line-ratio diagnostics (Baldwin, Phillips & Terlevich 1981; Veilleux & Osterbrock 1987).

Spectroscopic observations become more difficult at high redshifts, as the Hα line shifts into the near-infrared (NIR) at $z \sim 0.4$, while other tracers such as [O II] are subject to uncertain dust extinction and variation with metallicity (Jansen, Franx & Fabricant 2001; Kewley, Geller & Jansen 2004). The UV continuum is easily accessible (redshifted into the rest-frame optical at $z \sim 1-2$ or NIR at $z \gtrsim 3$) but can require very large and uncertain corrections for dust extinction (see Section 1.3.2). High-redshift Hα SFRs can be obtained from deep NIR spectroscopy, given long in-

tegration times on large ground-based telescopes (e.g. Erb *et al.* 2006), or from grism surveys utilising "slitless spectroscopy" (Pirzkal *et al.* 2004; Atek *et al.* 2010; Nelson *et al.* 2012). Another successful technique is to use photometric surveys in tunable narrow-band filters to pick out Hα emission at a specific redshift, which is a convenient way to collect a large sample of SFGs in a known cluster for example (Ly *et al.* 2007; Koyama *et al.* 2010; Sobral *et al.* 2012). A major issue with this technique is that different lines are selected at different redshifts by a single narrow-band filter, so alternative means must be used to confirm the redshifts of the objects selected.

1.2.2 Indirect Tracers: Radio, X-ray and Infrared

More indirect methods for measuring SFRs are useful to avoid some of the problems discussed above and are particularly suited for large surveys of SFGs, especially at high redshifts. The radio wavebands provide one such method which has been widely exploited (Daddi *et al.* 2007b; Ivison *et al.* 2007; Seymour *et al.* 2008; Carilli *et al.* 2008; Dunne *et al.* 2009a; Ibar *et al.* 2010; Ashby *et al.* 2011; Karim *et al.* 2011). They have the advantage of being accessible to ground-based facilities, unlike the IR or X-ray (see below), and do not suffer from any extinction or metallicity dependence, unlike the UV continuum and optical (metal) emission lines. Radio continuum emission from SFGs originates from two main sources. The dominant component at the frequencies that are usually observed in this context (e.g. 1.4 GHz – see Chapter 2) is synchrotron emission from cosmic-ray electrons (CREs), which are accelerated to relativistic velocities in shock fronts in expanding supernova remnants (SNRs) and subsequently travel through the galaxy's magnetic field. A shallower thermal component is also present due to bremsstrahlung (free-free) radiation from electrons in H II regions, but this becomes dominant only at high frequencies ($\gtrsim 30$GHz) and at 1.4 GHz only comprises $\sim 10\%$ of the radio flux (Condon 1992; Murphy *et al.* 2011).

Radio SFR estimators are calibrated to the IR (e.g. Condon 1992; Bell 2003), via the ubiquitous far-infrared–radio correlation (FRC; van der Kruit 1973). This forms the subject for Chapter 2 and so I leave further discussion until then. Suffice it to say that the universality and tightness of this correlation provides strong evidence for the validity of the radio tracer. AGN are the chief source of contamination for radio SFRs:

quasars (quasi-stellar radio sources, a variety of AGN common at high redshift) emit a strong non-thermal (synchrotron) spectrum from the nucleus. Radio-loud quasars can be identified as outliers on the FRC itself (if IR data are available), or by their X-ray emission (if X-ray data are available). However, the issue of whether radio-quiet quasars/AGN can also significantly contaminate SFRs is more subtle (Seymour *et al.* 2009; Padovani *et al.* 2011).

X-ray fluxes can provide a further indirect measure of the SFR. There are three main sources of X-ray emission in SFGs: high-/low-mass X-ray binaries (HMXBs/LMXBs) and SNRs (e.g. Kurczynski *et al.* 2010). X-ray binaries are accreting neutron stars (or occasionally black holes) with either a low-mass ($< 1\,\mathrm{M}_{\odot}$) companion star (LMXBs) or a high-mass ($> 8\,\mathrm{M}_{\odot}$) companion (HMXBs). The X-ray emission in both cases originates from interactions between the accretion flow and the neutron star's magnetic field. SNRs emit a thermal X-ray spectrum during the phases of free and adiabatic expansion (Persic & Rephaeli 2002). X-ray emission from HMXBs and SNRs therefore traces the SFR via the population of short-lived massive stars, but LMXBs are long-lived hence are uncorrelated with the SFR. The effectiveness of the X-ray tracer therefore depends on the relative contribution from these sources. Starburst galaxies can be strong X-ray sources (Persic & Rephaeli 2002); however AGN are also strong X-ray emitters, and the chief problem with the X-ray SFR tracer lies in identifying and removing the AGN contamination. Nevertheless, X-ray SFR estimators, calibrated to the far-infrared (FIR), have been successfully tested at both low and high redshifts (Ranalli, Comastri & Setti 2003; Persic *et al.* 2004; Reddy & Steidel 2004; Lehmer *et al.* 2010; Symeonidis *et al.* 2011).

The radio tracer is linked to core-collapse supernovae (Type II, plus Ib and Ic), while the X-ray tracer is linked to these as well as HMXBs. Both methods therefore trace high-mass stars, $M_{\mathrm{star}} \gtrsim 8\,\mathrm{M}_{\odot}$ (the only stars that produce these phenomena; Carroll & Ostlie 1996), which have lifetimes $< 10^7$ years. The non-thermal radio emission is additionally smeared out (both spatially and temporally) as the relativistic CREs travel through the galaxy emitting synchrotron radiation over lifetimes of order 10^8 years (Condon 1992).

Finally we come to the most important indirect SFR tracer, the IR continuum, upon

which both X-ray and radio methods are calibrated. The IR measures the emission from interstellar dust. Since this forms the basis of the thesis, I will give a more detailed review of the astrophysical and observational significance of dust in the following section.

1.3 The Importance of Dust

1.3.1 What is Dust?

It has long been known that the Milky Way and many other galaxies contain substantial amounts of interstellar dust that scatters and absorbs radiation at optical and UV wavelengths (Trumpler 1930; van de Hulst 1946; Oort & van de Hulst 1946; also see Figure 1.9). This dust is a substance similar to smoke or soot, consisting of small ($< 1\,\mu\mathrm{m}$ in size) grains of graphite and silicates, as well as large molecules such as polycyclic aromatic hydrocarbons (PAHs; Tielens & Allamandola 1987a; Draine *et al.* 2007; Draine & Li 2007). The dust is traditionally thought to form in the outer envelopes of intermediate-age stars with large mass outflow rates, in particular red giant branch (RGB) stars and thermally-pulsing asymptotic giant branch (TP-AGB) stars. These are stars with masses of $1 < M_{\mathrm{star}} < 8\,\mathrm{M}_{\odot}$ in a late phase of evolution after leaving the Main Sequence. The zero-age main sequence (ZAMS, measured from when they join the main sequence) ages of such stars vary between $\sim 10^{7}\,\mathrm{yr}$ ($8\,\mathrm{M}_{\odot}$) and $\sim 10^{10}\,\mathrm{yr}$ ($1\,\mathrm{M}_{\odot}$; Carroll & Ostlie 1996). For dust to be produced, stars must first form heavy elements (metals) through a chain of a nuclear reactions beginning with the triple-alpha process and the CNO cycle. In the former, high temperature and pressure in the cores of stars allow three ^{4}He nuclei to combine to form ^{12}C. This catalyses the CNO cycle, which produces nitrogen and oxygen from carbon and hydrogen, and further catalyses the synthesis of all elements lighter than ^{56}Fe. The combination of high densities ($\sim 10^{19}\,\mathrm{m}^{-3}$) and relatively low temperatures ($\sim 1000\,\mathrm{K}$) in the envelopes of RGB and AGB stars allows for metals to solidify into grains, which are either carbonaceous or silicate-based, depending on whether the star is carbon-rich (i.e. a carbon star) or oxygen-rich. Radiation pressure carries the grains out in the stellar wind as they cool and enter the ISM (Whittet 2003). It is also possible for dust to

form in the remnants of type II supernovae, the end-points of $> 8\,\mathrm{M}_{\odot}$ stars, although the yields are highly uncertain (Rho *et al.* 2008; Dunne *et al.* 2009a; Gomez *et al.* 2009; Barlow *et al.* 2010; Fallest *et al.* 2011; Matsuura *et al.* 2011; Lakićević *et al.* 2011; Temim *et al.* 2012). Dust can be formed in other phases of stellar evolution which involve rapid mass loss, including type Ia supernovae, novae, Wolf-Rayet stars, and planetary nebulae, although these mechanisms are thought to be comparatively less important (Cherchneff 2010; Gall, Hjorth & Andersen 2011; Gomez *et al.* 2012a; Nozawa *et al.* 2011). Once formed, grains can grow in the ISM if the conditions are right for them to acquire mantles of ices, which provide a substrate for metals to condense out of the ISM and adsorb onto the grain (Tielens & Allamandola 1987a; Blain *et al.* 2004). The relative importance of all these formation/growth modes is a topic of active research, but there is growing evidence that dust must be produced very rapidly by multiple mechanisms, for example from observations of the large masses of dust already present at high redshifts (e.g. Gall, Hjorth & Andersen 2011; Michalowski *et al.* 2011). In particular, the first dust produced in the early Universe must come from short-lived stars (age $\lesssim 1\,\mathrm{Gyr}$; mass $\gtrsim 3\,\mathrm{M}_{\odot}$) which have had time to form, produce metals, and lose mass through post-main-sequence stellar winds or supernovae, within the age of the Universe at $z > 6$ (Gall, Hjorth & Andersen 2011).w

Dust can also be destroyed in the ISM. The main processes for destruction are sputtering (collisions between gas atoms and the dust grains, particularly in dense environments) and shock waves from supernovae (Draine & Salpeter 1979; Tielens & Allamandola 1987a; Whittet 2003; Blain *et al.* 2004). Dust may even be removed by outflows if it is coupled to the gas which is removed by feedback processes as described in Section 1.1.3. As a result, dust has a finite lifetime in a galaxy, and old "red and dead" galaxies are not generally expected to contain large amounts of dust. There is however accumulating evidence for significant dust masses in early-type/red-sequence galaxies (Vlahakis, Dunne & Eales 2005; Stickel, Klaas & Lemke 2007; Rowlands *et al.* 2012; Bourne *et al.* 2012; Smith *et al.* 2012b). This will be discussed in more detail in Chapter 3.

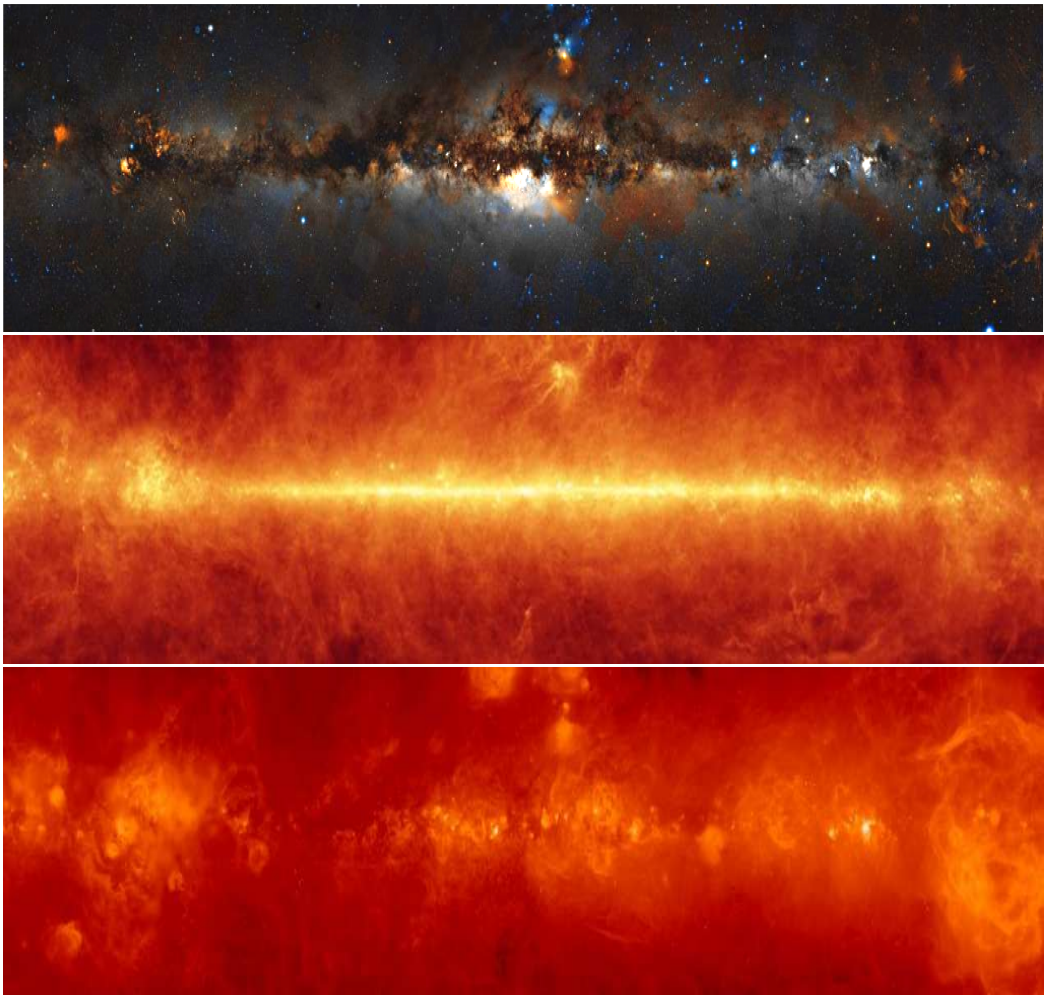

Figure 1.9: The Milky Way in the optical, FIR and Hα wavelengths respectively. As we look through the plane of the Galaxy, we see dark clouds where dust blocks the optical starlight (top panel). These appear red because blue light is preferentially scattered. The dust is seen glowing in the FIR (middle panel) due to its cold temperature. It glows brightest in regions where stars have recently formed, which are revealed by bright bubbles of Hα emission in H II regions (bottom panel). Images from `www.chromoscope.net`. Credit: DSS/Wikisky (optical); IRAS/NASA (FIR); WHAM/VTSS/SHASSA/Finkbeiner (Hα).

1.3.2 Reprocessing of Starlight

Dust is responsible for the extinction of starlight at short wavelengths via absorption and scattering processes. The combined effect of these processes leads to an extinction curve as a function of frequency that is dominated by a positive slope and a strong absorption feature centred at 2175 Å in the Milky Way (Figure 1.10), although the form can vary from one galaxy to another (Calzetti, Kinney & Storchi-Bergmann 1994). The slope leads to the observed reddening of optical light, which is often quantified by the difference in attenuation in the B and V bands: $E(B-V) \equiv A_B - A_V$. This results

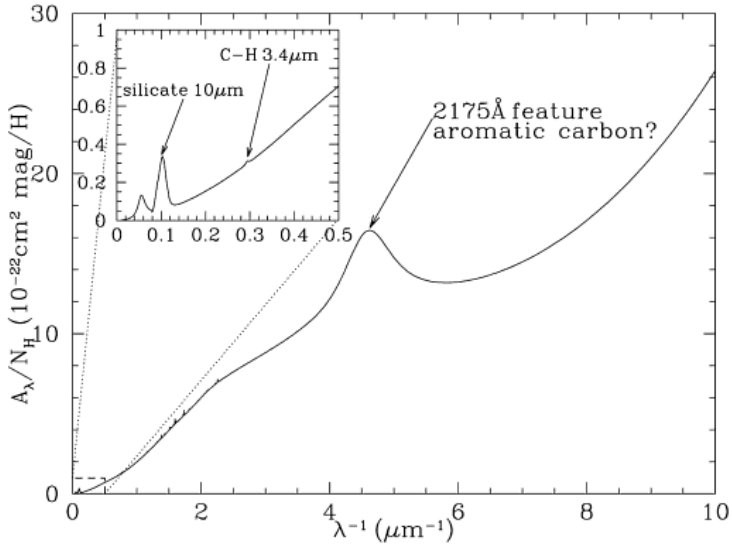

Figure 1.10: The Milky Way extinction curve for a typical sight-line in the local diffuse ISM. The extinction per unit hydrogen column density (A_λ/N_H) increases strongly from the optical on the left to the far-UV on the right. The inset shows extinction in the MIR-NIR. Particular absorption features are labelled; the exact species responsible for the 2175 Å feature has not been identified. Image from Draine (2011; Figure 21.1).

from the dependence of both absorption and scattering efficiencies with a/λ (the ratio of grain size to wavelength). Sizes range between $\sim 1\,$Å and $\sim 1\,\mu$m, while the wavelengths of interest range from $\sim 1000\,$Å (far-UV) to $\sim 10\,\mu$m (mid-IR; MIR). For the smallest grains, absorption dominates the extinction processes, but for larger ones, where a and λ are comparable, Mie scattering becomes important, as described in detail by Draine (2011).

This extinction has an effect on SFRs measured from optical emission lines and UV fluxes, which observers must correct for. Hα-based SFRs can be corrected using line ratios to determine the amount of reddening (e.g. Calzetti, Kinney & Storchi-Bergmann 1994), while UV-based SFRs can be corrected using the UV slope to estimate the reddening (Meurer, Heckman & Calzetti 1999; Kong *et al.* 2004). Without this information about the amount of UV light that is obscured by dust, it is impossible to reliably estimate SFRs. The obscuration can be very high, since dust tends to exist in the regions of galaxies where the star formation is occurring (Buat & Burgarella 1998; Iglesias-Paramo *et al.* 2004; Kong *et al.* 2004; Buat *et al.* 2005; Cortese *et al.* 2006, 2008). It is therefore helpful to complement measurements of the UV light that escapes a galaxy (from unobscured star-forming regions or dust-free lines of sight) with direct

observations of the light that has been obscured by dust. This is possible because the energy that the dust particles absorb is re-emitted as thermal continuum radiation, with characteristic blackbody temperatures on the order of tens of Kelvin. This emission from dust peaks in the FIR at around $100\,\mu\mathrm{m}$, and can constitute a large fraction of the total energy released by an SFG (e.g. Aaronson & Olszewski 1984; de Jong *et al.* 1984; Soifer *et al.* 1984; Houck *et al.* 1985).

Early IR observations in the 1980's revealed that dust exists in a number of different phases of the ISM (e.g. de Jong *et al.* 1984; Helou 1986; Lonsdale Persson & Helou 1987; Rowan-Robinson & Crawford 1989), with varying temperatures depending on the strength of the local interstellar radiation field (ISRF). Physical models for the absorption and emission by dust composed of graphite, silicates and PAHs, with a range of grain sizes, have been highly successful at reproducing the observations. Notable examples include the models of Draine & Lee (1984); Desert, Boulanger & Puget (1990); Silva *et al.* (1998); Charlot & Fall (2000); Dale & Helou (2002) and Draine & Li (2007).

1.3.3 Thermal Far-Infrared Dust Emission

In ISM regions that are remote from individual stars (i.e. not in H II regions), dust temperature T is linked directly to the total energy density U of photons in the ISRF via the Stefan-Boltzmann law (assuming a blackbody absorber):

$$U = \frac{4\sigma}{c} T^4 \tag{1.1}$$

(where $\sigma \approx 5.67 \times 10^{-8}\,\mathrm{W\,m^{-2}\,K^{-1}}$ is the Stefan-Boltzmann constant). The temperature is primarily dependent on the absolute intensity of the ISRF, and only weakly dependent on its colour (Whittet 2003). Hence dust around star-forming regions absorbs more energy from the strong ISRF originating from a dense population of bright stars and therefore is warmer than dust in more quiescent regions. It is worth remembering that the dust is in radiative equilibrium with the ISRF, and not in thermal equilibrium with the gas, due to the low density of the ISM. Collisional heating is only important in hot dense plasma, such as shock-heated gas in SNRs, but is not important in the ISM (Draine 2011). A consequence of this that the dust is generally cold in

the hot gas phase (interstellar H I and H II clouds), and is warm in the cold gas phase (molecular clouds), although very cold dust does exist in the densest clumps and cores of star-forming regions where the high optical depth shields it from the ISRF.

Thermal emission takes the form of a blackbody in the case of a perfect emitter; this is given by the Planck function:

$$B_\nu(T) = 2h\nu^3 \frac{1}{\exp(h\nu/kT) - 1} \tag{1.2}$$

The power output of a real emitter is modified by an efficiency term, known as the emissivity, which is a function of wavelength (e.g. Whittet 2003). In the case of FIR-emitting dust, the grain size is much smaller than the wavelength, which leads to a simple relation for emissivity as a function of wavelength or frequency:

$$\kappa_{\rm FIR} \propto \lambda^{-\beta} \propto \nu^{\beta}. \tag{1.3}$$

The power law index depends on the material, but the value $\beta = 2$ is expected for metals and crystalline dielectric substances (Tielens & Allamandola 1987b; Whittet 2003). This value is supported by observations of interstellar dust in the Milky Way and other galaxies (Reach *et al.* 1995; Boulanger *et al.* 1996; Sodroski *et al.* 1997; Bianchi, Davies & Alton 1999; Paradis, Bernard & Mény 2009), and recent estimates from the *Planck* space mission (Planck Collaboration *et al.* 2011a) indicate an average value of $\beta = 1.8$ (with a small dispersion ~ 0.2) for Milky Way dust in both dense and diffuse environments (Planck Collaboration *et al.* 2011e,f,g).

The spectrum of thermal emission is therefore described by a modified blackbody, or greybody function:

$$S_\nu(T) = \nu^\beta B_\nu(T) \tag{1.4}$$

The wavelength of the peak of the dust emission increases with decreasing temperature T; this is given by Wien's displacement law for a blackbody, although it is slightly modified for the greybody:

$$\lambda_{\rm peak}/\,\mu{\rm m} \;\approx\; 3000 \left(\frac{5}{\beta+5}\right) \frac{1}{{\rm T_{dust}/K}} \tag{1.5}$$

(Whittet 2003). It is useful at this stage to introduce the concept of the spectral energy distribution (SED), i.e. the distribution of the radiative energy output of a galaxy as a

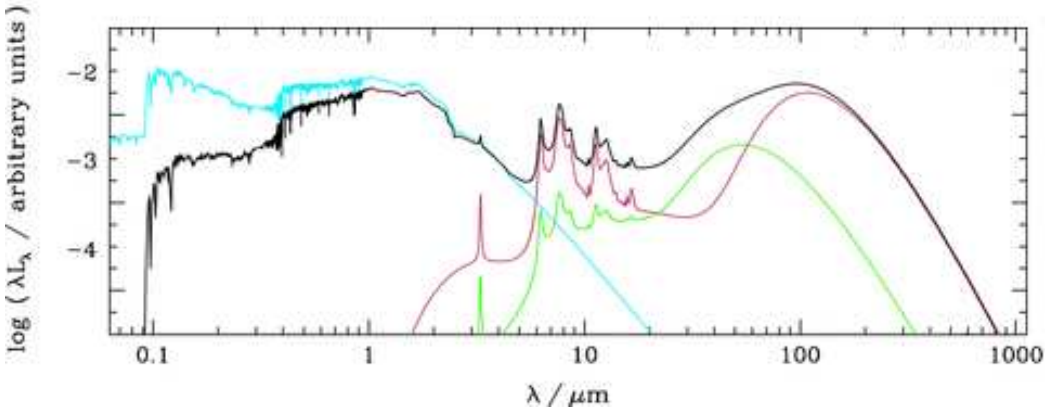

Figure 1.11: Model SED of a typical SFG, from da Cunha, Charlot & Elbaz (2008). The unattenuated starlight, shown in cyan, is absorbed by two components of dust: one associated with the stellar birth clouds, with an emission spectrum shown in green, and one in the cirrus ISM, emission shown in red. The resulting SED is shown in black. The y-axis has units λL_λ that accurately represent the amount of power radiated in each part of the spectrum. It can be seen that about half of the integrated energy is emitted in the FIR – energy from starlight that has been absorbed and re-emitted by the dust. The greatest attenuation occurs in the UV spectral range ($\lambda \lesssim 0.3\,\mu\mathrm{m}$), while the NIR emission ($1 \lesssim \lambda \lesssim 5\,\mu\mathrm{m}$) remains relatively unchanged. The emission from birth-cloud dust peaks at a shorter wavelength than the cirrus because it is kept at a higher temperature by the stronger ISRF. In starburst galaxies with high SFRs, this warm component dominates the bolometric luminosity of the entire galaxy. This SED also shows the relative strength of the PAH emission features in the MIR: these can account for up to 20 per cent of the total power output in an SFG. Figure adapted from da Cunha, Charlot & Elbaz (2008; Figure 5).

function of wavelength or frequency. Figure 1.11 shows the SED of a typical SFG, showing the attenuation of UV/optical starlight by dust, and re-emission of the energy at IR wavelengths. The emission at $\lambda \gtrsim 20\,\mu\mathrm{m}$ is dominated by two thermal components at different temperatures, one of which represents "warm" dust surrounding the molecular gas clouds from which stars and star clusters form. If there is a sufficient level of dust-enshrouded star formation then the FIR luminosity will be dominated by this warm component, which has temperatures of $T \sim 40 - 50\,\mathrm{K}$ (e.g. Dunne & Eales 2001; Sajina *et al.* 2006; Dye *et al.* 2007; Pascale *et al.* 2009). However, emission from a "cold" component at $T \sim 20 - 30\,\mathrm{K}$ becomes increasingly dominant at longer wavelengths. This cold dust exists in diffuse clouds (cirrus) throughout the galactic disk, and is associated with the atomic gas phase (H I). While the warm dust can dominate the bolometric luminosity in a high-SFR galaxy, the cold dust has been shown to contain most of the dust mass in many galaxies (Dunne & Eales 2001; Sauvage, Tuffs & Popescu 2005; Draine *et al.* 2007).

1.3.4 Mid-Infrared Dust and PAH Emission

While thermal dust emission in the ISM dominates the FIR emission of a galaxy, the MIR spectrum can be more complex. The Rayleigh-Jeans tail of thermal stellar emission from low/intermediate-mass stars dominates the NIR up to around $3\,\mu\mathrm{m}$, but at longer wavelengths, strong, broad emission bands from interstellar molecules dominate the MIR in SFGs (e.g. Leger & Puget 1984; Roche *et al.* 1991; Lutz *et al.* 1998; Allamandola, Hudgins & Sandford 1999; also see Figure 1.11). Previously known as the "unidentified infrared bands", these features centred at 3.3, 6.2, 7.7, 8.6, 11.3 and 12.7 $\mu\mathrm{m}$ are now attributed to polycyclic aromatic hydrocarbons (PAHs), a label which covers a variety of large planar molecules built of interlinked hexagonal rings of carbon atoms surrounded by hydrogen atoms. Other features in the MIR can be attributed to different molecules, most notable being the strong silicate absorption trough at $9.7\,\mu\mathrm{m}$ (also shown in Figure 1.10; Savage & Mathis 1979; Whittet 2003).

In addition to molecular bands, the MIR contains a non-thermal component resulting from very small grains of dust (VSGs). These grains have low heat capacity compared with the energy of photons in the ISRF, so do not attain thermal equilibrium but are heated stochastically to temperatures $\sim 50 - 500\,\mathrm{K}$ by the absorption of individual photons (Whittet 2003; Draine 2011). The temperature of VSGs therefore fluctuates on time-scales of order minutes to hours as they absorb energy from photons and re-emit the energy in the MIR. Because of the range of temperatures reached, their emission spectrum is non-thermal, and depends both on the size of the grains and the average wavelength of photons in the ISRF (e.g. Draine 2011).

Galaxies hosting an AGN often exhibit another component of emission from hot dust which is thought to exist in a torus surrounding the AGN itself. Intense high-energy radiation from the SMBH accretion disk can heat this torus to temperatures of order 500-1500 K (limited by the dust sublimation temperature) leading to strong thermal emission in the NIR and MIR (Jones *et al.* 1977; Rieke 1978; de Grijp *et al.* 1985; Miley, Neugebauer & Soifer 1985; Edelson & Malkan 1986; Sanders *et al.* 1989; Klaas *et al.* 2001; Deo *et al.* 2009). The MIR spectra of AGN appear as a power-law due to the range of dust temperatures contributing to the continuum, and PAH emission features are generally absent because those molecules are destroyed by the high tem-

peratures (Roche *et al.* 1991; Lutz *et al.* 1998; Klaas *et al.* 2001).

1.4 Observing Galaxy Evolution in the Far-Infrared and Sub-Millimetre

As we have seen, dust in and around star-forming regions absorbs most of its energy from the UV starlight of massive, short-lived OB stars. These stars are only present in regions where stars have been forming within the past $\lesssim 10^8$ years; (Kennicutt 1998a), and so the IR luminosity emitted by dust (at $\lambda \lesssim 100\,\mu\mathrm{m}$) is well correlated with the SFR (e.g. Lonsdale Persson & Helou 1987; Buat & Xu 1996; Kennicutt 1998a; Calzetti *et al.* 2007; Calzetti *et al.* 2010). This is dependent on the assumption of a particular IMF, as with all observational SFR tracers (see Section 1.2). The FIR can be combined with an unobscured SFR tracer such as UV or Hα flux (e.g. Kennicutt *et al.* 2009), but it is often used as the sole tracer, assuming that all of the UV light from young stars has been absorbed and re-emitted by dust. In the most IR-luminous SFGs, where most of the bolometric emission emerges in the FIR, this is a reasonable assumption, but in normal SFGs a significant fraction of the UV light escapes without being absorbed (Kennicutt 1998a; Bell 2003; Kennicutt *et al.* 2009). On the other hand, the fraction of star formation that is obscured, traced by the IR/UV ratio, does increase with redshift up to $z \sim 1$ (Le Floc'h *et al.* 2005; Buat *et al.* 2009; Cucciati *et al.* 2012; see also Figure 1.12) as well as with SFR (Calzetti 2001; Hopkins *et al.* 2001; Afonso *et al.* 2003; Cortese *et al.* 2008; Buat *et al.* 2009).

In spite of the limitations, the FIR has proved extremely useful in extending our understanding of galaxy evolution through star formation. Due to the opacity of the atmosphere at wavelengths greater than 14 $\mu\mathrm{m}$ (and in much of the spectrum between 1 and 14 $\mu\mathrm{m}$) it is necessary to use space observatories to observe in the MIR and FIR. In 1983 NASA launched the *Infrared Astronomical Satellite* (*IRAS*), which mapped over 96 per cent of the sky at 12, 25, 60 and 100 $\mu\mathrm{m}$ over its 10-month mission (Neugebauer *et al.* 1984; Soifer *et al.* 1987). The legacy of this survey can hardly be overestimated, since it led to a truly vast improvement of our understanding of star formation and dust in galaxies, a research area which has only grown over the past three decades.

IRAS made possible the discovery of high levels of dust-enshrouded star formation in about 24,000 nearby galaxies and distant quasars (about half of which were previously unknown; Soifer *et al.* 1987; Fullmer & Lonsdale 1989). This included the discovery of a new class of SFGs which emit most of their power in the FIR (Houck *et al.* 1985; Soifer, Neugebauer & Houck 1987), dubbed luminous IR galaxies (LIRGs; defined as having $L_{8-1000\,\mu\mathrm{m}} > 10^{11}\,\mathrm{L}_{\odot}$) and ultra-luminous IR galaxies (ULIRGs; $L_{8-1000\,\mu\mathrm{m}} > 10^{12}\,\mathrm{L}_{\odot}$). Following the launch of ESA's *Infrared Space Observatory* (*ISO*, launched 1995; Kessler *et al.* 1996), MIR spectroscopy (Genzel *et al.* 1998; Lutz *et al.* 1998) together with multi-wavelength follow-up (Sanders & Mirabel 1996) revealed these to be mostly post-merger systems undergoing extreme star-formation episodes (starbursts), which are fueled by cold gas falling into the nucleus during the interaction.

The *Spitzer Space Telescope* (launched by NASA in 2003; Werner *et al.* 2004) benefited from greatly improved sensitivity and spatial resolution and provided imaging from the NIR to FIR, as well as MIR spectroscopy. Meanwhile the wavelength range was extended into the sub-millimetre (sub-mm) and millimetre by bolometer arrays such as the Sub-millimetre Common-User Bolometer Array (SCUBA; Holland *et al.* 1999) and the Max Planck Millimeter Bolometer Array (MAMBO; Kreysa *et al.* 1998). These were both commissioned in the late 1990's at high-altitude ground-based sites to make use of the few windows of atmospheric tranmission in the (sub-)mm, for example at 850 μm and 1.2 mm. These sensitive instruments made it possible to detect emission from higher redshifts (e.g. Barger *et al.* 1998; Hughes *et al.* 1998; Eales *et al.* 1999; Lonsdale *et al.* 2003), and probe epochs when the galaxies in the Universe today were being formed.

Observations have shown that over half of the stellar mass in the present-day Universe is concentrated in massive galaxies with $M_{\star} > 10^{10}\,\mathrm{M}_{\odot}$ (Kauffmann *et al.* 2003), and was formed in a relatively short time between $z \sim 3$ and 1, a timespan of $\sim 3 - 4$ Gyr (Dickinson *et al.* 2003; Bundy *et al.* 2006; see also Section 1.1.2). The early Universe must therefore have seen much more rapid star formation than is occuring today. Lilly *et al.* (1996) and Madau *et al.* (1996) were the first to chart the cosmic star-formation history (CSFH) back to high redshifts, using photometric techniques to estimate the

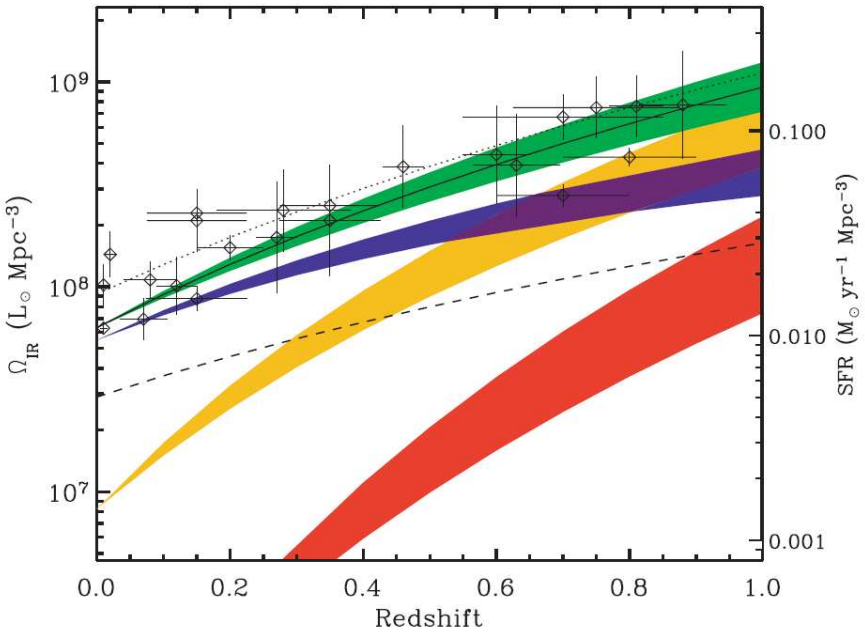

Figure 1.12: Evolution of the comoving IR energy density, or CSFH, up to $z = 1$, from Le Floc'h *et al.* (2005). The total energy density of Spitzer 24 μm sources is shown by the green region, while the contribution from low-luminosity galaxies is shown in blue, from LIRGS in orange, and from ULIRGs in red. The solid line indicates the best fit evolutionary function $\propto (1+z)^{3.9}$. The IR luminosity density can be interpreted as the obscured SFR density (scaled on the right-hand axis). For comparison, the dashed line indicates the unobscured SFR measured from the uncorrected UV luminosity density, and the dotted line is the sum of the obscured and unobscured SFR; note that the unobscured represents roughly a third of the total SFR at $z = 0$ but only about 15% at $z = 1$. At $z = 0$ the IR luminosity density and SFR are dominated by low-luminosity galaxies, but at $z = 1$ they are dominated by LIRGs. The figure is taken from Le Floc'h *et al.* (2005; Figure 14). Data for the CSFH are from (dust-corrected) UV, Hα, IR, and radio surveys: Connolly *et al.* (1997); Tresse & Maddox (1998); Treyer *et al.* (1998); Flores *et al.* (1999); Cowie, Songaila & Barger (1999); Haarsma *et al.* (2000); Machalski & Godlowski (2000); Sullivan *et al.* (2001); Condon, Cotton & Broderick (2002); Sadler *et al.* (2002); Serjeant, Gruppioni & Oliver (2002); Tresse *et al.* (2002); Wilson *et al.* (2002); Pérez-González *et al.* (2003); Pozzi *et al.* (2004).

evolution in the UV/optical luminosity density (see Figure 1.12). The CSFH undergoes a strong increase with look-back time up to $z \sim 2$, which is mirrored by a significant increase in the density of LIRGS and ULIRGs from the local Universe to $z \sim 2-3$ indicating that these extremely luminous systems constitute an important phase in the formation of the most massive galaxies (e.g. Caputi *et al.* 2006; Daddi *et al.* 2007b; Clements *et al.* 2008; González *et al.* 2011; Hickox *et al.* 2012).

Sub-mm telescopes have proved important for probing to such high redshifts for several reasons. Flux falls off with luminosity distance squared, so star formation can only feasibly be detected in deep continuum observations in the rest-frame UV, FIR or radio (see Section 1.2). In addition, the spectrum is redshifted so that a fixed bandpass

or filter will detect light emitted at shorter wavelengths in sources at higher redshifts. To account for this, the k-correction is used to convert an observed flux or magnitude to the expected value in the un-redshifted spectrum, i.e. artificially shifting the filter into the rest frame of the source. The negative slope (defined with respect to frequency) of the radio spectrum in an SFG means that, at increasing redshift, the part of the spectrum observed by a fixed filter is intrinsically weaker. This means that the k-correction is positive, i.e. the measured flux must be increased to correct to the rest frame, and it becomes increasingly difficult to detect the flux at increasing redshifts due to the compounded effects of distance and redshift. The slope of the UV spectrum can be positive (with respect to frequency) in a blue SFG, leading to a slightly negative k-correction which reduces the fall-off in flux with distance. Internal reddening by dust will have the opposite effect however, making the UV light weaker and the SFR calibration highly uncertain. Even in an unobscured galaxy, the spectrum hits a break at rest-frame 912 Å, the Lyman limit (see Figure 1.11), since light at shorter wavelengths is efficiently absorbed by H I in the line of sight. Hence a high-redshift source will be seen to "drop out" of any filter at rest-frame $\lambda < 912$ Å, but still be visible at longer wavelengths. This can be useful for selecting high-redshift galaxies in deep optical/NIR surveys (Steidel & Hamilton 1993; Madau 1995; Steidel *et al.* 1996), but high sensitivity is still required for high-redshift detections, and the SFR calibration from rest-frame UV is still subject to assumptions about dust obscuration.

The sub-mm wavelength range gets around both of these problems. The k-correction is negative and very strong because the spectrum is in the steep Rayleigh-Jeans limit of the greybody function [c.f. equation (1.4)]:

$$S_\nu \propto \nu^{(2+\beta)}. \tag{1.6}$$

Over a large range of redshifts this cancels out the fall-off with distance, so the flux can actually increase with redshift (between $1 < z < 10$ when observing at 850 μm, for example; Blain *et al.* 2002). This phenomenon has been used to great effect in blind sub-mm surveys with SCUBA (and similar instruments) to discover populations of distant ULIRGs at $z \sim 2$, dubbed sub-mm galaxies (SMGs; Smail, Ivison & Blain 1997; Smail *et al.* 2000, 2002; Hughes *et al.* 1998; Barger *et al.* 1998, 1999; Barger, Cowie & Richards 2000; Ivison *et al.* 1998, 2000, 2002; Eales *et al.* 1999, 2000; Chapman

et al. 2001, 2002, 2003a,b, 2005; etc). This population appears to differ from local ULIRGs, having longer-wavelength SED peaks suggesting colder average dust temperatures (Chapman *et al.* 2005; Huynh, Jackson & Norris 2007; Symeonidis *et al.* 2009; Magnelli *et al.* 2010), although it is likely that SMGs form a heterogenous population of both luminous starbursts and cold and dusty "normal" SFGs (e.g. Hayward *et al.* 2011; Magnelli *et al.* 2012).

In high-redshift sources the sub-mm traces the rest-frame FIR close to the $\sim 100\,\mu\mathrm{m}$ peak of the SED, so is a good tracer of the luminosity and mass of the cold dust at least. Nevertheless, accurate k-corrections based on knowledge of the shape of the SED are crucial (e.g. Seymour *et al.* 2009; Symeonidis *et al.* 2009; Elbaz *et al.* 2010; Hwang *et al.* 2010a; Bourne *et al.* 2011; Murphy *et al.* 2011; Nordon *et al.* 2012; Casey 2012; see also Chapter 2). In LIRGs and ULIRGs, where most of the luminosity comes from dust heated by an obscured starburst, this FIR emission is a good tracer of the SFR, in contrast with the UV which is mostly obscured. It is not so clear that $\gtrsim 100\,\mu\mathrm{m}$ luminosities are well-correlated with the SFR in less luminous galaxies due to the contribution from cirrus dust that could be heated by older stellar populations (e.g. Helou 1986; Lonsdale Persson & Helou 1987; Devereux & Young 1992; Walterbos & Greenawalt 1996; Boselli *et al.* 2010b; Buat *et al.* 2010; Boquien *et al.* 2011; Totani *et al.* 2011; Bendo *et al.* 2012). This issue will be revisited in Chapters 3 and 4.

Far-infrared and sub-mm astronomy have always presented particular technical challenges: the long wavelength limits resolution due to diffraction; atmospheric emission and absorption restrict ground-based observatories to very high altitudes and narrow wavelength "windows"; instruments must be cooled to very low temperatures to detect the very cold sources; and high sensitivity is difficult to achieve with bolometer arrays (Blain *et al.* 2002). The diffraction-limited resolution is given by the Rayleigh criterion:

$$\theta_{\mathrm{min}}(\mathrm{rad}) \approx \sin\theta_{\mathrm{min}} = 1.22\lambda/D. \tag{1.7}$$

Single-aperture instruments such as SCUBA and MAMBO are thus limited by the diameter (D) of their dishes (15m and 30m respectively), with angular resolutions of 15 and 11 arcseconds respectively. Significant improvements in this respect are achieved by interferometric cameras such as the IRAM Plateau de Bure Interferometer

(PdBI; Guilloteau *et al.* 1992) and the Sub-Millimeter Array (SMA; Ho, Moran & Lo 2004), but at the expense of field-of-view (restricted to the order of an arcminute) and integration time.

Many of these limitations were overcome by ESA's *Herschel Space Observatory* (launched April 2009; Poglitsch *et al.* 2006), with two photometric cameras: the Photodetector Array Camera and Spectrometer (PACS; Poglitsch *et al.* 2010) operating in the FIR at 70, 100 and 160 μm; and the Spectral and Photometric Imaging Receiver (SPIRE; Griffin *et al.* 2007) operating at 250, 350 and 500 μm. These wavebands span the peak of FIR emission from dust at redshifts $z \sim 1-4$. *Herschel* provides unprecedented mapping speed and sensitivity, enabling surveys to probe much larger volumes (by orders of magnitude) than were previously possible in the sub-mm; the largest being the *Herschel* Multi-Tiered Extragalactic Survey (HerMES; HerMES Collaboration *et al.* 2012), the PACS Evolutionary Probe (PEP; Lutz *et al.* 2011) and the *Herschel* Astrophysical Terahertz Large Area Survey (H-ATLAS; Eales *et al.* 2010a). H-ATLAS in particular has opened up a sub-mm window on a large volume of the local Universe, permitting observations of cold dust in large statistical samples at low redshift.

Sub-mm research in the coming years will be dominated by the huge amounts of data acquired by *Herschel* over its three-year mission, alongside two other important instruments. The long-awaited SCUBA-2[3] (commissioned in 2011) has replaced SCUBA, allowing greater sensitivity and mapping speed for surveys in the sub-mm, while the Atacama Large Millimetre/Sub-mm Array (ALMA[4]) came online in September 2011 and offers high-resolution interferometry with extremely high sensitivity.

1.5 Aims and Motivation for the Thesis

Clearly a great deal of knowledge has been acquired from IR and sub-mm observations of galaxies over the past three decades. Yet, as we have seen throughout the preceding review, many open questions still remain over the evolutionary processes which culminate in the diverse galaxy population seen in the present Universe. The processes of

[3] `http://www.roe.ac.uk/ukatc/projects/scubatwo/`
[4] `http://almascience.eso.org/`

star formation are poorly understood, but observed relations such as the SK law show that the density of gas plays an important role in controlling it. The well-used correlations between the IR and more direct star formation tracers similarly show us that warm dust is strongly linked to the occurrence of star formation, although the link with cold dust is less well established. The observational importance of dust was elegantly summarised by Andrew Blain (Blain *et al.* 2004; p14):

> *"The mass of dust in a galaxy is relevant for understanding its chemical evolution prior to the observation. The creation, destruction and recycling of dust are important for understanding both the process of star formation, and the feedback of processed metal-rich material into the ISM, in all galaxies. This is a potential advantage of studying galaxy evolution from dust emission. First, the currently active star-forming regions are picked out clearly by their powerful dust emission, without any delay as stars burn out of their dust-enshrouded nurseries to become visible at optical wavelengths. Secondly, the dust mass should give a direct measurement of the amount of heavy elements that have formed earlier, subject to few uncertainties about stellar astrophysics or the fraction of metals sequestered in stars, which can be probed using stellar spectroscopy."*

Thus far, FIR astronomy has taught us much about the most IR-luminous SFGs and starbursts which signal the location of the most intense star formation in the history of the Universe. The use of sub-mm telescopes has introduced us to the idea of cold dust being the dominant component of the dust mass in most galaxies. *Herschel* provides for the first time a view of the dust content in a large number of local and low-redshift galaxies that can be studied in detail at all wavelengths. While LIRGs and ULIRGs dominate the SFR density at high redshifts (see Figure 1.12) and reveal the build-up of the most massive galaxies, we also need to look at less luminous populations to see the growth of the whole population of galaxies. With these ideas in mind, this thesis will take three approaches to study populations of galaxies at different cosmic epochs.

In Chapter 2 I will describe a study of the FRC as a function of redshift in a galaxy sample selected in the NIR at redshifts $0 < z < 2$. The FRC is a well-established correlation in SFGs at low redshift, and underpins the assumption that the non-thermal

radio continuum can be used to trace the SFR. Until recently it had only been tested at high redshifts in samples selected in the MIR/FIR, which were biased towards the most luminous SFGs. Furthermore, the IR SEDs of high-redshift SFGs may differ from those at low redshift, which affects the calibration of fluxes at different redshifts via the k-correction. This chapter will describe the first analysis of the FRC and SEDs in a high-redshift sample selected in a waveband not directly related to the SFR (i.e. the NIR), using a "stacking" technique to recover average fluxes below the noise limits of the FIR and radio imaging. This work was previously published in the literature (Bourne *et al.* 2011).

The aims of Chapter 3 are to explore the sub-mm properties of ordinary galaxies selected in a low-redshift optical survey. Once again, the focus is on understanding a population that would not normally be detected in flux-limited samples at the wavelengths of interest. The unrivalled areal coverage of H-ATLAS has made possible for the first time a large-scale statistical census of the cold dust content of the typical galaxies selected in low-redshift surveys such as SDSS. I develop and refine the stacking techniques used in the previous chapter to accurately measure the average masses and temperatures of cold dust in galaxies as a function of stellar mass, optical colour and redshift, up to $z = 0.35$. The work described here has also been published in the literature (Bourne *et al.* 2012).

Chapter 4 will again make use of the wide areal coverage of H-ATLAS to pick out galaxies in the local Universe ($z < 0.05$). The most IR-luminous galaxies in the local Universe have been well studied since *IRAS* surveyed the sky at wavelengths from $12 - 100\,\mu\mathrm{m}$, but large blind surveys at longer wavelengths were impossible until the advent of *Herschel*. I use observations collected by my collaborators and myself, in addition to public archival data, to measure the gas content of a small sample of nearby galaxies from H-ATLAS with high $500\,\mu\mathrm{m}$ fluxes, a selection that has not previously been attempted in the local Universe. This constitutes an unbiased sample of the galaxies with the greatest dust masses, many of which have not previously been studied in detail since they are not luminous in the FIR bands of *IRAS*. I use this sample to explore the correlations between various components of the ISM: the cold dust probed by *Herschel*; warm dust probed by *IRAS*; molecular (H_2) gas estimated from CO ro-

tational transitions; and atomic (H I) gas detected in the 21 cm line. These are used to assess the reliability of the sub-mm bands as SFR tracers in low-SFR galaxies, and the likelihood of cold dust being heated by old stellar populations.

The results and conclusions of the research will be summarised in Chapter 5. I will discuss the relevance of the new understanding gained from this work in the context of our wider knowledge in the field of extragalactic astronomy, and I will explore the possibilities for future projects to follow up on the results described in the thesis with the next generation of instruments and surveys.

Chapter 2

The Far-Infrared–Radio Correlation in Massive Galaxies At High Redshift

2.1 Introduction

2.1.1 Background

In Chapter 1 we saw how star formation can be detected by observations in various parts of the spectrum. Two very successful techniques, which are universal and relatively easy to measure, are the continuum fluxes at FIR and radio wavelengths. These are linked by the FIR–radio correlation (FRC) which is observed in galaxies throughout the low-redshift Universe (van der Kruit 1973; Rickard & Harvey 1984; Helou, Soifer & Rowan-Robinson 1985; Condon 1992). The FRC is linear, remarkably tight and holds for a wide range of galaxy types over at least five orders of magnitude in luminosity (Figure 2.1; Yun, Reddy & Condon 2001). It can be explained in terms of ongoing star formation producing hot, massive ($M > 8\,\mathrm{M}_{\odot}$) stars with short lifetimes ($\lesssim 10^8$ years; Kennicutt 1998a). In an SFG, the UV radiation from these stars is the dominant heating source for dust in the ISM, hence the thermal FIR emission from dust is correlated with the SFR (see Section 1.3). Non-thermal radio continuum emission from SFGs arises from synchrotron radiation by cosmic ray electrons (CREs) accelerated in type-II SNRs, the endpoints of the same massive short-lived stars that heat the dust via their UV radiation (see Section 1.2.2). The radio emission is smeared

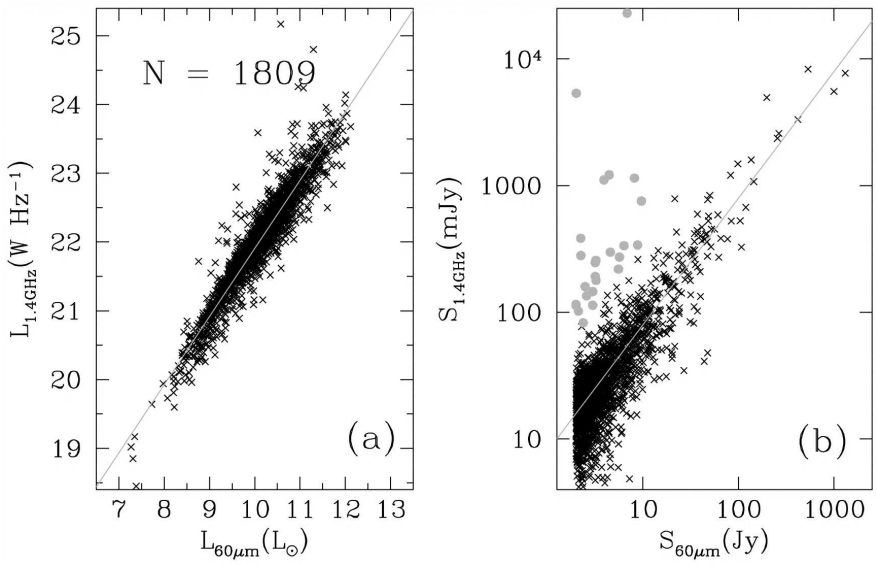

Figure 2.1: The linear correlation between luminosities $\log L_{\rm IR}$ and $\log L_{\rm 1.4GHz}$ (a), and between the fluxes (b), for an *IRAS* flux-limited sample of 1809 galaxies with $S_{60} > 2$ Jy (from Yun, Reddy & Condon 2001; Figure 5). Grey circles in (b) are radio-excess sources (radio AGN) which are relatively rare in FIR samples, but are easily picked out in this way.

out through the galaxy as the relativistic CREs travel through the galaxy over lifetimes of $\sim 10^8$ years, during which they emit synchrotron radiation via interactions with the galactic magnetic field (as described by Condon 1992, and shown observationally by Murphy *et al.* 2006).

Radio fluxes can also be boosted by the presence of AGN in SFGs. Radio-loud AGN can be picked out by their offset from the FRC (see Figure 2.1), although the uncertain contribution from more radio-quiet AGN can lead to scatter in the correlation. Likewise the FIR can be contaminated by sources which are unrelated to the SFR, particularly at long wavelengths by cold "cirrus" dust heated by older stars (Calzetti *et al.* 2010), while shorter wavelengths can be boosted by dust heated by AGN and by the variable contribution from PAH emission features and the 10 μm silicate absorption trough (see discussions in Sections 1.3.3 – 1.3.4). As these features are redshifted into observed bands such as *Spitzer*'s 24 μm, the use of such observations as SFR indicators at high redshift is subject to some contention (see e.g. Dale *et al.* 2005; Webb *et al.* 2006; Calzetti *et al.* 2007; Daddi *et al.* 2007b; Papovich *et al.* 2007; Young, Bendo & Lucero 2009; Rieke *et al.* 2009; Greve *et al.* 2010).

Nevertheless, the existence of such a consistent and ubiquitous linear FRC indicates that both FIR and radio photometry are tracing the same astrophysical phenomena.

More specifically, the linearity suggests that both radio and FIR luminosities are directly proportional to the SFR. Some observations have suggested a breakdown in the linearity at low luminosities ($L_{\rm IR} < 10^{10}\,{\rm L}_{\odot}$), and this is interpreted as being a result of FIR emission from dust heated by older stellar populations uncorrelated with the SFR (Fitt, Alexander & Cox 1988; Devereux & Eales 1989). However, the linearity and tightness of the correlation over a wide range of luminosities, for two such disparate emission processes, is difficult to explain theoretically. "Minimum energy" estimates of magnetic fields in galaxies (Burbidge 1956) imply a large variation between normal galaxies and extreme starbursts like Arp220. To explain a constant FIR/radio ratio between such disparate systems, complex physical solutions need to be provided, for example invoking strong fine-tuning to regulate electron escape and cooling time-scales, or short cooling time-scales with magnetic fields ~ 10 times stronger than the "minimum energy" argument suggests (Thompson *et al.* 2006).

Voelk (1989) first suggested a "calorimeter" model whereby both UV light from massive stars and CREs from SNRs are (a) proportional to the supernova rate, and (b) efficiently absorbed and reprocessed within the galaxy, so that the respective energy outputs in FIR re-radiation and radio synchrotron would both be tied to the supernova rate. This theory requires a correlation between the average energy density of the radiation field and the galaxy magnetic field energy density. Voelk argues that this is plausible if the origin of the magnetic field is a turbulent dynamo effect, since the turbulence would be largely caused by the activity of massive stars, and hence correlated with the supernova rate. Alternative non-calorimetric models include those of Helou & Bicay (1993), using a correlation between disk scale height and the escape scale length for CREs; and Niklas & Beck (1997), in which the FRC is driven by correlations with the overall gas density and equipartition of magnetic field and CRE energy.

Bell (2003) argues for a "conspiracy" to diminish both the FIR and radio emission originating from star formation in lower luminosity galaxies. In this paradigm, low-luminosity galaxies emit proportionally less IR light (in relation to their SFR) because of an increased escape fraction of UV photons, i.e. they are more optically thin. The non-thermal radio emission is also diminished at lower luminosities, possibly as a result of increased CRE escape probability (Chi & Wolfendale 1990). Bell argues

that the correlation is linear because both of these effects reduce the luminosity by the same amount: a factor ~ 2 for $\sim 0.01\,L^{\star}$ in comparison to $\sim L^{\star}$ galaxies (see also Price & Duric 1992). The calorimeter model of Lacki, Thompson & Quataert (2010; hereafter LTQ) invokes different conspiracies to preserve the correlation in low and high gas surface density regions respectively. The low-density conspiracy results from UV and CRE escape as in Bell (2003). At high densities, CREs lose more energy through Bremsstrahlung and ionisation processes, thus reducing the amount of energy apportioned to synchrotron emission by a factor of up to ~ 20 in starbursts. This is cancelled out, however, by additional non-thermal emission from secondary electrons and positrons, and by the fact that the 1.4 GHz flux probes lower-energy CREs at higher magnetic field strength (i.e. in starbursts).

The physical origin of the FRC therefore remains an open question. A full review of the theories is beyond the scope of this study, but a more detailed discussion of the literature can be found in Vlahakis, Eales & Dunne (2007), and a more in-depth treatment is provided by LTQ.

2.1.2 Research Project Aims

Current research on the FRC attempts to extend measurements towards high redshifts and low fluxes, in particular to explore whether there is any evolution (Appleton *et al.* 2004; Frayer *et al.* 2006; Ibar *et al.* 2008; Garn *et al.* 2009; Seymour *et al.* 2009; Ivison *et al.* 2010a,b; Sargent *et al.* 2010a,b; Huynh *et al.* 2010; Jarvis *et al.* 2010; Mao *et al.* 2011; Roychowdhury & Chengalur 2012). Measurements of any evolution (or lack thereof) would improve the accuracy of FIR-/radio-estimated SFRs at high redshift, and could shed light on the mechanism governing the FRC, as well as highlighting differences in the physical and chemical properties of SFGs at high and low redshift (Seymour *et al.* 2009).

In this chapter I describe an investigation of the FRC over a large redshift range, in a sample that is not limited by FIR or radio flux, which was published in Bourne *et al.* (2011). Using *Spitzer* FIR data and radio data from the Very Large Array (VLA) and the Giant Metre-Wave Radio Telescope (GMRT), I quantify the FRC as a function of redshift in massive galaxies selected from a NIR survey of the Extended Chandra Deep

Field South (ECDFS). I use equation (2.1) to define the "q" index, which quantifies the FRC as the logarithmic ratio between rest-frame monochromatic FIR flux ($S_{\rm IR}$ at 24, 70 or 160 μm, measured in filters with bandwidths of 4.7, 19 and 35 μm respectively), and 1.4 GHz radio flux ($S_{1.4\,\rm GHz}$, measured in a bandwidth of 25 MHz).

$$q_{\rm IR} \equiv \log_{10}\left(\frac{S_{\rm IR}}{S_{\rm 1.4GHz}}\right) \tag{2.1}$$

I also investigate the effects of using different FIR bands to quantify the FRC, and the effects of assumptions about the SEDs of the galaxies in the sample. I employ a "stacking" methodology to recover sufficient signal-to-noise ratios on faint objects to obtain measurements of the average properties of the sample. A concordance cosmology of $\Omega_{\rm M} = 0.27$, $\Omega_\Lambda = 0.73$, $H_0 = 71$ kms^{-1}Mpc^{-1} is assumed throughout this chapter.

2.2 Data

2.2.1 The Sample

The ECDFS is a $\sim$ 0.25 deg^2 square centred at $3^{\rm h}32^{\rm m}30^{\rm s}$, $-27^\circ48'20''$ (J2000). It is a much-studied region of sky, with a rich body of published data and studies of extragalactic sources at a broad range of wavelengths stretching from X-ray to radio regimes. I use radio synthesis imaging at 1.4 GHz from the VLA as described in Miller *et al.* (2008), and at 610 MHz from the GMRT as described in Ivison *et al.* (2010a). For the FIR, images from the Multi-band Imaging Photometer for *Spitzer* (MIPS) at 24, 70 and 160 μm were obtained from the FIDEL survey (DR3; Dickinson & FIDEL team 2007). Details of the depth and resolution of each data set can be found in Table 2.3.

To look at a range of galaxy types over a range of redshifts we must give careful thought to how the galaxies are to be selected. Selecting radio-bright galaxies will naturally favour active radio galaxies, while selection at 24 μm is likely to favour galaxies with dusty starbursts and/or obscured AGN components. These biases will affect the distribution of $q_{\rm IR}$ in the sample (see e.g. Sargent *et al.* 2010a). There is however a good body of evidence that distant massive galaxies in a range of phases of star-formation and nuclear activity can be effectively selected in NIR filters at $\sim 2\,\mu$m (e.g. Conselice *et al.* 2007; Daddi *et al.* 2007a; Williams *et al.* 2009). This part of the spectrum is

minimally affected by dust absorption, AGN and other components, hence is relatively insensitive to the "type" of galaxy or the shape of its SED. Furthermore it is insensitive to the age of the stellar population (hence SFR), because the light is dominated by old main-sequence stars that make up the bulk of the stellar mass in all galaxies. Hence the NIR rest-frame luminosity is primarily dependent on stellar mass only (Glazebrook *et al.* 1995; Gardner 1995).

In the ECDFS there exists NIR data from the *Spitzer* Infrared Array Camera (IRAC; Fazio *et al.* 2004), of which the two shortest wavelength bands (3.6 and 4.5 μm) can be used as an effective tracer of stellar mass (e.g. Serjeant *et al.* 2008). A catalogue of IRAC sources matched with optical–NIR photometry in the Multi-wavelength Survey by Yale–Chile (MUSYC; Gawiser *et al.* 2006) is collected in *Spitzer*'s IRAC and MUSYC Public Legacy of the ECDFS (SIMPLE; Damen *et al.* 2011). The catalogue was extracted from IRAC 3.6 and 4.5 μm images, and is limited by the mean of the AB magnitudes $([3.6]+[4.5])/2 < 21.2$, giving a total of 3841 sources (Damen *et al.* 2009b). The IRAC sources have been matched to multi-wavelength counterparts in MUSYC, providing photometry in $UBVRIz'JHK$ bands. Stars have been identified and excluded from the catalogue using the colour criterion $J-K<0.04$, and potential AGN were removed by excluding any matches with Chandra X-ray sources (Virani *et al.* 2006). Photometric redshifts were collated for all objects in the sample from COMBO-17 (Wolf *et al.* 2004), and by using the EAZY code (Brammer, van Dokkum & Coppi 2008) as described by Damen *et al.* (2009b). Damen *et al.* compared the photometric redshifts (z) to spectroscopic ones (z_s) where available, and showed that the median $\langle|z-z_s|/(1+z_s)\rangle = 0.033$ (0.079 at $z \geq 1$). Stellar masses were derived by Damen *et al.* by fitting the UV-to-8 μm photometry from SIMPLE with the spectral synthesis models from Bruzual & Charlot (2003), and were normalised to a Kroupa (2001) IMF. As described in Section 2.2.2, I divide the sample into bins with sizes $\Delta z/(1+z) \sim 0.2-0.4$, so it is safe to neglect these photometric uncertainties. The final catalogue used in this work, after matching and removing stars and X-ray sources, contains 3529 sources with photometric redshifts up to $z=2$, in the region of the ECDFS defined by the rectangle $52°51'48'' <$ RA $< 53°25'14''$, $-28°03'27'' <$ Dec $< -27°33'22''$ (J2000).

Table 2.1: Redshift bins and statistics of the sample

Bin	Boundaries			Median $\langle z \rangle$	Count
ALL	0.00	$\leq z <$	2.00	0.73	3172
ZB0	0.00	$\leq z <$	0.40	0.21	528
ZB1	0.40	$\leq z <$	0.61	0.53	529
ZB2	0.61	$\leq z <$	0.73	0.67	529
ZB3	0.73	$\leq z <$	0.96	0.87	528
ZB4	0.96	$\leq z <$	1.20	1.06	529
ZB5	1.20	$\leq z <$	1.42	1.29	264
ZB6	1.42	$\leq z <$	2.00	1.61	265

2.2.2 Binning and Stacking

Since sources are selected by their NIR flux across a range of SED types, many are likely to be faint or undetectable at the wavelengths of interest. In order to probe the evolution of fluxes as a function of redshift, I stack galaxies into seven bins in redshift (Table 2.1) and measure average fluxes in each bin. Bins were chosen to contain equal numbers of sources (thus giving similar error bars) and to obtain a stacked signal of at least 5σ significance in each band. In the highest redshift bin, the fluxes were high enough for the bin to be split into two to extend the redshift range (by increasing the median redshift of the last bin from 1.42 to 1.61). The great advantage of stacking is the gain in signal-to-noise ratio, as combining many sources reduces the random noise while maintaining the average level of the signal. This gain is at the expense of knowledge of the individual galaxies, but with careful application of criteria when binning the galaxies, and with a large enough sample, it can reveal properties of galaxies below the noise and confusion levels. The technique has been used to great effect many times in the literature; for example by Serjeant *et al.* (2004); Dole *et al.* (2006); Ivison *et al.* (2007); Takagi *et al.* (2007); White *et al.* (2007); Papovich *et al.* (2007); Dunne *et al.* (2009b); Ivison *et al.* (2010a).

We do not know the distribution of fluxes in the stacks, but since we select massive galaxies ($\gtrsim 10^{10}\,\mathrm{M}_{\odot}$ in most redshift bins; see Figure 2.2) with unknown SEDs at a range of redshifts, we may expect to be prone to some outliers. For example, radio-bright AGN have unusually high radio fluxes and are outliers on the FRC. We cannot be certain that these have been successfully removed from the sample by cross-matching with the Chandra catalogue, as we know that there is limited overlap between X-ray

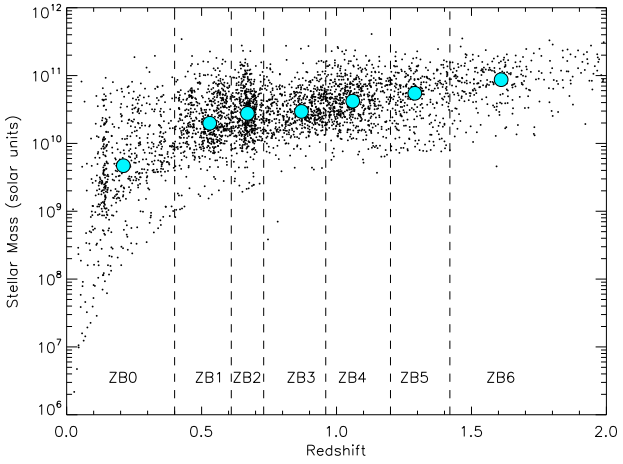

Figure 2.2: Scatter plot of stellar masses in the catalogue as a function of photometric redshift, with the divisions between the redshift bins marked as dashed lines. Large circles mark the median mass and redshift in each bin.

and radio-selected AGN samples (Rovilos *et al.* 2007; Pierce *et al.* 2010; Griffith & Stern 2010; although see Section 2.5.1). I therefore used the median statistic to represent the properties of the typical galaxies in each stack, because unlike the mean, the median is resistant to outliers (Gott *et al.* 2001; White *et al.* 2007; Carilli *et al.* 2008; Dunne *et al.* 2009b).

The most significant sampling bias is that of stellar mass. The stellar masses of galaxies in the catalogue have been estimated by Damen *et al.* (2009b), by SED-fitting with a Kroupa (2001) IMF. Any flux-limited sample is biased towards more luminous objects which are detected in a larger volume than intrinsically fainter ones; this is Malmquist bias (Malmquist 1922). Since the NIR luminosity is a proxy for stellar mass, the sample will be increasingly dominated by more luminous objects at increasing redshifts. Hence the median mass in the sample is lower at lower redshifts (because low mass galaxies dominate the population), but is higher at higher redshifts where only the more massive galaxies are detectable. This is illustrated in Figure 2.2, and I test the effect on the results in Section 2.5.1.

2.3 Stacking Methodology

2.3.1 Stacking into the VLA and GMRT Radio Images

The radio images have pixel units of $\mathrm{Jy\,beam^{-1}}$, and each pixel value is equal to the flux density of a point source located at that position. The assumption that the pixel value at the position of each catalogue object gives the correct radio flux density for that source is generally good, though requires a small correction to give the total integrated flux of the source. This integrated-flux correction accounts for any sources being extended over more than one beam, and also for any astrometric offset between the catalogue coordinates and the radio source position. When stacking, it is suitable to consider the overall effect on the median stacked source, so the integrated-flux correction is calculated from the stacked "postage-stamp" image of the full sample. This image is created by cutting out a 41×41 pixel square centred on each source, and stacking the images by taking the median value of each pixel. The integrated flux was calculated using the AIPS package JMFIT and the correction is simply the ratio of this to the value of the peak (central) pixel in the image. I tested whether the integrated/peak ratio varied significantly between different redshift bins, as might be expected if a large number of sources at low redshift were resolved. Repeating the JMFIT fitting on individual redshift bins at 1.4 GHz and 610 MHz, results were consistent within 1σ of the stack of all sources, so I conclude that the stacked sources are unresolved in all bins. The uncertainty on the correction is calculated from the noise in the postage stamp, which is taken into account in fitting the integrated flux. The integrated-flux corrections from the stack of the whole catalogue therefore have smaller errors, hence I used these to correct measured pixel fluxes in all the radio stacks. These corrections are 1.55 ± 0.08 for 1.4 GHz and 1.05 ± 0.12 for 610 MHz.

This correction also accounts for bandwidth smearing (an instrumental effect caused by the finite bandwidth of the receiver that results in sources appearing more extended with increasing angular distance from the centre of the pointing), since integrated flux is conserved by this effect.

2.3.2 Stacking into the *Spitzer* FIDEL Images

Measuring fluxes in the MIPS images requires a different technique, due to the large point spread function (PSF) which results from the diffraction-limited resolution of MIPS. The centre of the PSF can be described by a roughly Gaussian profile, with FWHM of 6, 18 and 40 arcsec in the 24, 70 and 160 μm bands respectively (Rieke *et al.* 2004). The outer portion of the 24 μm PSF consists of a pattern of Airy rings caused by diffraction and interference. The amplitude of these "wings" is known to vary between different pointings and different source colours. For this reason, and to allow for potentially resolved sources, I chose to measure 24 μm fluxes by aperture photometry, and adopted an aperture of 13 arcsec with an aperture correction of 1.16 based on the theoretical STINYTIM point response function (PRF)[1] and the results of the *Spitzer* Extragalactic First Look Survey (xFLS; Fadda *et al.* 2006),[2] to measure total fluxes in Jy. I also attempted to measure an empirical PRF from sources in the map (as recommended in the MIPS Data Handbook[3]), using the PRF_ESTIMATE module in the MOPEX package[4] to estimate a PRF from stacked catalogue sources. The PRF describes how the PSF (the shape of a point source having passed through the optics of the telescope) is translated by the detector and how it appears in the image, accounting for the finite size of pixels and any offset between the PSF centroid and the centre of the nearest pixel. For this analysis the image was resampled by a factor of 4 to allow for such offsets and PRF_ESTIMATE was used to measure a median PRF from stacked images of detected catalogue sources, and of bright, isolated point sources selected in the map. Poor agreement was found between the PRF and aperture corrections calculated in this way and the xFLS results. This could be because the chosen sources are not suitably isolated (so their flux is contaminated by neighbouring sources) or because they have too low signal–to–noise (so their flux is contaminated by spurious

[1] TINYTIM for *Spitzer* developed by John Krist for the *Spitzer* Science Center (SSC). The Center is managed by the California Institute of Technology under a contract with NASA. Web page available at `http://ssc.spitzer.caltech.edu/archanaly/contributed/stinytim/index.html`

[2] Sample xFLS and STINYTIM PRFs are available on the SSC website: `http://ssc.spitzer.caltech.edu/mips/psf.html`

[3] `http://ssc.spitzer.caltech.edu/mips/dh/`

[4] `http://ssc.spitzer.caltech.edu/postbcd/download-Mopex.html`

noise peaks). I therefore opted to use the published aperture correction of 1.16 for a 13″ aperture; any error in this correction is systematic and will affect all fluxes identically, so will not change the conclusions.

Due to poorer resolution in the 70 and 160 μm maps, it is sufficiently accurate to measure point source fluxes by applying a correction to the central pixel value: the factors used were 43.04 and 46.86 at 70 and 160 μm respectively (David T. Frayer, private communication). This converts the fluxes to units of $\mathrm{Jy\,beam^{-1}}$, and accounts for large-scale emission in the wings of the PSF, as well as a colour correction. No further correction is required to measure total (integrated) fluxes as we can confidently assume that none of the sources is extended in these two bands.

In stacking the FIDEL images it was necessary to exclude objects close to the edges of the map where the noise was higher, to ensure that noise in the stacks reduced as $1/\sqrt{N}$ and to prevent gradients being introduced into the postage stamps. This was achieved by placing lower limits on integration time. Limits were chosen based on stacks of random positions, resulting in the exclusion of 3.5, 8.6 and 9.9 percent of the 3529 catalogue sources in the 24, 70 and 160 μm bands respectively. Since these cuts are based on integration time alone, there is no correlation with the nature of the sources themselves, so no systematic effect on the measured properties of the galaxies will be introduced. Postage-stamp images of the stacked bins in the MIPS and radio maps are shown in Figure 2.3, including noise contours as described in the following section, while stacking results are shown in Table 2.2.

2.3.3 Analysis of Random Errors in Stacking

Random errors in any flux measurements arise from noise in the image. Simplistically these errors might be expected to arise purely from the variance of pixel values in the map, σ^2, and the error on N stacked measurements is then given by $\sigma/\sqrt{N}$. This assumption is valid for the radio images, so it is sufficient to use the RMS values at the corresponding positions on the RMS map. In the MIPS data maps, however, pixel covariance provides a non-negligible contribution to the error, so the RMS maps are not sufficient. In order to measure the total random error on a measured flux, I chose random positions in the sample region of the map and selected those that fell

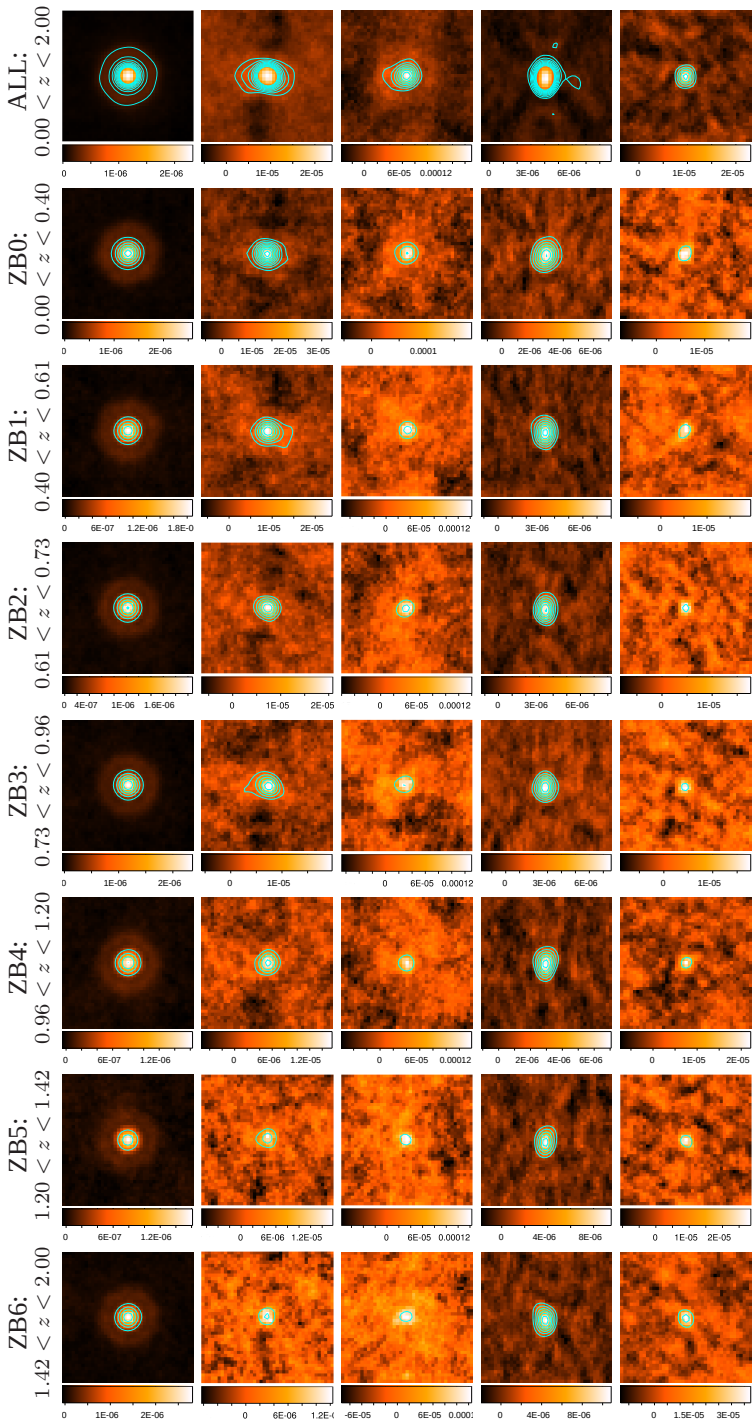

Figure 2.3: Postage-stamp images of the stacked targets in (from left to right) 24 μm, 70 μm, 160 μm, 1.4 GHz, 610 MHz. The top row is the stacked full sample; other rows are the stacks of redshift bins ZB0–ZB6 (from top to bottom) as described in the text. Images are coloured by flux in Jy pixel^{-1} units (MIPS) and Jy beam^{-1} units (radio), and colour scales are included below each. Contours of [3, 5, 7, … 19] times the pixel noise are overlaid. Each tile is a square 41 pixels on a side, which corresponds to 49.2, 164, 328, 20.5 and 61.5 arcsec for the five bands respectively.

Table 2.2: Summary of stacking results. Columns are as follows: (1) Redshift bin; (2) median redshift; (3) number of objects in stack; (4) Band; (5) Measured median flux before clustering– or k–corrections; (6) Measured 1σ noise (reduced by $\sqrt{N}$); (7) Signal-to-noise ratio; (8) q-index for IR band after clustering correction and radio k–correction; (9) 1σ error on q; (10) Median flux after k–corrections (using M51 template for MIPS and the measured $\alpha(z)$ for radio); (11) 1σ error on corrected flux; (12) Signal-to-noise ratio on fully corrected flux; (13) k–corrected q-index; (14) 1σ error on k–corrected q.

Bin	$\langle z \rangle$	N	Band	S_{med}, μJy	$\pm\sigma$, μJy	S/N	q	$\pm\sigma$	S_{corr}, μJy	$\pm\sigma$, μJy	S/N	q_k	$\pm\sigma$
(1)	(2)	(3)	(4)	(5)	(6)	(7)	(8)	(9)	(10)	(11)	(12)	(13)	(14)
ALL	0.73	3172	24um	146.1	1.3	114.4	1.03	0.02	178.1	3.1	57.2	1.19	0.02
.			70um	1037.1	21.9	47.4	1.91	0.02	760.9	22.3	34.2	1.82	0.02
.			160um	8058.3	378.0	21.3	2.69	0.03	4598.4	358.4	12.8	2.60	0.03
.			1.4 GHz	13.3	0.2	54.7			11.5	0.5	23.6		
.			610 MHz	24.4	1.3	18.2			21.1	1.4	14.9		
ZB0	0.21	528	24um	157.0	3.0	52.8	1.11	0.03	150.3	6.8	22.1	1.15	0.03
.			70um	1437.0	51.7	27.8	2.09	0.03	1075.4	64.2	16.8	2.00	0.03
.			160um	8574.0	887.2	9.7	2.81	0.06	5579.4	876.6	6.4	2.72	0.06
.			1.4 GHz	11.2	0.6	19.8			10.7	0.7	16.1		
.			610 MHz	20.7	3.1	6.6			19.7	3.1	6.4		
ZB1	0.53	529	24um	111.7	2.9	38.1	0.97	0.05	135.1	5.2	26.2	1.11	0.05
.			70um	1037.3	50.4	20.6	1.96	0.05	731.8	55.8	13.1	1.85	0.05
.			160um	6278.7	883.7	7.1	2.68	0.08	3851.7	801.1	4.8	2.57	0.08
.			1.4 GHz	12.2	0.6	21.9			10.4	1.0	10.9		
.			610 MHz	20.6	3.1	6.7			17.7	3.0	5.9		
ZB2	0.67	529	24um	117.5	3.0	39.7	0.99	0.06	132.9	6.3	21.0	1.15	0.06
.			70um	905.6	50.7	17.9	1.92	0.06	618.6	51.3	12.0	1.82	0.06
.			160um	6632.2	868.8	7.6	2.63	0.09	3160.5	698.1	4.5	2.53	0.09
.			1.4 GHz	11.8	0.6	21.1			9.4	1.1	8.6		
.			610 MHz	18.8	3.1	6.0			14.9	2.9	5.1		

Table 2.2 continued

Bin	$\langle z \rangle$	N	Band	S_{med}, μJy	$\pm\sigma$, μJy	S/N	q	$\pm\sigma$	S_{corr}, μJy	$\pm\sigma$, μJy	S/N	q_k	$\pm\sigma$
(1)	(2)	(3)	(4)	(5)	(6)	(7)	(8)	(9)	(10)	(11)	(12)	(13)	(14)
ZB3	0.87	528	24um	134.5	3.0	44.6	1.11	0.07	148.8	7.1	20.9	1.26	0.07
.			70um	823.2	51.5	16.0	1.94	0.07	608.9	50.7	12.0	1.87	0.07
.			160um	5376.2	900.3	6.0	2.60	0.11	2774.4	658.4	4.2	2.53	0.11
.			1.4 GHz	11.0	0.6	19.3			8.2	1.3	6.5		
.			610 MHz	17.0	3.2	5.4			12.6	3.0	4.2		
ZB4	1.06	529	24um	98.8	2.9	33.8	0.90	0.07	132.8	5.5	24.1	1.11	0.07
.			70um	676.5	49.9	13.6	1.77	0.07	578.2	48.8	11.8	1.75	0.07
.			160um	6549.6	853.9	7.7	2.66	0.09	4465.3	722.5	6.2	2.64	0.09
.			1.4 GHz	10.4	0.6	18.8			10.2	1.4	7.5		
.			610 MHz	23.5	3.1	7.6			23.1	4.2	5.6		
ZB5	1.29	264	24um	91.3	4.2	21.8	0.76	0.08	165.5	5.7	28.8	1.10	0.08
.			70um	548.2	71.8	7.6	1.57	0.09	546.0	66.0	8.3	1.62	0.09
.			160um	6776.8	1224.2	5.5	2.56	0.11	5384.5	959.6	5.6	2.61	0.11
.			1.4 GHz	14.1	0.8	17.8			13.2	2.2	6.0		
.			610 MHz	30.2	4.4	6.9			28.1	6.0	4.7		
ZB6	1.61	265	24um	154.2	4.3	35.8	0.86	0.07	227.1	8.5	26.7	1.11	0.07
.			70um	479.3	73.8	6.5	1.38	0.10	591.5	67.2	8.8	1.52	0.10
.			160um	5932.7	1257.1	4.7	2.38	0.12	5839.8	960.9	6.1	2.52	0.12
.			1.4 GHz	15.1	0.8	18.4			17.7	2.7	6.4		
.			610 MHz	39.7	4.5	8.8			46.6	8.6	5.4		

Table 2.3: Information on the FIDEL and radio images. Measured total noise values represent the 1σ error on a single flux measurement; for 24 μm this is the noise on a corrected aperture flux, for 70 and 160 μm it is the noise on a corrected point source flux, and for the radio it is the noise in a beam and does not include the integrated-flux correction. Background levels are in the same units, these are the values subtracted from the median source fluxes. Errors on background fluxes are standard errors from 1000 measurements as described in Section 2.3.4.

Band	Pixel scale arcsec	PSF/Beam FWHM arcsec	Noise level μJy	Background level μJy
24 μm	1.2	5.9	62	-37.60 ± 0.04
70 μm	4.0	18	1,200	$+2.2 \pm 0.8$
160 μm	8.0	40	20,000	$+2,000 \pm 10$
1.4 GHz	0.5	2.8×1.5	8.83	-0.014 ± 0.005
610 MHz	1.5	7.7	71.9	-0.01 ± 0.03

on empty regions of sky. This was tested by taking an aperture of radius 13 arcsec (the radius for aperture photometry at 24 μm) around each position and measuring the standard deviation of pixel values in that aperture. If the aperture contained any pixels that deviated from the aperture mean by more than 2.5σ, then the position was discarded. The positions were also required to be separated and not overlapping. Thus positions were chosen to represent regions of empty sky with no sources. The number of positions used was $N = 500$, to roughly match the sample size of bins used for stacking sources. For the 24 μm case, where aperture photometry was used, the fluxes at the 500 positions were measured in exactly the same aperture as was used for source photometry. The standard deviation of these sky fluxes was taken to represent the random error on an individual aperture measurement.

Consistent results were obtained by stacking random sky catalogues of varying sizes (ranging from $N = 10 - 500$), using 500 realisations of each to measure the noise from the standard deviation. This confirmed that the noise in a stack reduces as $1/\sqrt{N}$, and the distribution of flux values in the random catalogues was tested to be Gaussian with high certainty. All of this was repeated for the other two MIPS maps and also both radio maps, using the central pixel for flux measurement since this was the method used for source photometry in those bands. The radio error values were close to the average value in the RMS map, confirming that pixel covariance is negligible. The errors on individual measurements given in Table 2.3 are divided by $\sqrt{N}$ to give the errors on stacked fluxes.

In using the median to represent the fluxes of N sources in some bin, we must also

consider the width of the distribution of fluxes in that bin: if this is larger than the estimated measurement error$/\sqrt{N}$ then the latter is a poor indicator of uncertainty on the quoted median. For this reason I estimated 1σ uncertainties on the median following the method of Gott *et al.* (2001). This method sorts the N values in a bin, assigning each a unique rank r between 0 and 1. In the limit of large N, the expectation value of the *true* median of the population sampled is $\langle r \rangle = 0.5$, and its standard deviation is $\sigma_r = \langle r^2 - \langle r \rangle^2 \rangle^{1/2} = 1/\sqrt{4N}$. If the measurement at rank r is $m(r)$, then the median measurement is $m(0.5)$, which gives the expectation value of the true median of the population sampled. The error on this expectation value is then given by the average of the measurements at $r \pm \sigma_r$:

$$\sigma_s = \frac{m(0.5 + 1/\sqrt{4N}) - m(0.5 - 1/\sqrt{4N})}{2}. \tag{2.2}$$

I compared this statistical error to the estimated measurement error in each stack (the value in Table 2.3 divided by $\sqrt{N}$). At 160 μm, 610 MHz and 1.4 GHz I found the two to be about equal (see Table 2.2), confirming that the flux errors I have estimated cover the distribution of fluxes in the bins. At 24 μm the uncertainty on the median was around three times the size of the estimated flux error, and at 70 μm around twice the size, indicating that in these bands the flux distribution in each bin was somewhat broader than the estimated errors allowed for. It is possible that the method described in preceding paragraphs systematically underestimates the noise in these images, as a result of the constraints used to identify empty "sky" apertures. Those constraints were designed to distinguish true read-noise on the detector from confusion noise in the sky, but the 24 μm image in particular is highly confused, meaning that the constraints could lead to correlation in the empty apertures stacked, and increase the chance of underestimating the noise. For the analysis of stacked results I therefore quote the uncertainties on the median following the Gott *et al.* (2001) method.

2.3.4 Background Subtraction and Clustering Analysis

A similar methodology to the random error analysis was used to measure the background value to be subtracted. The method described above chooses empty apertures containing just sky, which is simplistically what needs to be subtracted before per-

forming aperture photometry, but in the case of MIPS the combination of high source density and low resolution require that source confusion is also accounted for. When stacking, the random boosting of fluxes on individual sources will average out to a constant correction that can be included in the background. Hence when measuring the background for subtraction, a catalogue of random positions were chosen and stacked, without any criteria on the existence or otherwise of sources close to these random positions. On average the random catalogue should coincide with sources with the same probability as the source catalogue does, assuming that sources are not clustered. Stacks of 3500 random positions (to match the sample size of the source catalogue) were made and repeated 1000 times in each of the three MIPS and two radio maps. The mean of the 1000 stacked fluxes was taken to be the background value, and the standard error was taken to be the uncertainty; results are given in Table 2.3.

Any clustering of the sources in the catalogue would lead to an increased probability of confusion for a catalogue source compared with a random position, hence with increased clustering the background subtraction becomes increasingly less effective. In order to estimate the size of this effect we would ideally need to understand the correlation function of sources in each image on scales smaller than the beam size. This is not possible since it would be necessary to extract individual sources from the image at angular scales smaller than the size of a point source. I therefore made the assumption that the correlation of sources in the images is approximately the same as that in the target catalogue. This may not fully account for confusion if the sources in the image are more clustered than the IRAC (catalogue) sources, but it does at least remove the possibility of double-counting the fluxes of confused sources in the catalogue.

I calculated the autocorrelation function $W(\theta)$ of positions in the catalogue, to estimate the excess probability of a background source appearing at a radius θ from a target source, compared with a random position. I used the Landy & Szalay (1993) estimator which counts pairs within and between the data (D) and random (R) positions as a function of annular radius θ:

$$W_{D,D}(\theta) = \frac{DD - 2\,DR + RR}{RR} \tag{2.3}$$

Results are shown in Figure 2.4, which includes a fit by linear regression given by

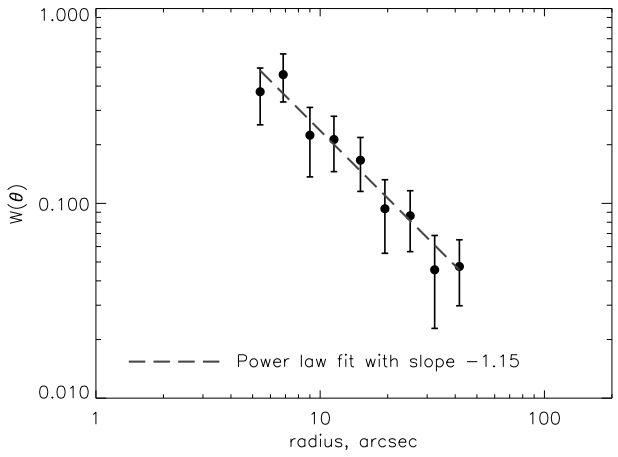

Figure 2.4: Autocorrelation function $W(\theta)$ of the SIMPLE catalogue. The dashed line is a power-law fit with index -1.15. Error bars are twice the Poisson errors, as described in the text.

$W(\theta) = 0.000269\,\theta^{-1.15}$, where θ is in degrees. By dividing the region into four eqaul quadrants and comparing the scatter between results in each, I found that the standard error was a factor 2.0 larger than the simplistic Poisson errors. I therefore quote error bars on all correlation functions of twice the Poisson error.

The strong clustering implies a significant correction to the measured fluxes from stacking catalogue sources, as a result of the significantly increased likelihood of confusion with a nearby source at a catalogue position in comparison to a random position. The correction must account for the flux contribution from any background sources separated by some angular distance θ from the target. This contribution, as a fraction of the average source flux, is given by a convolution of the correlation function $W(\theta)$ with the beam profile for the corresponding band (assumed to be Gaussian, $\exp(-\theta^2/2\sigma^2)$, with σ =FWHM$/(2\sqrt{2\ln 2})$), scaled by the number density of background sources n:

$$F = n \int_0^\infty W(\theta) e^{-\theta^2/2\sigma^2} 2\pi\theta d\theta \tag{2.4}$$

(e.g. Serjeant *et al.* 2008). This equation gives the average contribution of confused sources to a measured flux, hence a correction factor of $1/(1+F)$ must be applied to stacked fluxes.

For the $24\,\mu$m case a slightly different convolution must be used because aperture photometry is used. The contribution of a background source to a flux measurement then depends not only on where it falls on the beam profile, but on how much of its

beam falls within the aperture. I computed the convolution of the 24 μm PRF (from xFLS; see Section 2.3.2) with the 13-arcsec radius aperture, to give a curve of growth which represents the contribution of a background source to the aperture as a function of angular separation θ. This function is then substituted for the Gaussian beam profile in equation (2.4).

This method corrects a stacked flux using the average probability of confusion from another source at separation θ, scaled by the amount of flux expected from a distance θ from the centre of the beam. When correcting stacks of individual redshift bins, we must assume the same level of clustering in each bin if we are to use the autocorrelation of the full catalogue. To account for the probability of confusion of a target from a particular redshift range, while accounting for the contribution from background sources at all redshifts, we must consider the cross-correlation of the sources in the particular range (the "data" centres, D) with the full catalogue (the "reference" centres, E; see Figure 2.5). A modification of the Landy & Szalay (1993) method was used to calculate the cross-correlation function $W_{D,E}(\theta)$, given by

$$W_{D,E}(\theta) = \frac{DE - 2\,DR + RR}{RR} \tag{2.5}$$

The robustness of the results was tested by checking against the method of Masjedi *et al.* (2006), which gave indistinguishable results.

Thus I calculated the average, across all the data centres, of the excess probability of confusion with any of the reference centres. The correction to stacked flux was then calculated in the same way as described above, using $W_{D,E}$ in equation (2.4). It should be noted that using this estimate of the fractional contribution involves the implicit assumption that the average flux of background sources is equal to the average stacked flux. Since we can only correct for confusion with catalogue sources by this method (i.e. to avoid double-counting) this is a reasonable assumption.

I calculated the corrections for three redshift ranges by grouping the bins in pairs as shown in Table 2.4. Errors in the table were calculated using standard formulae for the propagation of errors, with the error bars on $W_{D,E}(\theta)$ as shown in Figure 2.5. The results in the table show that the FIR bands require significant corrections for confusion due to their poor resolution, while the radio images have sufficiently high resolution for the confusion to be negligible. The 160 μm band has the lowest resolution and

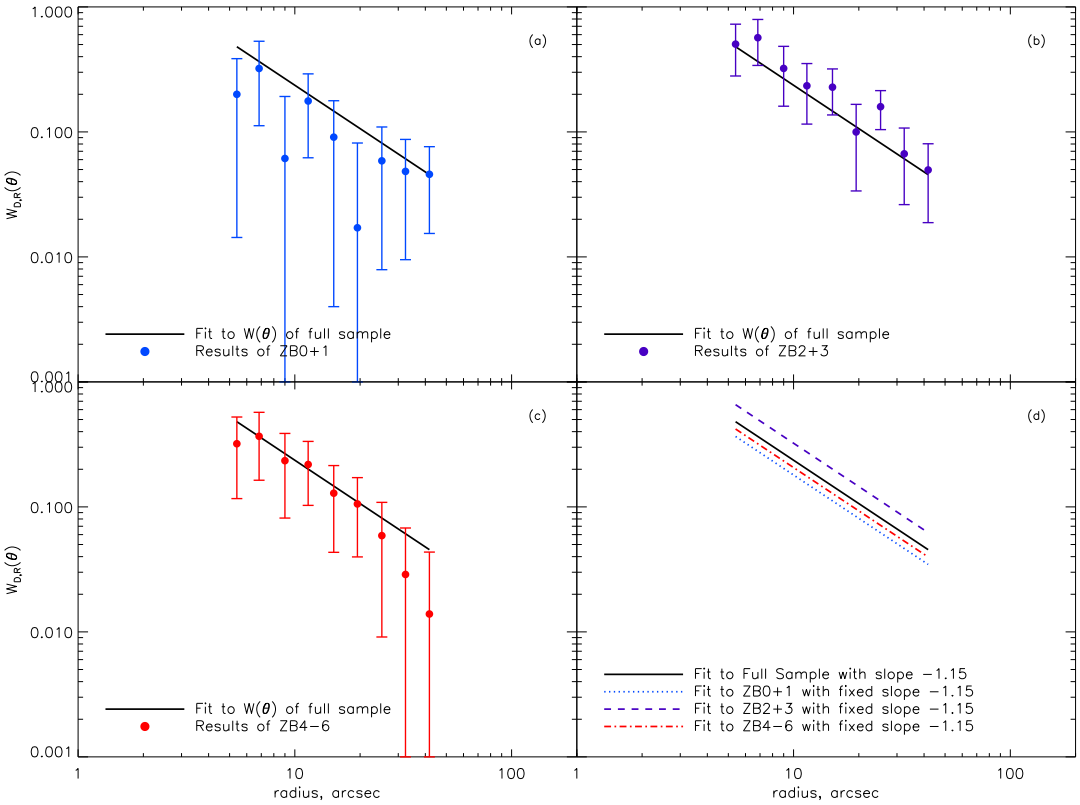

Figure 2.5: Comparing cross-correlation functions of three redshift ranges (D) with the reference catalogue (E) being the full SIMPLE catalogue: (a) $W_{D,E}(\theta)$ where D is the subset in $0.0 \leq z < 0.6$; (b) $W_{D,E}(\theta)$ where D is the subset in $0.6 \leq z < 1.0$; (c) $W_{D,E}(\theta)$ where D is the subset in $1.0 \leq z < 2.0$. On each of (a)-(c) the black line shows the fit to the autocorrelation function of the full catalogue for comparison. Error bars are twice the Poisson errors, as described in the text. The power-law fits to the four functions are shown in (d), where the slope has been fixed by the fit to the full catalogue.

therefore the greatest confusion, but the 24 μm band also suffers badly because fluxes are measured in apertures in this band, meaning that any background source whose flux contributes to the aperture must be accounted for, not just any source which blends with the *beam* at the catalogue position.

Table 2.4: Correction factors (C) to stacked source fluxes to remove contribution from correlated background sources, using the autocorrelation of the full catalogue and cross-correlations of three redshift ranges with the full catalogue. Errors were calculated as described in the text. Corrected flux $S_{\text{corr}} = S_{\text{stack}} \times C$

	C (cross-correlation)			C (autocorrelation)
Band	$0.0 \leq z < 0.6$	$0.6 \leq z < 1.0$	$1.0 \leq z < 2.0$	All
24 μm	0.86 ± 0.05	0.74 ± 0.04	0.80 ± 0.04	0.79 ± 0.03
70 μm	0.90 ± 0.04	0.80 ± 0.03	0.86 ± 0.04	0.84 ± 0.02
160 μm	0.81 ± 0.05	0.66 ± 0.04	0.74 ± 0.05	0.72 ± 0.03
1.4 GHz	–	–	–	1.000 ± 0.001
610 MHz	–	–	–	1.000 ± 0.002

2.4 SEDs and k–Corrections

2.4.1 Radio k–Correction

Observed fluxes were converted to rest-frame (emitted) monochromatic luminosities using equation (2.6). This contains a bolometric k-correction $k(z)$, accounting for the shift of the spectrum in relation to the receiver, and a further bandwidth correction $(1+z)^{-1}$, accounting for the stretching of the spectrum in relation to the bandwidth of the receiver (d_L is the luminosity distance to the source, while z is its redshift):

$$L_{\nu,em} = \frac{4\pi d_L^2 \, S_{\nu,\text{obs}} k(z)}{1+z} \tag{2.6}$$

The radio spectrum can be assumed to follow a simple power law ($S_\nu \propto \nu^\alpha$) resulting from the sum of the non-thermal synchrotron and thermal bremsstrahlung components. The power-law index in SFGs is typically $\alpha \approx -0.75$ at frequencies $\sim 1 - 10\,\text{GHz}$, where the non-thermal emission dominates and self-absorption is low, and has small dispersion $\sigma_\alpha \lesssim 0.1$ in SFG samples (Gioia, Gregorini & Klein 1982; Condon 1983, 1992). Steeper indices might be expected in AGN–dominated sources (Ibar *et al.* 2010), while spectra are flatter at frequencies $\gtrsim 30\,\text{GHz}$ where the thermal spectrum dominates, and at $\lesssim 1\,\text{GHz}$ where frequency-dependent self-absorption affects the spectrum (Condon 1992).

The k–correction to a monochromatic flux with a power-law spectrum is independent of the filter transmission function and is simply given by the ratio of the power-law at the observed and emitted frequencies:

$$k(z) = (1+z)^{-\alpha} \tag{2.7}$$

The radio spectral index for each bin was evaluated using the stacked fluxes in the two radio bands:

$$\alpha = \frac{\log\left(S_{610\,\mathrm{MHz}}/S_{1.4\,\mathrm{GHz}}\right)}{\log\left(610/1400\right)} \tag{2.8}$$

These spectral indices, shown in Figure 2.6, were used to k–correct each measured radio flux using equation (2.7), taking the observed median index for each bin to calculate k–corrections for all sources in that bin. Figure 2.6 shows an apparent evolution to steeper radio slopes at increasing redshift in this sample. A linear least squares fit to the $\alpha(z)$ values gives a slope of -0.39 ± 0.15; the slope is non-zero at the 2.6σ level. The evolution does not appear to be monotonic, however, so a linear trend may not be an accurate description. The data could also be described by a change occurring at $z \approx 1$ or even a decrease in spectral index with increasing flux. Whatever the cause, the varying $\alpha(z)$ is an unexpected result, and it is noteworthy that it was not observed in the stacked 24 μm sample of Ivison *et al.* (2010a), who used the same radio data and stacking technique; although their spectral indices do cover a similar range. The possible implications are discussed in Section 2.5.1, but note that using a single spectral index of -0.74 for k–corrections would lead to a slight rise in the q indices in the three highest redshift bins (a change of $\delta q = +0.17$ for the last bin at $\langle z \rangle = 1.6$).

2.4.2 Infrared k–Correction

In the MIR/FIR part of the spectrum sampled by the MIPS bands, the assumption of a simple power law is not valid and k–corrections must be calculated by evaluating equation (2.9), which defines the k–correction as the ratio of intrinsic luminosity to observed for a general filter transmission profile $T_\nu(\nu)$:

$$k(z) = \frac{\int_0^\infty T_\nu(\nu) L_\nu(\nu) d\nu}{\int_0^\infty T_\nu(\nu) L_\nu(\nu[1+z]) d(\nu[1+z])}. \tag{2.9}$$

This requires knowledge of both the filter transmission function[5] $T_\nu(\nu)$ and the SED $L_\nu(\nu)$. A well-studied local galaxy can be used as a template for high-redshift galaxies; commonly-used templates in FIR studies include Arp220 and M82, which are IR-luminous and therefore considered to be more typical of IR-selected galaxies at high

[5]The transmission functions for the MIPS filters are available on the SSC website at `http://ssc.spitzer.caltech.edu/mips/spectral_response.html`

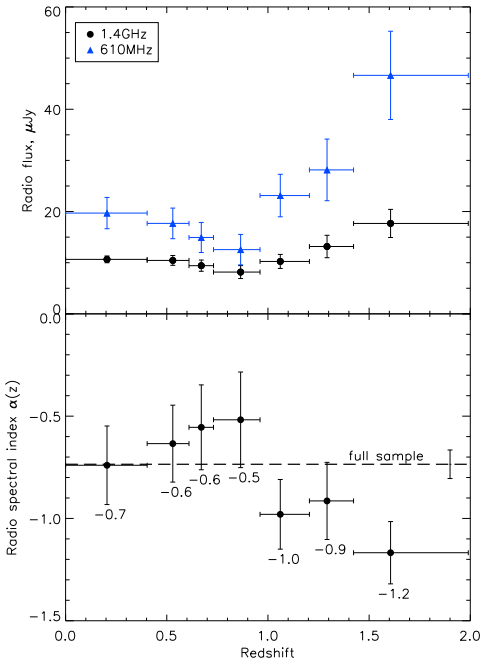

Figure 2.6: Top: stacked radio fluxes (and 1σ errors) as a function of redshift. Note the increase in 610 MHz flux at high redshift which appears to be the main driver for the evolution in radio spectral index shown below. Bottom: radio spectral index as a function of redshift, calculated from fluxes shown above. The dashed line (with error bar) represents the spectral index calculated from stacks of the full sample, -0.74 ± 0.07 (consistent with the mean of the indices of all the bins). The points represent the seven redshift bins and are labelled with the corresponding values of α, with 1σ errors of ± 0.2 calculated as described in Section 2.3.3. Horizontal error bars mark the widths of the bins.

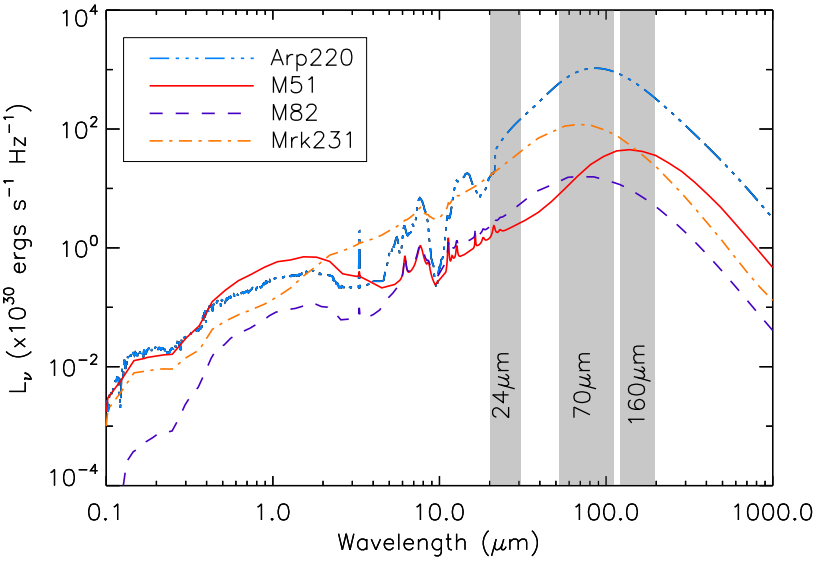

Figure 2.7: Comparison of four SED templates showing the relative positions of the MIPS filters. Note the differences in the shapes blueward of the filters, in particular the strength of the PAH and silicate features in Arp220, the power-law slope resulting from AGN-heated dust in Mrk231, and the cold-dust bump of M51 peaking at a longer wavelength.

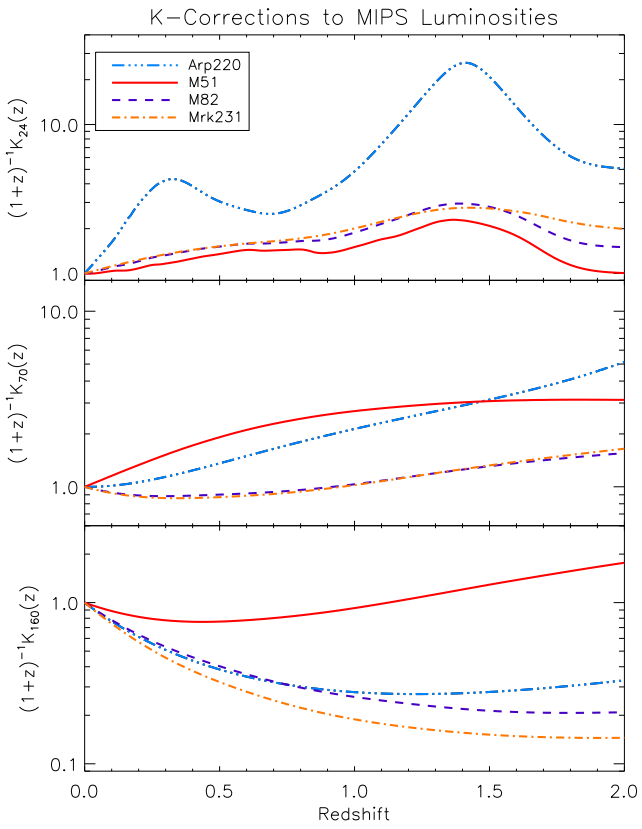

Figure 2.8: k–corrections for the three MIPS bands (from top to bottom, 24 μm, 70 μm, 160 μm), calculated from four different SED templates. Note the effect of the strong silicate troughs in Arp220 on the 24 μm flux at redshifts 1.4 (rest-frame wavelength of 10 μm) and 0.3 (rest-frame 18 μm), and the effect of the different dust temperatures of the galaxies on the 70 and 160 μm corrections.

redshift. In the current study there is no reason to presume that these dusty IR-luminous objects are representative of the stacks, since this sample is selected in the IRAC 3.6 and 4.5 μm channels. I therefore tried a range of different template SEDs to compare the results given by the various k–corrections. Four templates were chosen to represent different types of IR SEDs:

1. Arp220 (template from Pope *et al.* 2006): a bright ULIRG with a particularly large mass of hot dust and high star formation following a recent merger;

2. M51 (GRASIL template: Silva *et al.* 1998): A typical large late-type spiral with moderate star formation and cold dust distributed in the spiral arms;

3. M82 (GRASIL template: Silva *et al.* 1998): The prototype hot starburst galaxy, with intense star formation probably triggered by a tidal interaction with M81;

4. Mrk231 (GRASIL template: Vega *et al.* 2008): A Seyfert 1, probable merging system, with both starburst and AGN components.

The four SED templates are shown in Figure 2.7, and the k–corrections for the three MIPS filters are plotted in Figure 2.8. The stacking was repeated four times, using a different template for k–corrections each time, to compare the effects of different assumptions about the SEDs. The results are described in Section 2.5.2.

2.4.3 Limitations of the SED models

The SEDs considered here are only a small selection of possible SEDs, representing four archetypes of FIR-emitting galaxies. An alternative approach would be to use a library of SED templates based on data from a large sample of galaxies. For example, the library of Chary & Elbaz (2001; hereafter CE01) represents a range of SEDs of FIR-emitting galaxies as a function of total IR (TIR) luminosity, ranging from star-forming spirals with $L_{\rm TIR} = 10^{8}\,{\rm L}_{\odot}$ to the most extreme ULIRGs with $L_{\rm TIR} = 10^{13.5}\,{\rm L}_{\odot}$ ($8 - 1000\,\mu{\rm m}$). Neither the GRASIL nor CE01 templates parametrise the dust temperature, but the shift in the SED peak towards shorter wavelengths at higher luminosities in the CE01 library represents an increase in dust temperature. On this basis, the M51 GRASIL SED has a similar temperature to the CE01 template with $\log(L_{\rm TIR}/\,{\rm L}_{\odot}) \approx 9.5$ (although it has $\log(L_{\rm TIR}/\,{\rm L}_{\odot}) \approx 10.4$) while the M82 GRASIL SED has a similar temperature to the CE01 template with $\log(L_{\rm TIR}/\,{\rm L}_{\odot}) \approx 13.0$ (although its actual luminosity is only $\log(L_{\rm TIR}/\,{\rm L}_{\odot}) \approx 9.8$; Silva *et al.* 1998). The Arp220 and Mrk231 SEDs used above have similar temperatures consistent with the $\log(L_{\rm TIR}/\,{\rm L}_{\odot}) \approx 12.6$ and 13.4 respectively, and have luminosities $\log(L_{\rm TIR}/\,{\rm L}_{\odot}) \sim 12 - 12.5$ (Vega *et al.* 2008). The four templates used therefore span a range of potential SED shapes in the CE01 library, although they do not represent moderate luminosity sources from that library (i.e. $10 \lesssim \log(L_{\rm TIR}/\,{\rm L}_{\odot}) \lesssim 12$). However, the CE01 library has its own limitations, being based on a sample of IR-luminous sources in the local volume, so is not necessarily representative of high-redshift NIR-selected galaxies. The fact that the temperatures of the four template galaxies tend to match the CE01 templates with higher luminosities than their actual luminosities, indicates that the CE01 library does not sample the full parameter space.

It is possible that the CE01 templates might give more appropriate k-corrections than those in Figure 2.8, but with the three data points available it would be difficult to distinguish which is the best fit from such a large range of models. I therefore opt to use the four models for simplicity, and bear in mind the limitations of these assumed SEDs.

2.5 Results and Discussion

2.5.1 Evolution of Radio Properties of the Sample

The results indicate a significant increase in radio luminosity with redshift (see Table 2.5), greater than would be expected from the flux limit alone (see Section 2.5.4). This is to be expected if the radio emission is related to star formation, due to the increase in star-formation activity in the most massive galaxies from the local universe back to $z \sim 2$. The apparent evolution in radio spectral index over the redshift range (Figure 2.6) is more surprising and, notwithstanding the large error bars, hints at a fundamental change in the sample demographic, with different sources dominating the radio luminosity at $z < 1$ and $z > 1$ respectively. The most likely potential contaminant is radio flux from AGN, which would have a different spectral index than that from star formation, and would also have the effect of boosting radio luminosity. Radio-loud AGN source counts are known to evolve strongly at $z > 1$ (e.g. Wall *et al.* 2005).

The effect that AGN contamination would have on the median spectral indices is not entirely straightforward. While flat ($\alpha \gtrsim -0.5$) spectra are associated with radio-quiet quasars or low-luminosity AGN (Bondi *et al.* 2007; Huynh, Jackson & Norris 2007), steep spectra ($\alpha < -1$) have frequently been used to select powerful radio galaxies at high redshift (generally $z \gtrsim 2$; e.g De Breuck *et al.* 2000; Pedani 2003; Cohen *et al.* 2004). This is because AGN radio spectra are flat at low frequencies but steepen at high frequency, hence steep slopes are observed when the spectrum is highly redshifted (the frequency of the turnover varies, depending on properties such as magnetic field strength and electron density; Huynh, Jackson & Norris 2007). The evolving spectral

indices seen in Figure 2.6 could therefore be a sign of AGN dominating the radio signal at higher redshifts.

Matches with the Chandra X-ray catalogue (Virani *et al.* 2006) have been removed from the sample, reducing the likelihood of contamination from unobscured AGN. However, overlap between X-ray and radio AGN is known to be small (e.g Pierce *et al.* 2010). In order to identify any AGN that are obscured or undetected in X-rays, I used the MIR fluxes from the IRAC catalogue. The IRAC colours have been shown to provide some limited diagnostics for selecting obscured AGN based on the rest-frame MIR slope (e.g. Lacy *et al.* 2004; Stern *et al.* 2005; Alonso-Herrero *et al.* 2006; Donley *et al.* 2007, 2008). In Figure 2.9 I plot $S_{8.0\,\mu\mathrm{m}}/S_{4.5\,\mu\mathrm{m}}$ against $S_{24\,\mu\mathrm{m}}/S_{8.0\,\mu\mathrm{m}}$ for all the objects in the sample. This plot can be used as an AGN/starburst diagnostic since AGN have been shown to lie to the right, with $S_{8.0\,\mu\mathrm{m}}/S_{4.5\,\mu\mathrm{m}} > 2$ at intermediate to high redshifts (as the prototype Mrk231 does) while starbursts (such as Arp220) lie above and to the left (e.g. Ivison *et al.* 2004; Pope *et al.* 2008; Coppin *et al.* 2010). With the exception of bin ZB0 ($0.0 \leq z < 0.4$), the data lie well to the left in Figure 2.9, indicating flat spectral slopes at $< 8.0\,\mu\mathrm{m}$ (compared with Arp220) and negligible AGN contamination. The scatter in bin ZB0 is attributed to strong PAH emission at $7.7\,\mu\mathrm{m}$ which makes the diagnostic unreliable at low redshift (although it is noted that strong PAH emission is generally associated with star formation and not AGN).

Taking Figure 2.9 as evidence against significant AGN contamination, I deduce that the radio emission originates from star-formation activity, and that the index of the non-thermal continuum from CREs evolves. The model described by LTQ and Lacki & Thompson (2010) predicts steep radio spectra as a result of increasing CRE losses via inverse-Compton scattering with CMB photons [since the scattering timescale is a function of the frequency of synchrotron emission from the electron; LTQ equation (23)]. That model predicts these losses to become significant in normal galaxies at $z \approx 2$, which seems to be supported by these data. Alternatively, the steepening spectral slope can be a sign of increased electron calorimetry, as electron escape becomes less important relative to electron cooling (including synchrotron, bremsstrahlung and inverse-Compton losses; Lacki & Thompson 2010).

It is possible that the evolution in the radio spectral index is not a variation between

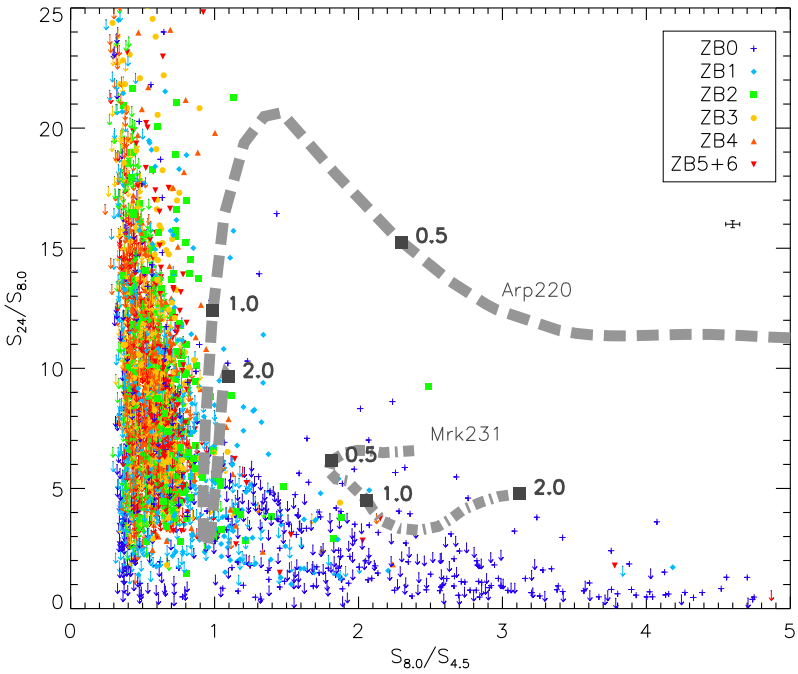

Figure 2.9: Observed-frame $S_{8.0\,\mu\mathrm{m}}/S_{4.5\,\mu\mathrm{m}} - S_{24\,\mu\mathrm{m}}/S_{8.0\,\mu\mathrm{m}}$ colour-colour plot of all objects in the sample, coloured by redshift bin (for ranges see Table 2.1). The $24\,\mu\mathrm{m}$ aperture fluxes are used where they are $\geq 5\sigma$ (roughly 30% of the positions). For the positions without a 5σ detection at $24\,\mu\mathrm{m}$, I use the 5σ upper limit (indicated by arrows). IRAC fluxes are from the SIMPLE catalogue. The representative error bar in the top right shows the median 1σ errors. Some scatter in the vertical axis is introduced by confusion at $24\,\mu\mathrm{m}$, but positions in the horizontal axis are reliable as signal-to-noise is good in both $4.5\,\mu\mathrm{m}$ and $8.0\,\mu\mathrm{m}$ and confusion noise is much lower. Tracks of starburst (Arp220) and AGN (Mrk231) SEDs are overlaid in grey, showing the locus of each on the diagram as a function of redshift between 0 and 2. The horizontal scatter in the data in bin ZB0 is attributed to the strong PAH emission feature at $7.7\,\mu\mathrm{m}$ contributing to the $8\,\mu\mathrm{m}$ band at low redshifts.

galaxies at different redshifts, but a function of the rest-frame frequency that is observed, and that the assumption of a single power-law spectrum is flawed. A curved spectrum with power-law index increasing with radio frequency would produce a similar effect when viewed at successively higher redshifts. The LTQ models predict a steepening of the spectral index by only $\sim 0.05 - 0.1$ dex (depending on gas surface density) between the frequencies probed by 1.4 GHz observations at redshifts from 0 to 2. The evolutionary fit to the data indicates a change of -0.8 ± 0.3 over this range, suggesting that actual evolution with redshift does occur in the sample.

To better understand the change in the sample demographic across the redshift bins, I consider the distribution of stellar masses in the respective bins. The differential effect of Malmquist bias in successive redshift bins means that the flux-limited sample is increasingly dominated by the most luminous (hence often the most massive)

galaxies towards higher redshifts. Repeating the stacking analysis with a mass limit of $\log(M_\star) \geq 10.5$ gave results for both α and q that were fully consistent with the full sample, although error bars were large (the lowest-redshift bin contained too few objects to obtain a reliable value of the radio spectral index). Results can be seen in Figure 2.13.

2.5.2 The Observed and k–corrected FIR–Radio Correlation

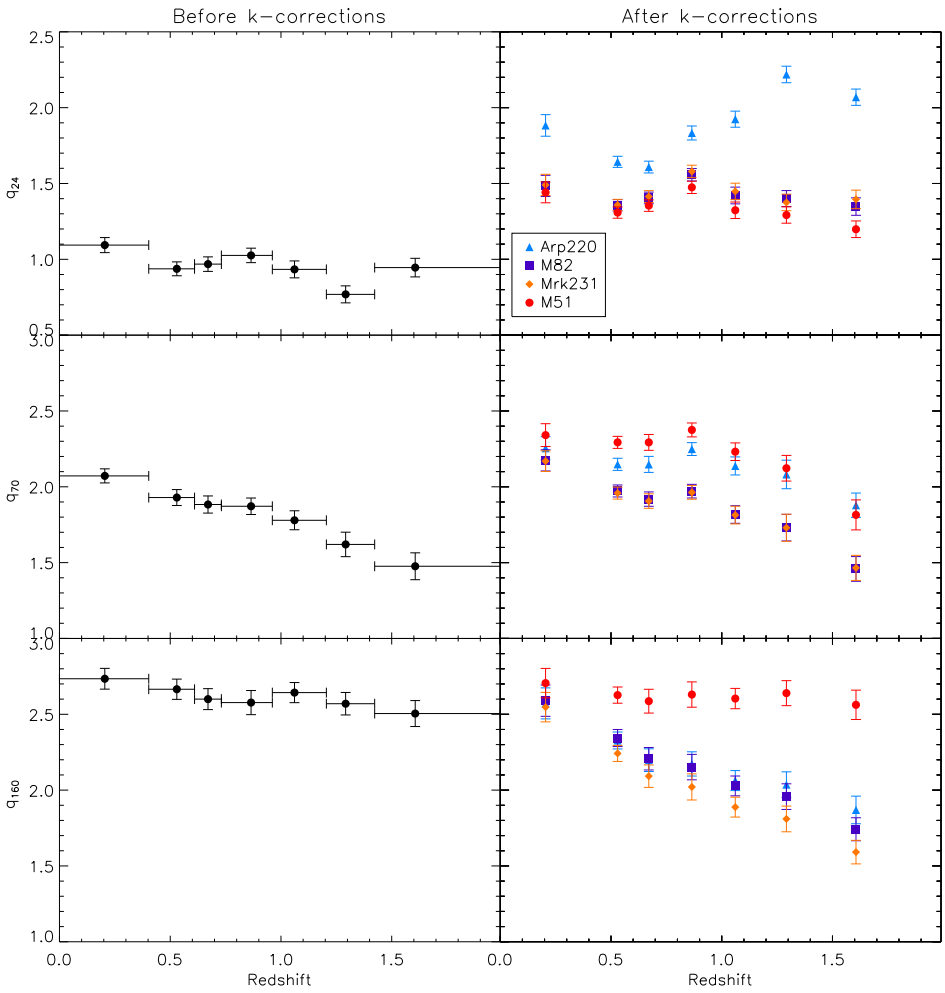

Figure 2.10: Far-infrared–radio relation (q) as a function of redshift for the three MIPS bands (from top to bottom, 24 μm, 70 μm, 160 μm). Ratios of stacked observed fluxes are plotted on the left. On the right are the ratios of stacked k–corrected fluxes: radio fluxes are k–corrected using the measured spectral index for each bin, and infrared fluxes are k–corrected using the four templates described in Section 2.4.2. Vertical error bars represent estimated 1σ uncertainties on the stacked medians, following Gott *et al.* (2001): they indicate the spread of the data, and are of similar size or larger than the noise, as described in Section 2.3.3. Horizontal bars in the left-hand panels mark the full width of each bin. Horizontal bars are omitted from the right-hand panels for clarity.

The q index was calculated for each stack and for each FIR band using equation (2.1). Details of the stacked fluxes and q ratios can be found in Table 2.2. Figure 2.10 displays the calculated q values as a function of redshift, both before and after k–corrections were applied. Fluxes were k–corrected individually, rather than after stacking, using the photometric redshift of each source, and for the radio, the stacked spectral index measured in the corresponding bin, and for the FIR, the corrections shown in Figure 2.8. The left panel of Figure 2.10 reveals a very slight downward trend of q in each of the three MIPS bands, with a more bumpy evolution in q_{24}. The anomalies in the observed q_{24} evolution can be explained by the redshifted 12.7, 11.3 and 8.6 μm PAH features boosting the observed 24 μm flux at z =0.9, 1.1 and 1.8 respectively, and the broad 10 μm silicate trough accounts for the dip in q_{24} at redshift 1.3. The width of the redshift bins and the use of photometric redshifts accounts for the breadth of redshifts over which these features appear to have an effect. The slightly higher value of all q indices in the lowest-redshift bin could be due to extended radio emission being resolved out by the high-resolution interferometers, which can underestimate extended flux (as suggested by Jarvis *et al.* 2010).

The right panel of Figure 2.10 shows the effects of k–correcting MIPS fluxes using the four SED templates introduced in Section 2.4.2. Overall, the M51 template gives rise to the least evolution in all three q indices. k–corrections using the Arp220 template give rise to an increasing q_{24}, due to the steeper MIR slope ($\lambda \lesssim 24\,\mu$m). In q_{160} the Arp220, Mrk231 and M82 templates all exacerbate the downward trend towards high redshift, while the M51 template removes it, as a result of the cooler dust temperature (longer wavelength of the peak) in M51. However, none of the templates removes the trend in q_{70}, implying either a real evolution in rest-frame 70 μm1.4 GHz flux ratios, or a steeper spectral slope at $\lambda \lesssim 70\,\mu$m in the galaxies sampled, in comparison to the templates chosen.

2.5.3 Infrared Spectral Energy Distributions

Interpretation of the results is evidently subject to the assumptions made about the "average" or typical SED of the sample. It is possible to better constrain the FIR k–correction by analysing the evolution of MIPS flux ratios (colours) as a function

of redshift. These colours are sensitive to the position of the peak of the thermal dust emission, hence the temperature of the emitting dust, as well as the slope of the SED on the short-wavelength side of the peak. Figure 2.11 shows the evolution in observed MIPS colours with redshift, plotted over the expected tracks for each of the SED templates, and reveals that the SED most consistent with observed colours at all redshifts is M51.

The important factor distinguishing the M51 template from the others used is the position of the peak of the SED at a longer wavelength. M51 is a quiescent SFG with an IR SED dominated by cold dust, and evidence from Figure 2.11 therefore points to a cold dust temperature for the galaxies in the sample, at least in the first three redshift bins. The 70–160 μm colour is directly sensitive to the position of the peak at low redshifts, but it is clear from the middle panel of Figure 2.11 that over the last four bins the M51 and Arp220 templates are barely distinguishable in this colour space, it is impossible to draw conclusions on the dust temperatures at $z \gtrsim 0.8$. This is because at these redshifts both bands are shortward of the peak of even the hottest IR SED, and probe the slope on the Wien side. The 70–160 μm colours of the high-redshift bins are consistent with the steeper slopes of M51 and Arp220, and not with the shallower slopes of M82 and Mrk231 (similarly the 24–70 μm and 24–160 μm colours rule out Arp220, due to its strong PAH emission). These steeper slopes are potentially an indication of a stronger contribution from "cold" dust (in the ambient ISM) relative to "hot" dust (in H II regions associated with star formation), or a dearth of emission from very small grains (VSGs). Alternatively they could even result from extremely optically thick systems where the SED is steepened by MIR dust attenuation. In this case, however, one would expect to see a stronger 10 μm silicate absorption feature such as that evident in the Arp220 k–correction at z~ 1.5. The stacked colours are not consistent with such a strong absorption which reduces the likelihood that optically thick MIR emission is responsible for the steeper rest-frame MIR slope at high redshift.

Cold dust temperatures are nevertheless consistent with the conclusions of studies such as Chapman *et al.* (2005) and Pope *et al.* (2006, 2008) for high-redshift SMGs, and Symeonidis *et al.* (2009), Seymour *et al.* (2010) and Giovannoli *et al.* (2011) for 70 μm-selected galaxies at $z \lesssim 1$. There are also parallels with a recent detailed study

Table 2.5: Stacked galaxy properties in each redshift bin: Rest-frame 1.4 GHz luminosity; SFR derived from $L_{1.4\,\mathrm{GHz}}$ using the Bell (2003) calibration; Total IR luminosity ($L_{\mathrm{TIR}} = L_{8-1000\,\mu\mathrm{m}}$) estimated from MIPS fluxes using the M51 template; SFR derived from L_{TIR} using the Bell (2003) calibration; corresponding q values calculated as described in the text. Errors on $L_{1.4\,\mathrm{GHz}}$ are directly translated from the 1σ flux errors. Errors on L_{TIR} are assumed to be 25% as described in the text, while errors on SFRs are directly translated from luminosity errors, and do not include any systematics from the conversion to SFR. All SFRs are calibrated to a Kroupa IMF.

z range	$L_{1.4\,\mathrm{GHz}}$ $10^{21}\,\mathrm{W\,Hz^{-1}}$	$\mathrm{SFR}_{1.4\,\mathrm{GHz}}$ $\mathrm{M_\odot yr^{-1}}$	L_{TIR} $10^9\,\mathrm{L_\odot}$	$\mathrm{SFR_{TIR}}$ $\mathrm{M_\odot yr^{-1}}$	q_{TIR}
0.00–0.40	1.03 ± 0.13	0.57 ± 0.08	5.8 ± 1.4	0.61 ± 0.17	2.76 ± 0.12
0.40–0.61	12.1 ± 0.6	4.23 ± 0.21	57 ± 14	4.8 ± 1.3	2.68 ± 0.11
0.61–0.73	21.5 ± 1.1	7.50 ± 0.37	99 ± 25	8.1 ± 2.1	2.67 ± 0.11
0.73–0.96	31.5 ± 1.9	10.98 ± 0.69	172 ± 43	18.4 ± 4.7	2.75 ± 0.11
0.96–1.20	74.8 ± 7.2	26.1 ± 2.5	327 ± 82	34.1 ± 8.8	2.65 ± 0.12
1.20–1.42	152 ± 14	53.0 ± 4.9	620 ± 160	64 ± 16	2.62 ± 0.12
1.42–2.00	363 ± 35	127 ± 12	1070 ± 270	109 ± 28	2.48 ± 0.12

of two massive K–selected galaxies at $z \sim 2$ by Muzzin *et al.* (2010), who fitted SEDs to data from *Spitzer*, BLAST (Devlin *et al.* 2009) and LABOCA (Siringo *et al.* 2009) instruments. Their best fits were star-formation-dominated SEDs with $L_{\mathrm{TIR}} \sim 10^{13}\mathrm{L_\odot}$, but with cold dust temperatures, in contrast to ULIRGs in the local Universe. Similar cool SEDs have also been determined for SMGs out to $z \sim 1$ from BLAST and *Herschel* studies (Dye *et al.* 2009; Amblard *et al.* 2010).

The current sample of massive galaxies is expected to probe the epoch of stellar mass build-up at $z > 1$. Indeed, Table 2.5 shows that both radio– and IR–derived SFRs do reach high values beyond this redshift. It seems a reasonable assumption that the IR and radio luminosities are dominated by star-forming activity. One does not expect a significant contamination from AGN-dominated galaxies in the sample, since X-ray detections have been removed and the MIR colours are inconsistent with AGN-heated dust (see Section 2.5.1); furthermore a large fraction ($\gtrsim 10$ per cent) of the sample would have to host luminous AGN for the median luminosity in the bins to be biased, and it is unlikely that so many escape both the MIR and X-ray diagnostics. I observe therefore that despite the tendency towards higher luminosities (and SFRs) in the sample at increasing redshifts, there is no evidence for a change in the SED towards the templates of local high-SFR galaxies such as Arp220 or M82.

In Table 2.5, I show indicative total IR (TIR) luminosities, derived for each bin using the rest-frame FIR luminosities in the MIPS bands, scaled up to $L_{8-1000\,\mu\mathrm{m}}$ assuming

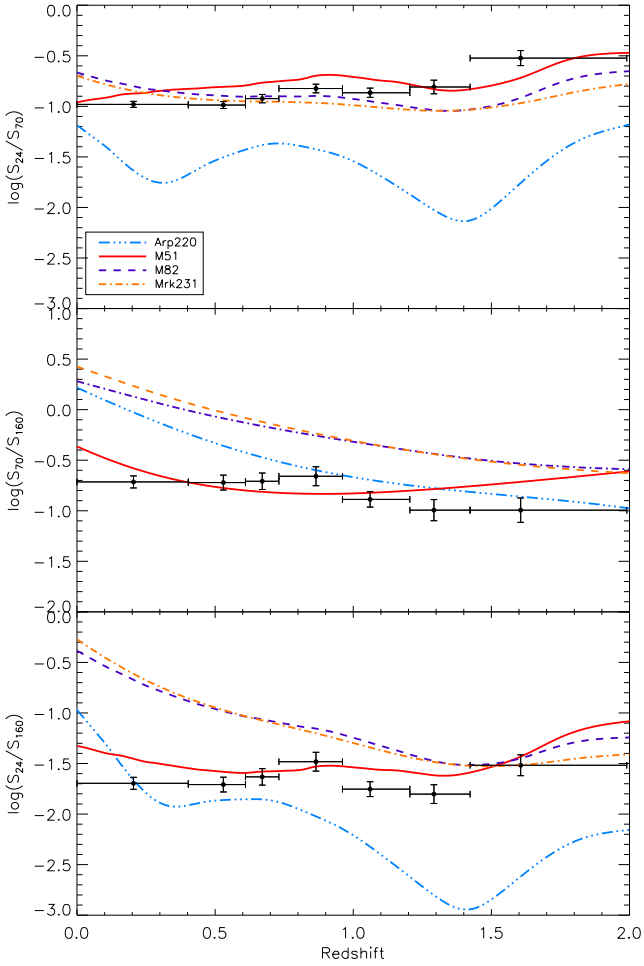

Figure 2.11: Observed MIPS flux ratios as a function of redshift for the three MIPS bands. From top to bottom: $\log(S_{24}/S_{70})$, $\log(S_{70}/S_{160})$, $\log(S_{24}/S_{160})$. Overlaid are the tracks of the four templates described in Section 2.4.2. Error bars are as in Figure 2.10.

the M51 template. This was done by using the luminosities in the three MIPS bands simultaneously to find the best-fitting normalisation of the M51 template. There will be some systematic uncertainties in the calibration, and for an idea of the size of these I consider another method to estimate $L_{\rm TIR}$ from MIPS luminosities. Dale & Helou (2002) offer one such formula for $L_{3-1100\,\mu{\rm m}}$, calibrated for a large sample of normal SFGs with a range of morphologies, colours and FIR luminosities (see also Dale *et al.* 2001); I therefore consider it appropriate for M51–like SEDs. The uncertainty on this calibration was shown to be $\sim 25\%$ by Draine & Li (2007), and using Dale & Helou's method yields values well within 25% (typically 6%, but as much as 16% for the highest-redshift bin) of those found using the M51 template over the same range. Hence assuming systematic errors of 25% on $L_{\rm TIR}$ is reasonable.

Notwithstanding these uncertainties, the results imply that the typical galaxies sampled have quiescent IR SEDs at low z, but rapidly evolve towards higher IR luminosities at increasing z (this cannot be accounted for by the selection; see below). By $z \sim 2$ they appear to reach ULIRG luminosities, as star-formation activity becomes significantly more prevalent in massive galaxies at these redshifts (e.g. Daddi *et al.* 2005). The rise in luminosity with redshift in this sample (from $\sim 10^{10}$ to $\sim 10^{12}\mathrm{L}_{\odot}$) may be partially attributed to increasing median stellar mass with redshift. This cannot be the full story however, since assuming a linear relationship between stellar mass and L_{TIR} implies an increase by a factor of 19, whereas L_{TIR} increases by a factor of ~ 180, and $L_{1.4\,\mathrm{GHz}}$ by ~ 220 over the redshift range. Indeed L_{TIR} is linked not to stellar mass itself, but to the SFR, which is well-known to rise with increasing redshift (Lilly *et al.* 1996; Madau *et al.* 1996; Pérez-González *et al.* 2008; Damen *et al.* 2009b; Magnelli *et al.* 2009; etc).

2.5.4 Evolution of Specific Star-Formation Rates

The SFRs given in Table 2.5 were calculated using the formulae of Bell (2003), which assume a Salpeter (1955) IMF:

$$\frac{\mathrm{SFR_{TIR}}}{\mathrm{M_{\odot}\,yr^{-1}}} = \begin{cases} 1.57\times10^{-10}\,\dfrac{L_{\mathrm{TIR}}}{\mathrm{L_{\odot}}}\left(1+\sqrt{\dfrac{10^9}{L_{\mathrm{TIR}}/\,\mathrm{L_{\odot}}}}\right) & L_{\mathrm{TIR}} > 10^{11}\,\mathrm{L_{\odot}} \\ 1.17\times10^{-10}\,\dfrac{L_{\mathrm{TIR}}}{\mathrm{L_{\odot}}}\left(1+\sqrt{\dfrac{10^9}{L_{\mathrm{TIR}}/\,\mathrm{L_{\odot}}}}\right) & L_{\mathrm{TIR}} \leq 10^{11}\,\mathrm{L_{\odot}} \end{cases} \tag{2.10}$$

$$\frac{\mathrm{SFR_{1.4\,GHz}}}{\mathrm{M_{\odot}\,yr^{-1}}} = \begin{cases} 5.52\times10^{-22}\,\dfrac{L_{1.4\,\mathrm{GHz}}}{\mathrm{W\,Hz^{-1}}} & L_{1.4\,\mathrm{GHz}} > L_c \\ \dfrac{5.52\times10^{-22}}{0.1+0.9(L_{1.4\,\mathrm{GHz}}/L_c)^{0.3}}\,\dfrac{L_{1.4\,\mathrm{GHz}}}{\mathrm{W\,Hz^{-1}}} & L_{1.4\,\mathrm{GHz}} \leq L_c \end{cases} \tag{2.11}$$

where $L_c = 6.4\times10^{21}\mathrm{W\,Hz^{-1}}$. All SFRs were converted to a Kroupa (2001) IMF by subtracting 0.2 dex, following Damen *et al.* (2009b), in order to ensure consistency with the stellar masses used. Radio- and TIR-derived SFRs appear to be roughly in agreement; the TIR values are generally higher, although mostly they are within the broad error bars given by the calibration of L_{TIR}. Agreement naturally depends upon the value of q_{TIR} as a function of redshift being equal to the local value [e.g. the median in Bell's (2003) sample was 2.64]. This will be discussed in the next section. Note that using a constant radio k–correction based on the overall median spectral index of

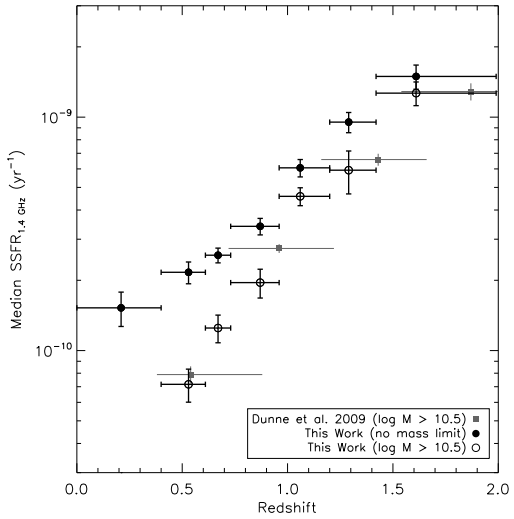

Figure 2.12: Median specific SFRs from the 1.4 GHz luminosities as a function of redshift. Solid black circles are the medians of the full stacked sample; open circles are using the mass limit $\log M_\star \geq 10.5$. Also plotted are the results of Dunne *et al.* (2009b) with the mass limit $\log M_\star \geq 10.5$ (small grey symbols). All vertical error bars denote the estimated 1σ uncertainty in the median following Gott *et al.* (2001); systematics in the SFR calibrations are not included. Horizontal bars mark the widths of the bins. All SFRs in this plot have been converted to a Kroupa IMF as described in the text.

-0.74 reduces radio SFRs in the last three bins but does not improve the agreement overall.

Figure 2.12 (black solid points) shows the median specific SFRs (SSFRs: calculated source-by-source as the radio SFR divided by the stellar mass) as a function of redshift. It is immediately apparent that median SSFRs increase strongly with redshift, indicating a rise in star-formation efficiency within the sample at increasing look-back times, a result seen many times in the literature (e.g. Cowie *et al.* 1996; Madau, Pozzetti & Dickinson 1998; Brinchmann & Ellis 2000; Bauer *et al.* 2005; Feulner *et al.* 2005; Pérez-González *et al.* 2008; Dunne *et al.* 2009b; Damen *et al.* 2009b; Oliver *et al.* 2010a). The black open points in Figure 2.12 show the results of the mass-limited subsample ($\log(M_\star) \geq 10.5$) in comparison to the full sample (filled points). This shows the effect of having lower median stellar masses in the full sample at low redshifts in particular (because SSFR is a function of stellar mass as well as redshift). The consistency between the results of this stacking study with the stacked K-selected sample of Dunne *et al.* (2009b) seems to support the idea that the IRAC selection targets a similar population to K selection.

2.5.5 Evolution of the FIR–Radio Correlation

The M51–corrected q indices in Figure 2.10, which have been shown to be the most appropriate, appear to show the least evolution in the FRC. It is important to note that the observed fluxes in the three MIPS bands trace different parts of the SED and are affected by different components of emission in the source galaxies. In particular, the observed 160 μm flux between $0 < z < 2$ is the closest tracer of the FIR peak of the SED (due to emission from large graphite and silicate grains, making up the majority of the dust mass), and q_{160} with the M51 k-correction displays no evidence of evolution. The q_{24} index is also broadly constant, despite 24 μm being a closer tracer of emission from PAHs than the bulk of the dust (e.g. Desert, Boulanger & Puget 1990). This lack of evolution is in agreement with previous studies of 24 μm-selected (e.g. Appleton *et al.* 2004; Huynh *et al.* 2010) and radio-selected samples (e.g. Ibar *et al.* 2008). Somewhat surprisingly however, some evolution is still apparent in q_{70} after M51 k–correction, at around 3σ significance.

Some of the anomalies in the k–corrected q_{24} and q_{70} evolution could be due to the MIR spectrum and/or the radio k–correction. The $z \approx 0.9$ bin, for example, coincides with the redshifted PAH feature at 12.7 μm, and the boost in k–corrected 24 μm flux at this redshift might be a sign of strong PAH emission in the sources. The radio k–correction could also play a part, since in this bin the measured spectral index is relatively flat. This explanation appears likely since a similar bump is apparent in q_{70} at the same redshift. Furthermore, there are particularly low values of q_{24} and q_{70} in the $z \approx 1.6$ bin, which coincides with the steepest measured spectral index. Repeating the stacking analysis using a constant spectral index of -0.74 ± 0.07 for radio k–corrections was found to have a small effect on both of these bins, changing each q index by -0.06 dex at $z \approx 0.9$ and $+0.17$ dex at $z \approx 1.6$. Similarly the values in the intermediate bins at $z \approx 1.1$ and 1.3 were raised by 0.07 and 0.06 respectively (changes in the low-redshift bins were negligible); however this still leaves a decline of 2σ significance in q_{70} when the M51 template is used. Clearly it is the FIR SED which dominates the evolution of monochromatic q indices, and not the radio spectrum.

One factor that could account for this decline in q_{70} is a steepening of the continuum slope shortward of 70 μm, relative to the M51 template. The SED in the MIR

region ($10\,\mu\mathrm{m} \lesssim \lambda \lesssim 70\,\mu\mathrm{m}$) is thought to be dominated by emission from VSGs (radii $\lesssim 10$nm) with fluctuating temperatures resulting from a mixture of thermal and single-photon heating (Desert, Boulanger & Puget 1990). A steepening of the the slope shortward of $70\,\mu\mathrm{m}$ might be due to an increase in the FIR ($\sim 100\,\mu\mathrm{m}$) luminosity (dominated by big grains) relative to the VSG contribution at shorter wavelengths, although this is not clear from the MIPS flux ratios (Figure 2.11).

In this context, it is interesting to compare with the results of Seymour *et al.* (2009), who measured $70\,\mu\mathrm{m}$ fluxes for a sample of faint radio sources and reported a decrease in observed q_{70} with redshift (both for detected sources and stacks), which is not fully accounted for by the k–correction of any single model SED. Seymour *et al.* concluded that their stacked data show a discrepancy at $0.5 \lesssim z \lesssim 1.5$ between increasing total L_{TIR} values (estimated from radio luminosities) and decreasing q_{70}, implying a change in the ULIRG SED at high redshift. Whatever the cause, it seems plausible that these two samples are similarly affected.

Some of the first results from *Herschel* provide further tantalising evidence for some change in star-formation activity at high redshifts: Rodighiero *et al.* (2010b) stacked 100 and $160\,\mu\mathrm{m}$ imaging from the PEP survey at the positions of IRAC ($4.5\,\mu\mathrm{m}$) sources that were optically classified as SFGs and were undetected in the $160\,\mu\mathrm{m}$ image. They found that SSFRs (derived from IR+UV luminosities) followed a power-law trend with mass, with an index of $-0.25^{+0.11}_{-0.14}$ at $z < 1$, in agreement with SSFRs from radio stacking (Dunne *et al.* 2009b; Pannella *et al.* 2009), but that the index steepened to $-0.50^{+0.13}_{-0.16}$ at $1 < z < 2$, deviating from the radio results. A change in the IR SED or q_{TIR} would be expected to produce such a deviation between SSFRs derived respectively from IR and radio (as is suggested by the data in Table 2.5).

In Figure 2.13 I plot the q indices calculated from L_{TIR} (listed in Table 2.5) using

$$q_{\mathrm{FIR}} = \log\left(\frac{L_{\mathrm{FIR}}/3.75\times10^{12}}{\mathrm{W}}\right) - \log\left(\frac{L_{1.4\,\mathrm{GHz}}}{\mathrm{W\,Hz^{-1}}}\right) \tag{2.12}$$

(Helou, Soifer & Rowan-Robinson 1985). Here I substitute L_{TIR} for $L_{\mathrm{FIR}} = L_{40-120\,\mu\mathrm{m}}$, (as in Bell 2003 and Ivison *et al.* 2010a, for example), and this difference should be noted when comparing to other work. As an indication, the ratio of $L_{\mathrm{TIR}}/L_{\mathrm{FIR}}$ in the M51 template is 2.1 (which implies $q_{\mathrm{TIR}} - q_{\mathrm{FIR}} = 0.32$), but this ratio is likely to be variable since much of the longer wavelength emission can include contributions from

dust heated by older stellar populations (as discussed for example by Bell 2003).

The results for $q_{\rm TIR}$ are shown in Figure 2.13 alongside the median result of Bell (2003) of $q_{\rm TIR} = 2.64 \pm 0.02$ for a FIR+FUV-selected sample of SFGs at $z \approx 0.0$. The results are generally a little higher than this value at $z < 1$, and it is only due to an apparent evolution that they are more in agreement at high redshift. The slight discrepancy is just within the errors allowed by the TIR normalisation, and may result from a systematic difference in the assumptions made about the SEDs and the associated calibration of TIR. A further possibility (as mentioned in Section 2.5.2) is that radio fluxes are underestimated at the lowest redshifts because the high-resolution interferometry resolves out extended emission (Jarvis *et al.* 2010). This would only affect the lowest redshift bin since the minor axis of the 1.4 GHz beam is $1.5'' \approx 8.0\,$kpc at $z = 0.4$. However, if 1.4 GHz flux was underestimated in this bin we should expect to see an anomalously low spectral index (since the 610 MHz beam is larger) yet this is not seen in Figure 2.6.

The slight decline in the $q_{\rm TIR}$ values with redshift is described by an error-weighted least-squares fit given by $q_{\rm TIR} \propto (1+z)^{\gamma}$ where $\gamma = -0.11 \pm 0.07$. Note that stacking with the mass limit $\log(M_{\star}) \geq 10.5$ gives very similar results, fit by the index $\gamma = -0.18 \pm 0.10$. In comparison, the 24 μm sample of Ivison *et al.* (2010a) showed evidence for evolution over redshifts from 0 to 3, with an error-weighted least-squares fit of the same form given by $\gamma = -0.15 \pm 0.03$. Most recently, Ivison *et al.* (2010b) showed that a sample of LIRGS detected by *Spitzer* and stacked into *Herschel* imaging at 100, 160, 250, 350 and 500 μm appear to exhibit evolution in $q_{\rm TIR}$ over $z = 0 - 2$, with $\gamma = -0.04 \pm 0.03$ (or -0.26 ± 0.07, discounting their 16 galaxies at $z < 0.5$ which were poorly matched in $L_{\rm TIR}$ to the higher-redshift bins).

A slight decline of a similar scale (~ 0.35 dex) in $q_{\rm TIR}$ with redshift ($0 < z < 1.4$) was also observed by Sargent *et al.* (2010a), in the median IR/radio ratios of their sample jointly selected in the IR and radio. However this was at low (2σ) significance and the possibility of intrinsic evolution was rejected by the authors because the median at $z \sim 1.4$ was within the scatter of their low-z value, and moreover because the average at $z > 2.5$ was very similar to the local value. Instead they considered that their sample was more contaminated by AGN at increasing redshifts, and that the hot

dust in these AGN caused q_{24} ratios to remain constant, while lower abundances of cold dust caused q_{70} and $q_{\rm TIR}$ to fall. It is interesting to note that these results similarly show constant q_{24} and falling q_{70} and $q_{\rm TIR}$, but the observation of constant q_{160} defies a similar explanation.

In a second paper, Sargent *et al.* (2010b) extended their earlier work using two volume-limited subsets of the joint sample: ULIRGs, and sources populating the bright end of the luminosity function defined by Magnelli *et al.* (2009). They showed that for both of these IR-bright populations, $q_{\rm TIR}$ was constant out to redshift 1.4. Following a correction for increased scatter in their data beyond this redshift, they concluded that it remained constant out to redshift 2.[6] This result disagrees with that of Ivison *et al.* (2010a), which is flux-limited as opposed to volume-limited, showing the potential importance of selection effects.

Mao *et al.* (2011) analysed the 70 μm data from the same FIDEL survey as used here, and used both stacking and survival analysis on the detected sample to test for evolution of the observed q_{70} and the bolometric $q_{\rm TIR}$ [the latter estimated by fitting 24+70 μm photometry to Chary & Elbaz (2001) templates]. Mao *et al.* found that q_{70} was consistent with the expected tracks of the SED templates (i.e. constant in the rest frame), while $q_{\rm TIR}$ showed a small downward evolution, by about 0.2, up to $z \sim 2$, although this did not continue to $z \sim 3$. However, their sample is likely to be more biased towards luminous SFGs than the NIR sample used here, since their stacked sample was based on radio detections while their survival analysis sampled 70 μm detections. Differences between the results of the two samples could easily result from different SEDs dominating the NIR and FIR samples, and from discrepancies between the true SEDs and the templates assumed.

The decline in $q_{\rm TIR}$ in Figure 2.13 may be an artificial effect resulting from the assumption of the M51 template; both $q_{\rm TIR}$ and q_{70} may be underestimated if the true SEDs were steeper at $\lambda \lesssim 70\,\mu$m. Alternatively if $q_{\rm TIR}$ really declines at high redshift then something must be causing galaxies to emit less in the IR relative to the radio at increasing redshifts. This could mean either a reduction in optical depth, causing more

[6] The current data are not affected by the bias in q described by Sargent *et al.* (2010a,b) due to the selection in the IRAC bands.

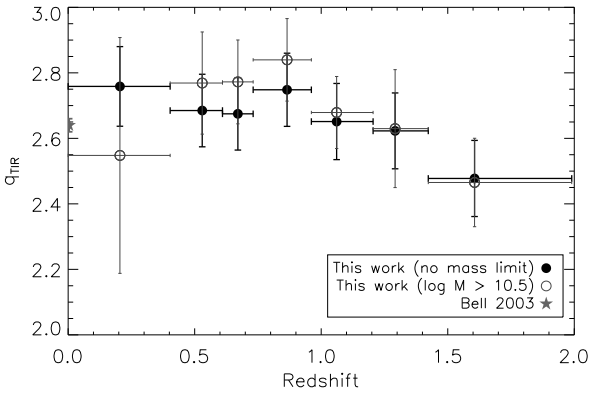

Figure 2.13: Total infrared luminosity–to–1.4 GHz luminosity ratio as a function of redshift for the full sample (black solid points) and for the mass limited sample ($\log(M_\star) \geq 10.5$; grey open points). Note that both sets of results decline similarly, implying that the evolution seen is not a symptom of Malmquist bias. Vertical error bars are dominated by the assumed systematic uncertainty of 25% in $L_{\rm TIR}$ (described in the text), but also include the 1σ error on the 1.4 GHz flux. Horizontal bars denote the full widths of the bins. The star at $z = 0$ represents the median $q_{\rm TIR} = 2.64 \pm 0.02$ from Bell (2003). Our results appear to be systematically higher than this value, except where they decline at $z > 1$, potentially as a result of different assumptions about the SEDs.

UV photons to escape, or an increase in the confinement and/or reprocessing efficiency of CREs leading to stronger radio emission. This latter possibility cannot be ignored in light of the steepening radio spectral index at redshifts $z \gtrsim 1$, since LTQ predict that steeper radio spectra are a sign of increasing electron calorimetry in normal galaxies.

In spite of these considerations, I remind the reader that the evolution in $q_{\rm TIR}$ is at low significance (similar to that of Sargent *et al.* 2010a), and the data are consistent within 1.5σ with no evolution. There is also the potential for some bias introduced by the variation of spectral index with redshift: applying a constant spectral index of -0.74 to the radio k–corrections reduces the $q_{\rm TIR}$ evolution to a level that is indistinguishable from being constant: $\gamma = 0.03 \pm 0.07$. The evolution in q_{70} however is not fully removed by this change. Using the measured spectral indices in each redshift bin I fit $q_{70} \propto (1+z)^{\gamma_{70}}$ with $\gamma_{70} = -0.15 \pm 0.05$, while using the constant spectral index I find $\gamma_{70} = -0.10 \pm 0.05$. Nevertheless, I emphasise that the measured spectral indices should give the most accurate k–correction, and Figure 2.6 shows that the overall median of -0.74 is certainly not appropriate to represent the flux ratios in all of the bins.

2.6 Conclusions

I have studied the FIR–radio correlation (FRC) as a function of redshift for NIR-selected massive galaxies in the ECDFS, a sample which is unbiased by star-formation activity. I used a stacking analysis to evaluate the ratios of median FIR/radio fluxes of all galaxies in the sample, divided into redshift bins. This technique traces the typical objects in the population of massive galaxies from low redshift back to their formation epoch. A thorough analysis of clustering of the sample was used to correct for the differential effects of confusion in the three FIR bands. k–corrections were derived in the radio and FIR using ratios of observed fluxes, ensuring as much as possible a self-consistent analysis. A mass-limited sub-sample was also stacked to confirm the robustness of the results to Malmquist bias.

The results for q_{24}, q_{70} and q_{160} show a slight decline in the *observed* relations, not dissimilar to the results of previous studies, which can be largely accounted for by the FIR k–correction using an M51 template. After k–corrections, q_{70} is the only monochromatic index to show signs of evolution, suggesting that the 70 μm k–correction may be less effective as a result of a steep slope in the SED from $\sim 25-35\,\mu$m (corresponding to $z \sim 1-2$) compared with M51. Observed MIPS colours at all redshifts are more consistent with the M51 template compared with hotter starburst galaxy templates, indicating that the typical IR SEDs of stellar-mass-selected galaxies at redshifts up to ~ 0.8 (at least) appear to be dominated by cold dust. At higher redshifts, it is not possible to constrain the dust temperature with MIPS colours, although it is still clear that M51 is the closest template. In contrast to this, both radio and total IR luminosities rise significantly with increasing redshift, as do the derived SFRs. The specific SFRs similarly rise steeply, in agreement with results in the literature.

The stacked radio data reveal tentative evidence for an evolution in radio spectral index across the redshift range, an unexpected result that implies some change in the radio loss processes in this sample towards higher redshifts. The most likely explanation seems to be a shift towards greater inverse-Compton losses of the CREs at $z > 1$, supporting the predictions of Lacki & Thompson (2010).

Overall the results show evidence that the FRC, measured from 24 μm fluxes or 160 μm

fluxes closer to the FIR peak, remains roughly constant up to $z \sim 2$, corresponding to 10 Gyr of cosmic time. This is similar to the conclusions of recent studies including Ibar *et al.* (2008); Garn *et al.* (2009); Younger *et al.* (2009); Ivison *et al.* (2010a) and Sargent *et al.* (2010a). The issue is clouded, however, by measurements at $70\,\mu\mathrm{m}$, which appear to show a declining q index with redshift, and when combined into a total IR luminosity, likewise show a slight decline (at low significance). This most likely implies a steeper spectral slope at wavelengths around $25 - 35\,\mu\mathrm{m}$ (compared with the M51 template), leading to insufficient $70\,\mu\mathrm{m}$ k–corrections. Yet a true evolution in the ratios of $70\,\mu\mathrm{m}$/radio luminosity and of TIR/radio luminosity is plausible, considering the apparent increase in electron-calorimetry behaviour at $z > 1$, and considering the fact that rest-frame 24, 70 and $160\,\mu\mathrm{m}$ fluxes can arise from different components of the dust in a galaxy. It is also consistent with the results of Seymour *et al.* (2009) for q_{70} and Ivison *et al.* (2010a,b) using BLAST/*Herschel* and *Spitzer* observations to measure q_{TIR}.

The general consensus in the literature is that the rest-frame FRC does not evolve (Ibar *et al.* 2008; Seymour *et al.* 2009; Ivison *et al.* 2010b; Jarvis *et al.* 2010; Sargent *et al.* 2010a; Mao *et al.* 2011; Roseboom *et al.* 2012), and therefore that FIR and radio tracers of star formation agree out to $z \sim 2$. If the correlation were to evolve, we would interpret this as evidence for either the radio or FIR luminosity failing to trace the SFR at high redshifts. In the radio case this could be a result of different CRE cooling processes, such as bremsstrahlung radiation and inverse-Compton scattering from the CMB, and in the FIR this could be caused by an increase in the UV photon escape fraction due to lower dust content or different spatial distributions of dust. These processes could still be important however, even with a constant FRC, since it has been shown that conspiracies between loss processes in the FIR and radio sources can maintain the FRC while both FIR and radio luminosities under-estimate the SFR (Bell 2003; Thompson *et al.* 2006; Lacki & Thompson 2010; and LTQ). A full understanding of the FRC will need to take into account theoretical considerations of magnetic fields, CRE production and cooling, and dust radiative transfer, as well as observational constraints from the FRC in faint and high-redshift galaxies, which are less well-studied, and at the sub-parsec scales of individual star-forming regions within galaxies. These are topics of ongoing research.

Chapter 3

The Sub-mm SEDs of Ordinary Galaxies at Low Redshift

3.1 Introduction

Dust in galaxies represents only a tiny fraction of the mass density of the Universe (e.g. Driver *et al.* 2007), but that fraction must increase towards higher redshifts as the sub-mm luminosity function (LF) evolves (Eales *et al.* 2009; Eales *et al.* 2010b; Dye *et al.* 2010; Dunne *et al.* 2011 [hereafter D11]). In this chapter I ask the question: what are the properties of dust in galaxies that are not selected to be dusty, and is there an evolution in their dust content with redshift equivalent to that seen in *Herschel*-selected galaxies?

Galaxies in the Universe comprise an extremely varied population, with a wide range of different properties. The galaxies that I will concentrate on in this chapter are the quintessential Hubble tuning-fork types, both spirals and ellipticals, that comprise the majority of galaxies selected in optical surveys (e.g. Driver *et al.* 2006). I make no prior selection with respect to dust content or FIR luminosity, but it may be expected that the typical galaxies sampled are quiescent in nature, and are not undergoing excessive starburst or nuclear activity (as in typical FIR-selected samples from *IRAS* or *Spitzer*). This sample may have more in common with the low redshift population in the H-ATLAS sample selected at 250 μm, which typically consists of optically lumi-

nous ($M_r \lesssim -20$), blue ($NUV - r < 4.5$) galaxies (D11; Dariush *et al.* 2011); but unlike H-ATLAS this sample is not biased towards dusty galaxies in any way.

Most large statistical studies of the FIR/sub-mm properties of FIR-faint galaxies selected by their stellar light have focused on high redshift samples selected in the NIR (Zheng *et al.* 2006; Takagi *et al.* 2007; Serjeant *et al.* 2008; Marsden *et al.* 2009; Greve *et al.* 2010; Oliver *et al.* 2010a; Bourne *et al.* 2011; Viero *et al.* 2012). Studies of dust emission from normal galaxies at low/intermediate redshifts have been restricted to small sample sizes and most have therefore focussed more on individual galaxies than populations (e.g. Popescu *et al.* 2002; Tuffs *et al.* 2002; Leeuw *et al.* 2004; Stevens, Amure & Gear 2005; Vlahakis, Dunne & Eales 2005; Cortese *et al.* 2006; Stickel, Klaas & Lemke 2007; Savoy, Welch & Fich 2009; Temi, Brighenti & Mathews 2009). This is simply because deep sub-mm imaging of large areas of sky is necessary to cover a large enough sample of low-redshift galaxies for statistical analysis. Until very recently, such data have not been available. Observations in the sub-mm, over the Rayleigh-Jeans tail of the dust SED at $\gtrsim 200\,\mu\mathrm{m}$, are crucial for constraining the mass of cold dust in the ISM of galaxies, since FIR studies using *IRAS* at $\lesssim 100\,\mu\mathrm{m}$ were only able to constrain the more luminous but less massive contribution from warm dust in star-forming regions (Dunne & Eales 2001).

Herschel-ATLAS is the first truly large-area sub-mm sky survey, and as such is ideal for this work. It is the largest open-time key project on the *Herschel Space Observatory* and will survey 550 deg^2 in five channels centred on 100, 160, 250, 350 and 500 μm, using the PACS and SPIRE instruments. For this study I use SPIRE maps of the three equatorial fields in the Phase 1 Data Release, which cover 135 deg^2 altogether, centred at R.A. of 9^{h}, 12^{h} and 14.5^{h} along the celestial equator (Dec.$\approx 0^{\circ}$). We are currently unable to use the H-ATLAS PACS maps for stacking due to uncertainties in the flux calibration at low fluxes, but this will be pursued in a follow-up paper.

In this chapter I use a large sample of optically-selected galaxies based on SDSS, bin by their stellar properties derived from the UV-NIR, and conduct an unbiased census of their dust properties in the sub-mm by stacking. Throughout this chapter I assume a cosmology of $\Omega_{\Lambda} = 0.7$, $\Omega_{\mathrm{M}} = 0.3$, and $H_0 = 70$ km s^{-1} Mpc^{-1}. All celestial coordinates are expressed with respect to the J2000 epoch.

3.2 Optical Data

3.2.1 Sample Selection

The galaxy sample was taken from the Galaxy and Mass Assembly (GAMA) redshift survey (Driver *et al.* 2009) which overlaps with the H-ATLAS equatorial fields at Dec.$> -1.0\,^\circ$ in the $9^{\rm h}$ field and Dec.$> -2.0\,^\circ$ in the other fields. The sample used for this study lies within the overlapping area between current H-ATLAS and GAMA coverage, approximately $126\,\mathrm{deg}^2$. The GAMA survey combines optical data from the Sloan Digital Sky Survey (SDSS DR6; Adelman-McCarthy *et al.* 2008), NIR data from the UKIRT Infrared Deep Sky Survey (UKIDSS) Large Area Survey (LAS DR4; Lawrence *et al.* 2007), and UV from the *Galaxy Evolution Explorer* (*GALEX*; Morrissey *et al.* 2005), with redshifts measured with the Anglo-Australian Telescope and supplemented with existing redshift surveys (see Driver *et al.* 2011 for further details).

I based the selection function on the GAMA "Main Survey" (Baldry *et al.* 2010), selecting objects from the GAMA catalogue which are classified as galaxies by morphology and optical/NIR colours, and are limited in magnitude to $r_{\rm petro} < 19.8$ or ($z_{\rm model} < 18.2$ and $r_{\rm model} < 20.5$) or ($K_{\rm model} < 17.6$ and $r_{\rm model} < 20.5$).[1] In fact only 0.3 per cent of the sample have $r_{\rm petro} > 19.8$, so the sample is effectively r selected. To simplify the selection function, I used the same selection in all fields, which reaches below the GAMA "Main Survey" cut of $r_{\rm petro} < 19.4$ in the $9^{\rm h}$ and $15^{\rm h}$ fields. Each galaxy has matched-aperture Kron photometry in nine bands: $ugriz$ from SDSS and $YJHK$ from UKIDSS-LAS, plus FUV and NUV photometry from *GALEX*. More details of the GAMA photometry can be found in Hill *et al.* (2011). All magnitudes used in this chapter have been corrected for galactic extinction using the reddening data of Schlegel, Finkbeiner & Davis (1998) and are quoted on the universal AB scale, $m_{AB} = -2.5\log_{10}(S_\nu/\mathrm{Jy}) - 48.6$. The Kron magnitudes from Hill *et al.* (2011) are used for the colours described in this section; however I use the Petrosian measurements for absolute magnitudes M_r. I purposely have not applied dust corrections based on the UV-NIR SED or optical spectra, because the aim is to study dust properties as a

[1] Model magnitudes are the best fit of an exponential and a de Vaucouleurs fit as described by Baldry *et al.* (2010).

function of empirical properties, excluding as much as possible any bias or prejudice to the expected dust content.

I used spectroscopic redshifts from GAMA (year 3 data) where they are available and reliable [flagged with Z_QUALITY $(nQ) \geq 3$]. These were supplemented with photometric redshifts computed from the optical-NIR photometry using ANNZ (for more details see Smith *et al.* 2011). The comparison of photometric and spectroscopic redshifts is shown in Figure 3.1. For this work I applied an upper limit in redshift of 0.35, because the number of good spectroscopic and photometric redshifts drops rapidly beyond this point. This means that the redshift bins would have to be made wider to sample the same number of sources (hence diluting any sign of evolution); it also means that I would only sample the brightest objects at the highest redshifts and their properties may not be comparable to the typically fainter objects sampled at lower redshift. I used photometric redshifts with relative errors $\delta z/z < 0.2$ only, which excludes most of the poor matches in Figure 3.1. This excludes eight per cent of the whole sample at $z < 0.35$ (seven per cent of $z_{\rm phot} < 0.35$), which means that the sample is still almost completely r-band limited. The limiting redshift error translates to a 20 per cent error on luminosity distance, a 40 per cent error on stellar mass, and an absolute magnitude error of 0.3. The criterion tends to exclude lower redshift objects, leading to a relative paucity of photometric redshifts at $z \lesssim 0.2$. This does not pose a problem since there is near complete spectroscopic coverage at these lower redshifts. Overall, 90 per cent of the redshifts used are spectroscopic, although the photometric fraction does increase with redshift out to $z = 0.35$. The histograms of spectroscopic and photometric redshifts are shown in Figure 3.2. I tested the effect of random photometric redshift errors on the results by perturbing each photometric redshift by a random shift drawn from a Gaussian distribution with width $\sigma = \delta z$. After making these perturbations, I made the same cuts to the sample and repeated all the analysis, and found that all stacked results were robust, changing by no more than the error bars shown.

A substantial number of photometric redshifts at $z > 0.3$ appear to be biased low in Figure 3.1. This explains why there appear to be more photometric redshifts than "all" redshifts at $0.3 < z < 0.35$ in Figure 3.2 – i.e. some of those objects have spectroscopic redshifts which are greater than 0.35 and hence do not appear in the

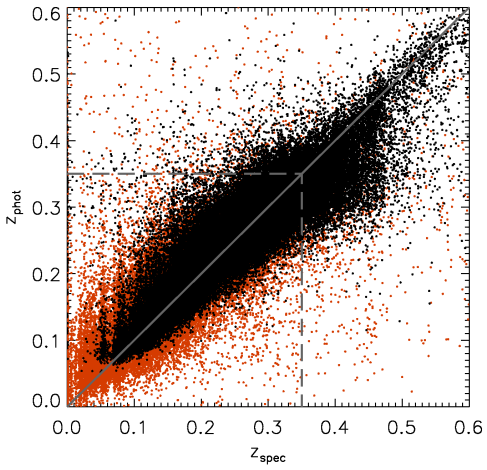

Figure 3.1: Comparison of spectroscopic ($nQ \geq 3$) and photometric redshifts for the objects in the sample which have both. Black points have photometric redshifts with relative errors < 20 per cent while orange points have greater errors. Using this limiting error and a limiting redshift of 0.35 (dashed lines) ensures a reliable set of photometric redshifts for the purpose of this study.

same bin in the "all redshifts" histogram. This issue could potentially affect the results in the highest redshift bin ($z > 0.3$); the effect would be to contaminate that bin with galaxies from a slightly higher redshift, which may complicate any evolutionary trends seen across the $z = 0.3$ boundary. I have chosen to leave the bin in the analysis because over 70 per cent of its galaxies have reliable spectroscopic redshifts, so the effect of a biased minority of photometric redshifts is considered to be small (and ultimately none of the conclusions hinge on this bin alone).

In total the sample contains 86,208 optically selected galaxies with good spectroscopic or photometric redshifts within the 126 deg^2 overlapping area of the SPIRE masks and the GAMA survey. I calculated k–corrections for the UV-NIR photometry using KCORRECT V4.2 (Blanton & Roweis 2007), with the spectroscopic and photometric redshifts described above. The final component of the input catalogue is the set of stellar masses from Taylor *et al.* (2011), which were computed by fitting Bruzual & Charlot (2003) stellar population models to the GAMA $ugriz$ photometry, assuming a Chabrier (2003) IMF.[2] Altogether there are stellar masses estimated for 90 per cent of the sample. The reason that 10 per cent are missing is that the sample reaches deeper than the GAMA Main Survey in two of the fields: I used the same magnitude limit in

[2]The NIR photometry were not used in deriving stellar masses due to problems fitting the UKIDSS bands as discussed by Taylor *et al.* (2011).

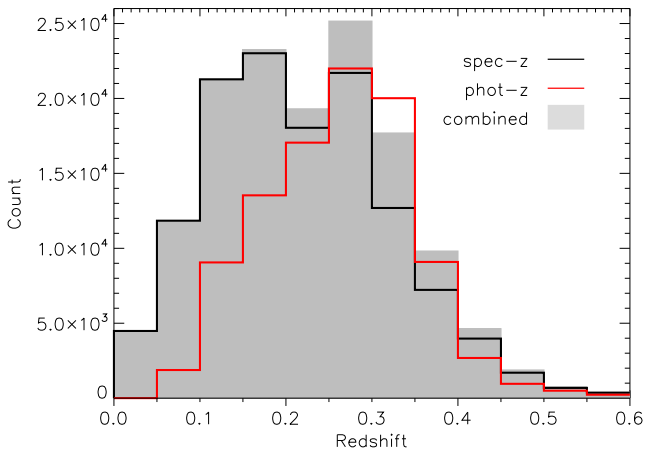

Figure 3.2: Histogram of redshifts available in the catalogue: spectroscopic with $nQ \geq 3$ (black line); photometric with $\delta z/z \leq 0.2$ (red line); all redshifts combined (grey shaded bars). In constructing the grey histogram I take all the spectroscopic redshifts in the black histogram and add any additional photometric redshifts from the red.

all three fields in order to sample as large a population as possible.

3.2.2 Colour Classifications and Binning

A simple way to divide the sample in terms of stellar properties is to make a cut in rest-frame optical colours. The bands which have good signal-to-noise data for the whole sample are the three central SDSS bands, hence the most reliable and complete optical colours to use are $g-r$, $g-i$, or $r-i$. I found very little difference between the distributions of colours in any of these three alternatives; each appears equally effective at defining the populations of galaxy colours. I chose to use $g-r$ since these bands have the best signal-to-noise hence greatest depths, and I plot the colour-magnitude diagram (CMD) in Figure 3.3.

In this figure the colour-magnitude space is sampled by a two-dimensional histogram in which the number density in each bin is weighted by $\sum 1/V_{\rm max}$ (Schmidt 1968) to correct for the incompleteness of a flux-limited sample. To achieve this I weighted each galaxy by the ratio of the volume of the survey (the comoving volume at $z = 0.35$) to the comoving volume enclosed by the maximal distance at which that galaxy could have been included in the survey. To measure the latter I used the $r_{\rm petro}$ limit which is the primary limiting magnitude of the sample (a negligible proportion of sources that

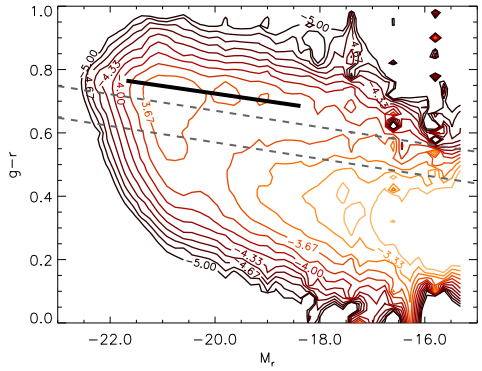

Figure 3.3: Two-dimensional histogram of the rest-frame $g-r$, M_r CMD for the full sample. Contours mark the $\log_{10}$ of the histogram density function, weighted with the $1/V_{\rm max}$ method to account for incompleteness as described in the text. Contours are smoothed by a Gaussian kernel with width equal to 0.8 of the bin width (1/50 of the range in each axis). The heavy black line is the red sequence fit given by equation (3.1). The two dashed lines mark the boundaries between red/green and green/blue classifications respectively, which are given by equation (3.2).

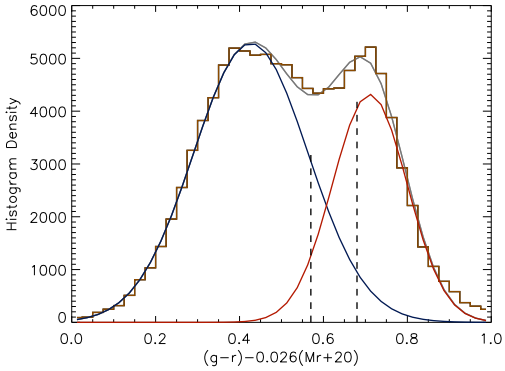

Figure 3.4: Histogram of rest-frame, slope-corrected $g-r$ colours across $-23 < M_r < -18$ (weighted with the $1/V_{\rm max}$ method). Overlaid are the two Gaussian functions fitted to the histogram as well as the sum of the functions. The dashed vertical lines show the boundaries of the colour bins described in the text.

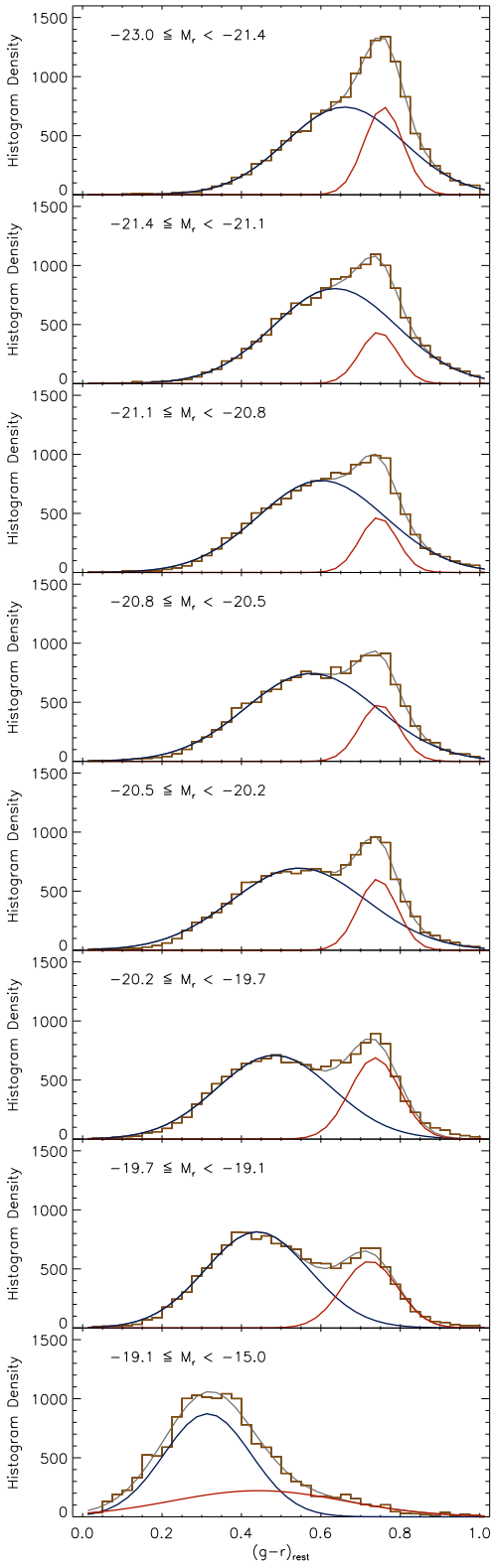

Figure 3.5: Histograms of rest-frame $g-r$ split into eight M_r bins between -23 and -15 (weighted with the $1/V_{\rm max}$ method). Overlaid are the two Gaussian functions simultaneously fitted to each histogram, representing the blue and red populations respectively, as well as the sum of the functions.

were selected by z or K have fainter $r_{\rm petro}$ magnitudes). The redshift limit of 0.35 was also considered (so no $V_{\rm max}$ is greater than the comoving volume at $z = 0.35$).

It is well established that the optical colours of galaxies fall into a bimodal distribution featuring a narrow "red sequence" and a more dispersed "blue cloud" (Tresse *et al.* 1999; Strateva *et al.* 2001; Blanton *et al.* 2003; Kauffmann *et al.* 2003; Baldry *et al.* 2004; Bell *et al.* 2004; Faber *et al.* 2007; etc). Baldry *et al.* (2004) have shown that the optical CMD can be successfully modelled as the sum of two Gaussian functions in colour, which evolve with absolute magnitude and redshift. In Figure 3.3 there is a clear bimodality in $(g-r)_{\rm rest}$ which can be modelled as a function of absolute magnitude M_r (Petrosian) by splitting the distribution into eight bins between M_r of -15 and -23, and computing the one-dimensional histogram of colours in each bin. These histograms were each fitted with the sum of two Gaussian functions, shown in Figure 3.5. For convenience these functions can be thought of as representing two populations, one peaking on the red sequence and one in the blue cloud, although this interpretation has limited physical meaning. A linear least-squares fit representing the red sequence was obtained from the means and standard deviations of the red population as a function of absolute magnitude across the eight bins. Note that the $M_r \geq -19.1$ bin has effectively no red sequence, and has no contribution to the linear fit because the standard deviations were used as errors in the fitting. I checked for any redshift dependency by splitting the population into three redshift bins as well as magnitude bins, but since no variation was found I used the red-sequence fit to the eight magnitude bins with no redshift binning. This fit is shown as a heavy black line in Figure 3.3, and is given by

$$(g-r)_{\rm rest} = 0.724 - 0.026(M_r + 20). \tag{3.1}$$

In order to divide red and blue populations as confidently as possible, I examine the distribution of $g-r$ colours across the range $-23 < M_r < -18$ in Figure 3.4. Here I plot the one-dimensional histogram of $C_{gr} = (g-r)_{\rm rest} - 0.026(M_r + 20)$, thus removing the slope in the red sequence to emphasise the bimodality. In Figure 3.4, I have excluded $M_r > -18$ because the red sequence becomes negligible at these faint luminosities and the distribution becomes dominated by the blue cloud, which hinders the two-component fitting (note I do not make any absolute magnitude cut when stacking). The distribution in Figure 3.4 was fitted with the sum of two Gaussians:

the red sequence has a mean of $\mu_{\rm r} = 0.71$ and standard deviation of $\sigma_{\rm r} = 0.09$; the blue cloud has $\mu_{\rm b} = 0.43$ and $\sigma_{\rm b} = 0.14$. To make a clean sample of red galaxies I made a cut at $C_{gr} > 0.67$ (i.e. $\mu_{\rm r} - 0.5\sigma_{\rm r}$). This cut was chosen to minimise the contribution of the "blue" functional fit, while also including the majority (55 per cent) of the area under the red fit. The fraction of this histogram at $C_{gr} > 0.67$ that belongs to the blue function is seven per cent. It is recognised that the functional fits do not necessarily represent two distinct populations of galaxies, and this fraction does not imply a contamination of the red bin since all galaxies with $C_{gr} > 0.67$ are empirically red. These cuts are largely arbitrary and the main purpose they serve is to separate the two modes of the colour distribution. Using similar arguments, I made a blue cut at $C_{gr} < 0.57$ (i.e. $\mu_{\rm b} + 1\sigma_{\rm b}$) which selects 86 per cent of the blue function; the fractional contribution of the red function in this bin is four per cent. The intermediate bin by its very nature is likely have a heterogeneous composition including some galaxies close to the red sequence, others that are part of the blue cloud, and some proportion of genuine "green valley" galaxies (Schiminovich *et al.* 2007; Martin *et al.* 2007). The relative contributions from each of these to the intermediate ("green") bin may vary as a function of redshift and absolute magnitude, which must be kept in mind when drawing any conclusions. However, the red and blue bins will be dominated by completely different populations with respect to each other at all redshifts and absolute magnitudes, which justifies the use of an intermediate bin to fully separate them. The $g-r$ colour bins are summarised in equation (3.2):

$$\begin{aligned}
&\text{RED:} && 0.67 + f(M_r) < (g-r)_{\rm rest} < 1.00 \\
&\text{GREEN:} && 0.57 + f(M_r) < (g-r)_{\rm rest} < 0.67 + f(M_r) \\
&\text{BLUE:} && 0.00 < (g-r)_{\rm rest} < 0.57 + f(M_r)
\end{aligned}$$

$$\text{where } f(M_r) = -0.026(M_r + 20) = -0.026M_r - 0.52 \qquad (3.2)$$

These divide the sample into 41,350 blue, 17,744 green and 27,114 red galaxies. A limitation of optical colours such as $g-r$ is the small separation in colour space between the red and blue populations. This would be improved by using a pair of bands which straddle the 4000Å spectral break, but the only Sloan band blueward of this is

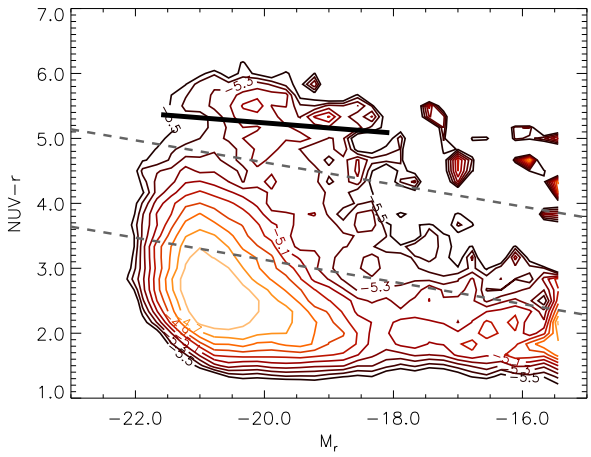

Figure 3.6: Two-dimensional histogram of the rest-frame $NUV-r$, M_r CMD for the full sample. Contours mark the $\log_{10}$ of the histogram density function, again using the $1/V_{\rm max}$ method to account for incompleteness as described in the text. Contours are smoothed by a Gaussian kernel with width equal to one bin (1/40 of the range in each axis). The noise in the top right is a result of a small amount of data close to the NUV detection limit having exceptionally high weights. The heavy black line is the red sequence fit to the data given by equation (3.3). The two dashed black lines mark the boundaries between red/green and green/blue classifications respectively, which are given by equation (3.4).

u, which has poor signal-to-noise and therefore a relatively shallow magnitude limit. It has been shown in the literature (e.g. Yi *et al.* 2005; Wyder *et al.* 2007; Cortese & Hughes 2009) that a UV–optical colour such as $NUV-r$ (or UV–NIR such as $NUV-H$) provides greater separation between red and blue and reveals a third population of galaxies in the green valley. A clear delineation of the populations would minimise contamination between the bins and should help to disambiguate trends in stacked results.

Figure 3.6 shows the $NUV-r$ CMD (since the r-band data are deeper than H, and this gives an NUV-limited sample). I was unable to successfully fit the $NUV-r$ colour distribution in bins of M_r using the simple double Gaussian function, due to a significant "green valley" excess. To overcome this I followed Wyder *et al.* (2007) by defining a clean red sample [$NUV-r > f(M_r)-0.5$] and blue sample [$NUV-r < f(M_r)-2.0$], where $f(M_r)=1.73-0.17M_r$ is the fit to a morphologically-selected red sequence by Yi *et al.* (2005). To these subsets I attempted to fit Gaussian functions for the red and blue distributions respectively, again in eight bins of M_r between -15 and -23. As before, I found a linear least-squares fit to the means of the red sequence,

given by

$$(NUV - r)_{\rm rest} = 5.23 - 0.08(M_r + 20). \quad (3.3)$$

The slope of this fit is somewhat flatter than the -0.17 found by Yi *et al.* (2005), but the uncertainty is large due to the fact that I have only performed the Gaussian fit in each bin to the upper part of the red sequence. As in Figure 3.4 I could subtract the slope and plot the histogram of the residual colour across all M_r, but due to the uncertainty on the slope this does not give any extra benefit. Instead, I simply adopted the colour cuts defined by Wyder *et al.* (2007) as the boundaries between blue, green and red samples:

$$\begin{aligned}
&\text{RED:} && f(M_r)-0.5 < (NUV - r)_{\rm rest} < 7.0 \\
&\text{GREEN:} && f(M_r)-2.0 < (NUV - r)_{\rm rest} < f(M_r) - 0.5 \\
&\text{BLUE:} && 1.0 < (NUV - r)_{\rm rest} < f(M_r) - 2.0
\end{aligned}$$

$$\text{where } f(M_r) = 1.73 - 0.17M_r \quad (3.4)$$

These divide the sample into 36,900 blue, 12,758 green and 3115 red galaxies. These numbers reveal two disadvantages of using the $NUV - r$ colour: that there are NUV detections for only about 60 per cent of the sample, and that the NUV selection naturally disfavours red $NUV - r$ colours leading to a smaller number of galaxies in the red bin. In contrast the r-band selection of the $g - r$ sample is relatively unbiased by the colour of the galaxy. However, the differentiation between blue and green populations should be more successful using $NUV - r$ compared with $g - r$. Therefore both alternatives have their merits. In Section 3.4.5.1, I compare the results obtained using the two alternative colour cuts, but for the bulk of the chapter I will refer to the $g - r$ colour cuts unless otherwise stated.

In this chapter I do not explicitly attempt to distinguish passive red galaxies from obscured, star-forming red galaxies; rather I focus on the sub-mm properties as a function of observed optical colours. One may therefore expect a somewhat mixed population in the red (and green) bins, even using $NUV - r$. There are various ways one might attempt to overcome this – applying dust corrections based on UV photometry or spectral line indices, or using the Sérsic index to predetermine the expected galaxy "type" – however, I opt to avoid biasing any of the results by any prior assumption about the

nature of galaxies in each bin.

3.3 Sub-mm Data and Stacking

3.3.1 Stacking into the SPIRE Maps

For the sub-mm imaging I used SPIRE images at 250, 350 and 500 μm of the three equatorial GAMA fields in H-ATLAS, which were made in a similar way to the science demonstration maps described by Pascale *et al.* (2011). The fields consist of 53.25 deg^2 at $9^{\rm h}$, 27.37 deg^2 at $12^{\rm h}$ 53.93 deg^2 at $14.5^{\rm h}$. Background subtraction was carried out using the NEBULISER routine developed by Irwin (2010) which effectively filters out the highly-varying cirrus emission present in the H-ATLAS maps, as well as extended background emission including the Sunyaev-Zel'dovich effect in clusters and unresolved clustered sources at high redshift.

All sources were treated as point sources, and fluxes were measured in cut-outs of the map around each optical position, convolved with a PRF. I accounted for sub-pixel scale positioning by interpolating the PRF from the PSF[3] at a grid of pixels offset from the centre by the distance between the optical source centre and the nearest pixel centre. This convolution with the PRF is the standard technique to obtain the minimum-variance estimate of a point source's flux (Stetson 1987). The PSFs at 250, 350 and 500 μm have FWHM equal to 18, 25 and 35 arcsec respectively.

I then measured fluxes in the maps at the positions in the optical catalogue, and stacked using a similar algorithm to that described in Chapter 2. I used the deblending algorithm described in Appendix A to avoid over-estimating the stacked flux of blended and clustered sources (with the caveat that sources not in the catalogue, i.e. below the optical detection limits, cannot be deblended). I divided the sample into three colour bins (as described in the previous Section), then split each into five bins of redshift, then six bins of absolute magnitude. Redshift and magnitude bins were designed to each contain an approximately equal number of objects, in order to ensure that the sample was evenly divided between the bins and maintain good number statistics in

[3]See also Section 2.3.2.

each. As in Chapter 2, I used the median statistic as a robust estimator of the typical flux in a bin.

I also measured the background in the maps, since although they have been sky-subtracted to remove the highly variable cirrus foreground emission, the overall background does not average to zero, and therefore has a significant contribution to stacked fluxes. Using a similar algorithm to that in Section 2.3.4, I created a sample of 100,000 random positions in each map, within the region covered by the optical catalogue. I masked around each source in the target (GAMA) catalogue with a circle of radius equal to the beam FWHM in order to avoid including these sources in the background stack. I then performed an identical stacking analysis at these sky positions, rejecting any positions with a measured flux greater than 5σ. The stacked background flux measured in this way is subtracted from the stacked fluxes of each target sample prior to further analysis. The average background levels are 3.5 ± 0.1, 3.0 ± 0.1 and 4.2 ± 0.2 mJy beam^{-1} in the 250, 350 and 500 μm bands respectively.

Fluxes measured in the SPIRE maps are calibrated for a flat νS_ν spectrum ($S_\nu \propto \nu^{-1}$), whereas thermal dust emission longward of the SED peak will have a slope between ν^0 and ν^2 depending on how far along the Rayleigh-Jeans tail a given waveband is. The SPIRE Observers' Manual[4] provides colour corrections suitable for various SED slopes, including the ν^2 slope appropriate for bands on the Rayleigh-Jeans tail. This is a suitable description of the SED in each of the SPIRE bands at low redshift, and I therefore modified measured fluxes by the colour corrections for this slope: 0.9417, 0.9498 and 0.9395 in the three bands respectively. At increasing redshifts, however, a cold SED can begin to turn over in the observed-frame 250 μm band. From inspection of single-component SEDs fitted to the stacks, I estimated that the SPIRE points in most of the bins fall on the Rayleigh-Jeans tail, although at the highest redshifts slopes can be as flat as ν^0 at 250 μm and $\nu^{1.5}$ at 350 μm. The corresponding colour corrections are 0.9888 and 0.9630 respectively. I tried applying these corrections to the highest redshift bins and found no discernible difference to any of the stacked results, hence the results are not dependent on the colour correction assumed.

[4]Available from `http://herschel.esac.esa.int/Docs/SPIRE/html/spire_om.html`

3.3.2 Simulations

The stacking procedure used was tested on simulated maps to ensure that it could accurately measure faint fluxes when stacking in confused maps with realistic noise and source density. As described in Appendix A, I was able to accurately reproduce median fluxes and correct errors, although fluxes of individual sources could be under-/over-estimated if they were blended with a fainter/brighter neighbouring source.

In addition I simulated various distributions of fluxes to test that the median measured flux is unbiased and representative when stacking faint sources close to and below the noise and confusion limits. The results of these simulations indicate that the median can be biased in the presence of noise (see also White *et al.* 2007). I show details of the simulations in Appendix B. In summary, I assumed a realistic distribution of fluxes described by $dN/dS \propto S^{-2}$, $S_{\rm min} < S < S_{\rm max}$; $R = \log_{10}(S_{\rm max}/S_{\rm min}) = 1.3$, and for this I estimated the amount of bias in the measured median as a function of the true median flux, and correct the stacked fluxes for this bias. Correction factors are all in the range $0.6 - 1.0$, and the effect is greatest for low fluxes ($\lesssim 10\,$mJy). If one considers the true median to be representative of the typical source in any bin, then relative to this, the bias in the measured median is always less than or equal to the "bias" in the mean resulting from extreme values (as I explain in Appendix B). I tested the sensitivity of the results to assumptions about the flux distribution, and found that although the level of bias does depend on the limits and slope of the distribution, all of the measured trends remain significant and all conclusions remain valid for any reasonable choice of distribution. This is equally true if no correction is made to the measured median.

I also tested the correlations found in the data by simulating flux distributions with various dependencies on redshift, absolute magnitude and colour. I first made simulations in which fluxes were randomised with no built-in dependencies but with the same scatter as in the real data, and saw that stacked results were equal in every bin (as expected). I tried simulations in which fluxes varied with redshift as a non-evolving LF (simply varying as the square of the luminosity distance, modified by the k–correction), with realistic scatter; and also as an evolving LF (log flux increasing linearly with redshift at a realistic rate), also with scatter. I also allowed flux to vary linearly with optical

colour and logarithmically with M_r, again including realistic scatter. In all simulations I was able to recover the input trends by stacking.

Finally I simulated fluxes in the three SPIRE bands to produce a randomised distribution of sub-mm colours (S_{250}/S_{350} etc) with scatter similar to that in the data but with no correlations built in. Results showed that no artificial correlations were introduced by stacking.

These results indicate that the correlations detected in the real data (described in the following section) should be true representations of the intrinsic distributions in the galaxy population, and are not artefacts created by the stacking procedure.

3.3.3 Errors on SPIRE Fluxes

Errors on stacked fluxes were calculated in two different ways. Firstly I estimated the instrumental and confusion noise on each source and propagated the errors through the stacking procedure. I estimated the instrumental noise by convolving the variance map at the source position with the same PRF used for the flux measurement. To this I added in quadrature a confusion noise term, as in Rigby *et al.* (2011). Since fluxes were measured by filtering the map with a kernel based on the PSF (see Appendix A), it is appropriate to use the confusion noise as measured in the PSF-filtered map. Pascale *et al.* (2011) measured confusion noises of 5.3, 6.4 and 6.7 mJy per beam in the PSF-filtered H-ATLAS Science Demonstration Phase (SDP) maps. I estimated that the confusion noise is at a similar level in the maps after PSF-filtering, by comparing the total variance in random stacks on the background to the average instrumental noise described above. Hence I combined these values of confusion noise with the measured instrumental noise of each source. In each stack the mean of these measured noises, divided by the square root of the number of objects stacked, and combined with the error on background subtraction, gives the "measurement error" ($\sigma_{\rm N}$) in Table C.1.

I also estimated errors on median fluxes and other stacked quantities from the distribution of values in the bin, using the method of Gott *et al.* (2001) described in Section 2.3.3 [equation (2.2)]. This method automatically takes into account measurement errors as well as genuine variation within the bin resulting from the underlying pop-

ulation from which it is drawn. The resulting statistical errors ($\sigma_{\rm S}$ in Table C.1) are typically three to four times larger than the measurement errors $\sigma_{\rm N}$, indicating that the uncertainty resulting from the spread of intrinsic fluxes in a bin is greater than the combined noise in the map at all the positions in the stack.

3.4 Results

3.4.1 Stacked Fluxes

The results of stacking SPIRE fluxes as a function of $g-r$ colour, redshift and absolute magnitude M_r are given in Table C.1. Secure detections were obtained at 250 and 350 μm in most bins, although many bins have low signal-to-noise at 500 μm. Note that the signal-to-noise ratios in the Table are based on the measurement error reduced by $\sqrt{N}$ (i.e. $\sigma_{\rm N}$), since this strictly represents the noise level (instrumental plus confusion) which I compare the detections against. When talking about errors in all subsequent analysis I will refer to the statistical uncertainty on the median ($\sigma_{\rm S}$) because this takes into account both instrumental noise and the distribution of values in the bin, both of which are contributions towards the uncertainty on the median stacked result.

Table C.1 also contains the results of Kolmogorov–Smirnov (KS) tests which were carried out on each stack to test the certainty that the stacked flux represents a signal from a sample of real sources and is not simply due to noise. This was done by comparing the distribution of measured fluxes in each bin with the distribution of fluxes in the background sample for the same SPIRE band. These background samples (described in Section 3.3.1) were placed at a set of random positions in the map, after masking around the positions of input sources. If any of the stacks did not contain a significant signal from real sources then the KS test would return a high probability that the distribution of fluxes is drawn from the same population as the background sample. The great majority of the bins were found to have an extremely small KS probability, meaning that we can be confident that the signals measured are real. The highest probability is 0.04, for a 500 μm stack in the highest-redshift, red-colour bin. A small

sample of the bins are explored in more detail in Appendix C, where I show stacked postage-stamp images and histograms on which the KS test was carried out.

Stacked fluxes at 250, 350 and 500 μm in the observed frame are plotted in Figure 3.7, showing the dependence on M_r and $g-r$ at different redshifts. The majority of the bins have stacked fluxes well below the 5σ point-source detection limits shown as horizontal lines on the figure. In all three bands there is a striking difference between the sub-mm fluxes of blue, green and red galaxies, and a strong correlation with M_r in the low-redshift bins of blue and green galaxies. These trends unsurprisingly indicate that the red galaxies tend to be passive and have lower dust luminosities than blue, and are generally well below the detection threshold in all SPIRE bands. They also show that sub-mm flux varies little across the range of M_r in red galaxies, while in blue galaxies it correlates strongly with M_r such that only the most luminous r-band sources have fluxes above the 250 μm detection limit – a point noted by Dariush *et al.* (2011) and D11. The variation with redshift is also very different between the three optical classes, with the fluxes of blue galaxies diminishing with redshift more rapidly than those of red galaxies. Fluxes in the green bin initially fall more rapidly with increasing redshift than those in the blue, but at $z > 0.18$ they resemble those in the red bin and evolve very little. This is potentially due to a change in the nature of the galaxies classified as green at different redshifts, which is unsurprising since this bin contains a mixture of different galaxy types in the overlapping region between the blue cloud and red sequence. It is likely that the relative fractions of passive, relatively dust-free systems and dusty star-forming systems in this bin will change with redshift, as the star-formation density of the Universe evolves over this redshift range (Lilly *et al.* 1996; Madau *et al.* 1996; etc). The evolutionary trends discussed in this section can be better explored by deriving sub-mm luminosities, which first requires a model for k–correcting the fluxes, as I will discuss in Section 3.4.4.

At this point it is worth considering some potential sources of bias in different bins in case they might impact on the apparent trends. For example, it is reasonable to expect that certain classes of galaxy are more likely than others to inhabit dense environments: in particular redder galaxies, and more massive galaxies, are known to be more clustered (e.g. Zehavi *et al.* 2011). While I have accounted for blending in the

flux measurements (see Appendix A), this is limited to the blending of sources within the catalogue. At increasing redshifts the catalogue becomes more incomplete, and it becomes more likely that the clustered galaxies will be blended with some unseen neighbour. I have made no correction for this effect, but expect the contamination to be small for the following reasons: the input sample is complete down to below the knee in the optical LF at $z < 0.3$ (see next section); I therefore account for the blending with most of the galaxies in the same redshift range. Contaminating flux would have to come from relatively small galaxies which are not likely to contribute a large amount of flux. Moreover, the blending corrections are on average very small in comparison with the trends observed (see Appendix A Table A.1), so a small additional blending correction should not significantly alter the conclusions.

3.4.2 Contamination from Lensing

There is a risk that the sub-mm fluxes of some galaxies in the sample are contaminated by flux from lensed background sources, via galaxy-galaxy lensing. This is especially likely in a sub-mm survey as a result of the negative k–correction and steep evolution of the LF (Blain 1996; Negrello *et al.* 2007). These factors conspire to make sub-mm sources detectable up to very high redshifts, therefore providing an increased probability for one or more foreground galaxies to intrude in the line of sight and magnify the flux via strong gravitational lensing. The strong potential for detecting lensed high redshift sources in H-ATLAS was conclusively demonstrated by Negrello *et al.* (2010). This study targets low redshift sources selected in the optical, but the sample will inevitably include some of the foreground lenses whose apparent fluxes are likely to be boosted by flux from the lensed background sources. The flux magnification is likely to be greatest for massive spheroidal lenses, as a result of their mass distribution (Negrello *et al.* 2010). This could pose a problem for the red bins, where spheroids will be mostly concentrated. To make matters worse, measured fluxes are lowest in the red bins which means that even a small lensing contamination of order 1 mJy could significantly boost the flux.

I made an estimate of the lensing contribution to stacked fluxes by considering the predicted number counts of lenses from Lapi *et al.* (2011), which are based on the

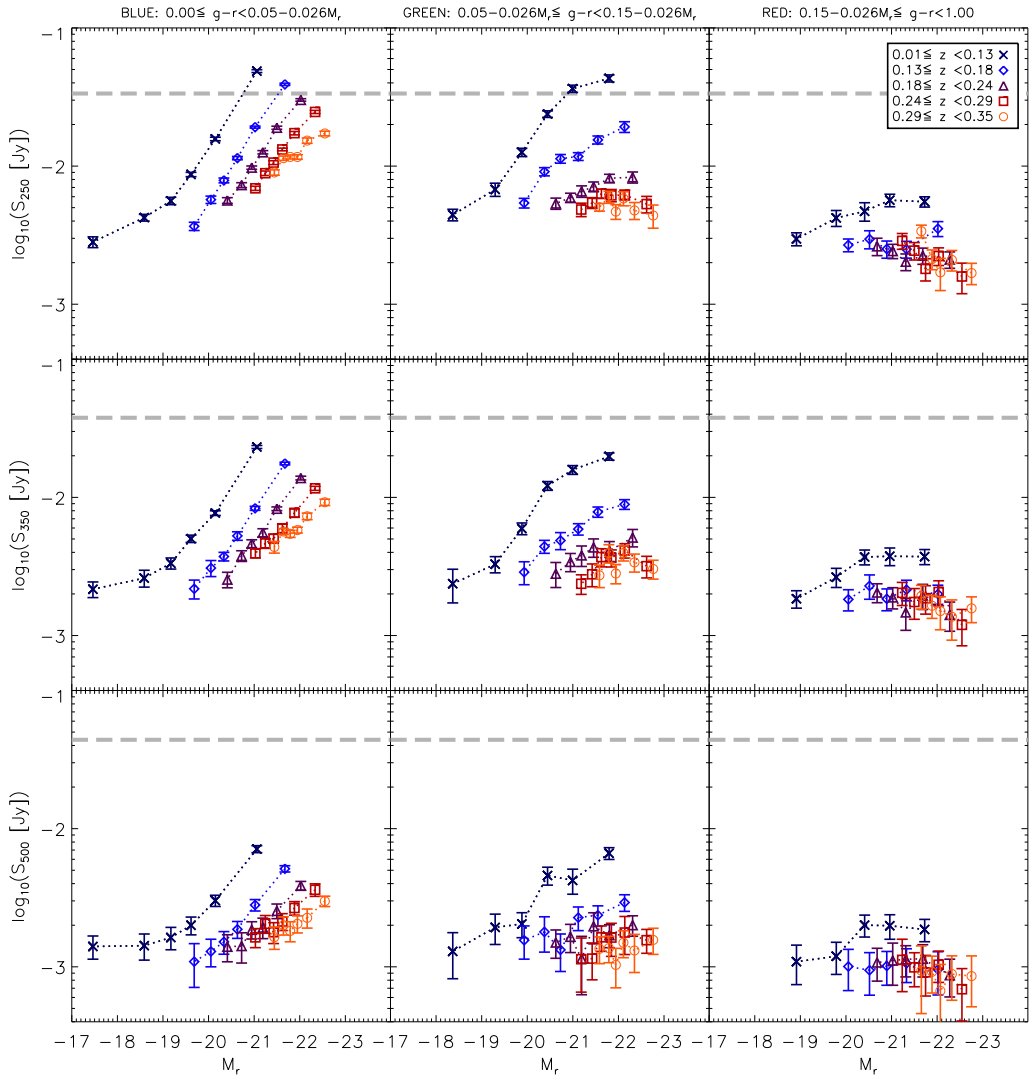

Figure 3.7: Stacked SPIRE fluxes (not k–corrected) as a function of $g - r$ colour, redshift and absolute magnitude M_r. Top: 250 μm, middle: 350 μm, bottom: 500 μm. Galaxies are binned by optical colour from blue to red (shown in panels from left to right) and by redshift (shown by plot symbols) and stacked fluxes in each bin are plotted against M_r. Error bars are the statistical 1σ errors in the bins as described in Section 3.3.3, and also include errors due to background subtraction. The horizontal dashed lines at 33.5, 39.5 and 44.0 mJy in 250, 350 and 500 μm, represent the 5σ point-source detection limits as measured in the PSF-convolved Phase 1 maps.

amplification distribution of strong lenses (amplification factors ≥ 2) from Negrello *et al.* (2007). Integrating these counts gives a total of 470 lensed sub-mm sources per square degree, and integrating their fluxes per square degree gives the total surface brightness of lensed sources shown in the first line of Table 3.1. However, the counts are not broken down by redshift, and only those at $z < 0.35$ will contribute to the stacks. It is not trivial to predict what fraction of strong lenses are in this redshift range, but recent results from H-ATLAS can provide us with the best estimate that is currently

possible. González-Nuevo *et al.* (2012) created a sample of 64 candidate strong lenses from the H-ATLAS SDP by selecting sources with red SPIRE colours which have no reliable SDSS IDs, or have SDSS IDs with redshifts inconsistent with the sub-mm SED. After matching to NIR sources in the VISTA Kilo-degree INfrared Galaxy survey (VIKING; Sutherland, W. *et al.* in preparation), they reduced this sample to 33 candidates with photometric redshifts for both the lens (using the NIR photometry) and source (using SPIRE and PACS photometry). For comparison, applying the same SPIRE flux limits to the Lapi *et al.* (2011) models yields an estimated two lensed and two unlensed high-redshift sources per square degree, which is consistent with the 64 flux-selected sources, of which 33 have low-redshift matches, in the 16 deg^2 SDP field (González-Nuevo *et al.* 2012). This sample, the H-ATLAS Lensed Objects Selection (HALOS), is unique in being selected in the sub-mm, enabling the selection of candidate lenses over a much larger redshift range than other lens samples to date (their lenses had photometric redshifts $\lesssim 1.8$, while other surveys were confined to $z < 1$). HALOS therefore provides the best observational measurement of the lens redshift distribution.

Seven of the 33 HALOS candidates have lens redshifts < 0.35. González-Nuevo *et al.* (2012) removed two of these from their final sample because the lenses were at $z < 0.2$, and they considered lenses at such low redshifts to have low probability both on theoretical grounds and on the evidence of previous surveys (Browne *et al.* 2003; Oguri *et al.* 2006; Faure *et al.* 2008). However, to avoid the risk of underestimating the number of low redshift lenses, I conservatively included those two in the analysis. The fraction of lenses at $z < 0.35$ is therefore $7/33 = 21^{+9}_{-5}$ per cent, using binomial techniques to estimate the 1-σ confidence interval (Cameron 2011). Using these results to scale the total lensed flux from all redshifts, I obtained the contribution from lenses at $z < 0.35$, as shown in Table 3.1. Assuming that all these low redshift lenses fall in the red bin of the sample, I compared these fluxes to the total stacked flux of the red bins as shown in Table 3.1, which indicates that about 10, 20 and 30 per cent of the 250, 350, and 500 $\mu\mathrm{m}$ fluxes respectively comes from high redshift sources lensed by the targets. This may be a slight overestimate since some of the lenses may fall in the other bins; however Auger *et al.* (2009) showed that 90 per cent of lenses are massive early type galaxies. Any lensing contribution to the blue or green bins would

Table 3.1: Total surface brightness of lensed sources from the Lapi *et al.* (2011) counts model, and estimated contribution from the low-redshift population of lenses assuming the lens redshift distribution from HALOS (González-Nuevo *et al.* 2012). This is compared to the total surface brightness of red galaxies ($g-r$ colour) at $z < 0.35$ from the stacks. I then estimate the fraction of the flux in each redshift bin of the red sample that comes from lensed background sources.

	250 μm	350 μm	500 μm
	Total surface brightness (Jy deg^{-2})		
All lensed flux	1.09	1.34	1.22
Lenses at $z < 0.35$	$0.23^{+0.09}_{-0.06}$	$0.28^{+0.12}_{-0.07}$	$0.26^{+0.11}_{-0.07}$
Red galaxies	2.6 ± 0.5	1.6 ± 0.2	0.8 ± 0.1
	Fraction lensed flux/red galaxy flux by z bin		
$0.01 < z < 0.12$	0.00 ± 0.00	0.00 ± 0.00	0.00 ± 0.00
$0.12 < z < 0.17$	0.06 ± 0.01	0.12 ± 0.02	0.21 ± 0.04
$0.17 < z < 0.22$	0.11 ± 0.02	0.20 ± 0.04	0.33 ± 0.06
$0.22 < z < 0.28$	0.16 ± 0.03	0.27 ± 0.05	0.44 ± 0.08
$0.28 < z < 0.35$	0.20 ± 0.04	0.35 ± 0.07	0.58 ± 0.11

be negligible compared to the fluxes measured in those bins.

The lensed flux is divided between the redshift bins of the red sample in a way that is determined by the product of the lens number distribution $n_l(z)$ and the lens efficiency distribution $\Phi(z)$. The numbers $n_l(z)$ are given by González-Nuevo *et al.* (2012), while the efficiency depends on the geometry between source, lens and observer. I estimated $\Phi(z)$ from the HALOS source and lens redshift distributions using the formula of Hu (1999), and computed the lens flux distribution from the product of total lensed flux, $n_l(z)$ and $\Phi(z)$. Comparing this to the total flux of red galaxies in each redshift bin, I computed the fractional contamination from lensed flux as shown in Table 3.1. Errors on the lensed flux per redshift bin are dominated by the Poisson error on the normalisation of $n_l(z)$, which is simply the Poisson error on the count of 33 lenses. The relative error on the lensed flux is therefore $\sqrt{33}/33 = 0.17$. The error on the stacked red galaxy fluxes is dominated by the 7 per cent flux calibration error (Pascale, E. *et al.* in preparation), hence the errors on the fractions in Table 3.1 are given by $\sqrt{0.17^2 + 0.07^2} = 0.19$. Using the fractions derived above, I removed the estimated lensed contribution to stacked fluxes in each redshift bin of the red sample. The effect of subtracting this fraction from the fluxes of red galaxies is minor in comparison to the trends described in Section 3.4.1. The effect on other derived results will be discussed later in the chapter.

3.4.3 Resolving the Cosmic Infrared Background

A useful outcome of stacking on a well-defined population of galaxies such as the GAMA sample is that one can easily measure the integrated flux from this population and infer how much it contributes to the cosmic infrared background (CIB; Puget *et al.* 1996; Fixsen *et al.* 1998). The cosmic background at FIR/sub-mm wavelengths makes up a substantial fraction of the integrated radiative energy in the Universe (Dole *et al.* 2006), although the sources of this radiation are not fully accounted for. For example, Oliver *et al.* (2010b) calculated that the HerMES survey resolved only 15 ± 4 per cent of the CIB into sources detected with SPIRE at 250 μm, down to a flux limit of 19 mJy. A greater fraction can be accounted for using $P(D)$ fluctuation analysis to reach below the detection limit of the map: in HerMES, Glenn *et al.* (2010) resolved 64 ± 16 per cent of the 250 μm CIB into SPIRE sources with $S_{250} > 2$ mJy. Stacking on 24 μm sources has also proved successful, utilising the greater depth of 24 μm maps from *Spitzer*-MIPS to determine source catalogues for stacking at longer wavelengths. Stacking into BLAST, Béthermin *et al.* (2010) resolved 48 ± 27 per cent of the 250 μm CIB into 24 μm sources with $S_{250} > 6.2$ mJy while Marsden *et al.* (2009) resolved 83 ± 21 per cent into sources with $S_{24} > 15\,\mu$Jy. However, these BLAST measurements included no corrections for clustering; the authors claimed that the effect was negligible, although this observation may appear to conflict with similar analyses in the literature (Negrello *et al.* 2005; Serjeant *et al.* 2008; Serjeant 2010; Chary & Pope 2010; Bourne *et al.* 2011).

Similarly one can stack the GAMA sample to estimate what fraction of the CIB at 250, 350 and 500 μm is produced by optically detected galaxies at low redshifts. To do this I measure the *sum* of measured fluxes in each bin and scale by a completeness correction to obtain the total flux of all $r_{\rm petro} < 19.8$ galaxies at $z < 0.35$. The correction accounts for two levels of incompleteness. The first is the completeness of the original magnitude-limited sample: Baldry *et al.* (2010) estimate that the GAMA galaxy sample (after star-galaxy separation) is $\gtrsim 99.9$ per cent complete. The second completeness is the fraction of the catalogue which have good spectroscopic or photometric redshifts (i.e. spectroscopic Z_QUALITY ≥ 3 or photometric $\delta z/z < 0.2$; see Section 3.2.1). This fraction is 91.9 per cent; however I have only included galax-

ies with redshifts less than 0.35, which comprise 86.8 per cent of the good redshifts. The redshift completeness at $z < 0.35$ may be higher than the overall completeness of 91.1 per cent, but it is unknown since we do not know how many galaxies in this redshift range do not have either spectroscopic or photometric redshifts measured. For simplicity I therefore assume the same fraction at $z < 0.35$; if this is an underestimate then the total corrected flux is overestimated by a maximum of 8.7 per cent. Finally I scale by the fraction of galaxies at $z < 0.35$ that are within the overlap region between the SPIRE mask and the GAMA survey, which is 72.4 per cent. The combined correction factor is $\eta = 1/(0.999 \times 0.919 \times 0.724) = 1.504$. The corrected flux is converted into a radiative intensity (nW m^{-2} sr^{-1}) by dividing by the GAMA survey area (0.0439 sr). I compare this to the CIB levels expected in the three SPIRE bands (Glenn *et al.* 2010) – these are calculated by integrating the CIB fit from Fixsen *et al.* (1998) over the SPIRE bands. I find that the optical galaxies sampled by GAMA account for $\lesssim 5$ per cent of the background in the three bands (see Table 3.2). In the Table I also show the percentage of the CIB produced by galaxies at $z < 0.28$, since in this range the catalogue is complete down to below the knee of the optical LF at $M_r^\star = -21.4$ (Hill *et al.* 2011).

3.4.4 The Sub-mm SED and *k*–corrections

Monochromatic luminosities at rest-frame 250, 350 and 500 μm were calculated as in Chapter 2, using equation (2.6). Unlike in the previous chapter, where k–corrections were uncertain due to the complex variety of SEDs, the SPIRE bands at low redshift sample a part of the SED that can be well modelled by a single-component greybody, a function of temperature $T_{\rm dust}$ and emissivity spectral index β [see equation (1.4)]. The k–correction for this SED is given by

$$k(z) = \left(\frac{\nu_{\rm o}}{\nu_{\rm e}}\right)^{3+\beta} \frac{e^{h\nu_{\rm e}/k_B T_{\rm dust}} - 1}{e^{h\nu_{\rm o}/kT_{\rm dust}} - 1}. \tag{3.5}$$

where $\nu_{\rm o}$ is the observed frequency in the 250, 350 or 500 μm band, $\nu_{\rm e} = (1+z)\,\nu_{\rm o}$ is the rest-frame (emitted) frequency, k_B is the Boltzmann constant and h the Planck constant.

Since one cannot fit an SED to individual undetected galaxies I instead examine the

Table 3.2: Total intensities of $r_{\rm petro} < 19.8$ galaxies from stacking at 250, 350 and 500 μm, in comparison to the corresponding CIB levels from Fixsen *et al.* (1998). I show the intensity as a percentage of the CIB for the full stack, and for the $z < 0.28$ subset which is complete in M_r down to $M_r^\star = -21.4$ (Hill *et al.* 2011). I also show the contributions of the individual redshift bins and $g-r$ colour bins. All contributions from red galaxies have been corrected for the lensed flux contamination using the fractions in Table 3.1. All errors include the statistical error bars from stacking, the error on the lensing correction (where applicable) and a 7 per cent flux calibration error (Pascale, E. *et al.* in preparation).

	250 μm	350 μm	500 μm
	Intensity (nW m^{-2} sr^{-1})		
CIB	10.2 ± 2.3	5.6 ± 1.6	2.3 ± 0.6
Total Stack	0.508 ± 0.036	0.208 ± 0.015	0.064 ± 0.005
$0.01 < z < 0.28$	0.428 ± 0.030	0.173 ± 0.012	0.054 ± 0.004
	Per cent of CIB		
Total Stack	4.98 ± 0.39	3.71 ± 0.30	2.79 ± 0.22
$0.01 < z < 0.28$	4.19 ± 0.34	3.08 ± 0.26	2.33 ± 0.19
$0.01 < z < 0.12$	1.57 ± 0.17	1.11 ± 0.13	0.81 ± 0.09
$0.12 < z < 0.17$	0.97 ± 0.10	0.71 ± 0.08	0.53 ± 0.06
$0.17 < z < 0.22$	0.85 ± 0.08	0.63 ± 0.07	0.49 ± 0.05
$0.22 < z < 0.28$	0.80 ± 0.08	0.63 ± 0.07	0.50 ± 0.05
$0.28 < z < 0.35$	0.78 ± 0.08	0.63 ± 0.07	0.46 ± 0.05
Blue	3.02 ± 0.26	2.34 ± 0.21	1.67 ± 0.15
Green	1.12 ± 0.10	0.84 ± 0.08	0.64 ± 0.06
Red	0.83 ± 0.08	0.64 ± 0.07	0.48 ± 0.05

ratios between stacked fluxes in each bin. Fluxes in the red bins are first corrected to remove the contribution from lensing as discussed in Section 3.4.2. The colour-colour diagrams in Figure 3.8 show the resulting flux ratios in the observed frame in each of the five redshift bins, alongside a selection of models with a range of temperatures. I tried both a single greybody and a two component model, but there is little to choose between them in these colours, since the SPIRE bands are at long wavelengths at which the SED is dominated by the cold dust, with little contribution from transiently heated small grains or hot dust. I therefore adopt a single component for simplicity.

The scatter in the data is large, as are the errors on the 350/500 μm flux ratio. Moreover, with all the data points on the longward side of the SED peak it is impossible to resolve the degeneracy between the dust temperature and the emissivity index (β). This is shown by the close proximity of the $\beta = 1$ and $\beta = 2$ models on Figure 3.8, which overlap in different temperature regimes. With these limitations I am forced to assume

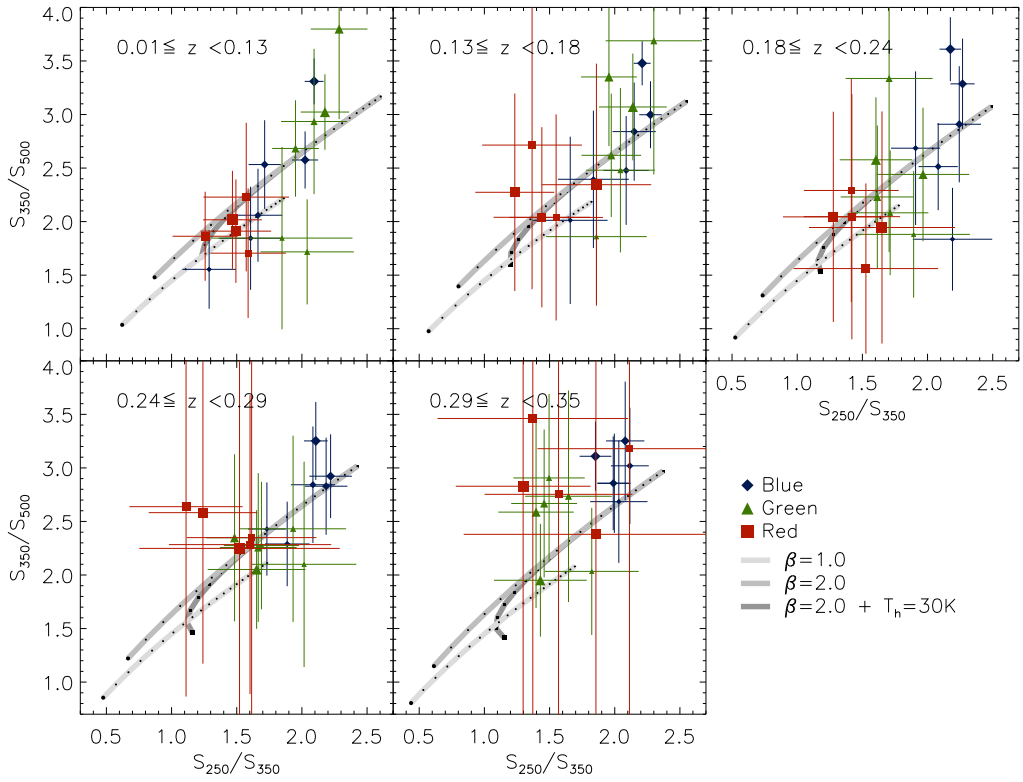

Figure 3.8: Colour-colour diagrams of the observed-frame SPIRE fluxes. The plot is divided into five redshift bins, in which the data from that bin are plotted along with the colours expected from various models as they would be observed at the median redshift in the bin. Data are divided into the three $g - r$ colour bins, denoted by symbols and colours, and six M_r bins denoted by the size of the data point (larger=brighter). Data points and error bars in the red bins include the lensing correction and its uncertainty. Three families of models are shown: two consist of isothermal SEDs with either $\beta = 1$ or $\beta = 2$, and various dust temperatures; the third is a two-component SED with $\beta = 2$, warm dust temperature $T_w = 30\,\mathrm{K}$, with a cold/hot dust ratio of 100. Each model is given a range of (cold) dust temperatures; the dots along the lines indicate 1 K increments from 10 K (lower left) to 30 K. Choosing a single component model with $\beta = 2$ leads to a range of temperatures between 13 and 22 K.

a constant value of β across all the bins. I choose a value of 2.0, which has been shown to be realistic in this frequency range (e.g. Dunne & Eales 2001; James *et al.* 2002; Popescu *et al.* 2002; Blain, Barnard & Chapman 2003; Leeuw *et al.* 2004; Hill *et al.* 2006; Paradis, Bernard & Mény 2009). For comparison, the Planck Collaboration found an average value of $\beta = 1.8 \pm 0.1$ by fitting SEDs to data at 12 μm–21 cm from

across the Milky Way (Planck Collaboration *et al.* 2011e; also references therein).[5]

Under the assumption of a constant β (whatever its value) the dust temperatures implied by Figure 3.8 take a wide range of values across the various bins (between 11 and 22 K for $\beta = 2$). This is not just random scatter; red galaxies tend towards colder temperatures than blue and green, while blue galaxies in some redshift bins show a trend towards lower temperatures at brighter M_r. For the purposes of k–corrections, I can estimate the temperature more accurately by fitting greybody SED models to the three data points at the emitted frequencies given by the observed frequency scaled by $1 + z$, using the median redshift in the bin.[6] In general one must be careful when using stacked fluxes in this way to examine the SED, since when stacking many galaxies with different SEDs, the ratios between the stacked fluxes can be unpredictable and not representative of the individual galaxy SEDs. In this case however one can be fairly confident of the results because the galaxies are binned in such a way that the SEDs within each bin should be similar, and so inferred dust temperatures and other derived parameters should be accurate.

The best-fit temperatures range between $12 - 28$ K, with a median value of 18.5 K. Using $\beta = 1.5$ instead, the temperatures are increased by a factor $1.2 - 1.6$, ranging from $13 - 46$ K with a median of 23.0 K. This median value compares reasonably well with temperatures derived from single-component fits in the literature. For example, Dye *et al.* (2010) derived a median isothermal temperature of 26 K ($\beta = 1.5$) for the detected population in the H-ATLAS science demonstration data, in agreement with the BLAST sample of Dye *et al.* (2009). The value of 26 K is within the range of the temperatures using $\beta = 1.5$, and only slightly higher than the median. Higher temperatures were found by Hwang *et al.* (2010b) in their PEP/HerMES/SDSS sample of 190 local galaxies: they reported median temperatures rising as function of IR luminosity, from around 26 K at $10^9\,\mathrm{L}_\odot$ to 32 K at $10^{11}\,\mathrm{L}_\odot$ and 40 K at $10^{12}\,\mathrm{L}_\odot$ ($\beta = 1.5$). These

[5] A further issue with fitting SEDs is that β may vary with frequency. For example Paradis, Bernard & Mény (2009) analysed data on the Milky Way from 100 μm to 3.2 mm and showed that β was generally steeper at $100 - 240$ μm than $550 - 2100$ μm. This is an effect that one cannot take any account of without many more photometric points on the SED, but it could have some effect on the fitted temperatures and therefore luminosities.

[6] The temperature fits and trends mentioned here, as well as any potential biases, are discussed further in Section 3.5.1.

temperatures may be higher because Hwang *et al.* required a detection shortward of the SED peak (i.e. in an *AKARI*-FIS or *IRAS* band) for galaxies to be included in their sample. Fitting a single greybody to an SED which contains both a cold ($\lesssim 20\,\mathrm{K}$) and a warm ($\gtrsim 30\,\mathrm{K}$) component (Dunne & Eales 2001) may give results that are not comparable to these, which fit only the cold component. On the other hand, Smith *et al.* (2012a) fitted greybodies with $\beta = 1.5$ to the H-ATLAS $250\,\mu\mathrm{m}$-selected sample of low redshift galaxies matched to SDSS, and found a median temperature of $25.9 \pm 1.2\,\mathrm{K}$, and unlike Hwang *et al.* they found no evidence for a correlation with luminosity.

The Planck Collaboration *et al.* (2011b) compiled a sample of around 1700 local galaxies by matching the *Planck* Early Release Compact Source Catalogue and the Imperial *IRAS* Faint Source Redshift Catalogue, and fitted SEDs to data between $60 - 850\,\mu\mathrm{m}$ using both single-component fits with variable β, and dual-component fits with fixed $\beta = 2$. In their single-component fits they found a wide range of temperatures ($15 - 50\,\mathrm{K}$) with median $T = 26.3\,\mathrm{K}$ and median $\beta = 1.2$. This median temperature is consistent with the *Herschel* and BLAST results, and the low value of β is likely to be due to the inclusion of shorter wavelength data. The authors state that the two-component fit is statistically favoured in most cases; these fits indicate cold dust temperatures mostly between $\sim 10 - 22\,\mathrm{K}$, consistent with the range in the current data.

In any case one does not necessarily expect to find the same dust temperatures in an optically-selected sample as in a sub-mm-selected sample. For the purposes of k–corrections this is relatively unimportant, at least at the low redshifts covered in this work. The choice between cold T/high β and hot T/low β makes very little difference to monochromatic luminosities, as crucially they both fit the data. Likewise the *range* of temperatures has little effect on k–corrections: using the median fitted temperature of 18.5 K in all bins gives essentially the same results as the using the temperature fitted to each bin separately. To remove the effect of the variation between models, I carry out all analysis of monochromatic luminosities using the median temperature of $T_{\mathrm{dust}} = 18.5\,\mathrm{K}$ and $\beta = 2.0$ to derive k–corrections using equation (3.5), except where stated otherwise. The implications of the fitted SEDs on the physical properties

of galaxies in the sample will be discussed in Section 3.5. First I will concentrate on the observational results of the stacking which are not dependent on the model used to interpret the sub-mm fluxes.

3.4.5 Luminosity Evolution

To calculate stacked luminosities I first convert each measured flux to a luminosity and then stack the results. The error on the stacked value is again calculated using the Gott *et al.* (2001) method. Note that this method is not the same as calculating the luminosity from the median flux and median redshift of each bin, since luminosity is a bivariate function of both flux and redshift. Fluxes of sources in the red bin are corrected for the fractional contributions from lensing given in Table 3.1, as explained in Section 3.4.2. The 1-σ errors on these corrections are included in the luminosity errors. Results in Figure 3.9 show a generally strong correlation between luminosities in the r-band and all three sub-mm bands, as is the expected trend across such a broad range, but the dependence is not on M_r alone. This becomes obvious when comparing the data points with the grey line, which shows the linear least-squares fit to the results from the lowest-redshift blue galaxies (the line is the same in each panel from left to right). In the blue galaxies, there may be a slight flattening of the correlation for the brightest galaxies and/or the higher redshifts, but this effect is much stronger in the green galaxies, which are intermediate between the blue and red samples. For the red galaxies the correlation disappears entirely but for the faintest bin at low redshift. The luminosities of the red galaxies all lie below the grey line, showing that red galaxies emit less in the sub-mm than blue or green galaxies of the same M_r, strongly suggesting that they are dominated by a more passive population than green and blue galaxies. These trends are greater than the uncertainties on the lensing correction.

Apart from this colour dependence there is also a significant increase in sub-mm luminosity with redshift for green and red galaxies of the same r-band luminosity. This evolution appears to occur at all M_r, without being particularly stronger for either bright or faint galaxies, but it is especially strong for red galaxies. This may indicate a transition in the make-up of the red population, with obscured SFGs gradually becoming more dominant over the passive population as redshift increases. Such a scenario

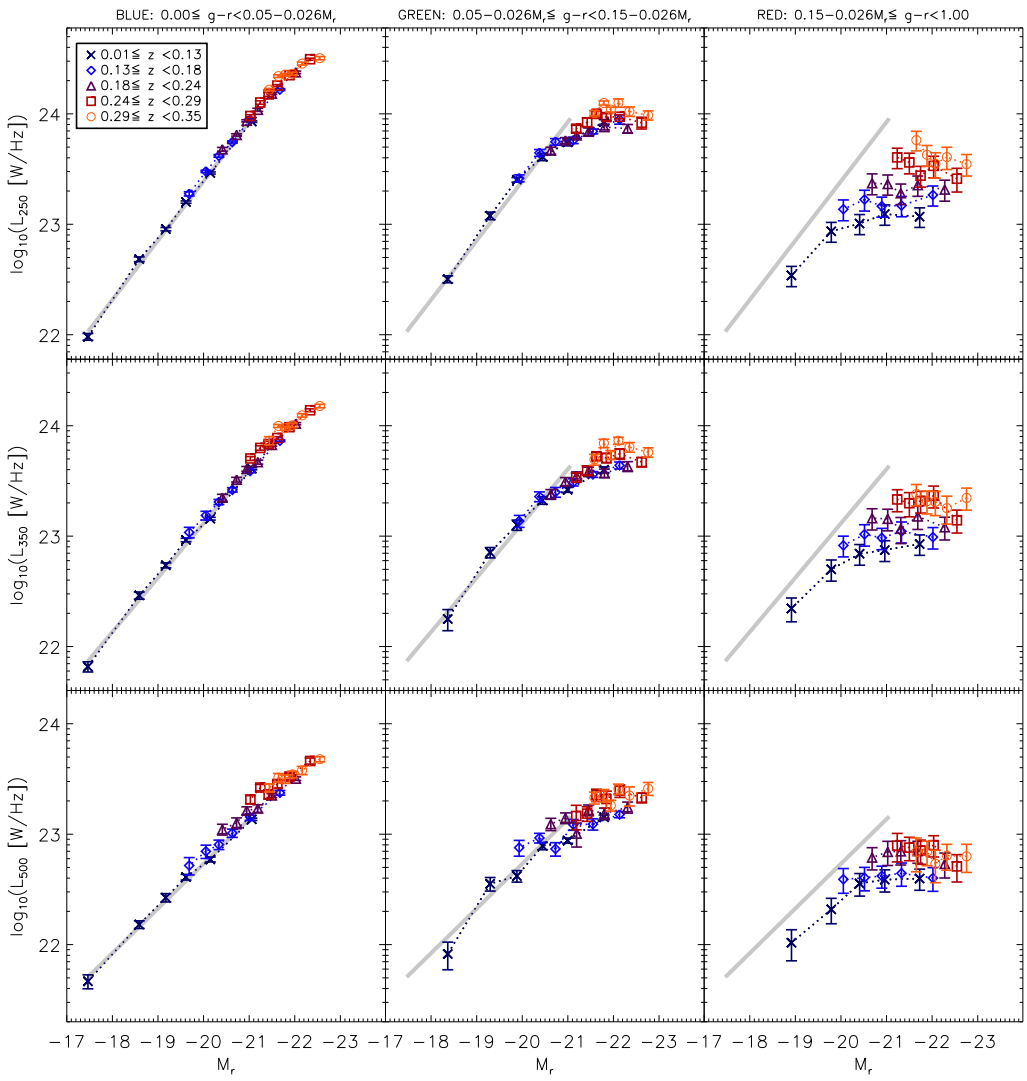

Figure 3.9: Stacked SPIRE luminosities as a function of $g-r$ colour, redshift and absolute magnitude M_r. Layout as in Figure 3.7. Error bars are the statistical 1σ errors in the bins as described in Section 3.3.3. Fluxes in the red bin have been corrected for the lensing contribution as described in Section 3.4.2, and error bars include the associated uncertainty. The thick grey line is the same from left to right, and is the linear least-squares fit to the results for the lowest-redshift blue galaxies.

might be expected as we look back to earlier times towards the peak of the universal star-formation history. This possibility might be tested by looking for a change in the shape of the UV–optical SED. Colour-colour diagnostics such as the rest-frame UVJ diagram effectively separate quiescent and star-forming galaxies, breaking the degeneracy between intrinsic colour and dust reddening (Williams *et al.* 2009). Spectroscopic indices such as the the strength of the 4000Å break and the Balmer lines of hydrogen are also good indicators of young stellar populations (Bruzual A. 1983). However, one might expect an increase in obscured star formation to be accompanied

by an increase in the dust temperatures at higher redshifts, for which there is no evidence in the SPIRE colours (Section 3.4.4).

Meanwhile the green sample shows similarities with the blue at low redshift and low r-band luminosity, but at high redshifts and stellar masses the luminosity dependence on M_r is flatter and more similar to that of red galaxies. This could be due to a shift in the dominant population of the green bin, between blue-cloud-like galaxies and red-sequence-like galaxies at different redshifts and M_r.

3.4.5.1 UV–Optical Versus Optical Colours

Splitting the sample by the $NUV - r$ colour index provides a slightly different sampling regime and reduces contamination between the colour bins because the red and blue populations are better separated (see Section 3.2.2). It therefore offers a useful test of the robustness of the results of stacking by $g-r$. Figure 3.10 shows that stacked 250 μm luminosities follow the same trends with colour, redshift and M_r as in the $g-r$ stacks (350 and 500 μm results are similar). Luminosities in the red $NUV - r$ bins (at the lowest redshifts at least) are lower than in the red $g - r$ bins, suggesting that the two samples are not identical, and that red $NUV - r$ colours may provide a purer sampling of the red sequence. However, the luminosities of the red sample in either $NUV - r$ or $g - r$ are still much lower than those in the blue or green sample (at a given M_r), indicating that both red bins are dominated by passive galaxies at $z < 0.35$.

Errors are slightly larger in the red bins of the $NUV - r$ sample, because the sample is limited to the 52,773 galaxies with NUV detections. Since results appear to be independent of the colour index used, I opt to use the more complete r-limited sample of 86,208 sources with $g - r$ colours for all subsequent analysis.

3.4.5.2 Stellar Mass Versus Absolute Magnitude

An alternative to dividing the sample by M_r is to use the stellar masses which were calculated from the GAMA $ugriz$ photometry by Taylor *et al.* (2011) assuming a Chabrier (2003) IMF. Stellar mass is a simple physical property of the galaxy so may reveal more about intrinsic dependencies; on the other hand it depends much more on the models

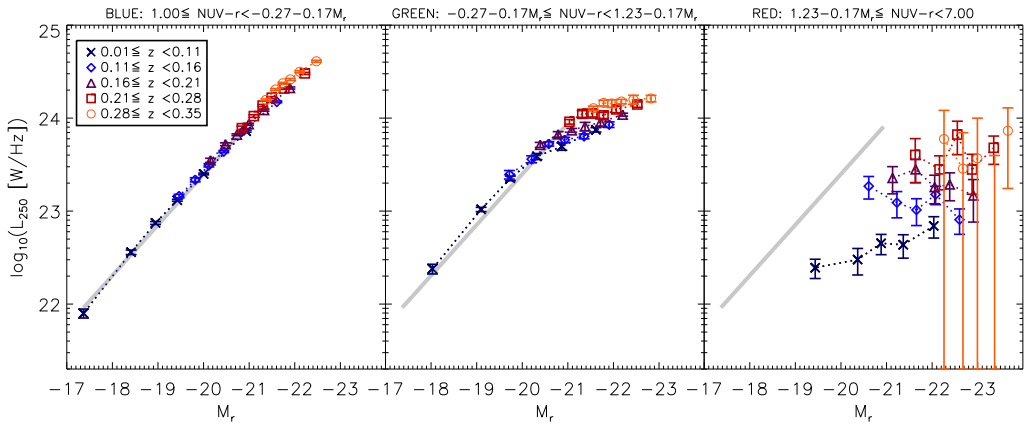

Figure 3.10: Stacked 250 μm luminosities as a function of $NUV - r$ colour, redshift and M_r. Error bars are the statistical 1σ errors in the bins as described in Section 3.3.3. Data and errors in the red bin incorporate the correction for lensing. The thick grey line is the same from left to right, and is the linear least-squares fit to the results for the lowest-redshift blue galaxies.

used to fit the optical SED than M_r, which is only subject to a small k–correction and the assumed cosmology (for a given redshift). Relative errors on stellar masses are dominated by systematics, but are small ($\Delta \log M_\star \sim 0.1$; Taylor *et al.* 2011). I confirmed that the results are robust to these errors by repeating all analysis after making random perturbations to the stellar masses, where the size of each perturbation was drawn from a Gaussian distribution with width $\sigma = \Delta \log M_\star$. No results were systematically affected by these perturbations, and random deviations in stacked values were smaller than the error bars.

Figure 3.11 shows that the results of stacking by $g - r$ colour and stellar mass differ slightly from the results of stacking by M_r (Figure 3.9). Again I found very little difference from these results when I stacked by $NUV - r$ colour and stellar mass. The results of stacking by mass seem to differ most in the blue bin. Whereas there was little luminosity evolution at fixed M_r, these results show evolution at fixed stellar mass. Furthermore this evolution is dependent on stellar mass, suggesting that smaller galaxies tend to evolve more rapidly. The samples in Figures 3.9 and 3.11 are slightly different since stellar masses were only available for 90 per cent of the full sample; however this is not responsible for the discrepancy since repeating the stacking by M_r with the stellar-mass sample gives identical results (the stellar-mass incompleteness does not vary between bins). The difference arises because M_r does not directly trace stellar mass, which leads to a mixing of galaxies of different masses within a given M_r

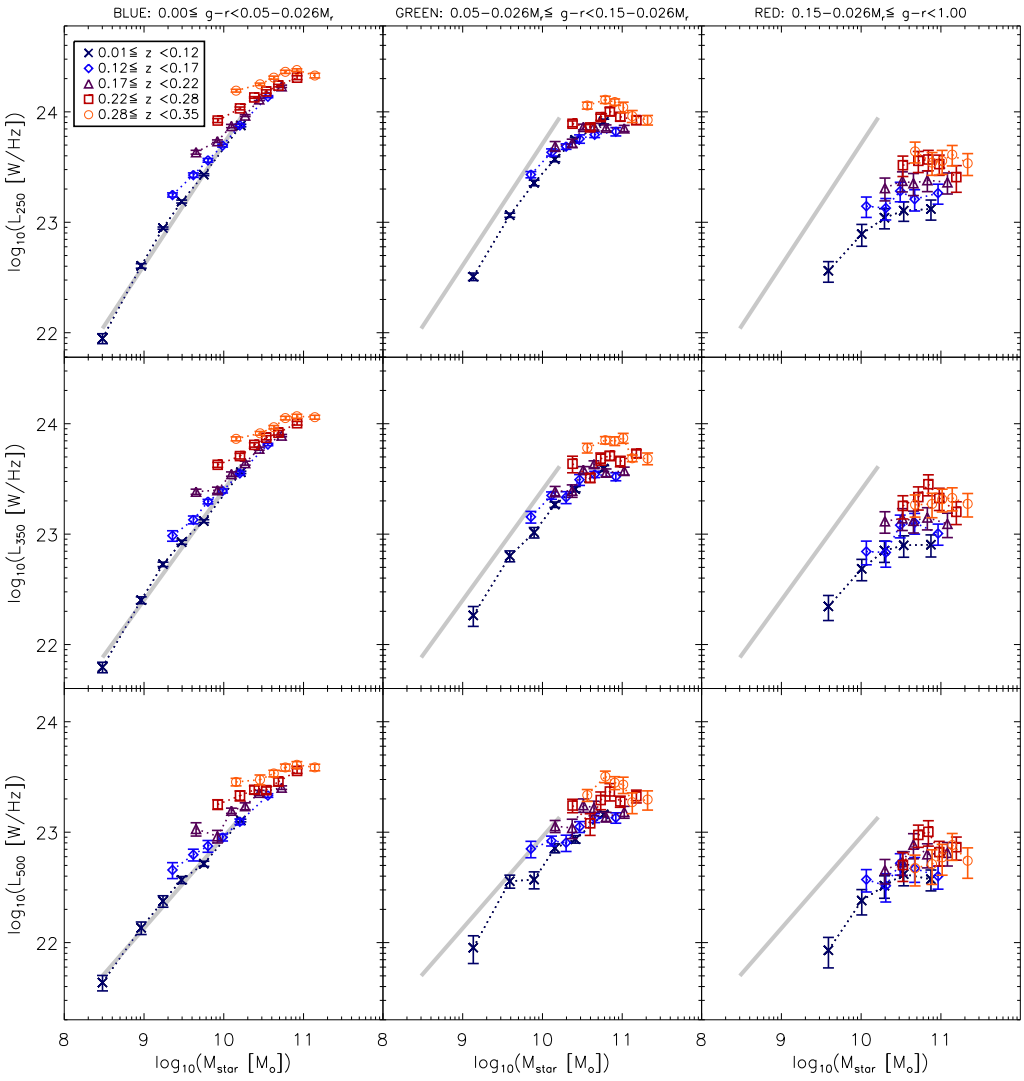

Figure 3.11: Stacked SPIRE luminosities as a function of $g-r$ colour, redshift and stellar mass. Error bars are the statistical 1σ errors in the bins as described in Section 3.3.3. Data and errors in the red bin incorporate the correction for lensing. The thick grey line is the same from left to right, and is the linear least-squares fit to the results for the lowest-redshift blue galaxies.

bin. This is unavoidable since the sample must be split in three ways (colour, redshift and mass/magnitude), because dust luminosity varies strongly as a function of all of these. I split the sample by colour first, then by redshift and finally divide into mass or magnitude bins, but each bin can still contain a relatively broad range of redshifts. Within each bin there will be a strong correlation between redshift and M_r, simply because M_r is a strong function of distance. In Figure 3.12, I plot stellar mass against M_r with the points colour-coded by redshift, showing that redshifts increase steadily from left to right, with decreasing M_r. A narrow range in M_r would select a narrow range of redshifts, while a similarly narrow range in mass selects a much broader range

of redshifts.

The effect of this on the blue bins in Figures 3.9 and 3.10 is a tendency for the data points of different redshift bins to lie along the same relation of L_{250} as a function of M_r. The degeneracy is (partially) broken when splitting by stellar mass, thus separating out the trends with redshift and with mass in Figure 3.11. This effect is much less noticeable in the red bin simply because the redshift evolution is much stronger while the mass dependency is very weak in the red sample.

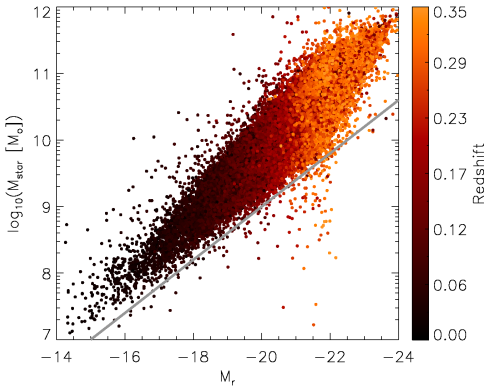

Figure 3.12: Stellar masses of the sample as a function of absolute magnitude and coloured by redshift, showing the degeneracy between M_r and z resulting from an r-band selection. To guide the eye, the slope of the grey line indicates direct proportionality between mass and luminosity, i.e. $\log_{10} M_\star = -0.4 M_r + C$ (for this line $C = 1.0$). The spread in the data perpendicular to this line reveals the broad range of mass-to-light ratios which is responsible for the differences between stacking by M_r and by $M_\star$

3.5 Discussion

3.5.1 Dust Temperatures and SED Fitting

In Section 3.4.4 I stated that assumptions about the dust temperature and β had negligible effect on the k–corrections to SPIRE fluxes at these low redshifts. Hence I chose to use the same SED model to compute monochromatic luminosities, assuming a single-component greybody with $T_{\rm dust} = 18.5\,{\rm K}$ and $\beta = 2.0$. However, in order to infer properties of the full IR SED, these considerations are much more important.

I fitted single-component SEDs with $\beta = 2.0$ to the stacked SPIRE fluxes in each

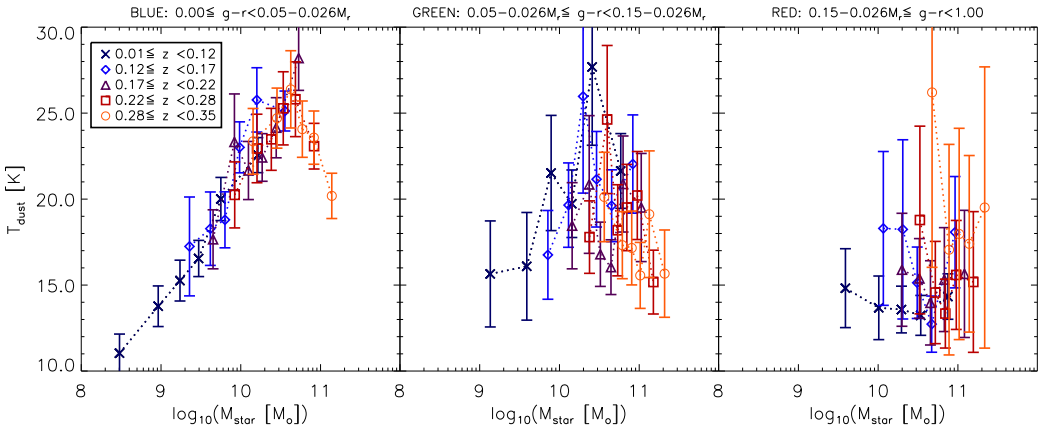

Figure 3.13: Results of fitting single-component greybodies with $\beta = 2.0$ to the observed (not k–corrected) fluxes in each bin to estimate dust temperatures. Fluxes in the red bin were corrected for lensing before fitting. Error bars are the 1σ errors on fitted temperatures computed by MPFITFUN.

bin, shifting the observed wavelengths by $(1 + z)$ using the median redshift in the corresponding bin. Fluxes in the red bin were first corrected for the predicted lensing contamination as described in Section 3.4.2. The effect of this is to increase the fitted temperatures in the red bin by around $1 - 3\,\mathrm{K}$, which is small compared with the range of temperatures observed, although the errors on temperatures are significantly increased. The fitting was carried out using the IDL routine MPFITFUN,[7] which performs Levenberg-Marquardt least-squares fitting to a general function. Best-fit values of the free parameters (temperature, normalisation) are returned with formal 1σ errors computed from the covariance matrix. Some examples of the fits are plotted in Appendix C, showing a range of fitted temperatures. The derived temperatures depend on the assumption of a fixed emissivity parameter (β). Varying this as a function of optical colour and/or stellar mass could to some extent account for the variation in sub-mm colours, which I interpret as a temperature variation. However, the variation in β would need to be severe ($\Delta\beta > 1$) to fully account for the trends in the stacked colours in Figure 3.8. It therefore seems likely that the cause for these variations is either temperature alone or a combination of β and temperature.

Figure 3.13 shows the results of all the temperature fits as a function of colour, stellar mass and redshift. There are strong deviations in some bins from the value that I have been using, and these show strong dependence on colour and stellar mass. In the blue

[7] MPFITFUN available from Craig Markwardt's IDL library:
`http://cow.physics.wisc.edu/~craigm/idl/idl.html`

bin, dust temperature is tightly correlated with stellar mass in all redshift bins, with a peak at around $5 \times 10^{10}\,\mathrm{M}_{\odot}$, but galaxies of higher masses appear to have colder dust. The temperature distribution in the the green bin is less well correlated and very noisy, but again there is evidence that the warmest galaxies are towards the middle of the mass range. There is no clear evolution with redshift. As with the luminosity results, the red bin appears very different from the other two, and there is no evidence for the temperature to increase with stellar mass. The most important result would seem to be that temperatures are generally much lower in the red than the blue bins. Over the mass range in which the bins overlap ($3 \times 10^{9} < M_{\star} < 3 \times 10^{11}$), the mean (standard deviation) of the temperatures in the blue bins is 23.0 (2.6) K, compared with 19.5 (3.1) K in the green and 16.2 (2.8) K in the red. The difference in the means is statistically significant, since an unpaired t-test gives a probability of 10^{-12} that the means of the red and blue bins are the same. The t-test assumes that the errors on each of the measurements are independent, but this is not true since the errors on the red stacks are dominated by the error on the lensing correction. The mean temperature error of the red stacks is 2.8 K, which means that, including the lensing uncertainty, the blue and red mean temperatures are only different at the 2.4σ level. The incidence of colder dust in redder galaxies may be explained by the relationship between dust temperature and the intensity of the interstellar radiation field (ISRF). The colour temperature of the ISRF is directly related to the stellar population. Old stars produce less UV flux, and so heat the dust less, which causes galaxies dominated by older stars to have cooler dust. Such a temperature differential is therefore consistent with the notion of red galaxies being passive. Meanwhile, colder dust temperatures in the least massive blue galaxies is consistent with these galaxies having more extended dust disks in comparison with their stellar disks, since the ISRF becomes weaker at greater galactocentric radii. Evidence for an extended dust disk in at least one low mass system has been reported by Holwerda *et al.* (2009), although larger samples would be needed to judge whether this is a widespread phenomenon.

It is possible when fitting the SPIRE bands that the SED shape could be biased by differential effects between the three bands. In particular the $500\,\mu\mathrm{m}$ band is the most affected by confusion and blending, as well as being the noisiest, and is also potentially subject to contamination from other emission mechanisms, including syn-

chrotron from within the galaxies, and extended radiation from the Sunyaev-Zel'dovich effect in galaxy clusters (although the latter should have been removed in background subtraction). To check for such bias, I also tried fitting only the 250 and 350 μm data, and found that the derived temperatures and trends were not significantly different.

I also tried removing all potentially blended sources from the stacks to test for any bias caused by differential blending. The assumption made in deblending is that blended flux is shared equally between the blended sources, in the absence of any knowledge of their true flux ratio. As noted in Appendix A, there is no bias to the average or median flux as a result of this assumption, but the individual fluxes of blended sources will not be correct in cases where the intrinsic flux ratio between the blended sources is large. In such cases, the faint source is always over-estimated and the bright one always under-estimated; it is therefore possible for stacked fluxes in bins containing many faint sources to be systematically high, and those in bins with many bright sources to be too low. The problem worsens with increasing wavelength (as a result of the larger beam size), which means that the temperatures of bins with fainter fluxes (i.e. red galaxies and low-mass galaxies) could appear to be colder than they really are. I repeated the stacking after removing all blends (any GAMA source within 35 arcsec of another) in order to test whether this could account for the trends seen in Figure 3.13. This reduced the catalogue size by about a third, so errors were consequently increased; however there was no systematic difference in the temperatures and the trends remained significant, so it appears that these results (and the masses that depend on them) are not biased by any blending effects.

3.5.1.1 Bolometric Luminosities

It can be useful to consider the total IR luminosities $L_{\rm TIR}$ $(8-1000\,\mu{\rm m})$ of galaxies as this allows some comparison between observations at different IR wavelengths and between data and the predictions of models. In all cases this entails making assumptions about the shape of the SED, which must be interpolated – and indeed extrapolated – from the limited photometric data available. In this particular case we are limited to just three SPIRE bands, all of which lie longward of the peak in the SED and as such do little to constrain the warmer end of the SED at $\lambda \lesssim 100\,\mu{\rm m}$. This is why they are

well fitted by single-component SEDs, representing a single component of cold dust. In contrast, the TIR luminosity is highly sensitive to emission from the hotter components of dust, especially the $\gtrsim 30\,\mathrm{K}$ dust associated with HII regions, which is heated by UV radiation from hot young stars.

Bearing in mind these limitations, I nevertheless consider it useful to make some attempt at estimating the TIR luminosities representative of the stacked samples. Since the sample is thought to be dominated by normal star-forming and quiescent galaxies, one must choose an appropriate IR SED template. A commonly used set of templates is that of Chary & Elbaz (2001; hereafter CE01). These templates are based on libraries of mid- and far-IR templates representing a range of SED types (from normal spirals to ULIRGs) fitted to data on ~ 100 local galaxies at 6.7, 12, 15, 25, 60, 100 and $850\,\mu\mathrm{m}$.[8] From these I select the most appropriate template for each stack by computing chi-squared between each of the templates and the rest-frame (lensing corrected) SPIRE luminosities, and assign to each stack the L_{TIR} of the template with the minimum chi-squared. Results are shown in Figure 3.14(a). Errors on L_{TIR}were estimated with Monte-Carlo simulations using the 1σ errors on the SPIRE luminosities and re-fitting the templates 200 times to obtain the 1σ error bar on the template L_{TIR}.

The CE01 templates are of limited value for this sample because they are fitted to *IRAS* and SCUBA data for a relatively small sample of local galaxies. The necessity for *IRAS* detections means that the galaxies in their sample may have been biased towards hotter SEDs, and may not be representative of the larger population sampled in this work. As an alternative one can compare the results of using the CE01 templates with a set of templates modelled on the H-ATLAS SDP source catalogue (Smith *et al.* 2012a). There is a danger that the opposite bias is active here, since the templates are based on sources selected at $250\,\mu\mathrm{m}$, which are more likely to have cold SEDs. However, by comparing the H-ATLAS L_{250} LF from D11 with the range of L_{250} of optical galaxies (Figures 3.9–3.11) we see that the luminosity ranges spanned by the two surveys are remarkably similar, implying that the SEDs of H-ATLAS sources could provide a reasonable representation of an optically selected sample. I use a single template based on the mean of all H-ATLAS SED models from Smith *et al.* (2012a).

[8] CE01 templates were obtained from `http://www.its.caltech.edu/~rchary/`

In Figure 3.14(b) I show the results of fitting this template to the stacked SPIRE luminosities, minimising chi-squared to obtain the correct normalisation and integrating the SED from 8–1000 μm to obtain $L_{\rm TIR}$ (errors were estimated from Monte-Carlo simulations using the 1σ errors on the SPIRE luminosities in the same way as for the CE01 templates).

The results of the two sets of templates are strikingly different, with the CE01 models suggesting significantly higher luminosities, reaching the level of "luminous IR galaxies" (LIRGs; $L_{\rm TIR} > 10^{11}\,{\rm L}_{\odot}$) at $z > 0.22$ or $M_{\star} \gtrsim 2 \times 10^{10}\,{\rm M}_{\odot}$. The H-ATLAS templates are much colder so give much more moderate luminosities, with around five times lower bolometric luminosity for the same L_{250}. With only the SPIRE data to constrain the SED I cannot conclusively say that either set of templates is better suited to describing the optical sample, although for the reasons outlined above I believe that the H-ATLAS templates are more likely to be suitable. The addition of data points at shorter wavelengths, from PACS in the FIR and *WISE* in the MIR, would permit a much more accurate derivation of the bolometric luminosity; I leave this for a future study.

Both parts of Figure 3.14 show trends in the bolometric luminosities that are similar to those seen in the monochromatic SPIRE luminosities. That is to say there is a clear evolution with redshift and that this is much stronger in the red than the blue sample. One can quantify this evolution in the form $L(z) \propto (1+z)^{\gamma}$ for the mass range in which the bins overlap. I fit this function in log-space by chi-squared minimisation, using the IDL routine LINFIT to fit the bins which fall in the mass range $M_{\star} = 1-5\times10^{10}\,{\rm M}_{\odot}$. I find that $L_{\rm TIR}$ from the H-ATLAS SEDs evolves with $\gamma = 4.3 \pm 0.2$ in the blue sample; $\gamma = 3.7 \pm 0.3$ in the green; and $\gamma = 6.1 \pm 1.0$ in the red. The same evolution is also seen in $L_{250}(z)$ in the same mass bins: this is described by $\gamma = 4.2 \pm 0.2$ (blue); $\gamma = 3.5 \pm 0.5$ (green); and $\gamma = 7.2 \pm 1.5$ (red). It appears counter-intuitive that the intermediate green bin should show the least evolution. The likely reason for this is the aforementioned possibility for the green sample to probe different populations at different redshifts (see Sections 3.4.5 and 3.4.1). Any sign of genuine luminosity evolution would be counteracted by sampling a less luminous population (e.g. with more passive red sequence galaxies in the green bin) at higher redshifts. I note however

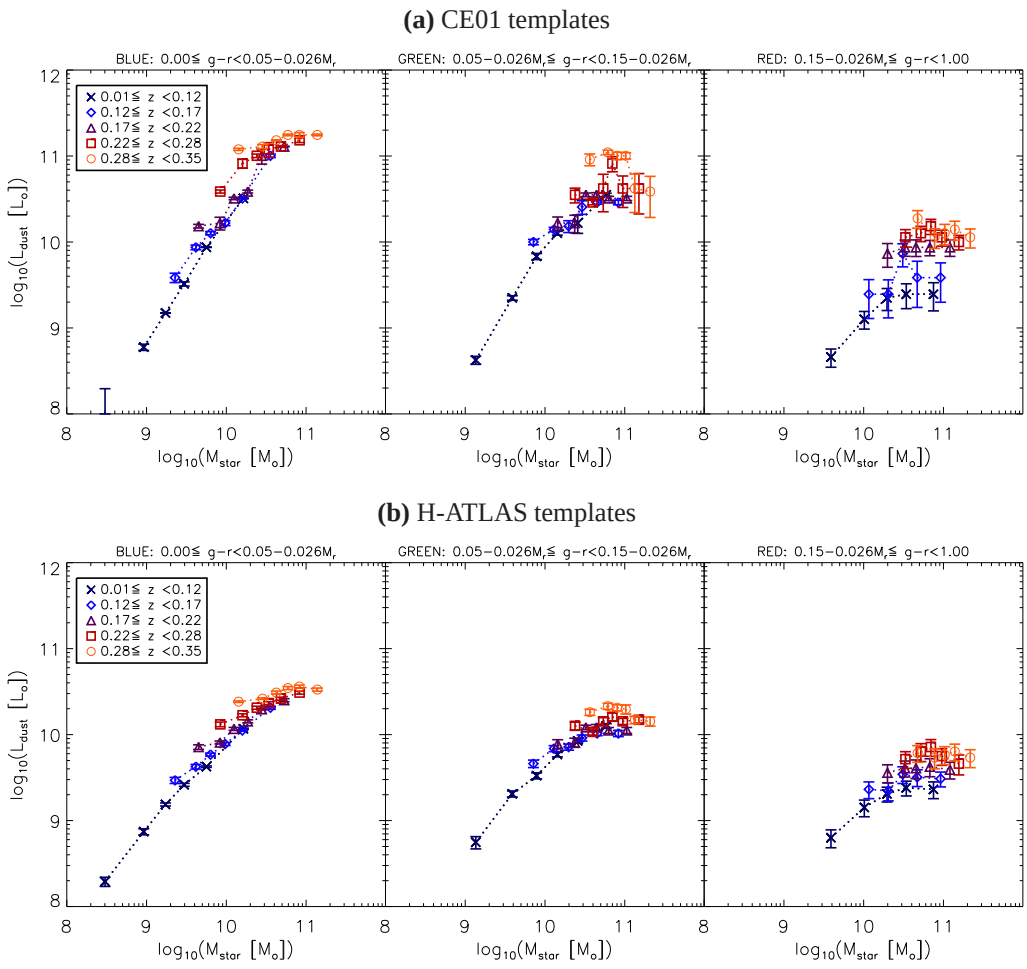

Figure 3.14: Integrated $L_{\rm TIR}$ (8-1000 μm) of (a) Chary & Elbaz (2001) and (b) H-ATLAS (Smith *et al.* 2012a) templates fitted to the stacked SPIRE luminosities in each bin as described in the text. Error bars are 1σ errors estimated from Monte-Carlo simulations using the 1σ errors on the SPIRE luminosities. Fluxes in the red bin have been corrected for the lensing contribution as described in Section 3.4.2, and error bars include the associated uncertainty. Note that in panel (a) the first point in the blue sample (i.e. lowest mass, lowest redshift bin) had SPIRE luminosities that fall below all of the CE01 templates, and so the luminosity of the faintest template is used as an upper limit.

that any evolution in the sub-mm SED of any of these samples (blue, green or red) would render these single template fits unreliable.

The evolution in $L_{\rm TIR}$ of normal galaxies was also observed by Oliver *et al.* (2010a) for a large sample selected in the optical and NIR with redshifts between $0-2$. Dividing their sample by redshift, stellar mass and optical class (each derived from broadband SED fitting of Rowan-Robinson *et al.* 2008) they stacked into 70 and 160 μm *Spitzer* images and showed that both "blue" galaxies (with spiral-like SEDs) and "red" galaxies (with elliptical-like SEDs) increased in specific IR luminosity (i.e. $L_{\rm TIR}/M_{\star}$) as a function of redshift. The evolution in specific IR luminosity of all galaxies in their

sample increased as $(1+z)^{4.4\pm0.3}$ (independent of stellar mass), which is nearly identical to the result for blue galaxies in the current sample. When they split the sample into red and blue colours, they also found that red galaxies evolved more strongly, with an index 5.7 ± 2.5, which is consistent with the index 6.1 ± 1.0 in this sample. Their blue sub-sample evolved with the index 3.4 ± 0.3 compared with 4.3 ± 0.2 in this sample. The agreement is not exact but general trends with redshift and colour are certainly compatible between the two samples. Assuming a correlation between IR luminosity and SFR (e.g. Kennicutt 1998a), one can also draw parallels with other *Spitzer*-stacking (such as Magnelli *et al.* 2009; Damen *et al.* 2009b,a) as well as radio-stacking studies (Dunne *et al.* 2009b; Pannella *et al.* 2009; Karim *et al.* 2011), all of which have shown similar dependence of (specific) SFR on stellar mass and redshift in NIR-selected massive galaxies covering larger redshift ranges (up to $z \sim 3$). These studies have variously reported redshift evolution in specific SFR with indices (γ) ranging from 3.4 to 5.0, all comparable with the luminosity evolution of blue galaxies in the current sample. It is unsurprising that the blue sample generally agrees with other samples selected by rest-frame optical light with no regard to colour, since the blue selection is by far the largest of the colour bins, comprising 50 per cent of the whole sample.

It is well reported in the literature that there is strong evolution in the IR LF out to at least $z = 1$ (Saunders *et al.* 1990; Blain *et al.* 1999; Pozzi *et al.* 2004; Le Floc'h *et al.* 2005; Eales *et al.* 2009; Eales *et al.* 2010b; Dye *et al.* 2010; Gruppioni *et al.* 2010; Rodighiero *et al.* 2010a; D11; Goto *et al.* 2011; Sedgwick *et al.* 2011). This requires an increase in the luminosity of the brightest ($\gtrsim L^{\star}_{\rm IR}$) galaxies, leading to an increase in the numbers of LIRGs and ULIRGs at higher redshifts. These results show that evolution occurs at low redshifts in ordinary galaxies well below the LIRG threshold; these are the galaxies that dominate the number density. Such an evolution in the IR luminosities of all galaxies leads naturally to an evolution in the characteristic luminosity $L^{\star}$. Exactly this sort of evolution in normal (i.e. non-merging) SFGs is predicted by the semi-analytic model of Hopkins *et al.* (2010), essentially as a result of an evolving gas fraction and using the Schmidt-Kennicutt law (Kennicutt 1998b). D11 also show that an evolving gas fraction is required to explain the luminosity evolution in the H-ATLAS sample, based on the chemical evolution model of Gomez, H. L. *et*

al. (in preparation).

3.5.2 The Cosmic Spectral Energy Distribution

Having discussed evolution in the IR luminosity density of the Universe, it is natural to consider the local luminosity density (at $z = 0$), since this provides a reference point for similar measurements at higher redshifts. In Section 3.4.3 I calculated the integrated intensity of low redshift galaxies and showed that they contribute a small fraction of the CIB at sub-mm wavelengths. Building on this result, one can estimate the $z = 0$ cosmic SED at sub-mm wavelengths, i.e. the integrated luminosity of all galaxies at $z = 0$. To do this I make use of the completeness-corrected integrated intensities in the range $0.01 < z < 0.12$ in Table 3.2, but apply k- and e-corrections to account for the redshifted wavelengths and luminosity evolution respectively. I divide by the comoving volume of the redshift bin (V_c) to obtain the luminosity per unit comoving volume,

$$\nu L_\nu = 4\pi d_L^2 \, \nu I_\nu \, \frac{k(z)}{1+z} \, \frac{4\pi}{V_c} \, e(z), \tag{3.6}$$

where I_ν is in W m^{-2} sr^{-1} Hz^{-1}, d_L is in m, V_c is in Mpc^3, and the luminosity νL_ν is expressed in units of $\mathrm{W\,Hz^{-1}\,Mpc^{-3}}\,h_{70}$ ($h_{70} = H_0/70\,\mathrm{km\,s^{-1}\,Mpc^{-1}}$). Note that while $V_c = 0.523\,\mathrm{Gpc}^3$ represents the total comoving volume of the bin, $d_L = 382.5$ Mpc is the luminosity distance of the median redshift in the bin, $\langle z \rangle = 0.084$. I use the median values of $k(z)/(1+z)$ for this redshift bin: 0.8094 (250 μm), 0.7586 (350 μm), and 0.7259 (500 μm); and for the evolution at all sub-mm wavelengths I take the fitted function $L_{250}(z) \propto (1+z)^\gamma$ from Section 3.5.1, assuming that the shape of the rest-frame SED does not evolve with redshift (which is supported by the non-evolving temperature results). I assume $\gamma = 4.2 \pm 0.2$, the value derived for the blue sample, since these represent roughly half of all galaxies; the evolution for all galaxies may be slightly stronger (red galaxies seem to evolve more strongly, although the green sample evolve less) but an index around 4 is consistent with other results in the literature (see discussion in Section 3.5.1). The evolution from $z = 0 - 0.084$ (the median redshift of the bin) is therefore a factor $(1+0.084)^{4.0} = 1.38$, hence the correction is $e(z) = 0.72$.

I thus calculate the luminosities of the cosmic SED at $z = 0$ to be $3.9 \pm 0.3 \times 10^{33}$, $1.5 \pm 0.1 \times 10^{33}$ and $4.3 \pm 0.3 \times 10^{32}$ W Hz^{-1} Mpc^{-3} h_{70} at 250, 350 and 500 μm respectively.

Errors are dominated by the 7 per cent calibration error on the SPIRE fluxes, which is correlated across the three bands. These results agree very closely with the sub-mm luminosities predicted from GAMA data by Driver *et al.* (2012), by calculating the total energy absorbed by dust in the UV-NIR and assuming it is reprocessed as FIR emission with templates from Dale & Helou (2002). They are also close to the pre-*Herschel*-era prediction of Serjeant & Harrison (2005), based on modelling the SEDs of IRAS sources with SCUBA sub-mm measurements. Using equation (7) of that paper, the predicted luminosities at 250, 350 and 500 μm are 4.52×10^{33}, 1.43×10^{33} and 3.48×10^{32} W Hz^{-1} Mpc^{-3} h_{70} respectively. The measurements from this study are within 3σ of these values, although they arguably suggest that the slope of the cosmic SED may be a little shallower than the prediction. These measurements are independent of the SEDs and temperatures assumed (since k–corrections are small) and of the lensing assumptions (the lensed flux is negligible at $z \lesssim 0.1$).

3.5.3 Evolution of Dust Masses

Dust mass is a quantity which one can expect to constrain much more accurately than $L_{\rm TIR}$ using the SPIRE luminosities, because the cold component that they trace is thought to dominate the total dust mass (Dunne & Eales 2001; and references therein). I therefore estimate the mass of the cold dust component described by the greybody fits and use this as a proxy for the total dust mass, assuming that any warmer components have a negligible contribution to the mass.

The dust mass as a function of temperature $T_{\rm dust}$ is estimated from the 250 μm flux:

$$M_{\rm dust} = \frac{S_{250}\ D_{\rm L}^2\ k(z)}{\kappa_{250}\ B(\nu_{250}, T_{\rm dust})\ (1+z)}. \qquad (3.7)$$

I use a dust mass absorption coefficient at 250 μm of $\kappa_{250} = 0.89\,{\rm m^2 kg^{-1}}$ (D11; and references therein).

Dust mass results depend strongly on the temperatures assumed (although not as strongly as the bolometric luminosities). They are therefore subject to the assumption of constant emissivity index (β), as well as the assumption of a constant absorption coefficient (κ). Any variation of κ with redshift, stellar mass, optical colour or indeed with dust temperature or dust mass itself could alter the apparent trends in dust mass.

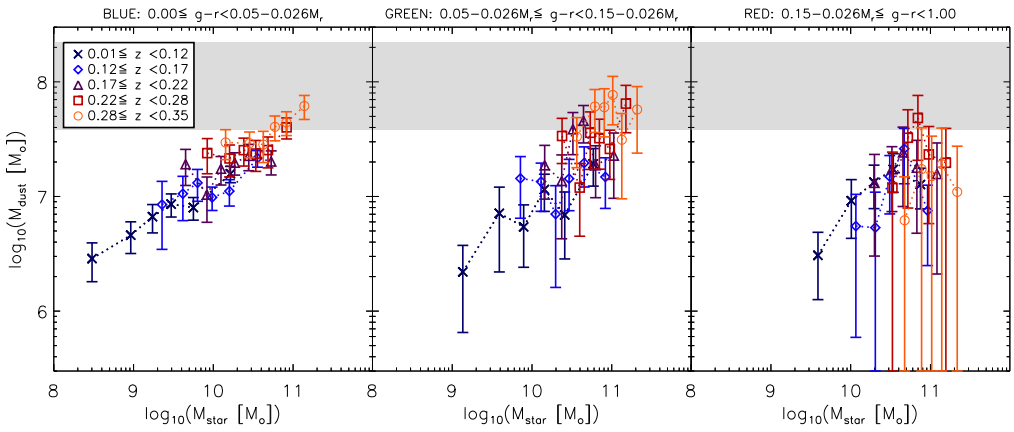

Figure 3.15: Stacked dust mass as a function of $g - r$ colour, redshift and stellar mass. Dust mass is derived from equation (3.7) using the fitted dust temperatures from Figure 3.13. Error bars include the statistical 1σ errors in the bins as described in Section 3.3.3, with an additional contribution due to the error on the fitted temperature. The lensing contribution has been removed from the red bins, and error bars include the associated uncertainty. The shaded region shows the range of characteristic dust masses measured by D11, which evolve from $3.8 \times 10^7\,\mathrm{M}_\odot$ at $z < 0.1$ to $2.2 \times 10^8\,\mathrm{M}_\odot$ at $z \sim 0.35$.

In Figure 3.15 I show the dust masses derived using the fitted temperatures from Figure 3.13. The dust mass is seen to range from around 2×10^6 to $8 \times 10^7\,\mathrm{M}_\odot$ across the sample. In all bins dust and stellar mass are correlated, but this may weaken slightly with increasing redshift and/or stellar mass. There is a definite evolution towards higher dust masses with increasing redshift. Following the evolutionary form $M_{\mathrm{dust}}(z) \propto (1+z)^\gamma$ I fit data in the range $M_\star = 1 - 5 \times 10^{10}\,\mathrm{M}_\odot$ with slopes of $\gamma = 3.7 \pm 1.7$ for the blue sample; $\gamma = 6.8 \pm 3.9$ for the green; and $\gamma = 0.8 \pm 5.0$ for the red. The slopes of the evolution are thus consistent with the evolution in luminosities (as might be expected from the lack of evolution in temperature). It is not possible to tell whether there is evolution in the dust masses of red galaxies, despite a significant detection of evolution in their luminosities. The reason for this is that the uncertainty of the lensing contribution increases the uncertainty in the fitted temperatures. If I assume that dust temperatures of the red sample do not evolve (as they do not for the blue and green samples) then the evolving luminosities must result from dust mass evolution. However, this may not be a valid assumption if the composition of the red sample changes with redshift.

If one ignores the highest redshift red bin, which has the largest errors due to lensing, then the results seem to suggest that the difference in dust mass between the red and

blue galaxies is weaker than the difference in luminosity, for a given stellar mass and redshift. The dependence of luminosity on colour therefore appears to be driven more by the temperature than the mass of the dust. I note that if the same temperatures were used in deriving the dust mass in every bin then the dust masses would be directly proportional to L_{250} and would follow the trends seen in Figure 3.11. This shows the vital importance of having photometry at multiple points along the SED, without which it would be impossible to constrain the SED shape and inferences about dust mass evolution would have to assume a constant temperature.

Significantly, this analysis suggests that the cold dust masses of red and blue galaxies are not strikingly discrepant in the stellar mass range $\sim 1 \times 10^{10} - 2 \times 10^{11}\,\mathrm{M}_{\odot}$. Previous studies fitting two-component dust models to normal spiral galaxies in the local Universe have derived ranges of *cold* dust masses comparable to this sample: $3\times10^{5}-1\times10^{8}$ (Popescu *et al.* 2002); $2\times10^{7}-1\times10^{9}$ (Stevens, Amure & Gear 2005); and $4 \times 10^{6} - 6 \times 10^{7}\,\mathrm{M}_{\odot}$ (Vlahakis, Dunne & Eales 2005). Dust masses measured from fits to the cold dust in local ellipticals (which should be akin to the red bin of this sample) are often a little lower: $2\times10^{5}-2\times10^{6}$ (Leeuw *et al.* 2004); $4\times10^{4}-5\times10^{7}$ (Temi *et al.* 2004); $2 \times 10^{4} - 2 \times 10^{7}\,\mathrm{M}_{\odot}$ (Savoy, Welch & Fich 2009). However, both Vlahakis, Dunne & Eales (2005) and Stickel, Klaas & Lemke (2007) reported little or no significant difference in the typical dust masses of galaxies of different Hubble types (including spheroidals, spirals and irregulars), although Stickel *et al.* reported that spheroidal and irregular types reached significantly lower dust masses. One particular issue noted by Vlahakis *et al.* was the possibility of contamination of their 850 μm fluxes with synchrotron emission, which would lead them to overestimate a few of their dust masses. I note the caveat that in contrast to the current unbiased sample, the references in this paragraph were studies of individual galaxies selected variously with *IRAS* or ISOPHOT in the FIR, or SCUBA in the sub-mm, so the range of dust masses sampled would not have been complete (with the exception of the optically selected sample of Popescu *et al.* 2002).

Popescu *et al.* (2002) observed colder dust in *later* Hubble types (which might be expected to be the bluest galaxies). Their sample of spirals would probably reside entirely within the blue bin in the current sample, so such a trend would not be apparent

between the colour bins if it does not extend beyond the blue cloud. However, there is a correlation between Hubble type and mass; later types have lower stellar masses, so the observation of a strong correlation between stellar mass and dust temperature in blue galaxies is entirely consistent with the findings of Popescu *et al.*

Meanwhile, results from the *Herschel* Reference Survey (HRS; Boselli *et al.* 2010a) indicate that early type galaxies (E+S0+S0a) detected by *Herschel* in a volume-limited sample of the local Universe have dust masses in the range $1\times10^5-2\times10^7\,\mathrm{M}_\odot$ (Smith *et al.* 2012b) – although they only detected 34 per cent of ellipticals and 61 per cent of S0's. Their sample have $NUV-r$ colours that place them in the "red" bin of my sample, yet their dust masses are much lower than the typical dust masses that I find for red galaxies. This is perhaps due in part to the higher derived temperatures of the HRS sample: $T_{\mathrm{dust}}=16-32\,\mathrm{K}$; with a mean of 24 K in comparison with the mean of 16.2 K for the red sample in the current data (both assuming $\beta=2$). Smith *et al.* concluded that the dust masses of S0's were around 10 times lower than those of the HRS spirals, while those of ellipticals were 10 times lower again (for the same stellar mass), which seems to contrast with the results presented here.

Rowlands *et al.* (2012) studied early type galaxies detected in H-ATLAS and found dust masses mostly between 2×10^7 and $2\times10^8\,\mathrm{M}_\odot$, with a mean dust mass similar to that of spirals ($5.5\times10^7\,\mathrm{M}_\odot$). However, the stellar mass distributions of spirals and early types were very different. The $NUV-r$ colours of the Rowlands *et al.* spiral sample lie mostly within the blue bin, and the early types mostly within the green bin. Their redshift range is similar to this study ($z<0.3$), and the mean dust and stellar masses of their spirals/early types lie within the locus of the blue/green bins in Figure 3.15. However, derived dust masses depend on the temperature assumed. The cold dust temperatures fitted by Rowlands *et al.* range from 15 to 25 K, while the temperatures in the blue/green samples for the same stellar mass range ($>10^{10}\,\mathrm{M}_\odot$) are between 15 and 28 K. The correspondence is not exact but the ranges are similar so average dust mass results should be comparable. For reference, changing the temperature from 15 to 25 K results in a drop in the derived dust mass by a factor 5, which is similar to the range of dust masses across the redshift range in Figure 3.15. Rowlands *et al.* (2012) compared their H-ATLAS-detected early types with a control sample of

undetected early-types selected to have a matching distribution of redshifts and r-band magnitudes. They concluded that the detected early types were unusually dusty compared with the control sample, and could be undergoing a transition from the blue cloud to the red sequence. It seems likely that those objects do indeed comprise the top end of the dust mass distribution (at a given stellar mass and redshift), although they do not appear to be exceptional outliers when compared with the median dust masses in this sample. This is surprising when one considers that Rowlands *et al.* found the detected early types to have around 10 times as much dust as typical early types: why are they not also outliers compared to typical *red* galaxies? The answer may be that typical red galaxies are generally dustier than typical early types, which supports the notion (as discussed in earlier sections) that the red sample is comprised of a mixture of different populations. The red bin is likely to contain most of the early type galaxies in the sample volume, and if these are relatively dust-poor then there must be a substantial population of red dusty galaxies boosting the median dust masses in the red bin. This could also explain the discrepancy between the red sample and the HRS early types (Smith *et al.* 2012b).

There is also the possibility of an environmental factor in the offset between the HRS results and this study. Many of the galaxies in the HRS sample reside in the Virgo cluster, while most of the galaxies in GAMA will be in lower density environments. The lower dust masses of HRS early types compared with GAMA red galaxies could be due to early types in clusters being dominated by passive red-sequence systems, while red galaxies in lower density environments are more likely to be dusty. Such a division is indeed suggested by the higher detection rate of early types outside of Virgo in HRS, compared to those inside (Smith *et al.* 2012b). It is however unclear whether such an effect could be strong enough to fully explain the discrepancy seen.

On the other hand, if the lensing contamination is slightly greater than I have predicted, then the derived dust masses of the red sample could be a lot lower; however this is only likely to affect the higher redshift bins due to the weak lensing efficiency at lower redshifts. The Rowlands *et al.* sample is less likely to be biased by strong lensing than this sample is, because they excluded detections. The HRS results are unlikely to be biased by lensing because their fluxes were much higher than the red galaxies in this

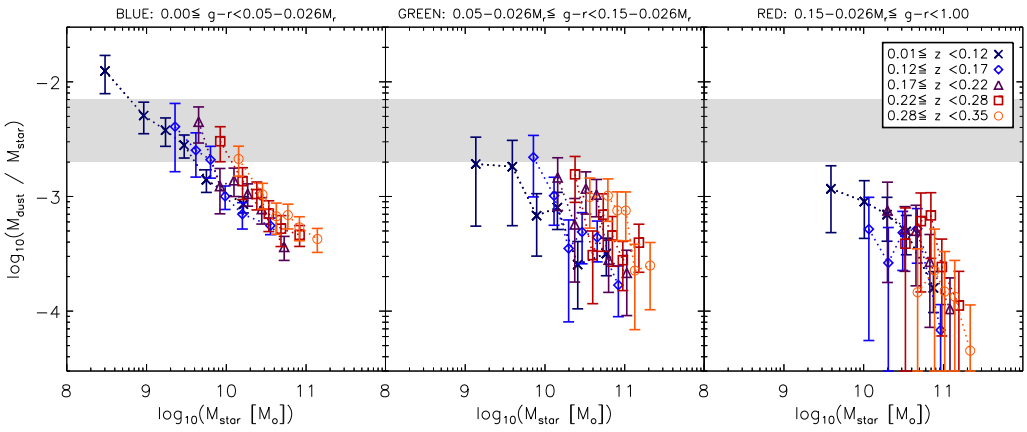

Figure 3.16: Stacked dust mass per unit stellar mass as a function of $g - r$ colour, redshift and stellar mass. Error bars include the statistical 1σ errors in the bins as described in Section 3.3.3, with an additional contribution due to the error on the fitted temperature. The shaded region shows the range from D11, from 2×10^{-3} at $z < 0.1$ to 7×10^{-3} at $z \sim 0.35$.

sample, and the low dust masses and high temperatures they derive (relative to this study) argue against their results being biased by lensing.

3.5.3.1 Dust-to-Stellar Mass Ratios

In Figure 3.16 I plot the ratio of dust to stellar mass across the sample, which shows several interesting features. Firstly there is in general a strong correlation with stellar mass: the more massive galaxies have smaller dust-to-stellar mass ratios. The correlation appears steeper for red galaxies of the highest masses in each redshift bin, but this is not so obvious in the blue and green samples which do not reach to quite such high stellar masses. Nevertheless it seems not unreasonable to observe that the most massive red galaxies, many of which will be passively evolving giant ellipticals, have especially low dust-to-stellar mass ratios. The data for each redshift bin are plotted in Figure 3.17, highlighting the weak dependence on optical colour at a given stellar mass (as discussed in the previous section).

It is worth pointing out the potential for a negative correlation between $M_{\rm dust}/M_\star$ and $M_\star$ to be produced artificially in binned data. This can occur if there is a large range of stellar masses with large errors, even when there is no correlation between $M_{\rm dust}$ and $M_\star$, since a bin that selects data with low $M_\star$ also selects those with high $M_{\rm dust}/M_\star$. In general the slope of the measured correlation could be affected by this artificial

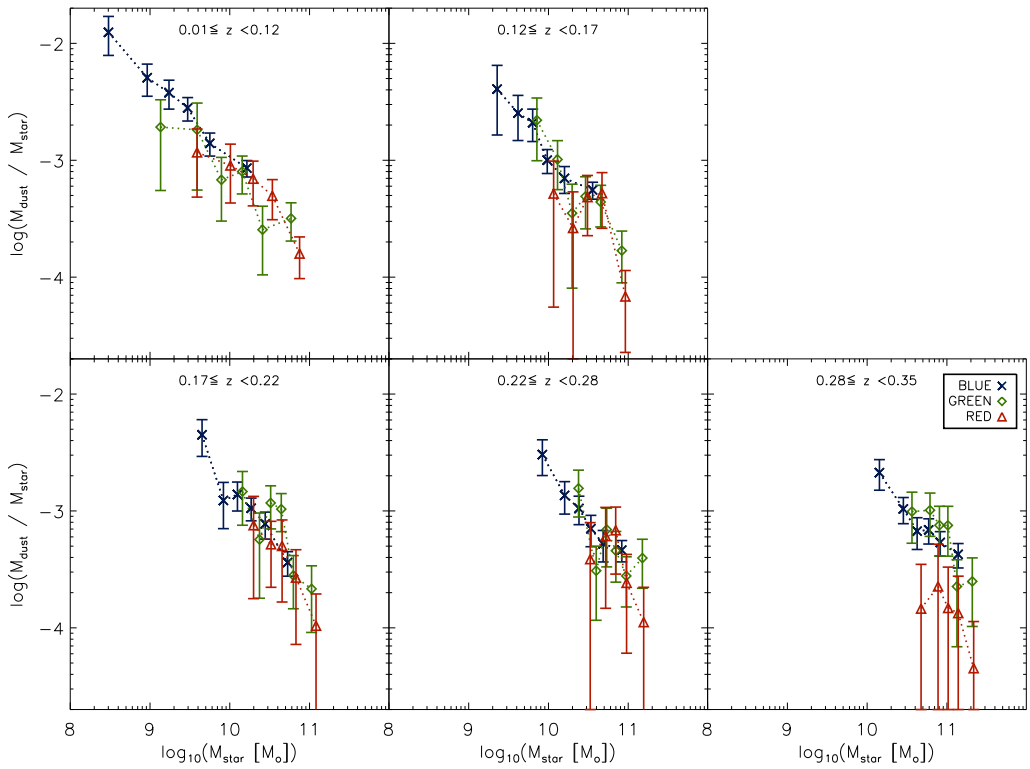

Figure 3.17: The dependence of the dust/stellar mass ratio on stellar mass and colour in each redshift bin. Error bars are as in Figure 3.16

phenomenon; however one can be sure in this case that the trends are real because they can also be discerned in the median $M_{\rm dust}$ values in Figure 3.15, and in any case the stellar mass errors are small ($\Delta \log M_\star \sim 0.1$; Taylor *et al.* 2011).

The aforementioned redshift evolution is very apparent in Figure 3.16, and although one naturally selects higher stellar masses at higher redshift, the dust masses in the sample rise more rapidly resulting in an increasing dust-to-stellar mass ratio with redshift. Using the $(1+z)^\gamma$ model once again I find that the evolution is consistent with the slopes derived for the dust mass evolution. This evolution in dust mass echoes the results of D11, who found a strongly evolving dust mass function (DMF) in H-ATLAS sources up to $z \sim 0.4$, as well as results from other surveys reaching higher redshifts (Eales *et al.* 2009; Eales *et al.* 2010b; Gruppioni *et al.* 2010; Rodighiero *et al.* 2010a). Using dust masses from SED fitting by Smith *et al.* (2012a), D11 showed that the characteristic dust mass ($M^\star_{\rm dust}$) of the H-ATLAS DMF increases from $3.8 \times 10^7\,{\rm M}_\odot$ at $z < 0.1$ to around $2.1 \times 10^8\,{\rm M}_\odot$ at $z \sim 0.35$ (although they note that this does not measure the true evolution because there is an accompanying fall in the characteristic

density $\phi^{\star}$). This range is indicated by the shaded region in Figure 3.15. In all of the bins, the typical dust masses reach lower than the minimum mass sampled in equivalent redshift slices in the D11 DMF, but the fact that we see evolution indicates that galaxies of a given stellar mass shift up the DMF at increasing redshifts. We can see this happening in galaxies of all colours and stellar masses, indicating that the evolution in the DMF is the result of changing dust masses in all galaxies, both passive and star-forming. The evolution (around a factor $3-4$) is similar to that seen by D11, who fitted two-component dust masses temperatures using a detailed physically-motivated SED model.

It is also interesting to compare $M_{\rm dust}/M_{\star}$ in these results with the detected H-ATLAS galaxies in D11. The H-ATLAS galaxies were found to have higher dust-to-stellar mass ratios than predicted by models, ranging from 2×10^{-3} at $z<0.1$ to 7×10^{-3} at $z\sim0.3$ (this range is shaded in Figure 3.16). These results are typically lower but the strong dependence on stellar mass means that they span a very wide range; many of the blue galaxies in the lower mass bins have much higher dust/stellar mass ratios than the H-ATLAS sample for the same redshifts. It is perhaps not surprising that this sample contains a much wider range than the H-ATLAS sources since the selection criteria in this study are independent of dust content. The dust/stellar mass results have implications for understanding the dust production mechanism, as I show by comparing the results from a chemical evolution model with the parameters obtained for the H-ATLAS galaxies (Gomez, H. L. *et al.* in preparation). The models (based on the framework in Morgan & Edmunds 2003) show that values of $M_{\rm dust}/M_{\star}>10^{-3}$ cannot be achieved with a purely stellar source of dust. Even including dust production in supernovae ejecta (e.g. Rho *et al.* 2008; Dunne *et al.* 2009a; Matsuura *et al.* 2011; Gomez *et al.* 2012b), models require the condensation efficiency in the ejecta to be close to 100 per cent to reach the high values of $M_{\rm dust}/M_{\star}\sim10^{-2}$ seen both in the H-ATLAS detected sample and in the lowest-mass blue galaxies in this sample. However, as discussed by D11 and Gomez *et al.* (in preparation), such high dust yields from supernovae are difficult to produce, leading to the invocation of alternative explanations such as dust grain growth in the ISM (Draine & Salpeter 1979; Dwek & Scalo 1980; Draine 1990; Edmunds 2001) or a top-heavy IMF (e.g. Harayama, Eisenhauer & Martins 2008). The models also indicate that the low mass galaxies with high $M_{\rm dust}/M_{\star}$ are less efficient

at turning their gas into stars (compared to high mass sources with low $M_{\rm dust}/M_{\star}$). In other words, low mass systems have a longer star formation time-scale, so although they produce less dust mass per year from stars, there are more metals and dust in the ISM for longer, in comparison to massive galaxies (Gomez *et al.* in preparation).

Moving on to higher redshifts, Santini *et al.* (2010) showed that the dust/stellar mass ratios of ordinary low-redshift galaxies are much lower than those of high-redshift sub-mm galaxies (SMGs) from the *Herschel*-PEP survey. The $M_{\rm dust}/M_{\star}$ values from stacking are consistent with their sample of low-redshift spirals from the SINGS survey (with typical stellar masses of $\sim 10^{11}\,{\rm M}_{\odot}$). Their dust masses were derived by fitting GRASIL models (Silva *et al.* 1998) to photometry spanning the FIR/sub-mm SED, and are consistent with the value of $\beta = 2$ that I have assumed. My results therefore support the conclusion of Santini *et al.* that high-redshift SMGs have much higher dust content (by a factor ~ 30) than local spiral galaxies. This offset is also consistent with the comparison between low-redshift H-ATLAS sources in D11 and high-redshift SCUBA SMGs in Dunne, Eales & Edmunds (2003). It has now become clear that the SMGs detected in early sub-mm surveys are exceptionally dusty systems in comparison with the low-redshift galaxy population.

There is evidence that the dust/stellar mass ratio correlates with the specific SFR (da Cunha *et al.* 2010; Smith *et al.* 2012a; Gomez, H. L. *et al.* in preparation), so these results imply that the least massive galaxies at low redshift are the most actively star-forming, and that all galaxies become more active towards higher redshifts. At $z \sim 0.3$, galaxies with $2 \times 10^{10}\,{\rm M}_{\odot}$ of stars have the same $M_{\rm dust}/M_{\star}$ as galaxies a quarter of that size do at $z \lesssim 0.1$, consistent with the picture of downsizing (see Section 1.1.2).

3.5.4 Obscuration

A further step that one can take towards understanding the nature of the galaxies is to investigate the relative luminosities at UV and sub-mm wavelengths, which can give information about the fraction of star-formation that is obscured by dust in the galaxies (e.g. Buat *et al.* 2010; Wijesinghe *et al.* 2011). The sub-mm luminosity represents the energy absorbed and re-radiated by dust. Naively, one might expect that this energy

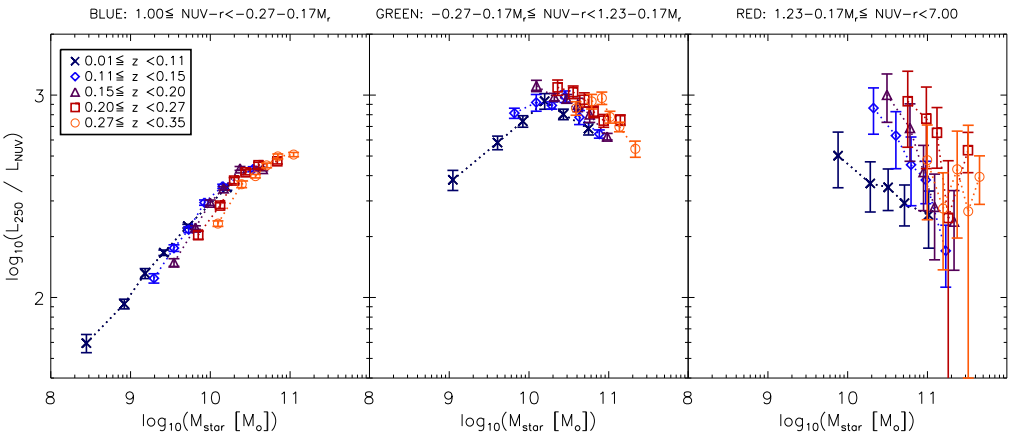

Figure 3.18: Stacked 250 μm/NUV luminosity as a function of $NUV - r$ colour, redshift and stellar mass. This fraction can be used as a proxy for the relative obscuration of star formation, subject to the limitations discussed in the text. Error bars are the statistical 1σ errors in the bins as described in Section 3.3.3. Data and errors in the red bin incorporate the correction for lensing described in Section 3.4.2.

originated as UV radiation from young stars, hence the ratio of sub-mm light to UV light detected is directly related to the fraction of UV light which is obscured by dust. If UV light is assumed to come primarily from star-forming regions, this is a measure of the ratio of obscured to unobscured star-formation. However both the UV and the sub-mm radiation could also trace populations unrelated to star-formation: there are open questions as to how much UV radiation can be produced by evolved stars (Chavez & Bertone 2011; and references therein) as well as how much of the dust probed at sub-mm wavelengths is heated by old stars in the galaxy (Bendo *et al.* 2010; Boselli *et al.* 2010b; Law, Gordon & Misselt 2011; see also Section 1.4). Radiative transfer calculations (e.g. Popescu *et al.* 2011), which have been used to make detailed predictions for a few well-studied spiral galaxies, can be used in the future to analyse statistical samples of galaxies to address this question in a quantitative way. For the moment, however, the generalisation to galaxy populations as a whole is uncertain.

In Figure 3.18 I stack L_{250}/L_{NUV} for the NUV-detected sample. Since I require NUV detections for this, I use the $NUV - r$ colour which is likely to be a cleaner colour separation, and I use L_{250} instead of $L_{\rm TIR}$ because the monochromatic luminosity is not model-dependent. Simulations showed that stacking this ratio is robust even for small 250 μm fluxes with low signal-to-noise, since the NUV fluxes all have reasonably high signal-to-noise (on the contrary stacking L_{NUV}/L_{250} was found to be unreliable

in simulations since this quantity diverges as the 250 μm flux approaches zero). As before, I correct 250 μm fluxes for the expected contribution from lensing as described in Section 3.4.2.

Some of the results implied by Figure 3.18 are not trivial to explain, and should be treated with caution since there is a strong bias introduced by the UV selection. It appears that the obscuration increases with increasing stellar mass for blue galaxies, but there appears to be a decrease with redshift, at least for stellar masses $\lesssim 5 \times 10^{10}\,\mathrm{M}_{\odot}$. This contrasts with the increase in 250 μm luminosity with redshift, which would imply that while the obscured SFR increases with redshift up to $z = 0.3$, the unobscured SFR (UV luminosity) must increase faster for the relative obscuration to fall. However, it is likely that these observations are affected by selection bias: we only detect the low mass galaxies in the UV if they are relatively unobscured, and as redshift increases we detect fewer and fewer of the obscured ones. This effect could cancel out any intrinsic increase in obscuration with redshift, and cause the observed L_{250}/L_{NUV} to decrease.

In contrast we see almost exactly the opposite trends in the red sample, and in the high mass end of the green sample, which suggests that the selection bias could hide similar trends in blue galaxies (which generally have much lower stellar mass for the same redshift). Number statistics are poor in the red bin because the selection is naturally biased against red galaxies, and errors are compounded by the uncertainty on the lensing contamination. Nevertheless the observed trends of increasing obscuration with increasing redshift and with decreasing stellar mass cannot be explained by the selection bias. These trends are both perfectly consistent with the trends in $M_{\mathrm{dust}}/M_{\star}$ in Figure 3.16: a higher amount of dust per stellar mass is almost certain to increase the obscuration of UV light. The red galaxy sample therefore appears to contain a larger fraction of obscured SFGs at higher redshifts and lower masses. This is consistent with the findings of Zhu *et al.* (2011) in an analysis of the mid-IR colours of optically-selected galaxies at redshifts between 0.1 and 0.5. It is also in agreement with Tojeiro *et al.* (2011), who stacked SDSS spectra of luminous red galaxies (LRGs), and fitted stellar population models to obtain representative star-formation histories, metallicity and dust content as a function of colour, luminosity and redshift. Their results showed

strong correlations of dust extinction with optical luminosity and redshift which are consistent with the findings of this work. Such agreement between independent measures of the dust extinction is encouraging.

In any case one must be careful in the interpretation of L_{250}/L_{NUV} as a tracer of obscuration, in particular due to the potential for L_{250} to be uncorrelated with star formation. I showed in Section 3.5.1 that the conversion from SPIRE luminosities to $L_{\rm TIR}$ is extremely model-dependent, and to plot the ratio $L_{\rm TIR}/L_{\rm UV}$ using SED fits for $L_{\rm TIR}$ would be misleading when $L_{\rm TIR}$ is based only on the SPIRE photometry. In addition, it has been shown by Wijesinghe *et al.* (2011) that the ratio of $L_{\rm TIR}$ (from fitting SEDs to GAMA/H-ATLAS data including PACS and SPIRE) to $L_{\rm UV}$ is poorly correlated with other measures of obscuration (the Balmer decrement and UV slope), probably because they trace a different component of the dust in galaxies. I therefore hesitate to take this particular analysis any further without the addition of shorter wavelength data to better constrain the IR SED.

3.6 Conclusions

In this chapter I have described the first sub-mm stacking analysis of a large sample of about 80,000 galaxies uniformly selected by optical (r-band) magnitude. I divided the sample by rest-frame colour, absolute magnitude/stellar mass and redshift ($0.01 \leq z \leq 0.35$) and stacked into SPIRE maps covering about 126 square degrees at 250, 350 and 500 μm. I used a simple (but effective) deblending method to avoid the problem of over-estimating the flux of blended sources when stacking in confused images; this ensures that stacked flux ratios are not biased by the increasing level of confusion at longer wavelengths. The main results are summarised below:

1. The sub-mm fluxes of all but the most massive optically-selected galaxies are below the 5σ limits of the H-ATLAS, yet with the large sample size made possible by the coverage of H-ATLAS and GAMA it is possible to probe more than an order of magnitude below these limits using stacking.

2. I estimate that the total emission from optically-selected galaxies at $r < 19.8$ and

$z < 0.35$ accounts for only 5.0 ± 0.4 per cent of the CIB at 250 μm. At $z < 0.28$, where the sample is complete to below $M^{\star}$, this fraction is 4.2 ± 0.3 per cent. Of this, roughly 60 per cent originates from blue galaxies, and 20 per cent each from the red and green bins of the sample.

3. I derive the total k- and e-corrected luminosity density of the Universe at $z = 0$ to be $3.9 \pm 0.3 \times 10^{33}$, $1.5 \pm 0.1 \times 10^{33}$ and $4.3 \pm 0.3 \times 10^{32}$ W Hz^{-1} Mpc^{-3} h_{70} at 250, 350 and 500 μm respectively.

4. I show that stacked fluxes of *red* galaxies can be significantly contaminated by the lensing of background SMGs. Using models for the lensing amplification distribution and observed lens number counts, I estimate that around 10, 20, and 30 per cent (at 250, 350 and 500 μm respectively) of the stacked fluxes is likely to result from lensing. I correct stacked results for this contamination to red galaxy stacks making reasonable assumptions for the redshift distribution of lensed flux, and include the uncertainty from the lens number counts.

5. I observe a strong dependence of sub-mm luminosity on optical colour ($g - r$) and stellar mass or M_r, with red galaxies being up to an order of magnitude less luminous than blue galaxies of equal stellar mass. The luminosities of green galaxies are intermediate between the two. The observed trends of SPIRE luminosities are not strongly dependent on the SED model assumed, and cannot be explained by lensing, which implies a fundamental difference between the dust emission properties of red and blue galaxies.

6. I measure cold dust temperatures that vary strongly as a function of stellar mass in blue galaxies, from ~ 11 K at 3×10^8 M$_\odot$ to ~ 28 K at 5×10^{10} M$_\odot$. Correcting for the contamination from lensing, red galaxies have dust temperatures ~ 16 K at all stellar masses between $3 \times 10^9 - 8 \times 10^{10}$ M$_\odot$ at $z < 0.35$. The dust temperatures of green galaxies appear to have a greater scatter (with mean $T = 19.5$ K) but are not correlated with stellar mass as with the blue; this is indicative of a mixed population. Temperature values depend on the assumption of a constant emissivity parameter $\beta = 2$; a variable β could alter the results slightly but would not be sufficient to account for the range of observed colours.

Furthermore, a range of temperatures is implied by the 250/350 μm colours alone suggesting that the trends are not the result of emissivity variations or any kind of sub-mm excess at 500 μm. Tests showed that they are not subject to any bias from blending which isn't accounted for by the naive deblending assumptions.

7. The temperature variation can account for much of the difference in luminosities between red and blue galaxies; however it is not responsible for an increase in sub-mm luminosity with redshift by a factor around 2 for blue galaxies at a given stellar mass. This appears to be due to an increase in the dust masses of galaxies of all stellar masses by a factor of $3-4$ between $z\sim 0$ and $z\sim 0.3$. The red sample exhibit a stronger luminosity evolution, for which the likely explanation is also dust mass evolution. Due to the lensing uncertainty one cannot rule out evolution in the temperatures of the red sample, although there is no temperature evolution in the other colour bins.

8. I fit the evolution in L_{250} (which is not dependent on the temperature) with the function $L(z)\propto(1+z)^{\gamma}$, and obtain indices for the three colour bins at $M_{\star}=2-7\times10^{10}\,\mathrm{M}_{\odot}$. I find $\gamma=4.2\pm0.2$ for blue galaxies, $\gamma=3.5\pm0.5$ for green and $\gamma=7.2\pm1.5$ for red (the larger error on the evolution of red galaxies is due to the uncertainty on the lensing correction). The evolution suggests a change in the dominant population of red galaxies, from passive systems at low redshift to obscured star-forming systems at higher redshift.

9. The redshift evolution of galaxies classified as green seems to indicate a change in the nature of galaxies selected in this way, from a sample dominated by blue-cloud-like galaxies at low redshift and low M_r (or $M_{\star}$) to a sample more similar to the red bin at the higher redshift and brighter M_r.

10. Deriving TIR luminosities is problematic with only the SPIRE data, and I show that the results obtained depend sensitively on the SED model used (therefore the dust temperature). The low temperatures implied by the SPIRE colours indicate that a cold model such as the H-ATLAS SED fits (Smith *et al.* 2012a) are more appropriate than earlier models based on *IRAS* and SCUBA data (CE01).

11. The dust-to-stellar mass ratio is strongly anti-correlated with stellar mass, vary-

ing by more than an order of magnitude between $M_\star \sim 10^8 - 10^{11}\,\mathrm{M}_\odot$. This relationship appears to vary little between different optical colours, although it evolves toward higher values with increasing redshift. These results provide a challenge to dust formation models that rely on a purely stellar source of dust, implying a need for dust formation in supernovae and/or the ISM to reach the high dust masses in galaxies at the lower end of the stellar mass function.

12. I attempt to explore the obscuration of galaxies in the sample using the L_{250}/L_{NUV} ratio, and see that red and green galaxies may become more obscured at increasing redshift and decreasing stellar mass (results for the blue galaxies are unclear due to selection bias). This conclusion is dependent on the assumption that this ratio is a good tracer of obscuration, but due to uncertainties in the heating mechanism for cold dust this may not be valid. Nevertheless, such trends in obscuration are consistent with the trends of luminosity and dust/stellar mass.

This study is the first of its kind and provides some tantalising glimpses of the characteristics of emission from dust in normal galaxies. Our understanding of the IR SED of optically-selected galaxies and of the obscuration of star formation would be greatly improved by the availability of data covering the peak of the SED. A future study stacking data from PACS and *WISE* would be able to make a much more detailed analysis of the full SED.

Chapter 4

The Molecular Gas Content of Local Sub-Millimetre-Selected Galaxies

4.1 Introduction

This chapter will diverge from stacking and large sample statistics and instead focus on the individual properties of a small number of local galaxies. The sample comprises an unbiased 500 μm-flux-limited selection of local galaxies from H-ATLAS, a selection function which is primarily sensitive to dust mass. These galaxies have been observed with the HARP and RxA instruments on the James Clerk Maxwell Telescope (JCMT) to measure the emission lines from the CO $J = (2–1)$ and CO $J = (3–2)$ transitions. The data are combined with H I 21 cm and IR fluxes from the literature to compare the mass of dense molecular gas, atomic gas, and warm and cold dust in the sample, and examine how well correlated these components are. Although this is a small sample, it represents a novel pilot study and is the first attempt at analysing molecular gas in a sample selected by dust mass. Here I present some preliminary results, to be published in a research paper at a later date.

4.1.1 Observing Gas in Galaxies

The gaseous ISM consists of a number of phases at varying temperatures and densities (see e.g. Draine 2011). Neutral atomic H I makes up most of the gas mass in quiescent

spiral galaxies like the Milky Way; this includes the warm ($\sim 5000\,\mathrm{K}$) and cool ($\sim 100\,\mathrm{K}$) neutral media (WNM and CNM). The more diffuse WNM fills much of the disk of the Milky Way, while the CNM is in denser clouds, some of which also contain diffuse molecular H_2. Gas also exists in the hot, ionised phase, in massive haloes surrounding galaxies (especially giant ellipticals), as well as in H II regions – bubbles embedded in the dense clouds, where gas is photo-ionised by the far-UV radiation from hot OB stars (Figure 4.1; see also Section 1.2.1).

Cold ($\sim 20\,\mathrm{K}$) molecular gas (H_2) occurs in the densest clouds and clumps, which provide the fuel for star formation. These clumps reach high enough densities for gravity to overcome the pressure and rotational stabilisation that maintains gas in the disk, thus it condenses to form stars and star clusters. The general mechanism for this collapse was described by Toomre (1977), although the full details and conditions are poorly understood (see also Kennicutt 1989, 1998b; Schaye & Dalla Vecchia 2008; Draine 2011). The CNM acts as a reservoir of material which can be converted into cold molecular gas under favourable conditions (Gould & Salpeter 1963; Papadopoulos, Thi & Viti 2002). The Milky Way contains approximately $8 \times 10^8\,\mathrm{M}_\odot$ of H_2, compared with about $3 \times 10^9\,\mathrm{M}_\odot$ of H I and $1 \times 10^9\,\mathrm{M}_\odot$ of H II (Draine 2011), although in more active SFGs and especially starburst galaxies, the H_2 component is the most massive.

The most direct way of observing cold interstellar gas is via the radio 21 cm line of H I, which results from the transition between the two opposing spin states of the electron in the ground state. The gas that is directly important for star formation, however, is in the molecular form. Since hydrogen is the most abundant element, the molecular gas consists chiefly of H_2, but this molecule has no convenient emission lines to observe. The electronic transitions of H_2 are seen in absorption in the far-UV but are only visible in low-extinction lines of sight (most molecular clouds are shrouded in dust). H_2 has vibrational transitions in the NIR, but these require very high excitation and only trace hot (starburst- or shock-heated) gas, while the symmetry of the molecule means it has no strong dipole moments hence the rotational transitions (in the MIR) are very weak and again require high excitation (Burton, Hollenbach & Tielens 1992; Blain *et al.* 2004).

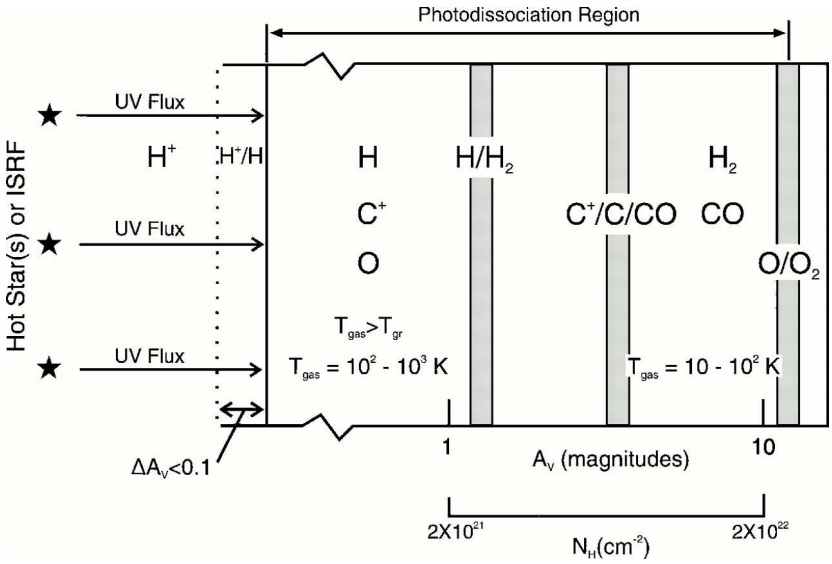

Figure 4.1: A schematic diagram of an H II region and photo-dissociation region (PDR) embedded in a molecular cloud in which stars have recently formed; from Hollenbach & Tielens (1997; Figure 3). The UV flux from a (young) massive star or cluster of massive stars (left) heats the surrounding ISM, creating a fully ionised H II region (left) surrounded by a PDR. As distance increases (to the right), the flux diminishes until first neutral H I and OI, then C, CO, H_2 and O_2 can exist. The attenuation of the UV flux is caused by dust in the PDR, as shown by the visual extinction A_V along the bottom of the diagram. The density (shown by the N_H scale) increases going out through the PDR, as the temperature drops from $\sim 10^4$ K in the H II region to ~ 20 K in the surrounding molecular cloud.

It has therefore become common practice to observe emission lines from less abundant molecules and use them as a tracer of the total molecular gas content. Carbon monoxide is the next most abundant molecule after H_2 (abundance ratio $\sim 10^{-4}$; Lee, Bettens & Herbst 1996), and has strong emission lines from transitions between its rotational excitation states, especially the ground state and first three excitation levels ($J = 0, 1, 2, 3$). These states are easily excited at relatively low densities ($\sim 10^4$ cm^{-3}; Blain *et al.* 2004), and transitions between them have energies ($E = h\nu$) that give rise to emission lines at a few hundred GHz which can be observed with mm/sub-mm instruments on ground-based telescopes. These emission lines from CO are used to trace the molecular gas content of galaxies and galactic clouds, but require a conversion factor (X) which is dependent on metallicity and on the density and temperature (which determine the excitation). More importantly, individual clouds are optically thick to emission lines of the most abundant isotopic species (^{12}C^{16}O), so the line intensity is not correlated with the mass of individual clouds. For entire galaxies it is common to invoke the "large velocity gradient" (LVG) approximation, which assumes that individual clouds are sufficiently offset from each other in velocity (due to their differential

rotation speeds within the galaxy) for their emission to be largely unobscured overall. Alternatively the virial approximation may be assumed, i.e. the assumption that the velocity dispersion of clouds, and therefore the total line *width*, is correlated with the total mass. Hence the conversion from line intensity to column density and molecular gas mass is highly uncertain, and is probably non-linear and variable (Dickman, Snell & Schloerb 1986; Scoville & Sanders 1987; Maloney & Black 1988; Young & Scoville 1991; Wilson 1995; Blain *et al.* 2004; Pelupessy & Papadopoulos 2009; Genzel *et al.* 2012; Narayanan *et al.* 2012).

Other molecules (e.g. HCN, CS, NH_3) become excited at higher densities so their rotational transitions can be used to trace dense clumps of molecular gas, and the higher transitions of CO [(3–2) and higher] are also only excited at relatively high densities. These dense gas tracers can be better tracers of the immediate capacity for star formation since stars form in the densest clumps; but CO(1–0) remains, for now, the most accessible tracer of the total molecular gas. In the near future this situation could change, as ALMA is capable of observing rotational lines of CI, which appears to exist throughout molecular clouds and suffers from fewer complexities than the CO tracer (Wilson 1997; Ojha *et al.* 2001; Ikeda *et al.* 2002; Papadopoulos, Thi & Viti 2002, 2004; Geach & Papadopoulos 2012).

Dust mass, estimated from the FIR/sub-mm, can also be used as a tracer of the H_2 mass, assuming a dust-to-gas mass ratio that is dependent on metallicity (e.g. Cox, Kruegel & Mezger 1986; Issa, MacLaren & Wolfendale 1990; Dunne *et al.* 2000; James *et al.* 2002). From sub-mm observations in the Rayleigh-Jeans limit, the uncertainty on dust mass itself is dominated by the uncertainty of the dust opacity, κ_ν, but this is relatively well constrained in the Milky Way and other galaxies (James *et al.* 2002; Hill *et al.* 2006; Paradis, Bernard & Mény 2009; Planck Collaboration *et al.* 2011f,g). Comparisons of the CO tracer with independent tracers of H_2 (such as dust) are used to test the metallicity dependence of the X factor (e.g. Wilson 1995; Dunne *et al.* 2000; Genzel *et al.* 2012), and recent measurements have shown evidence for "dark" H_2 gas with no associated CO emission (Grenier, Casandjian & Terrier 2005; Abdo *et al.* 2010; Planck Collaboration *et al.* 2011d,e).

4.1.2 The Relationship Between Gas and Star Formation

Schmidt (1959) was the first to report an observational link between molecular gas and SFR, which backs up the theoretical notion of molecular gas being the raw material for star formation. This link was cemented by Kennicutt (1998b), with the slight adaptation that the surface density of star formation in the disk is correlated with the surface density of molecular gas, in what is known as the star-formation law or Schmidt–Kennicutt (SK) law:

$$\Sigma_{SFR} \propto \Sigma_{H_2}^{n}. \tag{4.1}$$

Significant scatter in the SK law has led to many different values for the index (n) being reported, but it is generally thought to lie in the range $1.0 - 1.5$ (Narayanan *et al.* 2012). This index probably depends on the gas tracer: for example, the more fundamental relation is likely to be that between the dense gas (e.g. HCN, CO(3–2)) and the SFR, for which the relationship is roughly linear ($n \lesssim 1$), while the relationship between total molecular gas tracers (e.g. CO(1–0)) and the SFR have steeper indices ($n \approx 1.5$; Gao & Solomon 2004b; Krumholz & Thompson 2007; Narayanan *et al.* 2008; Juneau *et al.* 2009; Lada, Lombardi & Alves 2010) due to varying line ratios.

The law appears to be universal in ordinary (disk) SFGs of all luminosities, but the more vigorous mode of star formation in starbursts and high-redshift SMGs may cause them to deviate (Kennicutt 1998b; Bouché *et al.* 2007; Daddi *et al.* 2010b; Genzel *et al.* 2010). It is currently a matter of debate whether this results from a genuine difference in the relationship described by the law, from different sampling biases artificially creating a bimodality, or from a difference in the X factor between starbursts and disk star-forming regions (Daddi *et al.* 2010b; Genzel *et al.* 2010; Narayanan *et al.* 2012; Krumholz, Dekel & McKee 2012; Feldmann, Gnedin & Kravtsov 2012). Recent work from the HERA CO Line Extragalactic Survey (HERACLES; Leroy *et al.* 2009) has begun to dissect the SK law within nearby disk galaxies, suggesting that molecular gas and SFR are strongly and directly correlated in any given galaxy, but that significant scatter exists between the global properties of different galaxies (Bigiel *et al.* 2011; Schruba *et al.* 2011).

Figure 4.2 shows a compilation of data for the CO–FIR *luminosity* correlation (as distinct from the surface-area-averaged SK law). In this empirical relationship, it is

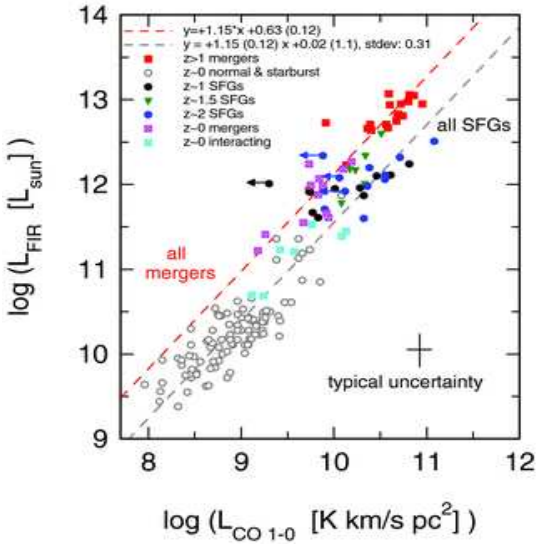

Figure 4.2: The correlation between FIR and CO luminosities for a compilation of literature data: normal and starburst galaxies at $z \sim 0$ (grey circles; Kennicutt 1998b; Gao & Solomon 2004b; Kuno *et al.* 2007; Graciá-Carpio *et al.* 2008; Leroy *et al.* 2008, 2009); optical/NIR-selected SFGs at $z \sim 1$ (black circles) and $z \sim 2$ (blue circles) from Tacconi *et al.* (2010) and at $z \sim 1.5$ (green triangles) from Daddi *et al.* (2010a). Also shown are merger samples at $z \sim 0$ (i.e. local LIRGs & ULIRGs; magenta squares; Kennicutt 1998b; Graciá-Carpio *et al.* 2008) and at $1.0 < z < 3.5$ (i.e. SMGs; red squares; Greve *et al.* 2005; Engel *et al.* 2010; Smail *et al.* 2011). The offset between mergers and SFGs is clear from the fits to the two groups, shown as red and grey dashed lines respectively (parameters of the fits are shown on the plot, with overall 3σ uncertainties in brackets; the slope of the mergers fit has been fixed to that of the SFGs fit). This figure taken from Genzel *et al.* (2010; Figure 2).

clear that low-redshift, ordinary SFGs (those on the "main sequence" of SFR($M_\star$); Noeske *et al.* 2007) lie along a single correlation, with a significant amount of scatter ($\sigma = 0.31$ dex in the fit shown). High-redshift SFGs selected in the optical/NIR appear to fall on the same sequence, while both low-redshift (U)LIRGs and high-redshift SMGs are offset towards higher $L_{\rm FIR}$ (hence SFR) for the same CO luminosity (Daddi *et al.* 2010b; Genzel *et al.* 2010). Such extreme systems are relatively rare, both at high and low redshifts, since they are dominated by major mergers (e.g. Sanders & Mirabel 1996; Engel *et al.* 2010); yet they are over-represented in flux-limited samples selected in the rest-frame FIR, since they have the highest luminosities.

4.1.3 Motivation for this Study

It is important to understand the gas–SFR relationship in SFGs of all luminosities, and to explore the biases resulting from different selection functions. Far-infrared selection favours high-SFR galaxies but does not necessarily select galaxies with massive ISM

content, hence the bias towards the upper extreme of the SK scatter. In contrast, there have been relatively few studies of the correlation in galaxies selected by gas mass. For example, Wilson *et al.* (2012) studied H I-selected galaxies as part of the JCMT Nearby Galaxies Legacy Survey (NGLS; Wilson *et al.* 2009), and found that they follow a different correlation compared to (U)LIRGs at low and high redshifts, echoing the conclusions of Genzel *et al.* (2010) and Daddi *et al.* (2010a).

In this chapter I describe the first study of the CO–IR relation in sub-mm-selected galaxies in the local Universe. Little is known about galaxies selected in this way since before *Herschel* it was impossible to conduct blind sky surveys in these wavebands. The largest local sub-mm survey prior to *Herschel* was the SCUBA Local Universe Galaxy Survey (SLUGS), which used the SCUBA camera to survey galaxies selected from *IRAS* (Dunne *et al.* 2000) and optical (Vlahakis, Dunne & Eales 2005) samples. Yao *et al.* (2003) observed nuclear CO emission in the SLUGS 60 μm sample and measured correlations of $L_{\rm CO}$ with $L_{\rm FIR}$ and $M_{\rm dust}$, using both the CO(1–0) *total* molecular gas tracer and the CO(3–2) *dense* gas tracer. Gao & Solomon (2004a,b) targeted a sample of galaxies known to have strong CO or IR fluxes and conducted a survey of HCN $J =$(1–0) emission to trace the dense gas in comparison to the CO(1–0). Gao & Solomon (2004b) concluded that $L_{\rm HCN}$ is linearly correlated with $L_{\rm FIR}$ and that the dense gas is the true driver of star formation, while the CO(1–0)–FIR relation is secondary. On the other hand, Yao *et al.* (2003) showed that CO(3–2) is linearly correlated with dust mass, but not with $L_{\rm FIR}$ due to more luminous galaxies having higher dust temperatures (possibly a sampling bias). In a recent study of spiral galaxies in the Virgo cluster, Corbelli *et al.* (2012) compared correlations between the CO(1–0) line and 100-500 μm fluxes from *Herschel*, and found that the molecular gas is more closely correlated with the cold dust traced by the sub-mm rather than the warm dust and SFR traced by shorter wavelengths.

The aims of the current chapter are to find out whether galaxies selected on their cold dust content in the local Universe have correspondingly high molecular gas content; to find out whether their dust/gas ratios are different from other samples; and to explore the validity of the sub-mm spectral range as a tracer of gas and star formation in galaxies.

4.2 The Sample

4.2.1 Sub-Millimetre Selection

The sample is selected by 500 μm flux, the longest-wavelength *Herschel* band, which is sensitive to cold dust and therefore total dust mass. I make use of the wide area and extensive multi-wavelength coverage in the equatorial fields of H-ATLAS Phase 1, which overlap with the GAMA survey as described in Section 3.2. These fields, centred at R.A. of approximately 9$^{\rm h}$, 12$^{\rm h}$ and 14.5$^{\rm h}$, and Dec. $\sim 0^{\circ}$, cover around $135\,\mathrm{deg}^2$ out of the plane of the Galaxy. Sources were selected out of the H-ATLAS Phase 1 catalogues, initially using a flux limit of $S_{500} > 80$ mJy to draw up a short-list of bright sources, then selecting from these an appropriate sample of local galaxies that could be observed in a reasonable time with the JCMT, as detailed below.

The Phase 1 catalogues available when the sample was constructed[1] (2010 August) contained 109 and 112 sources with $S_{500} > 80$ mJy in the G09 and G15 fields respectively. H-ATLAS sources are known to consist of two populations, one concentrated at low redshift and one at high redshift (Amblard *et al.* 2010; Lapi *et al.* 2011; Pearson *et al.* 2012), and so the first task was to remove any high-redshift sources from the sample. This was done by matching the source positions to the NASA/IPAC Extragalactic Database (NED)[2], and retaining only those sources that were matched to a low-redshift galaxy which was obviously nearby and extended in the optical images on NED.

Negrello *et al.* (2010) have shown that a large fraction of bright H-ATLAS sources (especially at 500 μm) are likely to be lensed systems, i.e. high-redshift sub-mm sources located behind a low-redshift galaxy which acts as a gravitational lens. In such situations, a match to NED would show a low redshift galaxy (the lens), and so these might not have been removed from the sample by visual inspection. In fact it is likely that most have been removed since González-Nuevo *et al.* (2012) showed that there are very few lenses at $z < 0.1$ (see also Section 3.4.2); most lenses picked up by H-ATLAS are at redshifts $0.2 < z < 1.2$ (the lensed sources themselves are mostly at

[1] Later catalogues may differ slightly due to improved techniques for measuring extended source photometry

[2] `http://ned.ipac.caltech.edu/`

$z \gtrsim 1.5$). Possible lenses in the SDP have been targeted for spectroscopic follow-up (Cox *et al.* 2011; Frayer *et al.* 2011; Omont *et al.* 2011; Lupu *et al.* 2012) (as well as several in Phase 1 data: Fu *et al.* 2012; Harris *et al.* 2012), by selecting sources with red sub-mm colours indicative of a high redshift. I removed one source (SDP 81) from the sample which had been identified as a lens in this way. There is a small possibility that some lenses remain in the sample; the lensed sources would have very red SEDs but this might not be detected if they are blended with the foreground lens. However, the probability of lensing is very small at such low redshifts since the population of sources that could be significantly lensed peaks at a distance of approximately twice the distance to the lensing galaxy, hence the source density is very low (see Treu 2010; for a review).

This resulted in a sample of 57 low-redshift ($z \lesssim 0.05$) galaxies in the $9^{\rm h}$ and $15^{\rm h}$ fields. I searched the literature and NED for previous CO data for any of the galaxies; only NGC 5713 had been observed in CO(3–2) as part of the SLUGS sample (Yao *et al.* 2003), but this was a single beam observation of the nucleus, and the galaxy was retained in the sample because the total CO flux had not been measured. I also checked the for any overlap with the NGLS (Wilson *et al.* 2009) and the HRS (Boselli *et al.* 2010b), and removed NGC 4030 and UGC 09215 which were to be observed with HARP as part of the HRS.[3]

I measured total 500 μm fluxes using elliptical apertures with radius given by the optical isophotal radius ($d_{25}/2$) added in quadrature to the 500 μm beam half-power beam width (HPBW$= 35''$), to account for smearing of the emission by the telescope beam. The final flux-limited sample consisted of 17 sources at $z < 0.05$ with $S_{500} > 250$ mJy. This includes three sources from the $12^{\rm h}$ field, for which SPIRE data became available while the proposal was being prepared. In addition, the sample contained the brightest source from the H-ATLAS Science Demonstration Phase (SDP), i.e. SDP 1; and the two brightest SDP sources visually classified as early-type galaxies by Rowlands *et al.* (2012), i.e. SDP 4 and SDP 15; these were included because their SEDs had been well-studied (Rowlands *et al.* 2012; Smith *et al.* 2012a) and the unusually high dust content of the early-types made them good candidates for further study of the molecular gas.

[3]A global CO(3–2) measurement for NGC 4030 was later obtained from the HRS team and is included in the analysis in Section 4.5.

Table 4.1 shows the details of the full sample.

Table 4.1: The CO sample, with the H-ATLAS Phase 1 IDs and basic data from NED. The 500 μm fluxes measured in elliptical apertures and 60 μm fluxes from *IRAS* Scanpi (see Section 4.2.2) demonstrate the wide range of 60/500 μm ratios. Everything down to NGC 2861 constitutes a complete sample of $z < 0.05$ galaxies with $S_{500} > 250$ mJy in the Phase 1 fields. SDP 1 is the brightest source in the SDP (and the Phase 1 9$^{\rm h}$) field; while the brightest early-type galaxies in SDP are listed on the final two rows.

H-ATLAS ID	NED ID	R.A.	Dec.	Redshift	S_{500} (Jy)	$r_{\rm ap}$ ($''$)	$\frac{S_{60}}{S_{500}}$
G12.v10.2	NGC 4030 [a]	12:00:24	−01:06:00	0.004887	5.66	104	3.7
G15.v10.7	NGC 5746 [b]	14:44:56	+01:57:18	0.005751	3.92	225	0.59
G15.v10.1	NGC 5713	14:40:12	−00:17:20	0.006334	2.28	91	10
G15.v10.3	NGC 5690	14:37:41	+02:17:27	0.005847	2.21	79	2.7
G15.v10.4	NGC 5719	14:40:56	−00:19:06	0.005781	1.82	97	4.8
G15.v10.42	NGC 5584	14:22:24	−00:23:16	0.005464	1.44	81	1.6
G15.v10.11	NGC 5740	14:44:24	+01:40:47	0.005243	0.99	84	3.0
G15.v10.108	NGC 5705 [b]	14:39:50	−00:43:07	0.005864	0.69	94	2.6
G15.v10.33	UGC 09215 [a]	14:23:27	+01:43:35	0.004660	0.58	75	1.6
G15.v10.30	NGC 5496	14:11:38	−01:09:33	0.005140	0.56	168	0.73
G15.v10.23	NGC 5750	14:46:11	−00:13:23	0.005627	0.51	74	1.2
G15.v10.12	NGC 5691	14:37:53	−00:23:56	0.006238	0.49	67	7.6
G12.v10.4	CGCG 013-010	11:57:06	+01:07:32	0.039503	0.40	41	7.9
G12.v10.6	NGC 3907B	11:49:24	−01:05:02	0.020774	0.30	50	2.4
G15.v10.10	CGCG 018-010	14:12:16	−00:37:59	0.025596	0.28	41	4.6
G15.v10.15	NGC 5478	14:08:09	−01:42:08	0.025147	0.26	48	2.6
– [c]	NGC 2861	09:23:37	+02:08:11	0.016965	0.25	50	3.0
SDP 1 / G09.v10.1	2MASX-J090401+012729	09:04:01	+01:27:29	0.053439	0.19	38	15
SDP 4 / G09.v10.12	CGCG 006-008	09:09:17	−01:09:59	0.027489	0.099	42	5.5
SDP 15 / G09.v10.42	2MASX-J091205+002656	09:12:06	+00:26:56	0.054493	0.056	44	14

Notes: (a) NGC 4030 and UGC 09215 are listed as part of the flux-limited sample but were not observed due to their inclusion in the HRS sample (CO data were requested from the HRS for inclusion in this study). (b) NGC 5746 and NGC 5705 were not observed due to time constraints; both would have required long integration times due to the large size of NGC 5746 and the low surface brightness of NGC 5705. (c) NGC 2861 is on the edge of the 12$^{\rm h}$ field and does not have an H-ATLAS ID because it is outside of the mask used for source extraction. SPIRE coverage this close to the edge of the map is shallower than elsewhere but is sufficient for imaging this bright source.

4.2.2 Far-Infrared Photometry

The H-ATLAS Phase 1 catalogues contain photometry at 100, 160, 250, 350 and 500 μm. SPIRE fluxes of point sources were measured using PSF fitting, and for extended sources using apertures as described in Section 4.2.1. I therefore used the catalogue fluxes for the analysis. I measured aperture fluxes by hand for NGC 2861,

which is not in the catalogue due to its location on the edge of the map.

PACS fluxes are problematic because the map-making procedure involves a high-pass filter (HPF) designed to remove large-scale fluctuations in the map. Sources were masked during this filtering to prevent their fluxes being affected, but flux from the outskirts of extended sources can still be lost if the mask does not cover the full extent of their emission. Hence most of sources in the sample have been flagged as bad measurements in the catalogues; only seven have reliable 160 μm fluxes and four have reliable 100 μm fluxes. In order to see if reliable aperture fluxes could be measured for the remaining sources, I compared the mask maps (which had been used to mask sources in the HPF) to the SPIRE maps, to check whether the extent of the SPIRE emission was smaller than the mask. If this is the case then the PACS flux should not have been reduced by the HPF. I found that the masks at 100 μm often did not cover the whole source, but at 160 μm all sources were fully masked apart from NGC 5705 and UGC 09215. I therefore measured aperture fluxes at 160 μm for the sources that were not in the catalogue and had been properly masked in the HPF.

Following the recommendations of the H-ATLAS data reduction team, I used elliptical apertures with semimajor axis given by the optical radius $d_{25}/2$ added in quadrature to $1.6 \times$ HPBW$_{160}$ (the 160 μm HPBW$= 13.1''$), and took the axis ratio and position angle from the HyperLEDA database[4] (Paturel *et al.* 2003). Each aperture was inspected by eye to ensure that it contained all the flux and was properly masked (see above) and axis ratios were reduced for unresolved sources. Fluxes were corrected by a calibration factor $1/1.043$ as recommended in the PACS Observing Manual, and aperture corrections (ranging from 1.00 to 1.23) were used to account for missed flux in the wings of the PSF, again following the methodology that was used for the H-ATLAS catalogues. All SPIRE and PACS 160 μm fluxes are listed in Table 4.2. 160 μm aperture fluxes agree with the catalogue values within 10 per cent. For the analysis, I used catalogue fluxes where available and aperture measurements otherwise.

The sample is covered by the FIR all-sky surveys of *IRAS* (Faint Source Catalogue, FSC; Moshir, Kopman & Conrow 1992) and *AKARI* (Yamamura *et al.* 2009). However, many of these nearby galaxies will be fully or partially resolved by these tele-

[4] `http://leda.univ-lyon1.fr`

Table 4.2: SPIRE and PACS 160 μm fluxes from the H-ATLAS Phase 1 catalogues, and 160 μm aperture measurements in ellipses with semimajor axis a_{160} and axis ratio a/b, as described in the text. Systematic calibration errors in parentheses are set at 10 per cent for PACS and 7 per cent for SPIRE, following the guidance of the Observing Manual and the data reduction team.

	Phase 1 Catalogues				Apertures		
Galaxy	S_{160} (Jy)	S_{250} (Jy)	S_{350} (Jy)	S_{500} (Jy)	a_{160} ($''$)	a/b	S_{160} (Jy)
NGC 4030	–	$33.79 \pm 0.08(2.37)$	$14.54 \pm 0.07(1.02)$	$5.00 \pm 0.05(0.35)$	73	1.4	$60.50 \pm 0.06(6.10)$
NGC 5746	–	$17.81 \pm 0.11(1.25)$	$8.82 \pm 0.12(0.63)$	$3.49 \pm 0.09(0.26)$	205	6.7	$24.45 \pm 0.11(2.50)$
NGC 5713	–	$15.64 \pm 0.08(1.10)$	$6.34 \pm 0.06(0.45)$	$2.05 \pm 0.04(0.15)$	50	1.0	$36.47 \pm 0.06(3.60)$
NGC 5690	–	$11.31 \pm 0.06(0.79)$	$5.16 \pm 0.07(0.37)$	$1.96 \pm 0.05(0.15)$	88	3.2	$20.85 \pm 0.07(2.10)$
NGC 5719	–	$10.00 \pm 0.11(0.71)$	$4.71 \pm 0.11(0.35)$	$1.68 \pm 0.08(0.14)$	91	2.4	$19.04 \pm 0.06(1.90)$
NGC 5584	–	$5.70 \pm 0.05(0.40)$	$3.18 \pm 0.05(0.23)$	$1.30 \pm 0.04(0.10)$	93	1.3	$8.29 \pm 0.11(0.84)$
NGC 5740	7.77 ± 0.07	$4.91 \pm 0.04(0.35)$	$2.34 \pm 0.04(0.17)$	$0.89 \pm 0.03(0.07)$	47	1.5	$7.44 \pm 0.05(0.75)$
NGC 5705	–	$1.74 \pm 0.05(0.13)$	$1.20 \pm 0.05(0.10)$	$0.61 \pm 0.04(0.06)$	41	2.3	$(>)^{b}0.82 \pm 0.04(0.09)$
UGC 09215	–	$2.13 \pm 0.05(0.16)$	$1.32 \pm 0.05(0.10)$	$0.53 \pm 0.04(0.05)$	50	2.1	$(>)^{b}2.23 \pm 0.05(0.23)$
NGC 5496	–	$2.55 \pm 0.06(0.19)$	$1.50 \pm 0.07(0.13)$	$0.71 \pm 0.05(0.07)$	93	4.6	$2.86 \pm 0.06(0.29)$
NGC 5750	3.85 ± 0.07	$2.59 \pm 0.04(0.18)$	$1.26 \pm 0.03(0.09)$	$0.46 \pm 0.03(0.04)$	57	1.9	$3.72 \pm 0.05(0.38)$
NGC 5691	6.35 ± 0.06	$2.92 \pm 0.03(0.21)$	$1.25 \pm 0.03(0.09)$	$0.46 \pm 0.02(0.04)$	31	1.3	$6.15 \pm 0.04(0.59)$
C 013-010	–	$2.87 \pm 0.05(0.21)$	$1.15 \pm 0.03(0.09)$	$0.40 \pm 0.02(0.03)$	33	1.0	$6.38 \pm 0.05(0.58)$
NGC 3907B	–	$1.80 \pm 0.04(0.13)$	$0.81 \pm 0.04(0.07)$	$0.29 \pm 0.03(0.03)$	51	3.6	$2.67 \pm 0.03(0.27)$
C 018-077	3.80 ± 0.05	$1.99 \pm 0.02(0.14)$	$0.82 \pm 0.02(0.06)$	$0.29 \pm 0.02(0.03)$	24	1.0	$3.74 \pm 0.03(0.35)$
NGC 5478	–	$1.76 \pm 0.02(0.13)$	$0.76 \pm 0.02(0.06)$	$0.26 \pm 0.02(0.03)$	29	1.5	$2.65 \pm 0.03(0.25)$
NGC 2861[a]	–	$1.90 \pm 0.02(0.13)$	$0.73 \pm 0.01(0.05)$	$0.25 \pm 0.01(0.02)$	21	1.1	$3.26 \pm 0.06(0.30)$
SDP 1	3.84 ± 0.05	$1.61 \pm 0.02(0.12)$	$0.61 \pm 0.01(0.04)$	$0.19 \pm 0.01(0.02)$	24	1.3	$3.75 \pm 0.03(0.35)$
SDP 4	1.34 ± 0.05	$0.69 \pm 0.02(0.05)$	$0.28 \pm 0.02(0.03)$	$0.10 \pm 0.02(0.02)$	29	1.0	$1.44 \pm 0.04(0.12)$
SDP 15	0.90 ± 0.03	$0.36 \pm 0.01(0.03)$	$0.14 \pm 0.01(0.01)$	$0.06 \pm 0.01(0.01)$	24	1.1	$0.93 \pm 0.02(0.09)$

Notes: (a) SPIRE fluxes for NGC 2861 were measured manually in an aperture since it is not in the catalogue. (b) These sources were not fully masked in the HPF so their total 160 μm fluxes could be significantly underestimated and were therefore omitted from the analysis.

scopes, so the point-source fluxes in the catalogues may not be representative of the total flux (the *IRAS* PSF has FWHM 0.77, 0.78, 1.44, 2.94′ at 12, 25, 60, 100 μm respectively – Soifer *et al.* 1989). Only the four brightest sources (NGC 4030, 5713, 5719 and 5690) have extended flux measurements in the *IRAS* Revised Bright Galaxy Sample (RBGS; Sanders *et al.* 2003), while extended flux measurements from AKARI have not yet been released. I therefore measured extended-source fluxes in the raw *IRAS* scans using the Scan Processing and Integration Tool (Scanpi)[5], following the procedures outlined by Sanders *et al.* (2003).

I set appropriate input parameters for Scanpi to integrate over scans within the measured 250 μm size (or the default fitting range for a point source, if larger). Multiple scans were combined using a noise-weighted mean, and fits to the resulting co-added scans were inspected visually in the plots output by Scanpi. Fluxes were automatically measured in these scans using four different methods: `peak`, the peak flux in the scan; `amp`, the amplitude of the best-fitting template; `fnu_t`, integrating in a range determined from the fit; and `fnu_z`, integrating between the zero-crossing points. These points are defined as the first point out from the centre, in each direction along the scan, at which the flux falls below -1σ. I followed the recommendations of the Scanpi User Guide[6] to objectively determine the best flux to use for each source and each band, depending on how strongly detected and how extended each was.

Results were inspected visually and with reference to the measurements in the RBGS and the FSC. The agreement was generally very good for the four bright sources in RBGS, though comparing with the FSC, the Scanpi results were generally higher for the most extended sources, as might be expected considering the more accurate source extraction of Scanpi. For unresolved sources, the agreement between Scanpi and FSC was within 15 per cent, which is equal to the systematic errors quoted by Soifer *et al.* (1989). Choices of the flux measurement method were refined in order to improve the agreement with published data.

Only five sources were detected at 12 μm, and 12 at 25 μm, which are insufficient for

[5]Scanpi provided by the NASA/IPAC Infrared Science Archive: `http://scanpiops.ipac.caltech.edu:9000/applications/Scanpi/`

[6]`http://scanpiops.ipac.caltech.edu:9000/applications/Scanpi/docs/overview.html`

Table 4.3: Scanpi results compared with *IRAS* catalogues for 60 and 100 μm.

Galaxy	60 μm flux (Jy)			100 μm flux (Jy)		
	Scanpi		Catalogue	Scanpi		Catalogue
NGC 4030	20.88 ± 3.13	T	18.49 ± 0.05 RT	45.87 ± 6.88	A	50.92 ± 0.12 MT
NGC 5746	2.31 ± 0.35	T	1.33 ± 0.08	10.37 ± 1.56	T	8.88 ± 0.44
NGC 5713	23.74 ± 3.56	T	22.1 ± 0.07 MT	36.55 ± 5.49	A	37.28 ± 0.09 UA
NGC 5690	5.99 ± 0.90	T	6.94 ± 0.03 RT	16.07 ± 2.41	A	16.84 ± 0.12 UA
NGC 5719	8.76 ± 1.31	T	8.61 ± 0.03 UA	17.68 ± 2.66	A	17.96 ± 0.09 UA
NGC 5584	2.32 ± 0.35	T	2.07 ± 0.10	5.28 ± 0.83	T	< 6.05
NGC 5740	2.98 ± 0.45	A	2.66 ± 0.266	6.68 ± 1.03	A	6.62 ± 0.40
NGC 5705	0.50 ± 0.10	A	0.516 ± 0.041	1.42 ± 0.33	A	1.46 ± 0.15
UGC 09215	1.51 ± 0.23	TB	1.15 ± 0.081	2.95 ± 0.46	TB	2.57 ± 0.23
NGC 5496	0.89 ± 0.14	T	0.682 ± 0.109	2.08 ± 0.37	AB	2.18 ± 0.26
NGC 5750	0.62 ± 0.11	A	0.592 ± 0.047	2.40 ± 0.38	A	2.39 ± 0.17
NGC 5691	3.72 ± 0.56	T	3.49 ± 0.21	6.61 ± 1.02	A	6.12 ± 0.37
C 013-010	3.14 ± 0.47	A	3.12 ± 0.22	7.12 ± 1.08	A	7.57 ± 0.53
NGC 3907B	0.70 ± 0.11	A	0.688 ± 0.062	2.18 ± 0.35	A	2.13 ± 0.19
C 018-077	1.30 ± 0.20	A	1.35 ± 0.10	3.29 ± 0.53	A	3.27 ± 0.26
NGC 5478	0.69 ± 0.13	AB	0.636 ± 0.064	1.80 ± 0.39	AB	1.63 ± 0.24
NGC 2861	0.76 ± 0.12	A	0.761 ± 0.053	2.13 ± 0.38	AB	2.24 ± 0.25
SDP 1	2.76 ± 0.42	A	3.06 ± 0.153	4.36 ± 0.67	A	4.42 ± 0.40
SDP 4	0.54 ± 0.09	A	0.53 ± 0.04	1.51 ± 0.27	A	1.50 ± 0.15
SDP 15	< 0.39	B	0.796 ± 0.056	< 0.72	B	1.19 ± 0.15

Notes: The Scanpi measurement method is indicated by the letter following the value: (T) `fnu_t` or (A) `amp`. This is followed by a flag (B) in cases where there was a variable baseline in the scan (which could affect the flux). Where no flux could be measured, a 3-σ upper limit is shown. Catalogue fluxes are from the FSC (Moshir, Kopman & Conrow 1992), except for NGC 5713, 5690, 5719 & 4030, which are from the RBGS (Sanders *et al.* 2003). The latter are flagged as follows: (R) resolved; (M) marginally resolved; (U) unresolved; and the measurement method given by (T/A) as above.

the analysis in this work and so these data were discarded. The 60 and 100 μm results were more successful and are shown in Table 4.3 alongside the catalogue data. Some 60 μm fluxes differ from the catalogues due to extended flux not being detected by the point-source fitting in the FSC. I used the Scanpi measurements at 60 and 100 μm in the analysis described in Section 4.5, adopting a 15 per cent flux calibration error (included in the errors in Table 4.3).

4.3 CO Data

4.3.1 Planning the Observations

The CO(3–2) line at 345.796 GHz (rest-frame) was observed with the HARP receiver array on the JCMT, with a HPBW of 14″, and the CO(2–1) line at 230.538 GHz was

observed with the RxA single receiver, with a HPBW of 21″. Integration times were calculated by estimating the CO line intensity from the 250 μm surface brightness, assuming a correlation similar to the SK law, and calculating the RMS antenna temperature required to detect the line after integrating across the velocity width. Integration times were typically around 30 minutes per source.

HARP is an array of 16 heterodyne receivers arranged in a 4×4 square grid with a field of view of 1.5 arcminutes, and spacing of 0.5 arcminutes, or roughly twice the HPBW. Receivers are arranged so that 16 pointings in a square grid at offsets of 7.5″ will produce a map of 16×16 pixels, each with a size of 7.5″, covering a $2 \times 2'$ field of view and providing Nyquist sampling of the source. This is achieved by the standard jiggle pattern "HARP4", which moves the telescope's secondary mirror to produce the successive offsets of 7.5″, and is ideal for mapping the majority of the sample, which have sizes of the order of one arcminute. For NGC 5690 and NGC 5584 it was necessary to use two HARP pointings to cover the whole of each galaxy. RxA is only a single receiver so extended sources were observed with a grid designed to cover the whole galaxy, while more compact sources were sufficiently covered by smaller jiggle patterns. The pixel size in these maps is 10″.

Galaxies were mapped in this way to capture the global flux from the entire emitting region, but since the purpose was not to investigate the distribution of CO, the integration times for most objects were chosen so that a detection would be obtained after integrating within an aperture covering the galaxy. For galaxies which were suitably extended and had high surface brightness (NGC 5713, NGC 5719, NGC 5690, NGC 5740, NGC 3907B and CGCG 018-077), the integration times were chosen to obtain a map of the CO emission region after binning pixels in 2×2 squares, since this could be done within a relatively short time.

4.3.2 Data Reduction

Calibrated data from the telescope take the form of three-dimensional timelines (receiver $\times$ sample $\times$ spectrum) and were reduced using the STARLINK software pack-

age,[7] following the steps described by the ACSIS Data Reduction Cookbook.[8]

The timeline data were cleaned to remove spikes, noisy receptors, bad baselines and noisy channels in the spectra, before combining timelines into data-cubes for each galaxy (2-dimensional maps with a third spectral dimension in each pixel). All spectra were de-spiked by masking individual channels with a $> 5\sigma$ spike surrounded by $< 2.5\sigma$ levels in the adjacent 6 channels. Individual receptors were masked in some of the HARP maps if they were especially noisy (due to high system temperatures) or had bad baselines that couldn't be adequately fitted (details are given below for each galaxy). In addition, one of the receptors (H14) was masked in all of the data because it was not operational at the time. A number of channels at the ends of all the spectra had to be masked due to end ringing, which can easily bias baseline fits if not carefully removed. In order to remove this (while retaining sufficient bandwidth for a baseline fit that is independent of any emission), 160 channels were clipped from each end of all HARP spectra and 300 from each end of all RxA spectra.

Baseline fitting is an important part of the procedure for obtaining accurate line intensities, by removing any continuum emission and other undesired contributions to the measured flux across the spectrum. This was done independently in each receptor and sample of the timeline by fitting a first-order polynomial to a masked spectrum. The spectrum was masked to remove any possible line emission within either one FWHM either side of the line centre (using the FWHM of the CO line or H I line from the literature), or $300\,\mathrm{km\,s^{-1}}$ either side of the line centre where no literature data were available.

4.3.3 Measuring Integrated Line Intensities

Line intensities were measured by integrating over the velocity range of the line and the spatial extent of emission. Since in most cases the signal-to-noise was only sufficient to detect the line after integrating the data in this way, this involved some iteration in order to maximise the signal while minimising background noise. Initial estimates of

[7] `http://starlink.jach.hawaii.edu/starlink`

[8] `http://www.jach.hawaii.edu/JCMT/spectral_line/data_reduction/acsisdr/`

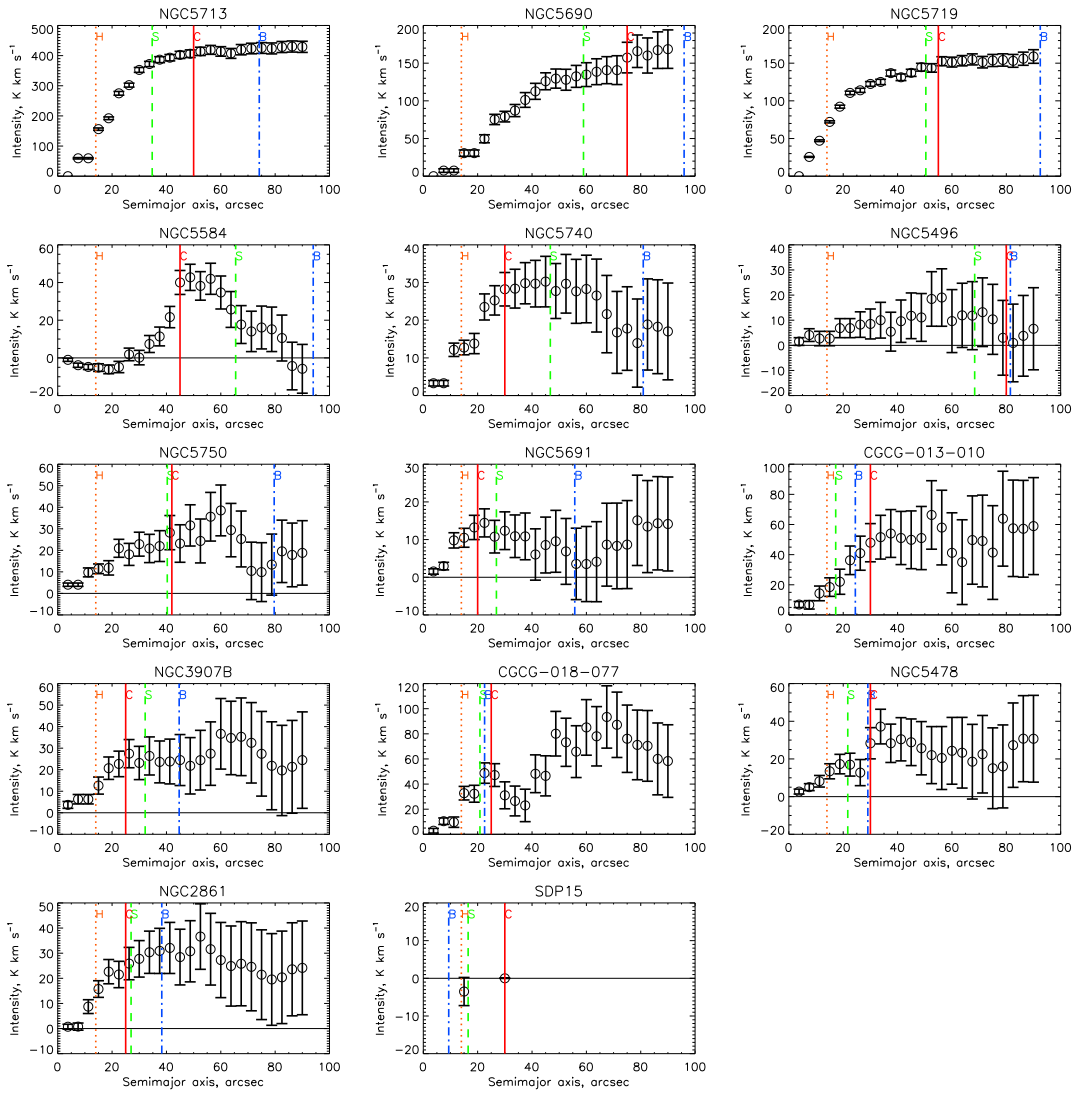

Figure 4.3: Integrated intensity of the CO(3–2) line as a function of aperture semimajor axis, for each of the galaxies mapped with HARP. Vertical lines: blue dot-dashed line (B) marks semimajor axis of B-band d_{25} isophote; orange dotted line (H) marks FWHM of HARP beam; cyan dashed line (S) marks semimajor axis of SPIRE Kron ellipse; red solid line (C) marks semimajor axis estimated to enclose all CO emission.

the line widths were based on the H I 21 cm line measured in the HIPASS cubes (see Section 4.4) and on ancillary CO data where available (see Table 4.4). The implicit assumption in comparing with the H I is that the maximal rotation speed or velocity dispersion of the molecular gas should not exceed that of the atomic gas; this is a safe assumption since in general atomic gas is more widespread throughout a galaxy than CO. The width used for integrating the CO line was reduced if it was obvious that it was narrower than the H I, in order to minimise noise.

Initially, the cubes were integrated across the chosen velocity window, and then the

Table 4.4: Details of the CO line measurements: radial velocity, cz; line widths for H I, CO(1–0) from NRO data, and CO measurements in the literature (see notes); line width measured in integrated spectra from cubes; elliptical aperture axis ratio a/b and position angle; semimajor axis used in HARP cube; total intensity (or 3σ limit) and signal-to-noise ratio; semimajor axis used in RxA cube; total intensity (or 3σ limit) and signal-to-noise ratio.

		Line width ($\mathrm{km\,s^{-1}}$)				Aperture		HARP cube CO(3–2)			RxA cube CO(2–1)			Line ratio
Galaxy	cz [a]	H I [b]	CO(1–0)[c]	Lit.[d]	Cube	a/b	P.A.	a_{32}	I_{32}	SNR	a_{21}	I_{21}	SNR	R_{32}
							$^\circ$ E of N	$''$	$\mathrm{K\,km\,s^{-1}}$ $(T_A^\star)$		$''$	$\mathrm{K\,km\,s^{-1}}$ $(T_A^\star)$		
NGC 4030	1465	413	474	360 [1]		1.2	33	53	490.3 ± 33.0[e]					
NGC 5746	1723	633 [L]	227			8.5	170							
NGC 5713	1899	390 [B]	248	140 [2]	200	1.0	27	50	405.2 ± 13.1	30.8	40	496.2 ± 31.4	15.8	0.82 ± 0.07
NGC 5690	1732	374	247	243 [3]	350	2.7	144	75	157.4 ± 20.3	7.8	45	197.3 ± 32.2	6.1	0.80 ± 0.21
NGC 5719	1756	660 [B]	516	400 [4]	460	2.3	112	55	149.3 ± 5.9	25.4				
NGC 5584	1652	267	165	136 [5]	220	1.6	149	45	40.0 ± 6.4	6.3				
NGC 5740	1579	413	350		320	1.7	163	30	28.2 ± 4.4	6.4				
NGC 5705	1732	320				1.5	47							
UGC 09215	1313	466				1.7	162							
NGC 5496	1559	373			370	3.8	173	80	<44.7		80	53.5 ± 20.9	2.6	<0.83
NGC 5750	1612	640	309		600	1.6	71	42	44.0 ± 12.3	3.6	80	<141.6		>0.31
NGC 5691	1879	214			210	1.3	101	20	14.3 ± 3.4	4.2	35	59.7 ± 12.2	4.9	0.24 ± 0.31
C 013-010	11843				220	2.0	144	30	47.9 ± 12.7	3.8	20	17.4 ± 7.0	2.5	2.76 ± 0.48
NGC 3907B	6228	408 [L]	497		400	2.2	72	25	25.8 ± 6.4	4.1	0			
C 018-077	7707	550	502		550	3.1	87	25	47.2 ± 9.1	5.2	25	<45.9		>1.03
NGC 5478	7505	430	501		380	1.2	19	30	28.3 ± 8.3	3.4	30	81.7 ± 12.8	6.4	0.35 ± 0.33
NGC 2861	5085		214		180	1.1	165	25	24.5 ± 6.2	3.9				
SDP 1	16072	240 [L]	563		400	1.3	45				20	45.4 ± 6.8	6.7	
SDP 4	8281				450	1.1	79				0	3.6 ± 0.5	8.0	
SDP 15	16326		316			1.1	20	30	<11.1		0	<1.8		

Notes: (a) Radial velocities are the centre of the H I line and agree with the centre of the CO line in HARP and RxA. (b) H I data labelled (L) are from HyperLEDA, and (B) from the HIPASS BGS (Koribalski *et al.* 2004); otherwise they are from the HIPASS cubes – see Section 4.4. (c) The CO(1–0) column contains line widths measured in spectra of the central regions of galaxies in the sample; these data are single-beam ($15''$ HPBW) pointings from the Nobeyama Radio Observatory (NRO), courtesy of Lerothodi Leeuw (private communication). (d) References for literature data: (1) Young *et al.* (1995); M.W.L. Smith et al. in prep. (2) Young *et al.* (1995); Yao *et al.* (2003); Albrecht, Krügel & Chini (2007). (3) Sauty *et al.* (2003). (4) Albrecht, Krügel & Chini (2007). (5) Sauty *et al.* (2003); Böker, Lisenfeld & Schinnerer (2003). (e) CO(3–2) measurement for NGC 4030 from the HRS data (Matthew W. L. Smith, private communication).

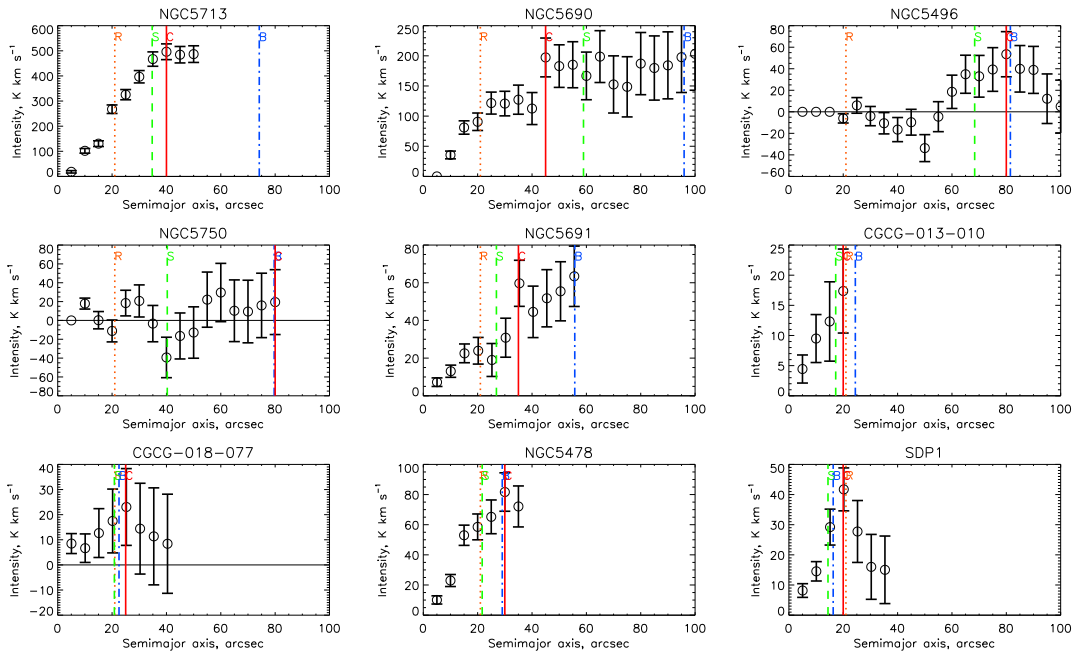

Figure 4.4: Integrated intensity of the CO(2–1) line as a function of aperture semimajor axis, for each of the galaxies mapped with RxA. Vertical lines: blue dot-dashed line (B) marks semimajor axis of B-band d_{25} isophote; orange dotted line (R) marks FWHM of RxA beam; cyan dashed line (S) marks semimajor axis of SPIRE Kron ellipse; red solid line (C) marks semimajor axis estimated to enclose all CO emission.

total intensities were measured in apertures. To define the apertures I first looked at the SPIRE 250 μm images, which I fitted with SExtractor (Bertin & Arnouts 1996) to find the Kron ellipse and FWHM ellipse, thus measuring the shape and orientation of the best-fitting elliptical profile, as well as some measure of the radius of this profile. The 250 μm images were used rather than the optical ones because the intrinsic distribution of molecular gas is more likely to trace the dust than the stars, and because the SPIRE 250 μm beam is of a similar size (18″ FWHM) to the HARP and RxA beams (14″ and 21″ respectively), so that the smearing of the true profile by the beam is similar in SPIRE, HARP and RxA images.

If the molecular gas distribution were to follow the dust exactly then it would be simple to integrate the intensity within an aperture of radius equal to either the SPIRE effective radius, FWHM or Kron radius, to obtain approximately 50, 90 or 100 per cent of the flux respectively. In fact, summing within fixed apertures in this way gives variable results: for some sources the aperture collects only a small fraction of the emission, for others it contains too much empty sky background which increases the noise. It is therefore necessary to make a more informed estimate of the gas distribution, which

can be done by trying a range of aperture sizes and plotting a curve of growth, showing the cumulative aperture flux as a function of radius. This was done by fixing the axis ratio and position angle of the aperture ellipse using the SPIRE profile fit, assuming that to first order this represents the shape of the CO emission region. This was necessary to reduce the number of degrees of freedom, otherwise it would be impossible to reliably choose the correct aperture.

I scaled these apertures to a range of radii (with increments of half a pixel in the RxA and HARP maps) and obtained curves of growth of the integrated intensity as a function of semimajor axis (a), shown in Figures 4.3 and 4.4. Using these I selected the optimal aperture for each source, by picking the smallest aperture that was necessary to contain the total emission. Where no detection was obtained I calculated 3σ upper limits using the error in an aperture equal to the optical size. Errors were calculated by integrating within the chosen aperture on a variance map, in which the variance of each pixel is calculated from the wings of the baseline-subtracted spectrum, masking out the expected velocity range of any emission, given by the line widths in Table 4.4.

I plotted the integrated spectra within these apertures, considering CO(3–2) and CO(2–1) spectra together where both were available, and used these to define the final velocity windows to integrate the CO emission over. Spectra were rebinned to both 20 and 40 $\mathrm{km\,s^{-1}}$ resolution to check that the velocity width was appropriate. Where the spectra were too noisy to tell the true line width, I used the H I spectrum to define the line edges; otherwise I changed the edges only where it was clear that the CO line was narrower than the H I. In either case I defined the line edges as the zero-crossing points measured on the relevant spectrum. In SDP1 the CO line appears to be broader than the H I; it is unusual for molecular gas to be more widespread than atomic gas in a galaxy, but this source is a known merger so in this case the broad CO line is plausible. Results are summarised in Table 4.4, in comparison to CO line widths from the literature. These latter may be narrower than in the HARP and RxA cubes because they are single-beam measurements containing only the central regions. H I line widths can differ in general because they trace a different gas component, although in the case of NGC 5713 and NGC 5719 the HIPASS spectra are blended because the two sources are confused in the Parkes beam and are at similar radial velocities.

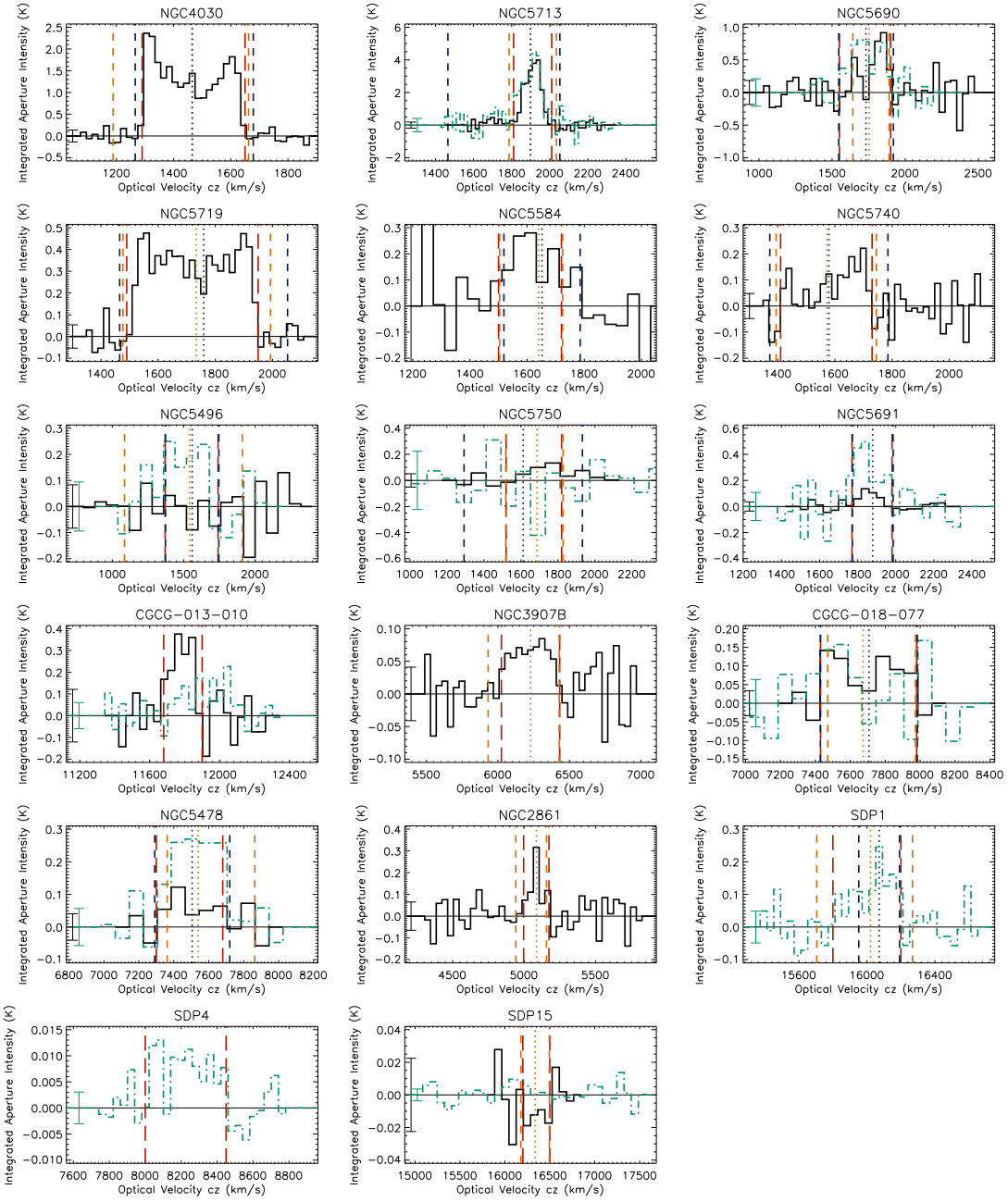

Figure 4.5: Spectra of the CO(3–2) (black solid line) and CO(2–1) (green dashed line) lines integrated across the chosen apertures and rebinned to either 20, 40 or 80 $\mathrm{km\,s^{-1}}$ resolution. Blue dashed vertical lines = H I line width from HIPASS; orange = CO line width from literature; red = total CO width used for measuring integrated flux.

I repeated the process of measuring curves of growth and selecting apertures and velocity windows to integrate over, until I was sure that I had measured the total CO intensities with the best possible signal-to-noise. Details of the apertures and integrated intensities are shown in Table 4.4. Some of the cubes produced fluctuating curves of growth that did not increase cumulatively, or increased outside of the region

of expected emission, as a result of bad baseline subtraction leaving artificial negative or positive signal in the maps. In most cases these were removed by masking noisy receptors or pixels and/or modelling the baseline as a second order polynomial (higher orders were not attempted due to the limited bandwidth available to fit baselines to). The HARP cube of NGC 5584 has the worst residual baselines that could not be adequately subtracted; this is clear from the curve of growth which falls with increasing radius. A total intensity was measured in a large aperture, but since many pixels in the map appear to have some small negative intensity, the measurement is considered unreliable, and will be excluded from statistical analysis. Some of the other curves of growth show either rising or falling aperture measurements at high radii, but most are within the errors indicating that any uncertainties in the baseline are covered by the error bar quoted. The HARP cube of CGCG 018-077 shows a jump of 2σ at around $50''$, well outside of the optical and sub-mm emission region. This is due to bad baselines in the outer part of the cube, but visual inspection of the raw and processed cubes indicates that the baselines in the centre have been adequately subtracted, and so the aperture measurement used is reliable.

Appendix D contains comments on individual galaxies, together with images of the optical and sub-mm emission, and integrated flux (zeroth moment) maps. Figure 4.5 shows CO(3–2) and CO(2–1) spectra integrated within the chosen apertures and smoothed to reveal the detected emission lines.

4.4 HI Data

4.4.1 Catalogues

Most of the objects in the sample have H I 21 cm line detections in the literature, which are useful both for the kinematics (velocity range/line width) and for probing the atomic gas mass. Data from many surveys are collected in the HyperLEDA database, which lists H I magnitudes for 15 of the sample. In addition, many of the sample have been covered by the H I Parkes All-Sky Survey (HIPASS; Barnes *et al.*

2001). The HIPASS tables were searched using the Vizier catalogue server[9], revealing two matches in the HIPASS Bright Galaxy Sample (Koribalski *et al.* 2004), seven in the main HIPASS catalogue (HICAT; Meyer *et al.* 2004), and one in the Northern HIPASS catalogue (NHIPASS; Wong *et al.* 2006). Data are shown in Table 4.5.

It is clear that there are discrepancies between the HyperLEDA and HIPASS fluxes for some sources, the worst being NGC 5719 and NGC 4030. This is because the homogenised photometry in HyperLEDA has been combined from a wide range of sources. For example, the H I flux of NGC 5719 is based on a combination of 10 different references, with individual flux measurements ranging from $15 - 106\,\mathrm{Jy\,km\,s^{-1}}$, measured on a variety of telescopes, and NGC 4030 similarly has 10 separate measurements ranging from $31 - 72\,\mathrm{Jy\,km\,s^{-1}}$. Measurements on different telescopes can vary depending on the uncertainty of the absolute flux calibration for each, whether the source is fully sampled by the telescope beam, and whether nearby galaxies at the same redshift are blended within a single beam.

The average HPBW in HIPASS (observed on the Parkes telescope in multi-beam mode) is 14.3′ (Barnes *et al.* 2001), so all sources in the sample are point sources. A search of NED revealed that some of the sources are potentially blended with others at the same redshift. NGC 5713 and NGC 5719 are close enough to be slightly confused, with an angular separation of 11.3′ and nearly equal redshifts. NGC 5740 and NGC 5746 are also close together, with an angular separation of 18.3′ and radial velocity offset of about $150\,\mathrm{km\,s^{-1}}$. NGC 4030 is 16.7′ away from UGC 07000 at the same redshift, but this galaxy is 3 magnitudes fainter in the optical and has an H I flux of $5.9\,\mathrm{Jy\,km\,s^{-1}}$ in HyperLEDA (6 times fainter than the HyperLEDA flux of NGC 4030), so it will not significantly bias the NGC 4030 measurement. For NGC 5713 and NGC 5719, therefore, the HyperLEDA fluxes may be more reliable since they combine data from telescopes with smaller beam sizes, including the Arecibo 305m dish and the NRAO Green Bank 91m dish. The same can also be said of NGC 5740 (which is much fainter than NGC 5746), but for the others the HIPASS measurements are reliable.

The best solution to obtain directly comparable results for a sample is to draw data from

[9] Vizier hosted by CDS, Strasbourg: `http://vizier.u-strasbg.fr/viz-bin/VizieR`

Table 4.5: Compilation of H I line measurements from HyperLEDA, HIPASS catalogues and HIPASS cubes, with self-absorption corrections (see notes below).

Galaxy	HyperLEDA			HIPASS catalogues			HIPASS cubes			Self-absorption correction				
	$v_{\rm rad}$	Δv	$S_{\rm H\,I}$	$v_{\rm rad}$	Δv	$S_{\rm H\,I}$	$v_{\rm rad}$	Δv	$S_{\rm H\,I}$	$i(^\circ)$	t	c	$f_{\rm H\,I}$	$S_{\rm H\,I}^{\rm corr}$
NGC 4030	1463	295	37.9 ± 1.6	1465	441	**72.0 ± 0.9**	1465	413	56.9 ± 1.5	40	4.0 ± 0.2	0.04	1.01 ± 0.01	72.8 ± 7.4
NGC 5746	1723	633	**26.3 ± 1.4**				1724	721	29.7 ± 1.5	84	3.0 ± 0.3	0.04	1.09 ± 0.09	28.7 ± 3.3
NGC 5713	1899	160	**35.8 ± 1.8**	1899	390	48.8 ± 5.1^B	1899	587	73.6 ± 1.4	48	4.0 ± 0.3	0.04	1.02 ± 0.02	36.5 ± 4.1
NGC 5690	1753	266	19.88 ± 0.68	1754	398	**25.6 ± 0.5**^{N}	1753	374	21.89 ± 0.89	76	5.4 ± 0.5	0.16	1.25 ± 0.25	32.1 ± 7.3
NGC 5719	1732	355	**31.7 ± 1.5**	1756	660	68.3 ± 5.1^B	1733	587	74.0 ± 1.2	71	2.4 ± 0.6	0.00	1.00 ± 0.00	31.7 ± 3.5
NGC 5584	1638	166	21.76 ± 0.92	1638	280	**27.1 ± 0.4**	1638	267	25.54 ± 0.62	42	6.0 ± 0.3	0.14	1.04 ± 0.04	28.3 ± 3.1
NGC 5740	1571	308	**21.90 ± 0.88**	1572	409	33.3 ± 0.5	1572	413	29.63 ± 0.80	55	3.0 ± 0.4	0.04	1.02 ± 0.02	22.3 ± 2.4
NGC 5705	1760	168	18.7 ± 1.2	1758	279	**27.9 ± 0.4**	1758	320	26.25 ± 0.72	65	6.5 ± 1.1	0.14	1.13 ± 0.13	31.5 ± 4.8
UGC 09215	1389	162	16.3 ± 1.0	1387	296	**23.7 ± 0.5**	1397	280	21.12 ± 0.57	64	6.4 ± 0.9	0.14	1.12 ± 0.12	26.6 ± 4.0
NGC 5496	1541	212	39.4 ± 1.4	1541	335	**60.9 ± 0.5**	1541	373	56.72 ± 0.73	82	6.5 ± 0.8	0.14	1.32 ± 0.32	80.3 ± 21.0
NGC 5750	1687	374	5.17 ± 0.30				1687	640	**13.8 ± 1.1**	66	0.4 ± 0.9	0.00	1.00 ± 0.00	13.8 ± 1.7
NGC 5691	1871	130	7.66 ± 0.28	1881	219	**5.5 ± 0.3**	1870	213	5.63 ± 0.71	44	1.2 ± 0.6	0.00	1.00 ± 0.00	5.5 ± 0.6
C 013-010	11843						11843	500	<**5.07**	65	1.5 ± 2.9	$0.00^{+0.04}_{-0.00}$	$1.00^{+0.04}_{-0.00}$	<5.07
NGC 3907B	6252	408	**3.28 ± 0.12**				6228	500	<5.81	84	3.1 ± 0.4	0.04	1.09 ± 0.09	3.6 ± 1.0
C 018-077	7676						7674	500	**5.44 ± 0.93**	74	6.0 ± 2.0	$0.14^{+0.02}_{-0.10}$	1.20 ± 0.20	6.5 ± 1.8
NGC 5478	7530						7539	430	**6.03 ± 0.78**	49	3.6 ± 0.6	0.04	1.02 ± 0.02	6.1 ± 1.0
NGC 2861	5134	120	**2.49 ± 0.09**				5086	500	<6.22	25	3.7 ± 0.6	0.04	1.00 ± 0.00	2.5 ± 0.3
SDP 1	9174	240	**0.53 ± 0.09**							42	0.4 ± 5.0	$0.00^{+0.16}_{-0.00}$	$1.00^{+0.05}_{-0.00}$	0.5 ± 0.1
SDP 4	8281						8241	500	<**4.82**	75	0.1 ± 2.0	0.00	1.00 ± 0.00	<4.82
SDP 15	16326									28	4.5 ± 5.0	$0.04^{+0.12}_{-0.04}$	$1.00^{+0.02}_{-0.00}$	

Notes: All fluxes are $\mathrm{Jy\,km\,s^{-1}}$; the final flux used for analysis is highlighted in boldface. HyperLEDA fluxes are calculated from magnitudes in the database using $\log S_{\rm H\,I} = (17.4 - m)/2.5$. HIPASS catalogue fluxes are from HICAT except where marked B (BGC) or N (NHIPASS). Radial velocities (cz, $\mathrm{km\,s^{-1}}$) from HyperLEDA are taken from the radio measurements (the `Vrad` parameter), while the line width (Δv) is estimated from the maximum velocity of the gas (`Vmaxg`$\times 2$). Velocities from the HIPASS catalogues are given by the `Vsys` or `RV50max` keywords, and widths are `RV2` – `RV1` (which generally exceeds `Vmaxg`$\times 2$). Fluxes were measured in the HIPASS cubes between the zero-crossing points, and where no line was detected a 5σ upper limit was measured assuming a width of $500\,\mathrm{km\,s^{-1}}$. Corrections for H I self-absorption ($f_{\rm H\,I}$) are given by equation (4.2), as a function of inclination angle i and de Vaucouleurs type t, following Haynes & Giovanelli (1984). Errors on $f_{\rm H\,I}$ include both the uncertainty on t (from HyperLEDA) and a 100% uncertainty on the self-absorbed fraction (see text). Errors on the final corrected fluxes ($S_{\rm H\,I}^{\rm corr}$) include the error on $f_{\rm H\,I}$ as well as measurement errors from on the flux and a 10% calibration error added in quadrature.

a single survey, which will have been measured on the same telescope at similar times, and reduced and calibrated in a self-similar way. I therefore opted to use H I fluxes from HIPASS as a priority, with the three exceptions noted above. For the brightest sources these were available from the catalogues, as shown in Table 4.5, while additional data for all sources were obtained from the public HIPASS archive as described below.

4.4.2 HIPASS 3-d Data

The full HIPASS dataset is publicly available to query and download via the ATNF H I Gateway[10]. This can be used to obtain spectra at any position within the surveyed areas, and measure line fluxes where they are detected. The spectra extend to a maximum radial velocity of $cz = 12,000\,\mathrm{km\,s^{-1}}$, so the two sources at $z > 0.04$ (SDP 1 and SDP 15) are not covered. All other galaxies in the sample are covered within this dataset.

I downloaded data cubes of the relevant survey areas, and used the MBSPECT routine in the MIRIAD software package[11] to measure point-source spectra at the required positions. The low resolution of the map compared to the size of the galaxies means that they will be point sources. A source can still be between pixels, however, so MBSPECT samples all pixels within a 5×5 box to produce a weighted spectrum representative of a point source at the requested position.

First-order polynomial baselines were subtracted from the spectra (except for NGC 2861, NGC 5478, CGCG 018-077 and SDP 4, which required fourth-order fits), and lines were measured between the zero-crossing points, as shown in Figure 4.6. Results are compared to the HIPASS catalogue results in Table 4.5. In general the results obtained from the cubes are similar to those in the HIPASS catalogues, with three notable exceptions. NGC 5713 and NGC 5719 are blended and at the same velocity, so the measured fluxes will depend on the pixels included in the weighted spectrum and on the line range chosen. The flux measurements in the HIPASS catalogues have not been deblended, but these galaxies were fitted as point sources so blended flux from the

[10] ATNF H I Survey Gateway hosted by CSIRO, Australia: `http://www.atnf.csiro.au/research/HI/hipass/`

[11] Available from `http://carma.astro.umd.edu/miriad/`

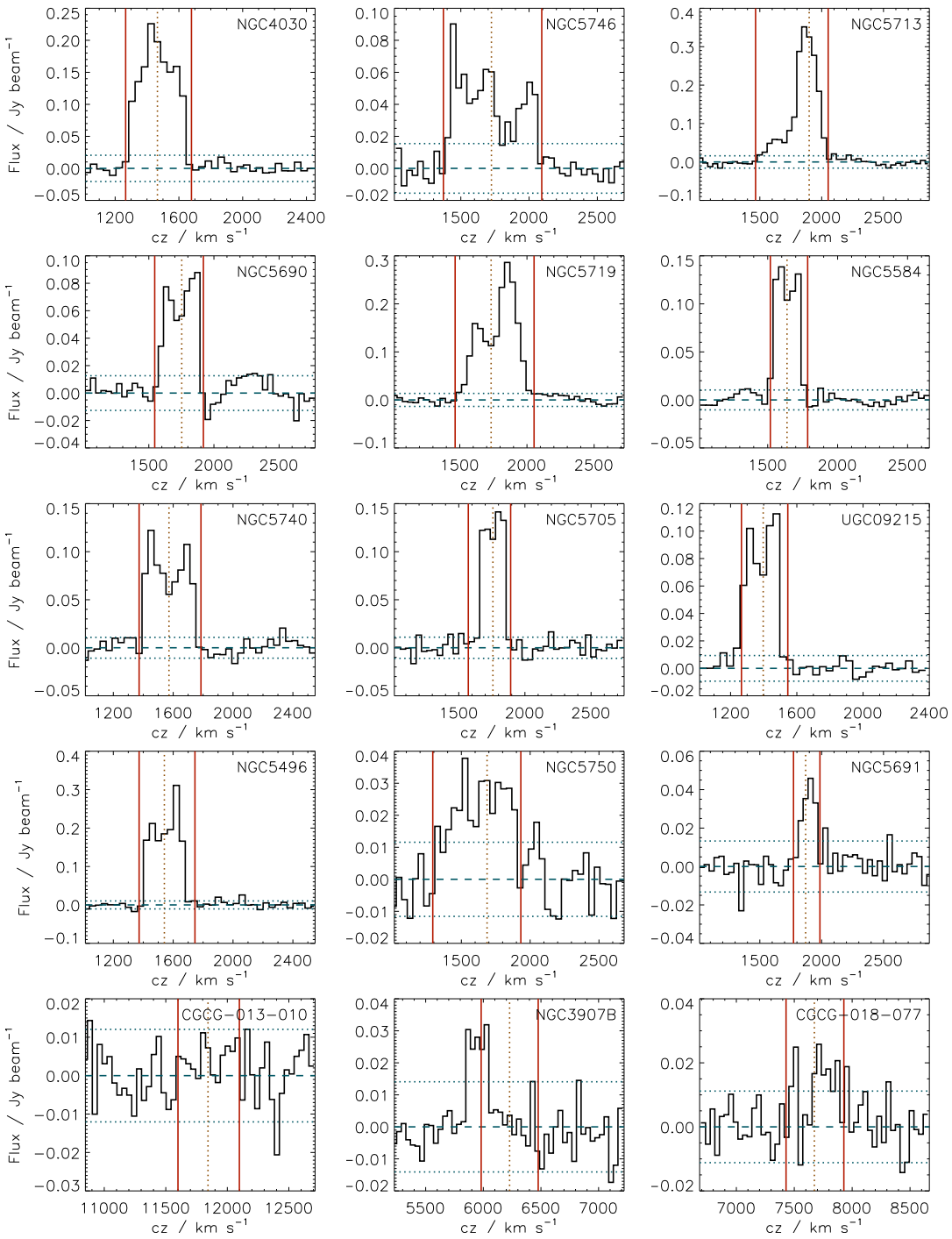

Figure 4.6: Baseline-subtracted spectra extracted from the HIPASS cubes at the positions of galaxies in the sample. Spectra are rebinned to 40 $\mathrm{km\,s^{-1}}$ resolution. The predicted centre of the line (given by the galaxy's redshift from NED) is marked as a dotted brown line. Red lines indicate the range between the zero-crossing points that is integrated to measure the total flux, or, for undetected sources, the range over which the 5-σ upper limit was measured. The turquoise horizontal lines mark the baseline-subtracted continuum level (i.e. zero) and the $\pm1\sigma$ RMS levels in the *raw* spectrum (measured in the wings of the spectrum outside the line). Note the similarity in the velocity range of emission in the NGC 5713 and NGC 5719 spectra, and also NGC 5746 and NGC 5740. This is due to the blending of these two pairs of galaxies in the HIPASS beam. Note that there is a detected emission line in the spectrum of NGC 3907B, but this is actually NGC 3907, which also falls within the beam but is at a slightly lower redshift. Figure continues on the next page.

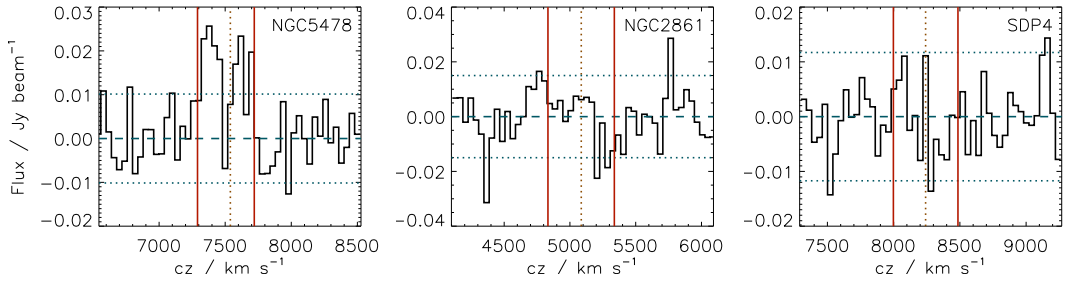

Figure 4.6 continued.

neighbouring source should have been minimised (see Meyer *et al.* 2004). The flux between the zero-crossing points in Figure 4.6 is certainly an overestimate in these cases, but the BGC measurements used a smaller velocity range so are likely to be more reliable. The third exception is NGC 4030, which is not significantly blended (as discussed in the previous section), neither is it extended relative to the HIPASS beam, so it is unclear why my measurement misses 20 per cent of the flux reported in HICAT.

NGC 5746 could be blended with NGC 5740 (as discussed above), although being the brighter of the two its flux isn't greatly biased (c.f. HyperLEDA flux in Table 4.5). The measured flux of NGC 5750 on the other hand is significantly higher than that in HyperLEDA, but this discrepancy cannot be accounted for by confusion. The nearest neighbour at the same redshift is LCSB F0044N (using NED), which is at 14.3′; this galaxy is 3 magnitudes fainter in the optical and has no H I measurement in HIPASS or HyperLEDA so is unlikely to be bright enough to significantly bias the measurement of NGC 5750.

To summarise, I used HIPASS catalogue measurements where they were available and not blended, and measured fluxes in the HIPASS cubes for sources not in the catalogues. I used HyperLEDA fluxes for galaxies that were not detected in the cubes or were blended in the Parkes beam. This left two sources with only upper limits from the cubes, and one with no data at all.

4.4.3 HI Self-Absorption Corrections

H I fluxes and masses will be underestimated if there is sufficient optical depth in the line of sight for H I clouds in the source galaxy to absorb emission from those behind

them. This optical depth can depend on the inclination of the galaxy, its morphological type, velocity dispersion and the thickness of the H I disk (e.g. Heidmann, Heidmann & de Vaucouleurs 1972), and also on the column density of individual H I clouds (Braun 2012). Self-absorption is often ignored or assumed negligible in the literature (e.g. HIPASS, Barnes *et al.* 2001; ALFALFA, Giovanelli *et al.* 2005; THINGS, Walter *et al.* 2008; GASS, Catinella *et al.* 2010), although HyperLEDA includes estimates of the attenuation due to self-absorption, following Heidmann, Heidmann & de Vaucouleurs (1972). Some of the galaxies in this sample are highly inclined and all are dust-rich, so the density of gas is likely to be high. It is therefore prudent to consider the possibility of H I self-absorption (and especially the uncertainty that this introduces) which could affect measured correlations between the H I flux and optically thin emission such as FIR and sub-mm.

Various approaches have been used to correct measured fluxes for self-absorption. Heidmann, Heidmann & de Vaucouleurs (1972) used observed H I column densities of 64 galaxies combined with geometrical arguments to derive a correction as a function of inclination angle i for a thin disk, obtaining correction factors up to 1.4 for $i < 85°$. However, they argued that for real galaxies with typical values for the scale height and velocity dispersion of H I, the correction would be less severe, and derived factors up to 1.19 for $i < 85°$. Inclination angles for the current sample are listed in HyperLEDA, and range from 25 to 85°. Using Heidmann, Heidmann & de Vaucouleurs's predictions, two of our sample (NGC 5746 and NGC 3907B) have correction factors of 1.19; all others are less than 1.10.

Haynes & Giovanelli (1984) took an empirical approach and derived correction factors as a function of axis ratio for various morphological types, using 21 cm observations of 1500 galaxies to measure the relationship between surface brightness of the line and axis ratio. The correction factor applied to measured fluxes is given by

$$f_{\mathrm{H\,I}} = r_i^{-c} \tag{4.2}$$

where $r_i \equiv \cos i$ is the observed axis ratio, and c varies from -0.02 to 0.16 depending on morphological type t (de Vaucouleurs *et al.* 1991). Using this formula, and type information from HyperLEDA, the two aforementioned galaxies have corrections of only 1.09 (because they are early-type spirals), while the correction factors for three highly

inclined late-type spirals are higher (1.20 for CGCG 018-077; 1.25 for NGC 5690; 1.32 for NGC 5496).

Lang *et al.* (2003) advocated even higher correction factors, which they argued were necessary to account for the observed H I mass function and the relative dearth of high inclination angles ($i \gtrsim 74°$) in the blind H I Jodrell All-Sky Survey (HIJASS). Those authors used the functional form of equation (4.2), but did not consider any dependence on morphological type, due to their smaller sample size (186 of their 222 detections had measured inclination angles). They used a subset of their sample with $i > 50°$ (105 galaxies) to derive the slope of this function, obtaining a value $c = 0.2$ steeper than those derived by Haynes & Giovanelli (1984), although the uncertainty on this value is large due to Poisson counting errors in their inclination bins. Following Lang *et al.* (2003), the five galaxies in the sample with $i > 74°$ have correction factors between 1.3 and 1.6.

In conclusion, the self-absorption corrections are uncertain, but unlikely to be negligible as is often assumed. The corrections proposed by Haynes & Giovanelli (1984) are based on empirical fits to a large sample and take into account morphological type as well as inclination angle, so I take these to be the most reliable. I apply corrections to galaxies in the sample with t-types between 3 (Sb) and 8 (Sdm), and to account for the scatter between different estimates of the correction, I conservatively allow a 100% error on the estimated self-absorbed fraction itself (i.e. a correction of 1.3 has the error ± 0.3, such that the error bar encompasses a null correction). Details of the corrections are shown in Table 4.5.

4.5 Analysis

4.5.1 Correlations between Global Fluxes

The aim of this project is a comparison between the gas and dust properties of this sample of local galaxies selected from H-ATLAS. As discussed in Section 4.1.2, it is known that the CO line intensity is correlated with FIR fluxes as a result of the SK law, and correlations have also been observed in the sub-mm in low-redshift galaxies

(Dunne *et al.* 2000; Yao *et al.* 2003; Corbelli *et al.* 2012; Wilson *et al.* 2012) and high-redshift SMGs (Greve *et al.* 2005; Iono *et al.* 2009; Engel *et al.* 2010; Magdis *et al.* 2011; Bothwell *et al.* 2012). The current sample is novel because it was selected from a blind survey at 500 μm, so is selected on cold dust mass rather than FIR luminosity or SFR (see Section 4.1.3). Since this sample has excellent coverage of the IR SED, one can explore whether there is a correlation between the CO lines and IR fluxes at various wavelengths, what the slope and scatter in this correlation are, and whether they vary systematically with the wavelength of the IR band (i.e. between the FIR, at $\lambda \lesssim 200\,\mu$m and the sub-mm at $\lambda \gtrsim 200\,\mu$m).

Figure 4.7 compares the global fluxes in the CO lines to the global fluxes in the IR from 60 to 500 μm, and to the H I fluxes described in Section 4.4. The total integrated intensities ($\mathrm{K\,km\,s^{-1}}$ $T_A^\star$) in Table 4.4 have been converted to flux in $\mathrm{Jy\,km\,s^{-1}}$ using

$$S_{\mathrm{CO}} = \frac{2k_B \Omega I_{\mathrm{CO}}}{\eta_{\mathrm{mb}} \lambda^2} \tag{4.3}$$

(e.g. Rohlfs & Wilson 2006), where η_{mb} is the main-beam efficiency of the telescope (which corrects for emission scattered outside of the central peak of the beam), which is taken to be 0.63 for HARP and 0.69 for RxA, following the JCMT Guide to Spectral Line Observing[12]. In this equation, Ω is the solid angle (in steradians) over which the intensity is averaged; for point sources measured in a single beam (i.e. SDP4 and SDP15 in RxA) this is the beam area, but the majority of sources are extended and measured in apertures. For these the relevant solid angle is the pixel area, which is (7.5 arcsec)^2 for HARP and (10.0 arcsec)^2 for RxA maps.

The flux measurement for NGC 5584 is included on the plots for comparison (the circled point), but due to poor baseline subtraction in the cube the errors on this point are likely to be larger than the error bar shown (which is estimated from the RMS measured in each pixel of the cube). Moreover, the curve of growth shows that both large and small apertures contain negative flux, suggesting that the total flux measured may be significantly underestimated if many pixels have residual negative baselines. For this reason, the CO(3–2) flux of NGC 5584 is excluded from the correlation analysis in this section.

In Figure 4.7, correlations clearly exist between the fluxes in both CO lines and all IR

[12] `http://www.jach.hawaii.edu/JCMT/spectral_line/`

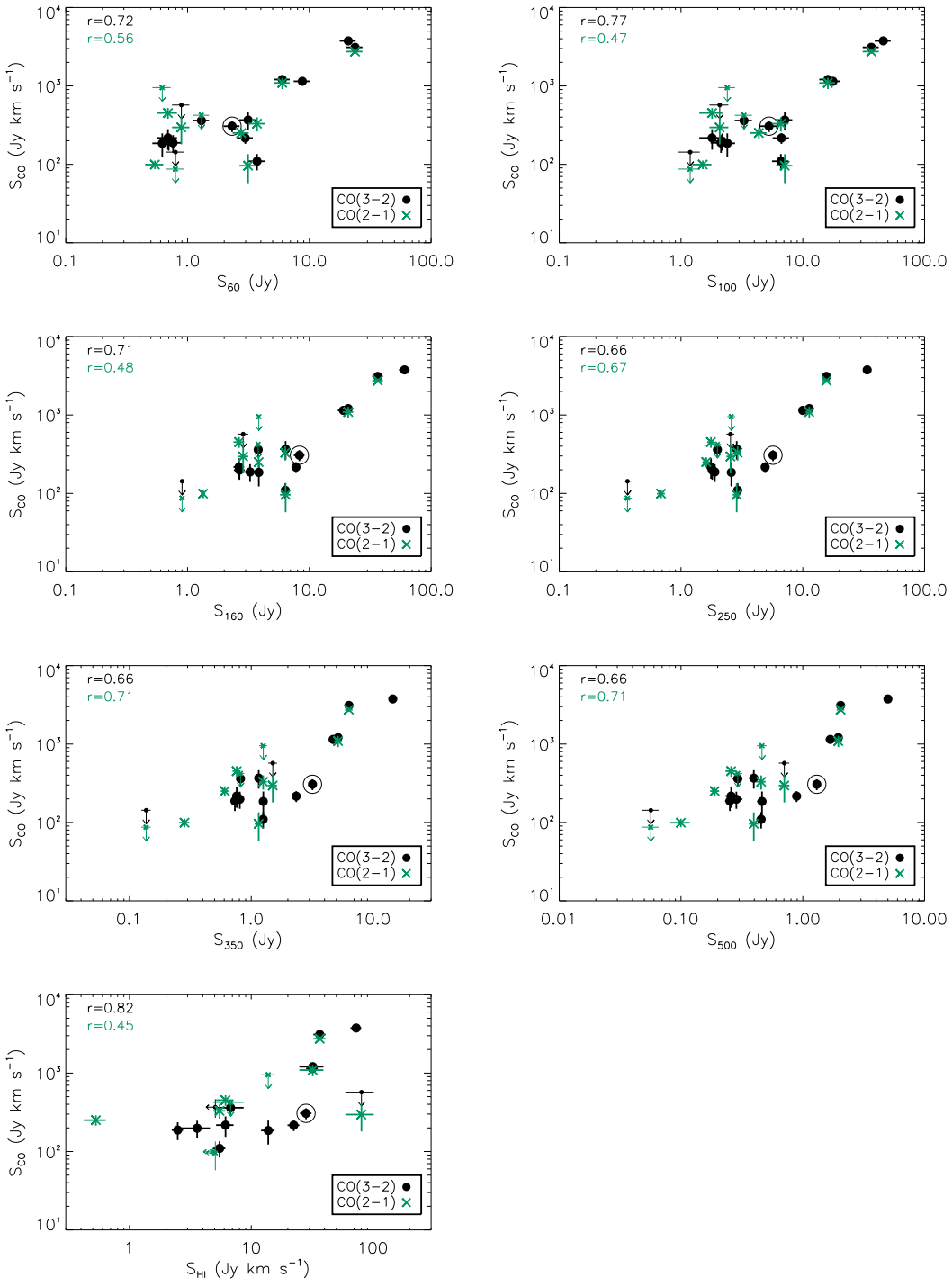

Figure 4.7: Scatter plots of global fluxes in each of the CO lines as a function of IR fluxes from *IRAS* 60 μm, 100 μm, PACS 160 μm, SPIRE 250 μm, 350 μm, 500 μm, and finally H I flux. Data from HARP and RxA are plotted as filled black circles and green crosses respectively. 5σ upper limits on CO and H I fluxes are also shown as thin arrows. The circled point is the HARP measurement of NGC 5584, which may be inaccurate as described in the text. Spearman's rank correlation coefficients are printed in the top-left corner of each panel.

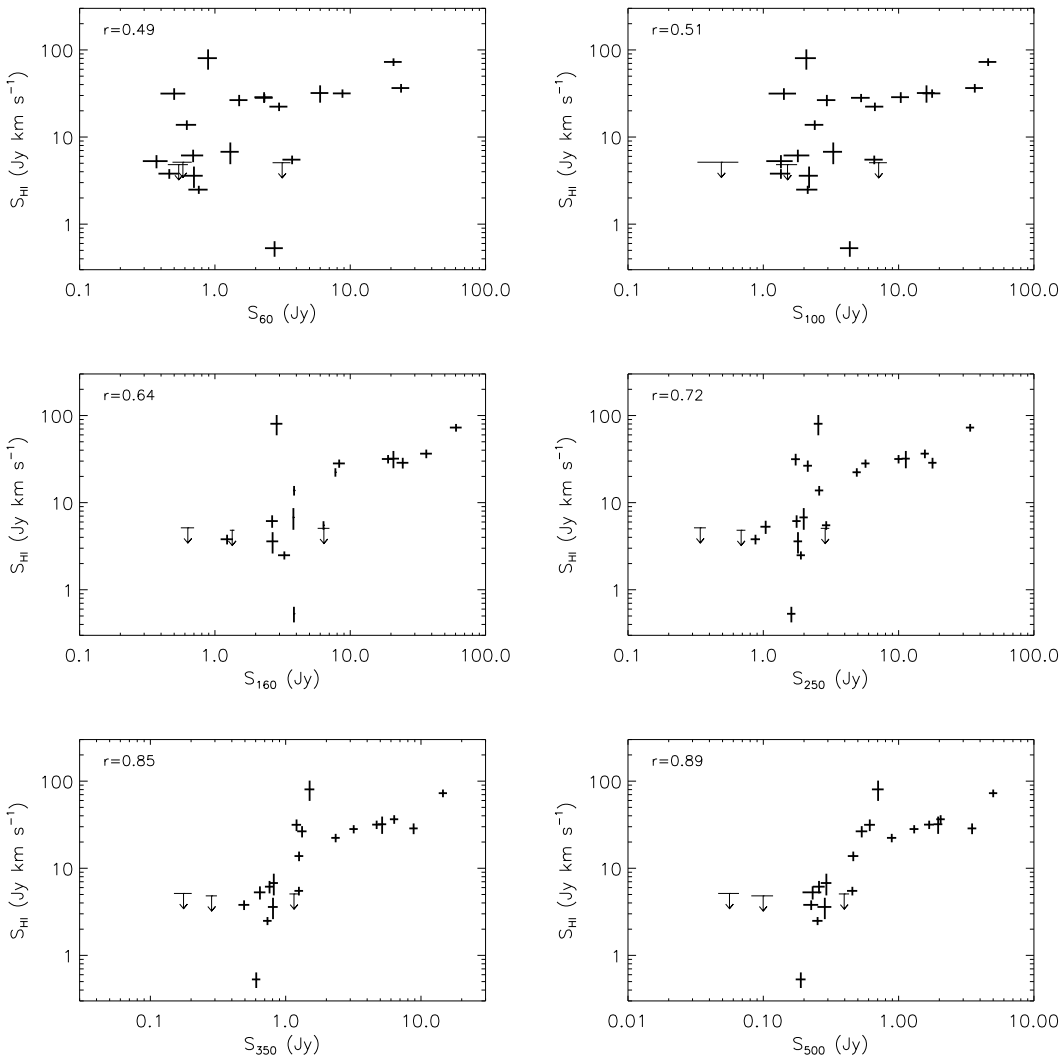

Figure 4.8: Scatter plots of global fluxes in H I and the IR bands (as in Figure 4.7). Spearman's rank correlation coefficients are printed in the top-left corner of each panel. For galaxies with no flux in the literature and no detection in the HIPASS cubes, 5σ upper limits estimated from the cubes are plotted as thin arrows.

bands, but there is considerable scatter outside of the error bars, indicating intrinsic variation within the sample. A correlation also exists between CO(3–2) and H I fluxes. There is no significant correlation between CO(2–1) and H I, although there are only six objects with both lines detected.

Figure 4.8 shows the correlations between the H I fluxes and the same IR bands. Scatter is particularly high in the correlation with the *IRAS* bands, but shows a marked reduction as the IR wavelength is increased. Two notable outliers persist through each of the plots in Figure 4.8, which are SDP 1 (with the lowest H I flux) and NGC 5496 (with the highest). These two are also outliers in the CO–H I correlation (Figure 4.7, last

panel), with SDP 1 having a very high CO(2–1)/H I ratio, and NGC 5496 having low CO(2–1)/H I and CO(3–2)/H I ratios (the latter being an upper limit). These outliers will be revisited in Section 4.5.5.

4.5.2 Scatter in the CO–IR Correlations

There are various ways to quantify scatter in order to make comparisons between different correlations. For example, Spearman's rank correlation coefficient r_s is a non-parametric measure of the correlation between the rank order of a set of data in two coordinates (x and y). Values of r_s for each correlation are printed in both Figures 4.7 and 4.8. These are calculated from the log fluxes using all detected points [except for NGC 5584 in CO(3–2)].

It is worthy of note that the r_s values show a decrease in the level of correlation between the IR and CO(3–2) flux as the IR wavelength is increased. The exception to this is the *IRAS* 60 μm band, which may be due to larger relative errors increasing the uncertainty on the correlation coefficient, or may result from a contribution of 60 μm emission from VSGs (I will discuss this possibility in Section 4.5.3). The decreasing trend at $\lambda \geq 100\,\mu\mathrm{m}$ is inverted in the correlations with H I fluxes, which show an overall increase in r_s with wavelength. The correlation of IR flux with the CO(2–1) line also shows a general increase in strength with wavelength, indicating that the emission in this line may be more closely related to cold dust, and possibly H I, than the CO(3–2). These trends are visualised in Figure 4.9 (left-hand panel), in which the errors on r_s are estimated from a jackknife resampling of the data. This accounts for the potential bias of individual data points which may be spurious (e.g. inaccurate as a result of poor baseline subtraction). With these errors on r_s it is apparent that the evolution in the H I–IR correlation is significant, but that in the CO(3–2)–IR and CO(2–1)–IR correlations is less so. It is also significant that CO(3–2) is better correlated with 100 μm than either CO(2–1) or H I, and H I is better correlated with the sub-mm (350 and 500 μm) than either CO line. The same trends are observed using alternative measures of correlation, including Pearson's coefficient r_p and Kendall's τ parameter.

None of these parameters take into account errors on the individual data points, which themselves contribute to the scatter and can thus reduce the apparent correlation. We

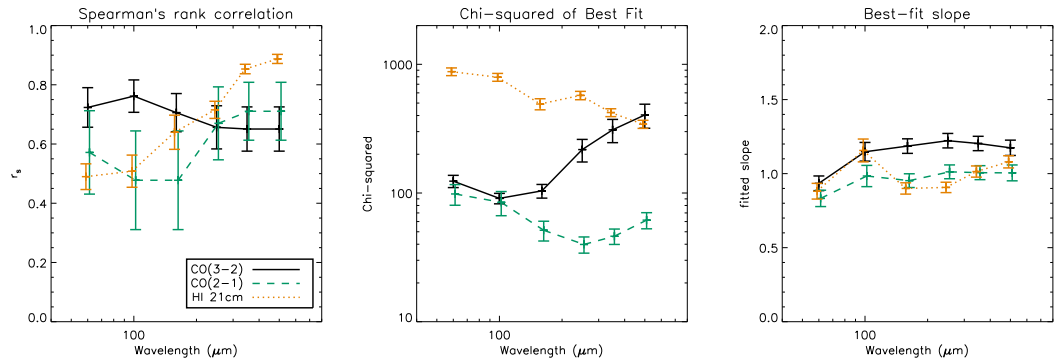

Figure 4.9: Spearman's rank correlation, χ^2 of the best fit, and slope of the best fit, for the relationship between line fluxes and IR fluxes as a function of IR wavelength.

therefore need an estimate of the additional scatter above that expected from the size of the error bars. A useful statistic for this measurement is χ^2, which is often used to test the goodness-of-fit of a model E_i to a set of N data points D_i, with errors σ_i:

$$\chi^2 = \sum_{i=0}^{N} \frac{(D_i - E_i)^2}{\sigma_i^2} \tag{4.4}$$

This explicitly describes the ratio of the measured deviation of the data from the model to the expected variance due to errors. Unlike non-parametric statistics such as Spearman's rank coefficient, χ^2 depends on the model that the data are compared to. Yet if one assumes a plausible model for the general trend in the data, one can use this to measure the scatter away from that trend. Straight line fits to the logarithmic data (power laws in linear space) were obtained, weighting by errors on both line fluxes and IR fluxes. Slopes close to unity were obtained in all cases (see Figure 4.9, right-hand panel), although there is some variation between different lines/bands, which may be genuine or may be biased by outliers in the individual plots. These fits represent the "model" in equation (4.4), and the χ^2 of the fit quantifies scatter away from that model, accounting for the error bars.

The χ^2 values for each of the correlations are shown in Figure 4.9 (middle), with errors estimated from a jackknife resampling of the data in the same way as the errors on r_s were obtained. These χ^2 values pertain to the best-fit slopes which vary between different correlations, but indistinguishable results were obtained using a model with the slope fixed to unity. The χ^2 values undergo an overall increase with IR wavelength for the CO(3–2) correlations, but an overall decrease for the CO(2–1) and H I correlations.

This is consistent with the inverse trends measured in the correlation coefficients (since χ^2 measures the opposite of correlation). Overall, the trends indicate that the CO(3–2) emission, tracing dense molecular gas in star-forming regions, is better correlated with $100\,\mu\mathrm{m}$ fluxes (at the peak of the SED) than fluxes at longer wavelengths (which are increasingly biased towards emission from cold dust). The fact that opposite trends are observed by substituting H I for CO(3–2) implies that the colder dust is more closely related to the H I content of the galaxy than the dense molecular gas. It is clear from Figure 4.9, however, that the evolution is not completely monotonic, and in particular it is unclear whether CO(2–1) is significantly better correlated with the SPIRE bands than with the *IRAS*.

Another ambiguous observation is that the χ^2 values for the H I–sub-mm correlations imply a similar level of scatter as in the CO(3–2)–sub-mm correlations, while the r_s results imply less scatter in the H I–sub-mm (see black and yellow lines in Figure 4.9). It is possible that this discrepancy arises from under-estimating the systematic errors on H I fluxes, which are from multiple sources, unlike the CO. Under-estimated errors would lead to higher χ^2 overall (since χ^2 measures scatter beyond the errors).

A simple way to quantify the confidence of the trends with wavelength is a linear least-squares fit to the data in the left and middle panels of Figure 4.9, resulting in an estimate of the slope and its uncertainty (from the jackknife error bars), assuming a linear trend. In fact the trend is unlikely to be linear, and a more sophisticated fit may give smaller errors, but in the absence of a more realistic model the simplest trend that we can test is a linear one. The results of these fits are as follows: for CO(3–2), $r_s(\lambda)$ has a negative slope with 1.3σ confidence, and $\chi^2(\lambda)$ has a positive slope with 4.1σ confidence. For CO(2–1), $r_s(\lambda)$ has a positive slope with 1.5σ confidence, and $\chi^2(\lambda)$ has a negative slope with 0.8σ confidence. For H I, $r_s(\lambda)$ has a positive slope with 10.4σ confidence, and $\chi^2(\lambda)$ has a negative slope with 9.0σ confidence. Thus one can say with a good level of certainty that the correlation of CO(3–2) with the IR becomes tighter with decreasing wavelength, and the correlation of H I with IR becomes tighter with increasing wavelength. The correlation of CO(2–1) with IR may also become tighter with increasing wavelength, but we cannot be certain from these data.

4.5.3 Relationships between ISM Tracers

An increase in the scatter between CO(3–2) and IR with increasing IR wavelengths may indicate that the amount of dense gas (which emits the higher excitation CO lines) is more strongly associated with warm dust (which dominates at $\sim 100\,\mu\mathrm{m}$) than cold dust (which dominates at longer wavelengths). This is consistent with the notion of dense gas being the fuel for ongoing star formation, which is directly traced by emission from warm dust. Applying similar arguments to the scatter in the H I/IR [and CO(2–1)/IR] indicates that atomic gas (and diffuse molecular gas) is more strongly associated with cold dust, although the situation is not clear-cut with CO(2–1).

The scatter in the CO(3–2)–60 $\mu\mathrm{m}$ correlation does not follow the trend of the other wavelengths, suggesting that the 60 $\mu\mathrm{m}$ emission also contains some contribution that is less well correlated with star formation than 100 $\mu\mathrm{m}$. One possibility is that the 60 $\mu\mathrm{m}$ fluxes contain some emission from VSGs (see Section 1.3.4), whose emission spectrum depends on transient heating by individual photons (Draine & Anderson 1985). The incidence of VSG emission varies between different spiral galaxies and may be better correlated with cold cirrus dust rather than warm dust and SFR (Draine & Anderson 1985; Walterbos & Schwering 1987; Xu & Helou 1994).

Looking at longer wavelengths, Corbelli *et al.* (2012) used the CO(1–0) line to trace the molecular gas content in Virgo spirals with *Herschel* data from HeVICS. This line traces the total molecular gas mass (modulo uncertainties in the X factor), and those authors found that it was better correlated with cold dust than warm dust. Since CO(2–1) tends to be more closely associated with CO(1–0) than CO(3–2) (Israel *et al.* 1984; Braine *et al.* 1993; Sakamoto *et al.* 1995), one would expect correlations involving CO(2–1) to follow the same trends, as is suggested (but not proved) in the current sample.

There are also parallels in the results of Wilson *et al.* (2009), who mapped three spirals in the Virgo cluster in CO(3–2) and CO(1–0), and concluded that the CO(3–2) transition was better correlated with two different SFR indicators – 24 $\mu\mathrm{m}$, tracing warm dust, and Hα, tracing ionising radiation from OB stars. Likewise, Iono *et al.* (2009) and Gao & Solomon (2004b) found strong correlations between dense gas tracers [CO(3–2) and HCN respectively] and the FIR, while Wilson *et al.* (2012) observed a

strong CO(3–2)–FIR correlation in low redshift H I–selected galaxies from the NGLS.

All of these results constitute strong evidence for dust at different temperatures inhabiting different phases of the ISM, with warm dust being associated with dense molecular clouds and cold dust with the diffuse ISM. It also directly implies that cold dust is less strongly associated with star formation than warm dust is, since star formation is fueled by the dense gas. This could have implications for theories of the heating mechanism for cold dust, since if it is less well correlated with SFR (i.e. $L_{\rm FIR}$) then it may be heated by sources other than young OB stars. AGN are a potential source of dust heating, but they are known not to contribute at the wavelengths of interest here (Schweitzer *et al.* 2006; Gallimore *et al.* 2010; Hatziminaoglou *et al.* 2010). It is likely that the cold dust is heated at least partially by old stars (e.g. Walterbos & Greenawalt 1996; see also Section 1.4). There is much observational evidence to support this theory, from the correlations between FIR colours and photometric tracers of old and young stars, both in resolved regions within galaxies (Boquien *et al.* 2011; Komugi *et al.* 2011; Bendo *et al.* 2012; Groves *et al.* 2012; Smith *et al.* 2012c) as well as in the global properties of galaxies (Totani *et al.* 2011; Boselli *et al.* 2012).

The high level of scatter in the correlations between the dense CO and the long-wavelength bands in particular shows that these wavelengths are poor tracers of the SFR in sub-mm-selected galaxies. Even the 100 μm band shows considerable scatter suggesting a significant contribution from cold dust not correlated with the SFR. Reliable IR SFRs can only be obtained from full SED fits to data covering the peak, and allowing for emission from at least two components of dust.

4.5.4 Slope of the CO–IR Correlation

The slope of the relationship between SFR and molecular gas mass, or between their densities (the SK law), is of interest for understanding how star formation is regulated in galaxies. As discussed in Section 4.1.2, the slope of the CO–FIR relation will vary from the underlying physical relationship, depending on the linearity of the conversion from the particular CO tracer to molecular gas mass.

The slope of the CO–IR flux relationships, plotted in Figure 4.9, vary for different IR

wavelengths and for the two CO lines. The slope is close to 1.0 for all combinations, but for 60 μm fluxes (which are most closely related to the SFR, assuming they are dominated by large grains) the slope for both lines is less than unity. The photometric data can be used to estimate integrated $L_{\rm FIR}$, a commonly-used estimate of the SFR that is less likely to be biased by VSG emission than the 60 μm flux. I therefore used the six photometric points for each galaxy (or five where S_{160} was unreliable; see Section 4.2.2) to fit a two-component SED model. Dust exists at a range of temperatures, but in general the SED in this wavelength range can be adequately described by a combination of a warm component ($T_w \sim 50$ K), representing dust in star-forming regions, and a cold component ($T_c \sim 20$ K), representing diffuse dust in the ISM. The spectrum of each component follows a greybody law, given by equation (1.4), and the full two-component model is given by

$$L_\nu(\nu) = 4\pi\,\kappa_{850} \left(\frac{\nu}{\nu_{850}}\right)^\beta \left[M_w B_\nu(\nu, T_w) + M_c B_\nu(\nu, T_c)\right]. \qquad (4.5)$$

This contains a dust emissivity term $\kappa_\nu \propto \nu^\beta$, normalised at $\kappa_{850} = 0.077\,\mathrm{m^2\,kg^{-1}}$ at $\nu_{850} = c/(850\,\mu\mathrm{m})$ (Dunne *et al.* 2000). Uncertainty in this value leads to a systematic uncertainty in the normalisation of dust masses, but assuming that large dust grains (which dominate this part of the spectrum) have similar emission properties in different galaxies, the trends observed in the results will be robust. Results will also be comparable to others in the literature since this is the value that is typically assumed. The spectral index of emissivity was fixed at $\beta = 2$ (e.g. Dunne & Eales 2001; also see discussion in Section 3.4.4). The remaining free parameters are the masses of warm and cold dust, M_w and M_c; and their temperatures T_w and T_c. Without additional short-wavelength data it is not possible to adequately constrain T_w, but the other parameters were well constrained after fixing T_w. I tried a range of values for T_w between 30 and 60 K, and I chose 45 K because it gave the minimum χ^2. Fitted values of T_c range between 13 and 25 K; M_w/M_c between 0.0006 and 0.03; and $M_{\rm dust} = M_w + M_c$ between 3×10^6 and $2 \times 10^8\,\mathrm{M_\odot}$. Note that the uncertainty of T_w means that M_w (hence M_w/M_c) is unconstrained, but the SFR, which depends on luminosity, is well constrained, as is the total dust mass which is dominated by M_c. The potential for a varying β leads to a small uncertainty in T_c and M_c; for example using $\beta = 1.5$ leads to a temperature increase by up to 7 K and a change in mass of up to $\pm$10 per cent.

In addition to the fitted parameters of these models, I obtained $L_{\rm FIR} = L_{40-120\,\mu{\rm m}}$, a good proxy for SFR (e.g. Kennicutt 1998a), by integrating the model SED ($L_{\rm FIR}$ is independent of β). In Figure 4.10 I plot $L_{\rm FIR}$ against the CO luminosity in each of the two emission lines, defined as

$$L_{\rm CO} = \frac{I_{\rm CO}\Omega d_L^2}{(1+z)^3}\ {\rm K\,km\,s^{-1}\,pc^2} \tag{4.6}$$

where d_L is the luminosity distance in pc. In general one should be cautious in analysing correlations between luminosities where the errors are large, since the two sets of variables being compared are not independent (unlike the fluxes). The conversion to luminosity includes a factor d_L^2 that is common to all bands, which means that the correlation can easily become dominated by this strong function of distance (to the second power) rather than the weaker function of flux (to the first power). In order to remove this confounding effect, I plot the ratio of luminosities against $L_{\rm CO}$ in the right-hand panel of Figure 4.10.

The scatter in these plots confirms that CO(3–2) is better correlated with the integrated FIR than CO(2–1), as was also seen in the flux correlations. The $L_{\rm FIR}/L_{(3-2)}$ ratio appears to be roughly constant across the sample, although one galaxy is a notable outlier (NGC 5691, which has the lowest $L_{(3-2)}$ and the highest ratio). This is a very blue spiral galaxy which appears to be highly star-forming; it also has a relatively high M_w/M_c ratio from the SED fit, indicative of a hot SED.

To measure the slope in the correlations, I fitted linear models to the log data in the right-hand panel of Figure 4.10, including error bars in both the x and y axes. These indicate that the slope of the $L_{\rm FIR} \propto L_{\rm CO}^n$ relationship is $n_{32} = 0.75 \pm 0.05$ ($\chi^2 = 38$) for CO(3–2), and $n_{21} = 0.43 \pm 0.05$ ($\chi^2 = 150$) for CO(2–1), although the high χ^2 of the latter fit suggests that n_{21} is highly uncertain. For reference, Yao *et al.* (2003) fitted a slope $n_{32} = 1.4$ in their 60 μm-selected SLUGS sample (although they only measured CO in the central 15″ of the galaxies), while Iono *et al.* (2009) found $n_{32} = 0.93$ for a sample of local and distant LIRGs covering five orders of magnitude in luminosity. However, the index may vary between different luminosity regimes (e.g. Genzel *et al.* 2010; Wilson *et al.* 2012), and most of the current sample are not LIRGs (see Figure 4.10).

Gao & Solomon (2004b) fitted a slope of $n_{10} = 1.25$ to the $L_{(1-0)}$ – $L_{\rm FIR}$ relation

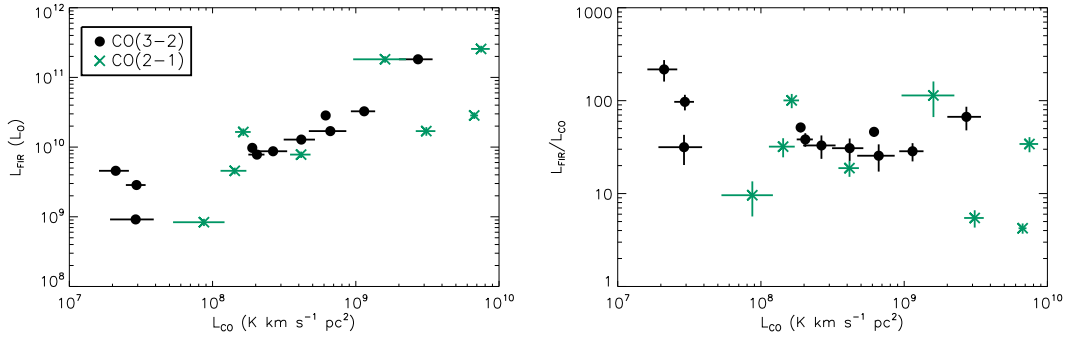

Figure 4.10: Integrated FIR luminosity $L_{\rm FIR} = L_{40-120\,\mu{\rm m}}$, from two-component SED fits, versus CO luminosity (left); and the ratio $L_{\rm FIR}/L_{\rm CO}$ versus $L_{\rm CO}$ (right).

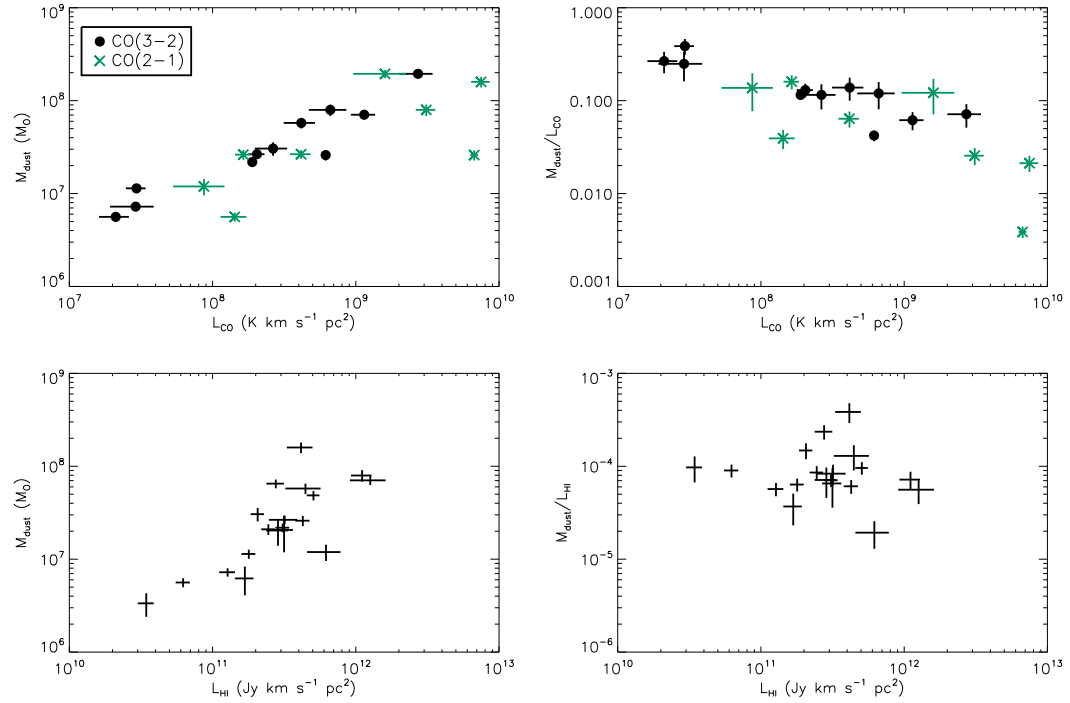

Figure 4.11: Total dust mass from two-component SED fits versus CO luminosity (top left), and the ratio $M_{\rm dust}/L_{\rm CO}$ versus $L_{\rm CO}$ (top right); dust mass versus H I luminosity (bottom left) and $M_{\rm dust}/L_{\rm HI}$ versus $L_{\rm HI}$ (bottom right).

in a large sample of nearby galaxies, yet a much flatter slope of $n_{10} = n_{32} = 0.87$ was fitted by Mao *et al.* (2010) to both CO(1–0) and CO(3–2) data spanning over four orders of magnitude in luminosity (Gao & Solomon's data spanned 2.5 orders of magnitude). Finally, Wilson *et al.* (2012) analysed a sample of H I–selected galaxies in the NGLS and SINGS, in comparison to the LIRG sample of Iono *et al.* (2009). They split the local galaxies in the NGLS into two luminosity ranges and found that galaxies with $8.3 < \log_{10} L_{\rm FIR} < 9.5$ had systematically higher $L_{\rm FIR}/L_{(3-2)}$ ratios than $9.5 < \log_{10} L_{\rm FIR} < 10.7$ galaxies (i.e. $n_{32} < 1$; see Figure 5 of Wilson *et al.* 2012). This

is consistent with the sub-linear correlation seen in the current data. On the other hand, Wilson *et al.* (2012) showed that the LIRGs from Iono *et al.* (2009) had higher ratios, and Wilson *et al.* fitted a slope $n_{32} \sim 1.2$ for all the galaxies with $\log_{10} L_{\rm FIR} > 9.5$. The galaxies in the current sample fall in the range $8.7 < \log_{10} L_{\rm FIR} < 11.4$ (though only two have $\log_{10} L_{\rm FIR} > 11$) and the mean (standard deviation) of $\log_{10}(L_{\rm FIR}/L_{(3-2)})$ is 1.74(0.33). This is consistent with galaxies in the same range from Wilson *et al.* (2012) and significantly lower than the mean for (U)LIRGs and SMGs.

Clearly there is a large amount of uncertainty on the slope of this correlation, with different results being obtained in different samples and in different luminosity ranges. If different metallicity ranges are probed by the various samples then this must surely play a role, since metallicity affects the CO/H_2 conversion factor (I will return to this possibility in the next section). It is certain that galaxies selected to be luminous at FIR wavelengths at low and high redshifts have systematically higher $L_{\rm FIR}/L_{\rm CO}$ ratios than ordinary, main-sequence SFGs (as shown in Figure 4.2), while local sub-mm-selected galaxies appear to follow the latter.

4.5.5 CO, H I and Dust Mass

Figure 4.11 shows the dust mass from the SED models as a function of $L_{\rm CO}$ and $L_{\rm HI}$, as well as the ratios as in Figure 4.10. Errors on dust mass include a 10 per cent error due to the uncertainty of β (see above), added in quadrature to the random errors from the SED fit. The scatter indicates that the CO(3–2) is more closely correlated with $M_{\rm dust}$ than CO(2–1) is, although CO(2–1) is still better correlated with $M_{\rm dust}$ than it is with $L_{\rm FIR}$ (see below). The galaxy with the lowest $M_{\rm dust}/L_{\rm CO}$ in both CO lines is NGC 5713. This galaxy is atypical of the sample as it is a starburst galaxy from the SLUGS sample. Apart from this one outlier, there is a generally strong correlation between $M_{\rm dust}/L_{\rm CO}$ and $L_{\rm CO}$, with a slight negative slope.

The scatter in $M_{\rm dust}/L_{\rm HI}$ is greater than in $M_{\rm dust}/L_{\rm CO}$, implying that dust traces CO (and potentially H_2) more closely than it traces H I. This is in spite of the implication from the flux correlations (see r_s in Figure 4.9) that the sub-mm is better correlated with H I than with CO. It is not clear why this is not observed in the mass/luminosity trends, but it is possible that scatter is introduced by the range of fitted dust temperatures, which

may be real or may be a symptom of variations of β within the sample. Nevertheless, this casts doubt on the assertion that the dust mass is primarily associated with H I. The dust/gas ratio is likely to vary between galaxies of different metallicities, and this will affect the CO/H_2 ratio (e.g. Issa, MacLaren & Wolfendale 1990). Hence the correlation between CO and $M_{\rm dust}$ may be stronger because galaxies with different metallicities fall on the same relation, even though they have varying dust/H_2 and dust/H I ratios.

Two particular outliers stand out in the $M_{\rm dust}/L_{\rm HI}$ correlations: SDP 1 (with the highest $M_{\rm dust}/L_{\rm HI}$) and NGC 5496 (with the lowest). Both of these were also outliers in the CO–H I correlation, and in H I–IR, as discussed in Section 4.5.1. SDP 1 is a spectroscopically identified AGN as well as being the brightest source in the H-ATLAS SDP field. The visual morphology indicates a merger and its $L_{\rm FIR} = 2.6 \times 10^{11}\,{\rm L}_\odot$ makes it a LIRG, so it is atypical of the sample. It is also possible that the H I self-absorption is underestimated for this source (in which case it should have a lower $M_{\rm dust}/L_{\rm HI}$) – the correction in Section 4.4.3 is based on morphology and inclination alone, but this is likely to be unreliable for mergers. The object with the second-highest $M_{\rm dust}/L_{\rm HI}$ is NGC 5746, which is a dust-rich edge-on spiral, and it is possible that the self-absorption correction was underestimated for this galaxy also. NGC 5496, which has the lowest $M_{\rm dust}/L_{\rm HI}$, is another edge-on disk galaxy but is very blue and has low surface brightness (unlike NGC 5746 for example). Due to the high inclination, the H I flux has been corrected by a factor of 1.32 for self-absorption; however without this correction this object remains a significant outlier, so it appears to have an intrinsically low dust/gas ratio. It is also likely to have low metallicity since it is a blue, low-surface-brightness galaxy (McGaugh *et al.* 1991).

Fitting the slope in the $M_{\rm dust}/L_{\rm CO}$ and $M_{\rm dust}/L_{\rm HI}$ ratios (as in the previous section), I estimate that the slope of $M_{\rm dust} \propto L_{\rm CO/HI}^m$ is $m_{32} = 0.43 \pm 0.05$ ($\chi^2 = 44$) for CO(3–2), $m_{21} = 0.16 \pm 0.05$ ($\chi^2 = 107$) for CO(2–1), and $m_{\rm H\,I} = 1.00 \pm 0.06$ ($\chi^2 = 165$) for H I. Excluding two outliers (SDP 1 and NGC 5496, which may have unreliable self-absorption corrections) from the H I correlation yields $m_{\rm H\,I} = 0.99 \pm 0.06$ with $\chi^2 = 95$. The high χ^2 values are a result of intrinsic scatter in the data, rather than an inadequate model, but as a result the uncertainty on the slopes is probably higher than the formal errors quoted. The χ^2 values demonstrate that the scatter is smallest

in the $M_{\rm dust}/L_{(3-2)}$ data, as discussed above. However, it is likely that the correlation in $M_{\rm dust}/L_{(2-1)}$ would be much improved if more data points were available, since this is more closely linked with total molecular gas mass (c.f. Corbelli *et al.* 2012). Nevertheless, according to these χ^2 values, CO(2–1) appears to be better correlated with $M_{\rm dust}$ than with $L_{\rm FIR}$, while CO(3–2) is marginally better correlated with $L_{\rm FIR}$ than $M_{\rm dust}$, consistent with the results in Section 4.5.1.

The slope of the $M_{\rm dust}$–$L_{(2-1)}$ and $M_{\rm dust}$–$L_{\rm HI}$ correlations is inconclusive from these data given the error bars and the χ^2 of the fits, but the correlation of $M_{\rm dust}$ and $L_{(3-2)}$ is very tight, and has a significantly sub-linear slope of $m_{32} = 0.43 \pm 0.05$. In comparison, Yao *et al.* (2003) fitted a slope equivalent to $m_{32} = 1.05 \pm 0.08$ to the SLUGS 60 μm sample. Corbelli *et al.* (2012) fitted correlations between $L_{(3-2)}$ and luminosities in each of the PACS and SPIRE bands, finding roughly linear slopes and an evolution in the slope from short to long wavelengths. This evolution is not apparent in the fits to $S_{(3-2)}$–$S_{\rm IR}$ correlations in Figure 4.9, although it is qualitatively consistent with the difference between n_{32} ($\sim$ slope of the short-wavelength luminosity correlation) and m_{32} ($\sim$ slope of the long-wavelength luminosity correlation). On the other hand, the highly sub-linear slope found in the current sample is inconsistent with that found in either SLUGS (Yao *et al.* 2003) or HeVICS (Corbelli *et al.* 2012). This indicates that the relationship between dust mass and CO luminosity varies between different samples just as the relationship between $L_{\rm FIR}$ (or SFR) and CO luminosity, as shown in Section 4.5.4.

The negative slope of $M_{\rm dust}/L_{\rm CO}$ is interesting, and indicates some underlying intrinsic variation across the sample. There are a number of possible explanations. A variation in metallicity will lead to a variation in the CO/H_2 ratio, so that $L_{\rm CO}$ no longer traces $M_{\rm H_2}$ consistently. For a constant dust/H_2 ratio, this will lead to higher dust/CO at lower $L_{\rm CO}$, which is seen in Figure 4.11. Yao *et al.* (2003) and Corbelli *et al.* (2012) both probed high-metallicity galaxies, but it is possible that the current sample contains a broader range – particularly as the optical colours and morphologies are diverse, including blue low-surface brightness disks, dusty spirals, and early-type galaxies (see Appendix D). Schruba *et al.* (2012) have shown that low-metallicity dwarf galaxies in the HERACLES survey have much lower CO content than is implied from their SFRs

and the SK law, which supports this interpretation.

Alternatively, a higher dust/gas ratio in lower mass galaxies could also explain this trend. In Chapter 3 I found that the lowest-mass galaxies in the blue cloud had the highest dust-to-stellar mass ratios. Analogous results from the COLD GASS survey have shown that the gas fractions of low-redshift galaxies are higher in lower-mass galaxies, both using CO(1–0) to trace H_2 (Saintonge *et al.* 2011) and using H I (Catinella *et al.* 2012). A direct comparison between these results is not entirely accurate because the GASS results do not account for non-detections correctly (either setting their fluxes to zero or to the upper limit), and because the gas fraction is dependent on other variables such as colour and possibly redshift (c.f. Chapter 3). However, the GASS galaxies that were detected in both H_2 and H I are mostly in the blue cloud and at $z < 0.05$ (see Saintonge *et al.* 2011; Catinella *et al.* 2012), so a comparison to the stacked $M_{\rm dust}/M_\star$ in the low-redshift blue bin of Chapter 3 is reasonable. Using these data, the slope of $\log(M_{\rm dust}/M_\star)$ versus $M_\star$ is -0.67, while the slope of $\log(M_{\rm H_2}/M_\star)$ versus $M_\star$ in the detected sample of Saintonge *et al.* is -0.20 (rising to -0.46 if non-detections are included and set to the upper limit). This suggests that the dust/H_2 fraction is likely to be higher in low-mass galaxies. The results of Catinella *et al.* suggest a steeper slope in $\log(M_{\rm H_2}/M_\star)$ versus $M_\star$ (I fit a slope of -0.79 to their weighted medians, which is steeper than the slope in $M_{\rm dust}/M_\star$), and Saintonge *et al.* showed that the H_2/H I fraction increases with stellar mass. It is therefore possible that the dust/H I fraction or the dust/(H I+H_2) fraction is constant with stellar mass, while the H_2 fraction decreases. In fact it is likely that both metallicity and dust/gas ratio vary across the sample; for example Draine *et al.* (2007) showed that dust/gas ratio correlates with metallicity in the SINGS sample. In future it will be necessary to analyse samples covering the full spectrum of galaxy properties, and to account for the metallicity dependence of the X factor, in order to test these possibilities. Future results from surveys such as HERACLES, GASS or NGLS may provide the answers.

4.6 Conclusions

In this chapter I have presented the results of a search for CO emission in local sub-mm-selected galaxies. Very little is known about galaxies selected in this way in the local Universe, despite extensive literature on the properties of high-redshift sub-mm-selected galaxies (i.e. SMGs). This is simply because a blind selection at these wavelengths in the local Universe requires coverage of a large sky area in order to probe a statistically significant volume, and prior to *Herschel* this was simply not possible.

Galaxies selected in this sample are generally dust-rich late-type spirals, with one or two mergers/starbursts (e.g. SDP 1, NGC 5713), some blue low-surface brightness galaxies (NGC 5584, NGC 5691, NGC 5496) and dusty early-type disks (e.g. NGC 5719, NGC 3907B). They are clearly distinct from the high-redshift SMG population which are mostly ULIRGs and likely to be mergers (e.g. Engel *et al.* 2010).

The FIR/CO luminosity ratios of this sample are in line with low/moderate luminosity SFGs in the local Universe, and not with (U)LIRGs and high-redshift SMGs. The slope of the correlation appears to be sub-linear in this sample: the measured index of the $L_{\rm FIR}$–$L_{(3-2)}$ correlation is 0.75 ± 0.05, which is lower than that measured in most other samples (Yao *et al.* 2003; Iono *et al.* 2009; Mao *et al.* 2010), although the relatively small number of data points and small luminosity range in this sample may account for the difference. The slope of the $L_{\rm FIR}$–$L_{(2-1)}$ correlation is inconclusive considering the scatter and small sample size. I also find significantly sub-linear slopes in the $M_{\rm dust}$–$L_{(3-2)}$ and $M_{\rm dust}$–$L_{(2-1)}$ correlations, in comparison to approximately linear slopes in the 60 μm SLUGS sample (Yao *et al.* 2003) and the Virgo cluster spirals in HeVICS (Corbelli *et al.* 2012). The explanation for these slopes could be a greater range of metallicity across this sample, in comparison with other samples. Lower metallicity at lower luminosity and lower $M_{\rm dust}$ leads to lower CO luminosity for the same H_2 mass (c.f. Schruba *et al.* 2012). It is also possible that dust/gas fractions are higher in lower-mass galaxies, as suggested by a comparison of results from Chapter 3 and the COLD GASS survey (Saintonge *et al.* 2011; Catinella *et al.* 2012). Additionally, there is the possibility of a sampling bias towards higher dust fractions at lower stellar masses in this sub-mm-selected sample. Further analysis of larger samples will be necessary to find the cause(s) of this trend, and future results from COLD GASS or NGLS may

provide the answer. If there is a strong variation in the gas-to-dust ratio with stellar mass or metallicity, then the use of the sub-mm as an independent probe of the H_2 mass (e.g. for calibration of the X factor) is brought into question.

I measure correlations between the CO and IR fluxes in all FIR and sub-mm bands from 100 to 500 μm, and find that scatter in the correlations evolves with the IR wavelength used. The CO(3–2) line is better correlated with shorter wavelength FIR bands, consistent with it being a dense gas tracer and the FIR being correlated with the SFR. The CO(2–1) line appears to be better correlated with the sub-mm than the FIR, although the trend is not statistically significant and would need to be confirmed with a larger sample. It is clear however that the CO(2–1)–IR correlations have a different wavelength dependence to the CO(3–2)–IR correlations, suggesting that CO(2–1) and CO(3–2) trace different components of the molecular gas. Using data from HIPASS, I test the correlations between the H I 21 cm line and the FIR/sub-mm, finding that scatter in the correlation follows opposite trends with wavelength to the CO(3–2). This is strong evidence for dust at different temperatures occupying different phases of the ISM, with warm dust being more associated with dense molecular gas clouds, and cold dust inhabiting the diffuse neutral (H I) ISM. The evidence suggests that dense gas (the fuel for star formation) is less well correlated with cold dust than with warm dust. This is consistent with cold dust being at least partially heated by radiation from older stellar populations rather than young OB stars, as shown by independent evidence (e.g. Boquien *et al.* 2011; Bendo *et al.* 2012; Boselli *et al.* 2012). An implication of this is that sub-mm fluxes in general should be interpreted with some caution; the sub-mm appears to be a poor tracer of the SFR in sub-mm-luminous galaxies at low redshifts, based on the correlation with dense gas. Fluxes at the peak of the SED (100 μm) are better correlated with the dense gas, however there is still significant scatter in this sample, and it is likely that, in sub-mm-selected galaxies, even the 100 μm fluxes contain significant emission from cold cirrus dust.

This pilot study of a small sample has revealed some interesting trends in the correlation of various gas tracers with the FIR and sub-mm, but many questions remain unanswered. Additional data for CO(2–1) and CO(1–0) in particular would enable a better understanding of the correlations between total CO mass and the FIR/sub-mm,

and by comparing to H_2 gas masses estimated from the dust mass, it would be possible to investigate any variation of the CO X factor in these dust- and gas-rich (and potentially high-metallicity) galaxies. Observations of CI emission with ALMA would also be useful for such a comparison, and would improve our ability to interpret measurements of the more readily observable CO lines.

Chapter 5

Conclusions

5.1 Summary of the Thesis

Far-infrared and sub-mm astronomy have enjoyed great successes over the past three decades and have enabled a huge improvement in our knowledge of the history of the Universe and the build-up of galaxies via star formation. Much has been learned about the growth of massive galaxies through rapid star formation and starburst activity, especially in the most luminous IR sources at both low and high redshifts. In this thesis, however, I have used the FIR and sub-mm wavebands to explore less luminous systems, including unbiased samples of galaxies selected by their stellar light alone, as well as a novel sample selected in the sub-mm in the local Universe. I made use of large surveys of the distant Universe from *Spitzer* and of the low-redshift Universe with *Herschel*, in order to probe the larger population of galaxies and explore star formation in the typical galaxies selected in the optical and NIR.

5.1.1 The Power of Stacking

In Chapters 3 and 2, I demonstrated that stacking is a powerful technique for studying unbiased samples and exploring global trends and dependencies in galaxy populations, at fluxes below the noise and confusion limits of the surveys. I found that stacking can be subject to a number of biases, but that these can be removed by statistical corrections that do not require any knowledge of the individual objects in the sample.

Thus, I was able to correct for the problem of clustered and blended sources in the highly-confused FIR/sub-mm maps by measuring the correlation functions or by making simple assumptions to deblend fluxes. Another important correction is required for the contribution of lensed flux to intrinsically faint sources at moderate redshifts. This is a particular problem in the sub-mm, where the negative k–correction and the steep number counts conspire to make lensing relatively common. Since some of the faintest sub-mm sources (giant ellipticals on the red sequence) are especially likely to be lenses, it was necessary to correct their flux for the non-negligible contribution from lensed high-redshift SMGs. It was possible to make a statistical correction based on the number counts and redshift distribution of lenses from both observations and theoretical models (Lapi *et al.* 2011; González-Nuevo *et al.* 2012).

5.1.2 The Far-Infrared–Radio Correlation

In Chapter 2, I studied the FIR–Radio Correlation, an important relationship that underpins the use of non-thermal radio flux as an SFR tracer. I found that it remains approximately constant in massive galaxies up to high redshifts ($z < 2$). The sample traces the most massive galaxies from low redshift back to their formation epoch, and it was the first to target high-redshift galaxies selected independently of their SFRs (Bourne *et al.* 2011). I used FIR colours to derive k–corrections, and found that the SEDs of galaxies in the sample were best approximated by a quiescent spiral-galaxy template (M51), rather than a hotter starburst or ULIRG template.

The rest-frame FRC showed no evolution from the 24 μm or 160 μm results, consistent with other samples studied in the literature. A slight evolution in the 70 μm results may suggest that the 70 μm k–corrections were under-estimated as a result of a steep slope in the SED at $\sim 25{-}35\,\mu$m (at $z \sim 1{-}2$), compared with the M51 template. This could be explained by a relative dearth of emission from hot dust or very small grains, which contribute to the MIR continuum. On the other hand, a true evolution in the rest-frame 70 μm/radio ratio, and even total-IR/radio, is plausible considering that rest-frame 24, 70 and 160 μm fluxes can arise from different components of the dust in a galaxy. This possibility is consistent with the observed steepening radio spectral indices at $z > 1$, which suggest greater inverse-Compton losses of cosmic-ray electrons (as predicted

by Lacki & Thompson 2010). It is also consistent with the results of Seymour *et al.* (2009) from 70 μm/radio data, and Ivison *et al.* (2010a,b) who used BLAST/*Herschel* and *Spitzer* data to measure the total-IR/radio ratio.

5.1.3 Cold Dust in Low-Redshift Galaxies

In Chapter 3, I used stacking to target low-redshift, optically-selected galaxies from the GAMA survey, and measured the dependence of cold dust properties on colour, absolute magnitude, stellar mass and redshift. The work described here was the first large-scale statistical survey of cold dust in optically-selected galaxies, and was only possible with the unprecedented volume of the low-redshift Universe probed by *Herschel*-ATLAS in the sub-mm (Bourne *et al.* 2012). I estimated that the total emission from optically-selected galaxies at $r < 19.8$ and $z < 0.35$ accounts for around five per cent of the CIB at sub-mm wavelengths, of which roughly 60 per cent originates from blue galaxies, and 20 per cent each from the red sequence and green valley. I also derived the total luminosity density of the Universe at $z = 0$, obtaining results in approximate agreement with predictions from IRAS and SCUBA data (Serjeant & Harrison 2005), and from GAMA UV–NIR data assuming a prescription for attenuation and re-radiation by dust (Driver *et al.* 2012).

The results of stacking revealed a strong dependence of sub-mm luminosity on optical or UV–optical colour, and stellar mass or M_r, with red galaxies being up to an order of magnitude less luminous than blue galaxies of equal stellar mass. The observed trends of SPIRE luminosities are not strongly dependent on the SED model assumed, and cannot be explained by lensing, hence they imply a fundamental difference between the dust emission properties of red and blue galaxies. Fitting single-component greybody SEDs suggested that this luminosity difference is primarily due to different (cold) dust temperatures; dust is colder in red galaxies than blue in the stellar mass range $3\times10^9 < M_\star < 8\times10^{10}\,\mathrm{M}_\odot$. Dust temperature was also found to be strongly correlated with stellar mass in blue galaxies, although this was not seen in red galaxies. Results showed a strong increase in sub-mm luminosity with redshift for galaxies of all colours and stellar masses. Since no evolution in temperatures was apparent, this seems to imply an increase in the dust masses of galaxies of all stellar masses, by a factor of $3-4$

between $z \sim 0$ and $z \sim 0.3$.

Especially strong evolution in the red bin suggests an increasing contribution from obscured star-forming systems in the red sequence at increasing redshifts. This is supported by an increasing 250 μm/NUV luminosity ratio, which may be used to trace the fraction of star-formation that is obscured (under certain assumptions). Galaxies in the green valley have intermediate luminosities and temperatures between those of blue and red galaxies, and probably comprise a mixed population of both obscured SFGs and passive galaxies with young stellar populations.

5.1.4 Molecular Gas in Local Dusty Galaxies

In Chapter 4, I exploited the wide areal coverage of the *Herschel*-ATLAS survey to select a sample of nearby galaxies at 500 μm, a selection that is sensitive to total dust mass rather than total IR luminosity and SFR. Unlike FIR-luminous galaxies and high-redshift SMGs, the galaxies in this sample have been poorly studied in the past due to the lack of wide sub-mm sky coverage prior to *Herschel*. I used CO emission-line data obtained from the JCMT, with additional data from *Herschel*, *IRAS*, and H I line measurements in the literature, to explore the correlations between the cold and warm dust, and molecular and atomic gas in these galaxies.

The sample consists of mainly star-forming spirals with high dust masses and atomic gas masses. Their FIR/CO luminosity ratios are in line with low/moderate luminosity SFGs in the local Universe, and not with (U)LIRGs and high-redshift SMGs. The slope of the FIR–CO and $M_{\rm dust}$–CO correlations appears to be sub-linear, and is lower than that measured in most other samples (Yao *et al.* 2003; Iono *et al.* 2009; Mao *et al.* 2010; Corbelli *et al.* 2012).

I measured correlations between the CO and IR fluxes in all FIR and sub-mm bands from 100 to 500 μm, and found that scatter in the correlations evolves with the IR wavelength used. The CO(3–2) line is better correlated with shorter-wavelength FIR bands, consistent with it being a dense gas tracer and the FIR being correlated with the SFR. The CO(2–1) line may be better correlated with the sub-mm than the FIR, although the trend is not statistically significant and would need to be confirmed with

a larger sample. It is clear however that the CO(2–1)–IR correlations have a different wavelength dependence to the CO(3–2)–IR correlations, suggesting that CO(2–1) and CO(3–2) trace different components of the molecular gas.

Scatter in the H I–IR correlation follows opposite trends with wavelength to the CO(3–2). This is strong evidence for dust at different temperatures occupying different phases of the ISM, with warm dust being more associated with dense molecular gas clouds, and cold dust inhabiting the diffuse neutral ISM.

5.1.5 The Cold Interstellar Medium

A recurring theme throughout the thesis has been the importance of the cold ISM, and especially cold dust, in ordinary galaxies at all redshifts. While the SEDs of the most IR-luminous galaxies at low redshifts are dominated by warm dust in star-forming regions, we know that much of the IR luminosity in the vast majority of galaxies results from cold dust in the diffuse ISM (Dunne & Eales 2001; Sauvage, Tuffs & Popescu 2005; Draine *et al.* 2007). The importance of cold dust is implied by the apparently cold SEDs of the NIR-selected galaxies in Chapter 2, which had FIR colours indicative of a quiescent spiral template, despite the fact that these massive galaxies have typically high SFRs at $z \gtrsim 1$. Even more telling are the high dust masses derived from stacking GAMA galaxies at $z < 0.35$ in Chapter 3. The inferred dust/stellar mass ratios showed a strong anti-correlation with stellar mass and strong evolution with redshift, and may imply the need for dust to be formed in supernovae or to grow in the ISM. The surprisingly weak correlation with optical colour contrasts with observations of low dust masses in morphologically-selected elliptical galaxies on the red sequence (e.g. Smith *et al.* 2012b), which may suggest an environmental dependence (due to the denser environments probed by Smith *et al.*).

Finally, the CO/sub-mm fluxes of local sub-mm-selected galaxies in Chapter 4 revealed a decrease in the ratio of CO to dust mass with increasing CO luminosity. This could be due to a variation in metallicity leading to a varying CO/H_2 ratio (this sample is likely to trace a broad range of metallicities). On the other hand, the dust/gas or dust/H_2 fraction could be higher in lower-mass galaxies, just as the dust/stellar mass fraction was found to be.

Understanding trends such as these is crucial for disentangling the various factors which may determine how galaxies evolve. The ISM content of a galaxy contains information on the past star-formation history, in the metals and dust produced by stars, and on the potential for future star formation, through the gas reservoirs, and the dense molecular gas in particular. Far-infrared fluxes in SFGs are correlated with the recent SFR (averaged over the past $\sim 10^8$ years), as a result of young stars heating the dust that emits at these wavelengths, but the cold dust which emits in the sub-mm may be heated by older stellar populations. Analysis of the correlations between sub-mm and CO fluxes in Chapter 4 supports this interpretation, which is independently inferred from many other observations (Boquien *et al.* 2011; Totani *et al.* 2011; Bendo *et al.* 2012; Boselli *et al.* 2012).

5.2 Future Work

Sub-millimetre astronomy has now entered a golden age and will undoubtedly play a central role in advancing our understanding of the Universe over the coming years. During this time we will benefit from the huge amounts of data acquired by *Herschel* over its three-year mission, as well as data obtained from SCUBA-2 in its Legacy Surveys, and the ALMA interferometric array. In this thesis I have used data from the first release of the H-ATLAS survey, as well as multi-wavelength data from many other sources, to explore the FIR and sub-mm Universe through statistical analyses. The results have shed new light on the IR emission properties, and the dust and gas content of populations of galaxies selected in various ways, but many open questions still remain for the future.

The IR SEDs of galaxies selected in different ways can vary greatly, depending on the amount of dust in different phases of the ISM, the temperature of that dust, and the source of heating – whether by old or young stars. Understanding the star-formation history of the Universe, and the evolutionary paths of different types of galaxies, depends on accurately measuring the obscured SFRs in galaxies of all types, at all redshifts. The amount of cold dust in passive or quiescent galaxies is uncertain, but is probably highly variable. Results from stacking the GAMA sample suggest that red-

sequence galaxies have considerable dust masses, comparable to blue SFGs. The nature of passive galaxies could be better understood by selecting on visual morphology as well as colour, thus breaking the degeneracy between dust obscuration and stellar-population age. The SEDs could also be better constrained with additional data at shorter wavelengths (e.g. from PACS, AKARI and WISE) to cover the peak of the SED and emission from dust at warmer temperatures. Likewise, longer-wavelength (sub)mm bands (e.g. from SCUBA-2 and *Planck*) provide a better handle on the dust emissivity parameter β, which is otherwise degenerate with the cold-dust temperature. Full SED modelling with self-consistent Bayesian techniques (e.g. da Cunha, Charlot & Elbaz 2008; Smith *et al.* 2012a) is the best way to accurately constrain the SED parameters in large samples with extensive multi-wavelength coverage.

A full understanding of the processes within galaxies can only be obtained with observations of all the components which make up a galaxy, including the stars, gas, dust and dark matter. Warm, dense, molecular gas feeds star formation, and this is supplied from the larger cold-gas reservoir; but star formation feeds energy back into the gas and dust, and none of these processes is very well understood. The Schmidt–Kennicutt law describes the relationship between gas and SFR density, but the universality and the slope of this relationship are in question, and depend on the observational tracer of the gas. In this thesis I tested correlations between the dense gas traced by CO emission lines and various FIR and sub-mm wavebands, but the CO tracer is far from being a perfect indicator of gas mass, since correlations based on CO appear to vary from one sample to another. The small sample studied in Chapter 4 revealed some interesting trends in the various correlations between gas tracers and the FIR/sub-mm, but much remains to be investigated with larger samples and more sensitive data. Additional data for CO(2–1) and CO(1–0) in particular would enable a better understanding of the correlations between total CO mass and the FIR/sub-mm. Also, by comparing these to H_2 gas masses estimated from the dust mass, it would be possible to investigate any variation of the CO/H_2 conversion factor in these dust- and gas-rich (and potentially high-metallicity) galaxies. Observations of [CI] emission with ALMA would also be useful for such a comparison, and would improve our ability to interpret measurements of the more readily-observable CO lines.

This is an exciting time to be involved in extragalactic astronomy. An enormous amount of data has been gathered from observations spanning the full electromagnetic spectrum especially in the last decade, and upcoming facilities such as ALMA, SKA and *JWST* promise to enhance the pool of data even further. We will soon have observations of entire galaxy populations spanning the era of galaxy evolution, from the epoch of reionisation through to the present day. It will be the task of the next few decades to mine these data and interpret them in the context of simulations and models, and to use them to explain how the diverse and complex Universe of today came into being.

Appendices

Appendix A

Algorithm for Stacking and Deblending Faint Sources in Highly Confused Maps

Below I describe a method that I developed for deblending confused sources with low signal-to-noise in SPIRE maps. I used this algorithm to measure fluxes of sources below the noise level for the stacking in Chapter 3. In Section A.2 I show that this gives comparable results to the statistical clustering correction used in Chapter 2.

A.1 Deblending Individual Sources

When stacking sources in confused maps, one must be careful not to double-count the flux of blended sources, which would lead to over-estimation of stacked fluxes. The problem is worst in bins whose galaxies are more clustered, and in the longer wavelength images which have lower resolution. Since many sources are close to or below the noise level in the images it is impossible to model them from the images themselves, and since sub-mm flux is poorly correlated with optical flux, we have no other prior information to base models on. We must therefore make some simplifying assumptions in order to avoid over-counting flux in stacks.

Consider that two or more sources may be blended, but we do not know the true flux

of either or their brightness ratio. How can we decide how much of the blended flux to attribute to each source? I first make the assumption that all sources are unresolved and therefore have a shape given by the PSF. I treat the image pixel-by-pixel and assume that the fractional contribution to a pixel from each of the nearby blended sources is dependent only on the distance of that pixel from the source in question. The concept is visualised in one dimension in Figure A.1. Panel (a) shows two sources A and B at positions x_A and x_B, whose fluxes are distributed across the image as $f_A(x)$ and $f_B(x)$ (Jy pixel^{-1}). The sources are blended in the image and the measured data (solid line) is given by

$$f_{\rm tot}(x) = f_A(x) + f_B(x). \tag{A.1}$$

In Figure A.1(b) the sources are modeled by PSFs of equal height (p_A, p_B; thin black lines). I convolve the image data with the PSF of A to give the function

$$F_{p,A}(x') = p_A * f_{\rm tot}. \tag{A.2}$$

To compute the convolution the PSF is shifted so that the peak is at the origin. The convolution is a function of the offset x', and the source flux is strictly given by the value at $x' = x_A$,

$$f_{p,A} = F_{p,A}(x_A)/\Sigma p_A^2 \tag{A.3}$$

(and similarly for B). The division by the sum of the PSF squared normalises the flux. However, both $f_{p,A}$ and $f_{p,B}$ now contain too much flux because both include all of the flux that is blended. This blended flux would therefore be counted twice if the sources were stacked. Instead of doing this, the PSF p_A can be weighted by the function

$$g_A(x) = p_A(x)/[p_A(x) + p_B(x)] \tag{A.4}$$

which is simply the fractional contribution from the PSF p_A at position x to the total $p_A + p_B$. Thus one can replace p_A and p_B with "deblended" PSFs

$$q_A(x) = g_A(x)\, p_A(x) \tag{A.5}$$

[and similarly $q_B(x)$] which are given by the thick grey lines in Figure A.1(b). Convolving the image data with each of these deblended PSFs gives a more conservative estimate of the total flux,

$$F_{q,A}(x') = q_A * f_{\rm tot}. \tag{A.6}$$

Again the flux is given by the value of the convolution at $x' = x_A$:

$$f_{q,A} = F_{q,A}(x_A)/\Sigma p_A^2. \tag{A.7}$$

The total (deblended) flux $f_{q,A} + f_{q,B}$ is the same as the total input flux under the functions in Figure A.1(a), whereas the total of $f_{p,A} + f_{p,B}$ is greater because blended flux has been double-counted. This deblending method always conserves total flux, whatever the ratio of the fluxes. On the other hand, the individual fluxes measured using equation (A.7) are not exactly correct because blended flux is shared evenly between the two sources, whereas ideally it should be distributed according to the flux ratio of the sources. Hence in this example the recovered flux of A is too low and that of B too high (this effect is worsened by closer proximity of the sources). However with no prior information on the true flux ratio this is the best estimate that can be made.

To generalise this method to a two-dimensional image with multiply-blended sources I start with an image array of the same dimensions as the data image, filled with values of zero. To this I add a PRF for every source in the input catalogue, centred on the pixel where the source is located and interpolated from the PSF with a small offset to correctly account for sub-pixel-scale positioning. In the region of an isolated source this image will be identical to the individual PRF, but where sources are blended it is equal to the sum of the PRFs [analogous to the sum of the thin black lines in Figure A.1(b)]. Thus all multiple blends are automatically accounted for, and the image I have constructed is analogous to the denominator in equation (A.4), i.e. $p_A + p_B + ...$ For each source i, I derive the weighting function $g_i(x, y)$ as the ratio of the PRF to a cutout region of the all-PRFs image, as in equation (A.4). In other words, the weight given to the flux in a pixel (x, y) is the value of the PRF of the target at (x, y) divided by the sum total of the contributions of all PRFs in that pixel. I measure the flux of each source by convolving the *data* image (Jy pixel^{-1}) with the weighted PRF, as in equation (A.6). I tested the method in simulated maps with realistic source densities and using the PRFs of the three SPIRE bands. I found that the correct mean and median fluxes were always recovered when stacking, and that convolving with the PRF without any deblending always led to an overestimate of the median and mean fluxes.

The deblending technique is carried out before any binning, so all catalogue sources

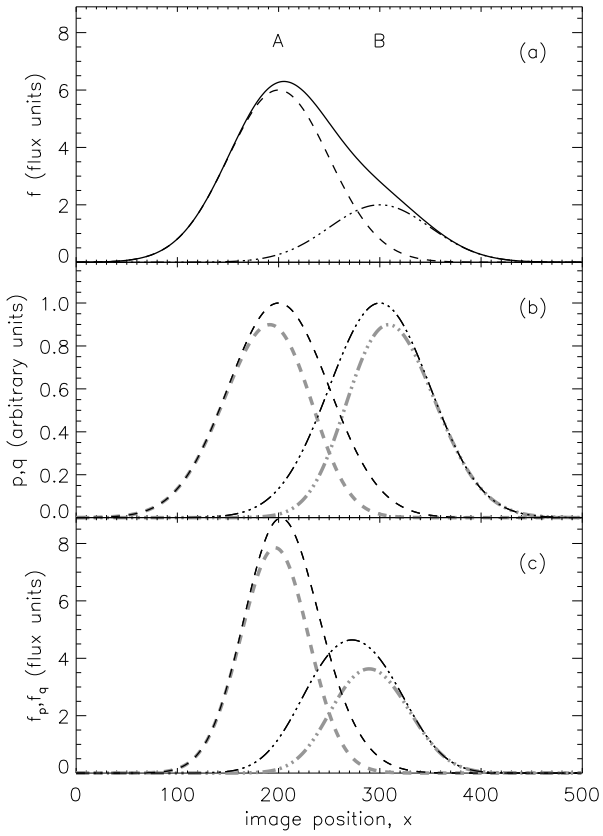

Figure A.1: **(a)** Two simulated point sources A and B in a one-dimensional image, modeled with the same PSF but different normalisations, represented by the dashed and dash-dotted curves respectively. The total flux in the image as a function of position x is given by equation (A.1) and is represented by the solid line. **(b)** The thin black lines are the PSFs, p_A and p_B, centred at $x = 200$ and $x = 300$ respectively. Both PSFs have width $\sigma = 50$. The thick grey lines are the PSFs weighted for deblending, q_A and q_B, given by equation (A.5). **(c)** The reconstructed sources given by the image data (solid line in panel a) weighted by the PSFs in the middle panel. The thin black lines are obtained using the unweighted PSFs p in equation (A.2), and the thick grey lines using the weighted PSFs q in equation (A.6).

in the field are automatically deblended, not just those in the same bin as the target in question. Note that the method is essentially very similar to the "global deblending" technique described by Kurczynski & Gawiser (2010), which was demonstrated by those authors to minimise bias and variance in stacks.

A.2 Comparison to a Statistical Approach

The problem of stacking into confused maps is not a new one, and other methods for removing the excess flux due to blending have been used in the literature. The advantages of the method described above are that it automatically takes into account

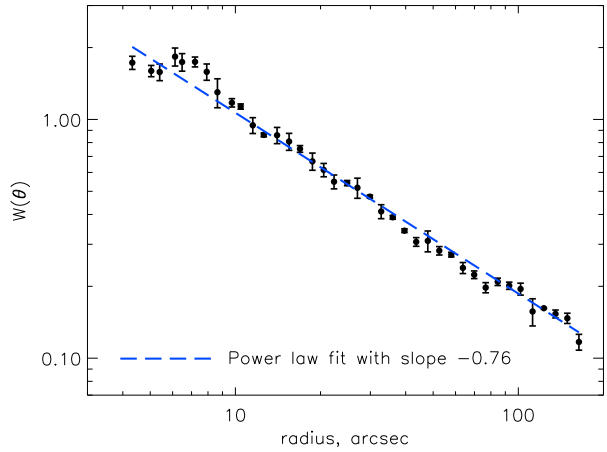

Figure A.2: The two-point angular correlation function of the GAMA catalogue used in this work, averaged over the G09, G12 and G15 fields. Error bars are the standard errors between the values obtained in the three fields. A power-law fit by linear regression (with free slope and normalisation) gives $w(\theta) = (0.012 \pm 0.001)\theta^{(-0.76\pm0.03)}$.

blending between objects in different bins, and also allows for the possibility of different bins having different amounts of blending (e.g. due to the stronger clustering of more massive and red galaxies – Zehavi *et al.* 2011). To check that the results of this method are reasonable, I compare them to the statistical clustering correction used in Section 2.3.4.

Using the Landy & Szalay (1993) estimator [equation (2.3)], I measured the correlation function of the GAMA catalogue by counting pairs in 40 radial bins logarithmically spaced between 4 and 180 arcsec. The results, averaged over the three fields, are shown in Figure A.2 together with a power-law fit by linear regression, described by $w(\theta) = (0.012\pm0.001)\theta^{(-0.76\pm0.03)}$. This fit is in good agreement with previous results from SDSS r-limited data (Connolly *et al.* 2002).

Using the fit to $w(\theta)$ and the beam sizes at 250, 350 and 500 μm (18, 25, and 35 arcsec FWHM), I obtained the fractional contribution to stacked fluxes due to blended, clustered sources, according to equation (2.4). Results are summarised in Table A.1. This average statistical correction factor is broadly similar to the typical correction to individual fluxes using the deblending technique [equation (A.7)]. The deblending technique has the advantage of correcting the flux of each target individually, so however the sample is binned the appropriate average correction is made. This is not the case using the correlation function of the entire catalogue, since that only gives a sin-

Table A.1: Flux correction factors $C = 1/(1 + F)$ based on the method in Chapter 2, compared with the typical/average ratios of deblended to non-deblended flux using equations (A.7) and (A.3).

	Statistical correction (C)	Mean (median) deblending correction
250 μm	0.9702 ± 0.0001	0.937 (1.000)
350 μm	0.9550 ± 0.0002	0.932 (0.987)
500 μm	0.9326 ± 0.0003	0.989 (0.902)

gle correction factor. It would be possible to calculate separate correction factors for each bin, using the cross-correlation between the bin and the full sample (as in Chapter 2), but the uncertainties would be significantly increased since each bin contains a relatively small number of objects.

Appendix B

Simulations of Bias in the Median

In Chapter 3 I stack sources with extremely low signal-to-noise, which can lead to bias in the estimate of the median intrinsic flux. In order to investigate the possible effect on the results, I simulated power-law distributions of fluxes with Gaussian noise added, and found that in certain cases the median measured flux (true flux plus noise) was biased high with respect to the median true flux, as a result of noise in the measured values. The amount of bias depends on (i) the flux limits of the distribution; (ii) the 1σ noise level in relation to the flux limits; and (iii) the slope of the power law describing the underlying flux distribution. The bias only becomes apparent when considering distributions with a median signal-to-noise less than 5σ.

In order to ascertain the level of bias that could be present in the stacks one must consider the shape of the underlying (true) flux distribution of sources in the stacks. In order to do so one must look at the distribution of fluxes in the much brighter H-ATLAS detected sample, which are not dominated by noise. The situation is helped considerably by the fact that the sample is binned according to M_r and redshift, meaning that each bin is likely to have a limited range of fluxes with a distribution determined by the LF. To estimate the flux limits in a given bin one can look at the sub-mm fluxes of the galaxies with the highest optical fluxes. D11 show the distribution of r magnitude and S_{250} in the SDP ID catalogue. At $r < 16$ the catalogue contains the full range of sub-mm fluxes, which at a given r spans 1.3 dex in S_{250}. I inspected the Phase 1 reliable IDs with good spectroscopic redshifts (250 μm sources matched to SDSS data using the same method as Smith *et al.* 2011; these will be described in a forthcoming

paper from H-ATLAS. I found the same range of 1.3 dex in $r < 16$ sources in Phase 1 as in SDP.

I therefore assume that any bin of M_r and redshift will have fluxes within a limited range. The actual limits of this range, $S_{\rm max}$ and $S_{\rm min}$, will depend on the range of M_r and z sampled by the bin (although the majority of fluxes at all M_r and $z < 0.35$ will lie within the range 0.1-100 mJy). However, since the range in a bin is determined by the LF, I can safely assume that the logarithmic range $R = \log_{10}(S_{\rm max}/S_{\rm min}) = 1.3$ will be consistent in all bins. Similar ranges of 1.3 dex are expected at all three SPIRE wavelengths (although of course fluxes at different wavelengths will be offset with respect to each other due to the shape of the SED). Within these limits the fluxes are assumed to follow a power-law distribution: in the Phase 1 IDs this is approximately described by differential number counts $dN/dS \propto S^{-2.5}$, although this is unreliable due to the incompleteness of the ID catalogue. A similar slope is apparent in the 250 μm number counts from $P(D)$ analysis of the HerMES maps (Glenn *et al.* 2010), although there is some evidence in that data for a shallower slope at $S_{250} \lesssim 10$ mJy. We must however remember that the number counts in the bins will not follow the overall sub-mm number counts, since the bins contain only a narrow distribution of M_r and particularly of redshift. In sufficiently narrow redshift bins the distribution of the counts will approach the sub-mm LF: this has a slope of -1.01 at the faint end ($L < L^{\star}$) of the H-ATLAS LFs derived by D11. We can therefore be confident that in finite redshift bins the slope will be intermediate between -1 and -2.5. Lapi *et al.* (2011) have modelled the number counts to fit the data from H-ATLAS, HerMES and BLAST. I split these into redshift bins ($\delta z = 0.05$) and found that the faint-end differential counts at $z < 0.35$ follow a slope of approximately -2. The redshift bins have similar widths ($0.05 \lesssim \delta z \lesssim 0.11$) hence it is reasonable to assume that the flux distributions in the bins will have a similar slope.

For these reasons I conclude that a simulated flux distribution that spans a range $R = 1.3$ dex with a power law $dN/dS \propto S^{-2}$ is representative of the bins. I therefore created 16 simulated distributions with these parameters, with a range of lower limits between $0.1 - 30$ mJy: the corresponding upper limits are 20 times larger, given by $R = 1.3$. The resulting distributions have medians in the range $0.3 - 70$ mJy, which is

sufficient to cover all the bins in the real data. I added random noise to these true flux distributions, where the noise values were drawn from a Gaussian distribution with zero mean, and σ given by the average total noise level (instrumental plus confusion) in the Phase 1 maps: $\sigma = 6.7, 7.9, 8.8\,\mathrm{mJy\,beam^{-1}}$ at 250, 350, 500 μm respectively. I then compared median measured flux (true flux plus noise) to the median true flux, and quantified the bias factor as the ratio of measured to true median flux.

I corrected the measured median fluxes in the stacked data by interpolating the relationship between true median flux and measured median flux from the simulations. This was done separately for each of the three bands (since the bias behaves differently as a result of the different noise levels). All correction factors are in the range $0.6 - 1.0$, which is generally small in comparison to the range of stacked fluxes resulting from true differences between the bins.

For these corrections I have assumed that the slope of differential number counts is -2 and that fluxes in each bin lie in a range given by $R = 1.3$ dex. However, the bias factor depends on both of these variables, as I show in Figure B.1. To test the sensitivity of the results to these parameters, I tried correcting the results by the bias factors obtained using different values. I tried slopes of dN/dS ranging from -0.5 to -4 and R-values between 1 and 2. The level of bias varies, indicating that there is some uncertainty in the correction, but note that the corrections for slopes between -1.5 and -2 give almost identical corrections (for $R = 1.3$). We can be sure that the slope is between -1 and -2.5, and over this range the bias corrections do not vary by more than 15%. Increasing the range R has a greater impact on the correction; however the value of 1.3 is well motivated and in narrow bins of M_r and redshift there is good reason to expect the flux range to be limited.

Crucially, all of the conclusions remain valid, and all trends remain significant, for any combination of slope (-0.5 to -4) and range (1 to 2). This is equally true if no corrections are made.

An alternative to these corrections would be to use the mean instead of the median when stacking. The mean is not altered by the effects of noise as I found the median to be; however the mean will be highly biased simply by the skewed shape of the distribution. In fact the bias in the mean at *all* flux levels is equal to the maximum

bias seen in the median at the lowest flux levels. The reason for this is simple: at the lowest flux levels, where noise dominates over the true flux, the distribution of measured fluxes closely resembles the noise distribution – a symmetrical Gaussian – but instead of being centred on zero as the noise is, it has the same mean as the true flux distribution. The mean is not altered by the addition of noise if the mean noise is zero. The measured flux distribution is therefore symmetrical in this case, hence the median is equal to the mean. Thus the maximum amount of bias in the median occurs when the shape of the distribution becomes dominated by the noise rather than by the true fluxes.

In conclusion, I choose to use the corrected median estimator rather than the mean, because at all but the lowest fluxes the median is a better descriptor of the underlying (true) flux distribution. At the lowest fluxes the median becomes biased and approaches the mean of the distribution. However as a result of the binning scheme one can make a good estimate of the shape of the underlying flux distribution and can be reasonably certain of the correction factors for the bias. The fact that all of the ultimate conclusions remain valid for any reasonable choice of the distribution indicates the robustness of the results to these corrections.

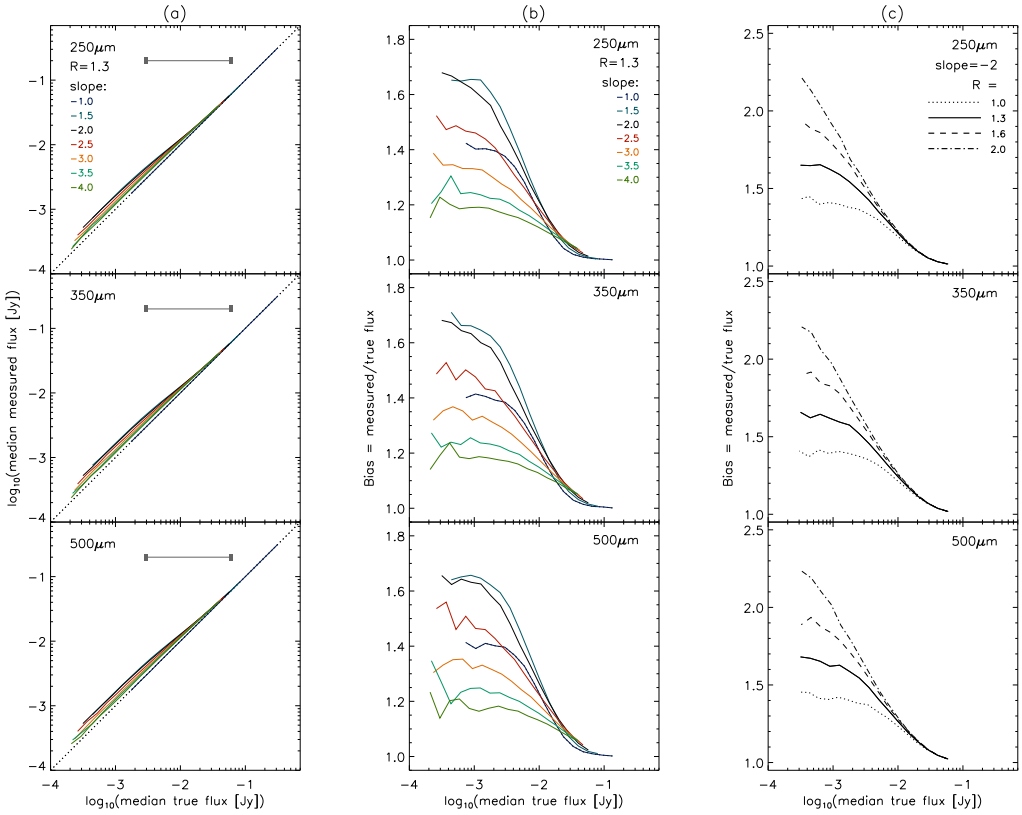

Figure B.1: Results of a set of stacking simulations: **(a)** Comparing median measured flux and median true flux, for distributions in various flux ranges. The range in each simulation is given by $R = \log_{10}(S_{\rm max}/S_{\rm min}) = 1.3$ (the length of the grey horizontal bar), and the simulations were run 16 times with different $S_{\rm min}, S_{\rm max}$ values to produce distributions with a range of median (true) fluxes. Each coloured line in the Figure connects 16 data points, one point from each simulation, showing how the median measured flux (after adding noise) varies as the median true flux is varied. Noise is drawn from a Gaussian distribution centred on zero, with $\sigma = 6.7, 7.9, 8.8\,{\rm mJy\,beam}^{-1}$ at 250, 350, 500 μm respectively. Different coloured lines correspond to sets of simulations with different slopes of dN/dS between -1 and -4. **(b)** Bias factor (ratio of median measured to median true flux) as a function of median true flux, for the same set of simulations, showing how the bias depends on the slope of dN/dS for $R = 1.3$. Note that bias does not vary monotonically with slope for fixed R, but is greatest for a slope of -1.5 in this case. **(c)** Bias factor as a function of median true flux, showing the effect of increasing the range of true fluxes. Different lines correspond to sets of simulations with different values of R between 1 and 2; in each of these the slope of dN/dS is -2.

Appendix C

Results of Stacking the GAMA Sample

In Figures C.1 – C.4 I choose some example bins from Chapter 3 to show the stacked postage-stamp images, the distribution of measured fluxes, and the SED data and model. The figures below contain the following information:

Postage stamps of the stack in the three SPIRE bands are shown with contours at signal-to-noise levels of 5, 10, 15, 20, 25, 50, 100, 150, 200 & 250. The images are each 41 pixels square, corresponding to $3'25''$ at 250 μm and $6'50''$ in the other two bands. These images are illustrative only, and were made by stacking in the PSF-filtered, background-subtracted SPIRE maps (I do not measure fluxes in these maps but using the deblend filter method described in Appendix A). The flux and signal-to-noise reached in the central pixel of each postage stamp agree with the stacked values in Table C.1, although the postage stamps show slightly boosted fluxes due to blending not being accounted for. Similar agreement was found in all stacks, although only a selection are shown here for brevity.

I also show histograms of the measured fluxes in the stack (red) and of a set of fluxes measured at random positions in the background (blue), as described in Section 3.4. The number shown is the KS probability that these two samples were drawn from the same distribution. Beneath these is plotted the single-component SED fitted to the three stacked fluxes (plotted in the rest frame), assuming $\beta = 2$. The SED is fitted to obtain the temperature which is printed over the SED, as described in Section 3.5.

Statistics and results for all of the stacks from Chapter 3 are included in Table C.1.

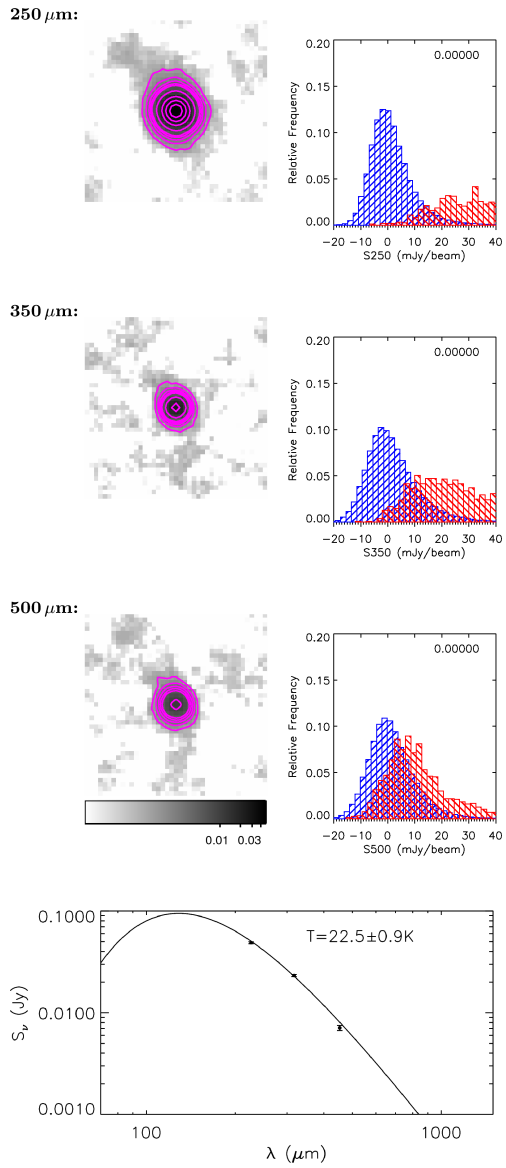

Figure C.1: A stack of galaxies with blue $g-r$ colours, median $M_r = -21.1$, median $z = 0.11$. This stack is one of the brightest in sub-mm flux, and contains 1567 objects. Stacked, PSF-filtered postage stamps are shown with a logarithmic greyscale between $0.0001 - 0.05\,\mathrm{Jy\,beam^{-1}}$ and signal-to-noise contours at 5, 10, 15, 20, 25, 50, 100, 150, 200, 250. Histograms of the measured fluxes in the stack (red) and in a random background stack (blue) are shown with the KS probability that they were drawn from the same distribution. Also plotted is the rest-frame SED fit with the temperature indicated, assuming $\beta = 2$. More details are given in the text above.

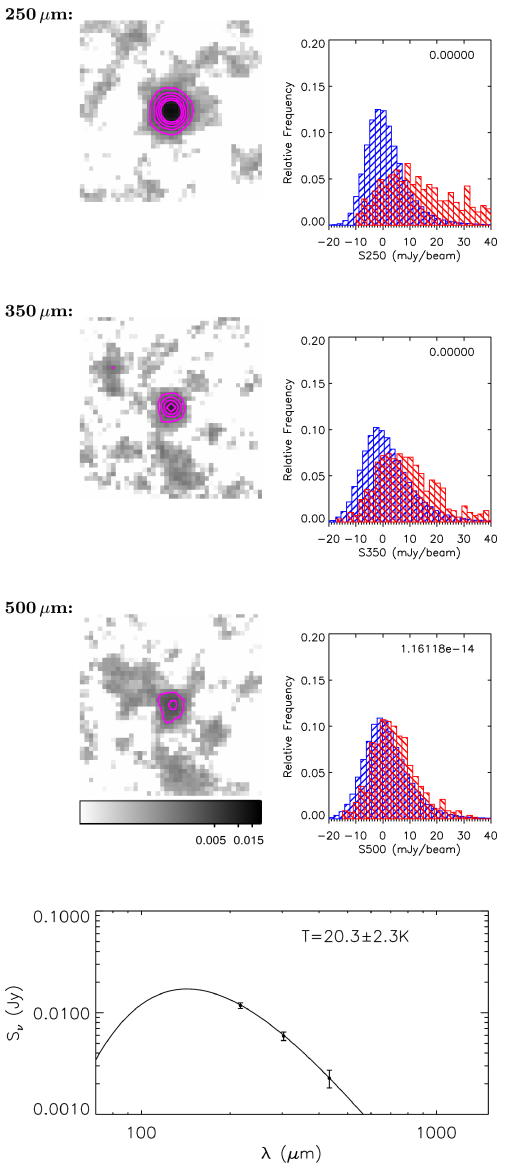

Figure C.2: A stack of galaxies with green $g-r$ colours, median $M_r = -21.1$, median $z = 0.15$. This stack has moderate sub-mm flux, and contains 570 objects. Plots are as in Figure C.1 except that the postage stamps are plotted on a logarithmic greyscale between $0.0001 - 0.02\,\mathrm{Jy\,beam^{-1}}$.

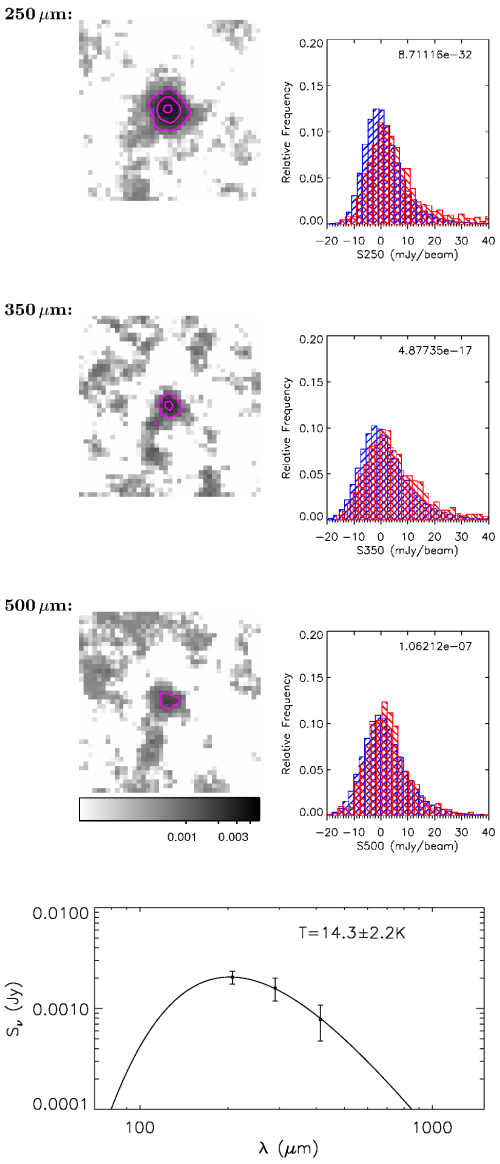

Figure C.3: A stack of galaxies with red $g-r$ colours, median $M_r = -21.7$, median $z = 0.21$. This stack has among the faintest sub-mm fluxes, and contains 1111 objects. Plots are as in Figure C.1 except that the postage stamps are plotted on a logarithmic greyscale between $0.0001 - 0.005$ Jy beam^{-1}.

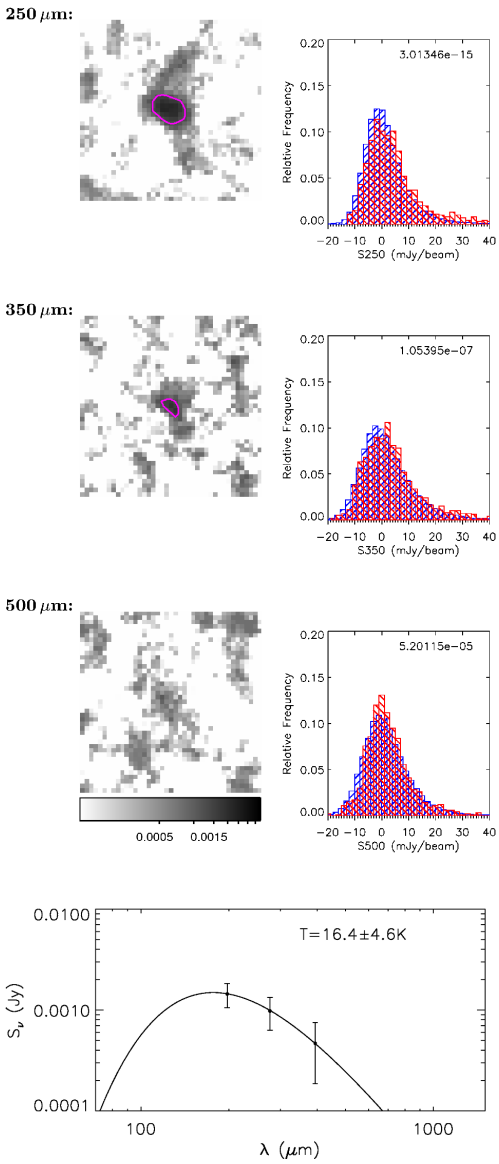

Figure C.4: A stack of galaxies with red $g-r$ colours, median $M_r = -22.5$, median $z = 0.27$. This stack has among the faintest sub-mm fluxes, and contains 1002 objects. Plots are as in Figure C.1 except that the postage stamps are plotted on a logarithmic greyscale between $0.0001 - 0.004$ Jy beam^{-1}.

Table C.1: Results of stacking in bins of $g-r$ colour, redshift, and absolute magnitude (M_r). Columns are as follows: colour bin C = B (blue), G (green), R (red); median redshift $\langle z \rangle$ in bin (approximate z bin boundaries are 0.01, 0.12, 0.17, 0.22, 0.28, 0.35); median M_r; count N in the bin. The following columns for each of the three SPIRE bands: background-subtracted flux S in mJy; signal-to-noise ratio $S/\sigma_{\rm N}$; measurement error $\sigma_{\rm N}$ (mJy) computed from the mean variance of positions in the stack, divided by $\sqrt{N}$, and including the error on background subtraction; statistical error on the median flux ($\sigma_{\rm S}$, mJy) following Gott *et al.* (2001); KS probability that the distribution of fluxes in each bin is the same as that at a set of random positions.

				250 μm					350 μm					500 μm				
C	$\langle z \rangle$	M_r	N	S	SNR	$\sigma_{\rm N}$	$\sigma_{\rm S}$	KS	S	SNR	$\sigma_{\rm N}$	$\sigma_{\rm S}$	KS	S	SNR	$\sigma_{\rm N}$	$\sigma_{\rm S}$	KS
B	0.11	-21.1	1567	48.69	286.4	0.17	1.15	0	23.15	178.1	0.13	0.58	0	7.11	59.3	0.12	0.41	0
B	0.10	-20.1	1568	15.72	104.8	0.15	0.46	0	7.70	70.0	0.11	0.30	0	3.01	30.1	0.10	0.28	0
B	0.10	-19.6	1567	8.69	62.1	0.14	0.31	0	5.02	45.6	0.11	0.31	0	2.00	20.0	0.10	0.29	3E-39
B	0.09	-19.2	1568	5.60	43.1	0.13	0.34	0	3.33	33.3	0.10	0.31	0	1.63	16.3	0.10	0.30	5E-21
B	0.08	-18.6	1567	4.24	35.3	0.12	0.24	0	2.60	26.0	0.10	0.36	9E-43	1.42	14.2	0.10	0.30	1E-17
B	0.04	-17.5	1567	2.82	23.5	0.12	0.25	0	2.16	21.6	0.10	0.28	1E-26	1.40	14.0	0.10	0.27	7E-14
B	0.15	-21.7	1300	39.05	216.9	0.18	0.73	0	17.58	125.6	0.14	0.39	0	5.12	42.7	0.12	0.27	0
B	0.15	-21.0	1300	19.14	112.5	0.17	0.32	0	8.34	64.2	0.13	0.28	0	2.80	25.4	0.11	0.27	0
B	0.15	-20.6	1300	11.42	71.4	0.16	0.31	0	5.26	43.8	0.12	0.37	0	1.87	17.0	0.11	0.26	1E-25
B	0.15	-20.3	1300	7.88	52.5	0.15	0.32	0	3.73	33.9	0.11	0.27	0	1.52	13.8	0.11	0.28	1E-14
B	0.15	-20.1	1300	5.71	40.8	0.14	0.35	0	3.08	28.0	0.11	0.41	6E-45	1.29	11.7	0.11	0.29	7E-14
B	0.14	-19.7	1299	3.67	28.2	0.13	0.25	0	2.18	19.8	0.11	0.34	8E-27	1.09	9.9	0.11	0.38	2E-06
B	0.21	-22.0	1295	30.11	167.3	0.18	0.61	0	13.80	98.6	0.14	0.44	0	3.86	32.2	0.12	0.28	0
B	0.21	-21.5	1295	18.94	111.4	0.17	0.49	0	8.27	63.6	0.13	0.26	0	2.54	23.0	0.11	0.31	0
B	0.21	-21.2	1295	12.59	78.7	0.16	0.35	0	5.55	46.3	0.12	0.38	0	1.92	17.5	0.11	0.33	4E-22
B	0.21	-20.9	1295	9.75	65.0	0.15	0.27	0	4.63	38.6	0.12	0.30	0	1.85	16.8	0.11	0.27	6E-23
B	0.20	-20.7	1295	7.29	48.6	0.15	0.30	0	3.77	34.3	0.11	0.33	0	1.41	12.8	0.11	0.35	7E-14
B	0.19	-20.4	1294	5.64	40.3	0.14	0.27	0	2.54	23.1	0.11	0.33	3E-34	1.40	12.7	0.11	0.31	5E-12

Table C.1 continued

				250 μm					350 μm					500 μm				
C	z	M_r	N	S	SNR	$\sigma_{\rm N}$	$\sigma_{\rm S}$	KS	S	SNR	$\sigma_{\rm N}$	$\sigma_{\rm S}$	KS	S	SNR	$\sigma_{\rm N}$	$\sigma_{\rm S}$	KS
B	0.27	-22.3	1323	24.65	145.0	0.17	0.64	0	11.63	89.5	0.13	0.39	0	3.61	32.8	0.11	0.38	0
B	0.27	-21.9	1324	17.31	108.3	0.16	0.50	0	7.72	64.3	0.12	0.52	0	2.66	24.2	0.11	0.30	4E-44
B	0.27	-21.6	1324	13.19	82.4	0.16	0.30	0	5.97	49.8	0.12	0.42	0	2.13	19.4	0.11	0.30	7E-33
B	0.27	-21.4	1324	10.59	70.6	0.15	0.34	0	5.03	41.9	0.12	0.37	0	1.78	16.2	0.11	0.31	1E-17
B	0.26	-21.2	1324	8.88	59.2	0.15	0.33	0	4.65	42.3	0.11	0.38	0	2.05	18.6	0.11	0.30	2E-27
B	0.26	-21.0	1323	6.90	49.3	0.14	0.24	0	3.94	35.8	0.11	0.29	0	1.63	14.8	0.11	0.26	1E-20
B	0.30	-21.4	1377	8.99	59.9	0.15	0.40	0	4.37	39.7	0.11	0.43	0	1.64	16.4	0.10	0.30	7E-17
B	0.32	-22.6	1377	17.22	107.6	0.16	0.67	0	9.22	76.8	0.12	0.48	0	2.99	27.2	0.11	0.26	0
B	0.32	-22.2	1377	15.30	95.6	0.16	0.67	0	7.30	60.8	0.12	0.40	0	2.26	20.5	0.11	0.36	2E-34
B	0.32	-21.9	1377	11.64	77.6	0.15	0.43	0	5.80	48.3	0.12	0.29	0	2.05	18.6	0.11	0.29	2E-29
B	0.32	-21.8	1377	11.65	77.7	0.15	0.39	0	5.45	49.5	0.11	0.32	0	1.82	18.2	0.10	0.30	3E-23
B	0.31	-21.6	1377	11.41	76.1	0.15	0.41	0	5.66	51.5	0.11	0.28	0	2.00	18.2	0.11	0.30	2E-30
G	0.11	-21.8	452	43.13	139.1	0.31	2.57	0	19.79	82.5	0.24	1.20	0	6.64	31.6	0.21	0.65	0
G	0.10	-21.0	452	36.34	121.1	0.30	2.18	0	15.82	65.9	0.24	1.16	0	4.22	21.1	0.20	0.87	1E-37
G	0.10	-20.4	452	23.80	82.1	0.29	1.30	0	12.13	55.1	0.22	0.88	0	4.58	22.9	0.20	0.68	8E-29
G	0.10	-19.9	452	12.58	46.6	0.27	0.87	0	5.95	29.8	0.20	0.58	0	2.04	11.3	0.18	0.42	1E-10
G	0.10	-19.3	452	6.78	27.1	0.25	0.74	0	3.28	17.3	0.19	0.44	7E-23	1.93	10.2	0.19	0.48	6E-08
G	0.06	-18.4	452	4.44	19.3	0.23	0.43	3E-37	2.37	13.2	0.18	0.65	4E-12	1.29	7.2	0.18	0.47	1E-04
G	0.15	-22.1	569	19.23	76.9	0.25	1.71	0	8.91	46.9	0.19	0.72	0	2.92	18.3	0.16	0.40	3E-24
G	0.15	-21.5	570	15.47	61.9	0.25	1.04	0	7.85	41.3	0.19	0.67	0	2.36	14.8	0.16	0.40	7E-18
G	0.15	-21.1	570	11.74	48.9	0.24	0.76	0	5.89	32.7	0.18	0.56	0	2.27	13.4	0.17	0.44	1E-14
G	0.16	-20.7	570	11.31	49.2	0.23	0.82	0	4.87	28.6	0.17	0.69	4E-41	1.33	8.3	0.16	0.40	3E-09
G	0.15	-20.4	570	9.12	39.7	0.23	0.63	0	4.41	25.9	0.17	0.47	2E-34	1.79	11.1	0.16	0.51	1E-07
G	0.14	-19.9	569	5.40	25.7	0.21	0.43	0	2.88	18.0	0.16	0.54	3E-20	1.56	9.8	0.16	0.42	1E-07

Table C.1 continued

				250 μm					350 μm					500 μm				
C	z	M_r	N	S	SNR	$\sigma_{\rm N}$	$\sigma_{\rm S}$	KS	S	SNR	$\sigma_{\rm N}$	$\sigma_{\rm S}$	KS	S	SNR	$\sigma_{\rm N}$	$\sigma_{\rm S}$	KS
G	0.21	-22.3	619	8.30	39.5	0.21	0.77	0	5.12	32.0	0.16	0.74	3E-38	2.00	13.3	0.15	0.34	2E-17
G	0.21	-21.8	620	8.17	38.9	0.21	0.55	0	4.11	25.7	0.16	0.68	2E-36	1.70	11.3	0.15	0.32	3E-10
G	0.21	-21.5	620	7.09	33.8	0.21	0.58	0	4.34	27.1	0.16	0.66	3E-35	1.96	12.3	0.16	0.50	8E-12
G	0.21	-21.2	619	6.56	31.2	0.21	0.62	0	3.80	23.8	0.16	0.64	2E-29	1.14	7.6	0.15	0.52	2E-05
G	0.21	-20.9	620	5.90	28.1	0.21	0.46	0	3.41	21.3	0.16	0.51	6E-27	1.65	10.3	0.16	0.38	8E-11
G	0.20	-20.6	619	5.36	26.8	0.20	0.50	0	2.80	17.5	0.16	0.58	8E-20	1.50	9.4	0.16	0.35	4E-07
G	0.27	-22.6	662	5.31	27.9	0.19	0.73	0	3.18	21.2	0.15	0.57	2E-23	1.56	11.1	0.14	0.31	8E-09
G	0.27	-22.1	663	6.19	31.0	0.20	0.50	0	4.13	25.8	0.16	0.49	5E-34	1.77	11.8	0.15	0.54	1E-10
G	0.27	-21.8	662	6.14	30.7	0.20	0.63	0	3.65	24.3	0.15	0.52	6E-26	1.63	10.9	0.15	0.44	4E-09
G	0.27	-21.6	663	6.31	31.6	0.20	0.49	0	3.69	23.1	0.16	0.56	2E-31	1.63	10.9	0.15	0.34	8E-09
G	0.27	-21.4	662	5.42	27.1	0.20	0.49	0	2.78	18.5	0.15	0.52	4E-17	1.15	7.7	0.15	0.34	3E-04
G	0.26	-21.2	662	4.85	25.5	0.19	0.54	0	2.37	15.8	0.15	0.38	2E-18	1.14	7.6	0.15	0.48	2E-05
G	0.32	-22.8	653	4.39	23.1	0.19	0.84	0	3.03	20.2	0.15	0.47	7E-24	1.57	11.2	0.14	0.34	9E-10
G	0.32	-22.4	653	4.78	25.2	0.19	0.67	0	3.38	22.5	0.15	0.50	9E-25	1.31	8.7	0.15	0.40	8E-08
G	0.32	-22.1	653	5.84	29.2	0.20	0.68	0	3.96	24.8	0.16	0.50	1E-32	1.49	9.9	0.15	0.33	1E-09
G	0.32	-21.9	653	4.68	24.6	0.19	0.57	0	2.81	18.7	0.15	0.45	5E-22	1.03	6.9	0.15	0.33	4E-04
G	0.31	-21.8	653	5.97	29.9	0.20	0.59	0	3.95	24.7	0.16	0.60	8E-29	1.37	9.1	0.15	0.30	6E-07
G	0.30	-21.6	653	5.04	26.5	0.19	0.32	0	2.73	18.2	0.15	0.50	4E-20	1.35	9.0	0.15	0.30	6E-07
R	0.10	-21.7	991	5.52	34.5	0.16	0.47	0	3.72	31.0	0.12	0.47	2E-43	1.86	15.5	0.12	0.34	3E-24
R	0.10	-21.0	992	5.66	35.4	0.16	0.59	0	3.75	28.8	0.13	0.55	5E-43	1.98	16.5	0.12	0.40	2E-17
R	0.10	-20.4	991	4.71	29.4	0.16	0.72	0	3.70	28.5	0.13	0.46	3E-39	2.00	16.7	0.12	0.36	9E-17
R	0.10	-19.8	992	4.21	28.1	0.15	0.56	0	2.65	22.1	0.12	0.42	2E-23	1.19	9.9	0.12	0.31	4E-07
R	0.08	-18.9	991	2.97	21.2	0.14	0.32	6E-45	1.84	15.3	0.12	0.27	1E-16	1.09	9.1	0.12	0.35	2E-05

Table C.1 continued

				250 μm					350 μm					500 μm				
C	z	M_r	N	S	SNR	$\sigma_{\rm N}$	$\sigma_{\rm S}$	KS	S	SNR	$\sigma_{\rm N}$	$\sigma_{\rm S}$	KS	S	SNR	$\sigma_{\rm N}$	$\sigma_{\rm S}$	KS
R	0.15	-22.0	1177	3.52	27.1	0.13	0.44	0	2.00	20.0	0.10	0.32	3E-22	0.96	9.6	0.10	0.33	2E-11
R	0.15	-21.3	1177	2.50	19.2	0.13	0.35	2E-42	2.15	19.5	0.11	0.37	2E-23	1.06	9.6	0.11	0.29	4E-12
R	0.15	-20.9	1177	2.51	19.3	0.13	0.36	3E-38	1.84	16.7	0.11	0.33	3E-15	1.01	9.2	0.11	0.28	6E-08
R	0.15	-20.5	1177	2.96	22.8	0.13	0.44	0	2.29	20.8	0.11	0.46	9E-21	0.94	8.5	0.11	0.32	9E-06
R	0.14	-20.1	1177	2.68	20.6	0.13	0.28	5E-44	1.83	16.6	0.11	0.32	2E-16	1.01	9.2	0.11	0.33	4E-06
R	0.21	-22.3	1110	2.11	16.2	0.13	0.29	3E-28	1.41	14.1	0.10	0.34	3E-13	0.87	7.9	0.11	0.27	7E-10
R	0.21	-21.7	1111	2.25	17.3	0.13	0.30	9E-32	1.94	17.6	0.11	0.40	5E-17	1.14	10.4	0.11	0.30	1E-07
R	0.21	-21.3	1110	2.03	15.6	0.13	0.28	8E-27	1.47	13.4	0.11	0.38	3E-11	1.13	10.3	0.11	0.29	7E-06
R	0.20	-21.0	1111	2.43	18.7	0.13	0.29	9E-35	1.89	17.2	0.11	0.33	1E-16	1.11	10.1	0.11	0.38	2E-06
R	0.19	-20.7	1110	2.63	18.8	0.14	0.38	5E-42	2.05	18.6	0.11	0.32	4E-19	1.08	9.8	0.11	0.29	4E-06
R	0.27	-22.5	1002	1.59	12.2	0.13	0.40	3E-15	1.19	10.8	0.11	0.35	1E-07	0.69	6.3	0.11	0.28	5E-05
R	0.27	-22.0	1002	2.23	15.9	0.14	0.33	6E-28	2.07	17.3	0.12	0.42	4E-15	1.04	8.7	0.12	0.26	4E-07
R	0.27	-21.7	1003	1.80	12.9	0.14	0.33	2E-20	1.86	16.9	0.11	0.43	8E-14	0.91	7.6	0.12	0.30	2E-04
R	0.27	-21.5	1002	2.44	17.4	0.14	0.35	2E-31	1.75	14.6	0.12	0.44	2E-12	0.99	8.3	0.12	0.27	2E-06
R	0.26	-21.2	1002	2.87	20.5	0.14	0.38	6E-42	2.04	17.0	0.12	0.39	6E-17	1.12	9.3	0.12	0.46	1E-04
R	0.32	-22.8	903	1.68	12.0	0.14	0.30	1E-16	1.57	13.1	0.12	0.33	9E-10	0.86	7.2	0.12	0.34	2E-05
R	0.32	-22.3	904	2.09	14.9	0.14	0.36	2E-22	1.37	11.4	0.12	0.44	1E-10	0.89	7.4	0.12	0.31	6E-05
R	0.32	-22.1	903	1.70	12.1	0.14	0.45	1E-18	1.50	12.5	0.12	0.40	6E-09	0.67	5.2	0.13	0.37	4E-02
R	0.32	-21.9	904	2.12	15.1	0.14	0.35	2E-26	1.64	13.7	0.12	0.31	4E-11	0.92	7.7	0.12	0.27	3E-04
R	0.30	-21.7	903	3.38	22.5	0.15	0.36	8E-45	1.93	16.1	0.12	0.38	3E-13	0.94	7.8	0.12	0.48	1E-03

Appendix D

Images, Spectra and Notes on Galaxies in the 500 μm Sample

The following pages contain SDSS gri colour images, 250 μm contour maps, integrated CO spectra and CO zeroth moment (integrated intensity) maps for each of the galaxies observed with HARP and RxA. The size of each SDSS image is equal to the HARP footprint, i.e. 2′ on a side, for ease of reference. Adjacent to the colour image is a SPIRE 250 μm contour map (contours at 10, 30, 50, 70, 90 per cent of the maximum pixel value) overlaid on the r-band grey-scale, which is linearly scaled between the 2$^{\rm nd}$ and 98$^{\rm th}$ percentiles. These images are also shown for the galaxies not observed in CO.

HARP/RxA moment maps are rebinned spatially by a factor 2×2, and are masked outside of the elliptical apertures used. Maps are presented at a common angular scale, with ellipses indicating the extent of the sub-mm and optical emission. Spectra are rebinned to 20 $\mathrm{km\,s^{-1}}$ resolution where the signal-to-noise is high, or 40 $\mathrm{km\,s^{-1}}$ or 80 $\mathrm{km\,s^{-1}}$ resolution where necessary to make the line stand out. Many of the detections have too low signal-to-noise for the moment maps to be instructive, yet their integrated intensities constitute significant detections as shown in Section 4.3.3.

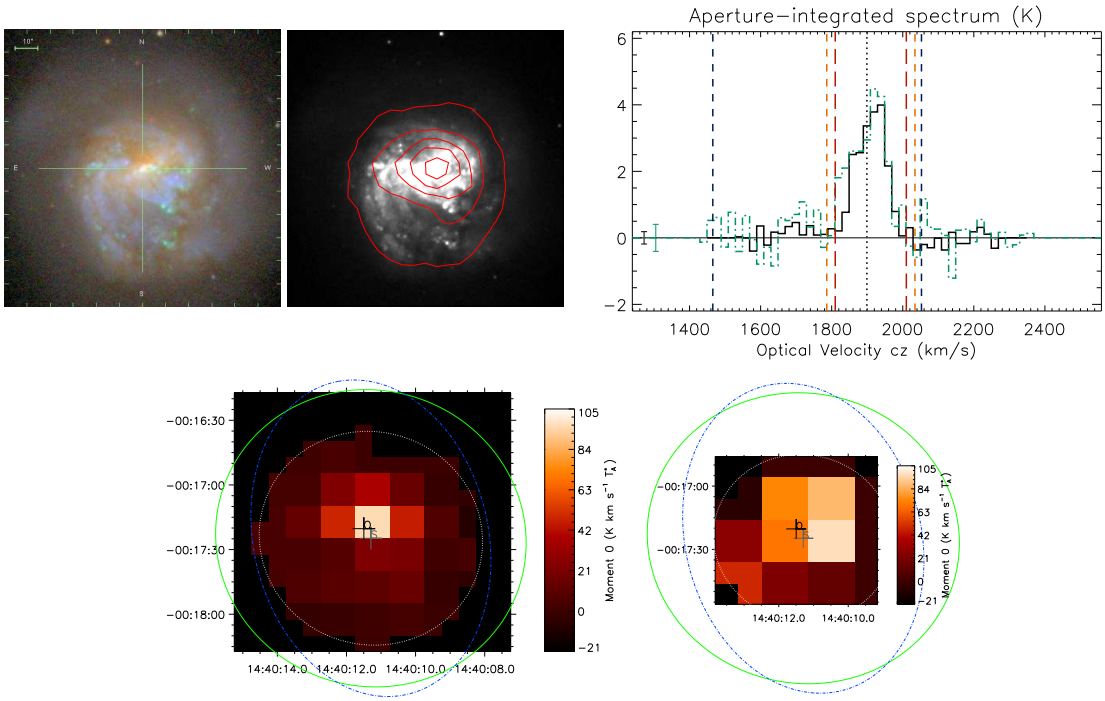

Figure D.1: NGC 5713. Top: SDSS image, 250 μm contours, and aperture-integrated spectra in HARP (black) and RxA (green). Blue lines = H I line width from HIPASS; orange = CO line width from literature; red = CO width integrated over for moment maps. Below: rebinned moment maps in HARP (left) and RxA (right). In these, O marks the optical centroid and S the SPIRE centroid; the green line is the SPIRE Kron ellipse and blue is the B-band D_{25} isophote. The white line marks the aperture within which the total flux was integrated.

NGC 5713: This face-on spiral galaxy was well detected and mapped in both emission lines, and both CO(3–2) and CO(2–1) components are extended in the galaxy. The overall line ratio is $R_{32} = I_{32}/I_{21} = 0.82 \pm 0.07$, which is consistent with typical spiral galaxies, but the CO(3–2) emission is more centrally concentrated than the CO(2–1) indicating a higher line ratio in the nucleus. The galaxy is classified SABbc on NED, and is flagged as peculiar and an HII emitter. It is in a pair with NGC 5719, at a projected separation of about 80 kpc (11.3′) with approximately the same radial velocity. It also has a high 60/500 μm flux ratio (see Table 4.1), only exceeded by SDP 15 and SDP 1 which are both classified as AGN in NED. All of this is consistent with NGC 5713 being a starburst galaxy (e.g. Albrecht, Krügel & Chini 2007), in which the CO excitation is higher in the warm, dense starbursting environment (e.g. Papadopoulos *et al.* 2012). This galaxy is therefore unusual compared with the rest of the sample, which is dominated by cold, dusty galaxies.

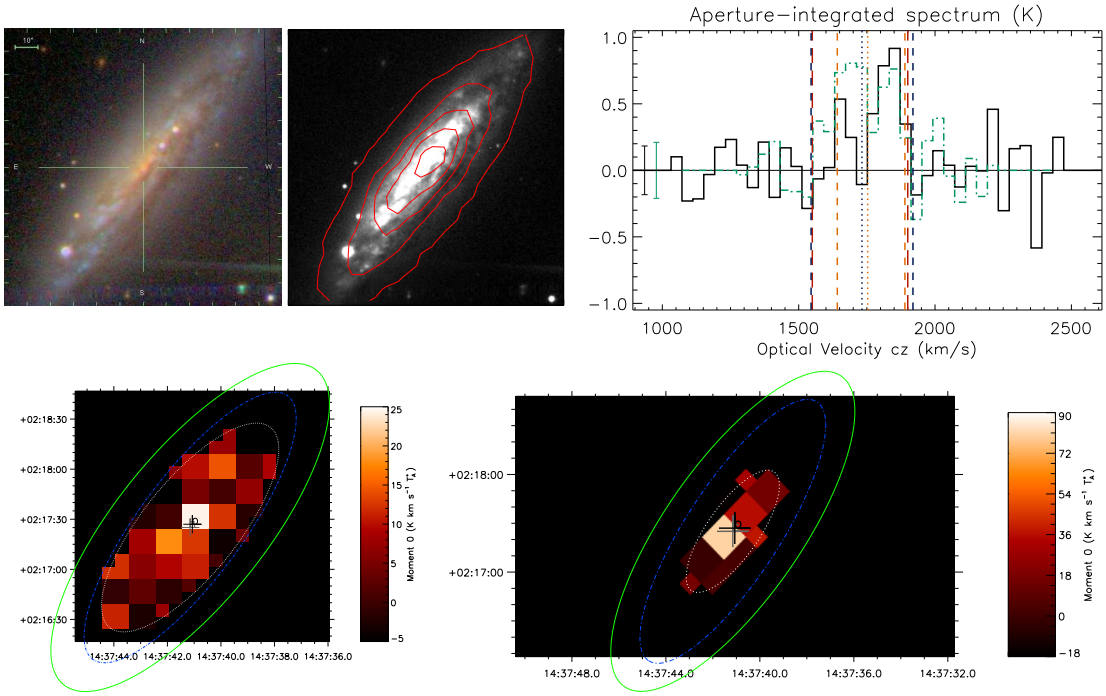

Figure D.2: NGC 5690. Top: SDSS image, 250 μm contours, and aperture-integrated spectra in HARP (black) and RxA (green). Blue lines = H I line width from HIPASS; orange = CO line width from literature; red = CO width integrated over for moment maps. Below: rebinned moment maps in HARP (left) and RxA (right). 'O' marks the optical centroid and 'S' the SPIRE centroid; the green line is the SPIRE Kron ellipse and blue is the B-band D_{25} isophote. The white line marks the aperture within which the total flux was integrated.

NGC 5690: This galaxy is an isolated, highly inclined and extended spiral (type Sc). It is detected in both images and can be coarsely mapped; a rotation curve was evident in the spectra in the cube. Intensity grows in the curve of growth out to $a = 45''$ in CO(2–1), and to around $75''$ in CO(3–2), which is within the optical size. It is unlikely that the CO(3–2) is more extended than the CO(2–1), and the discrepancy is more likely due to differences in the noise in the two maps; the signal-to-noise is lower in the CO(2–1) map so that any rise in the curve of growth at high radii may be undetectable. On the other hand, the extent of the SPIRE emission is only $60''$ so the apparent rise in the HARP curve of growth beyond this may simply be noise (the flux within $60''$ is consistent within 1σ of the flux within $75''$). The overall line ratio is $R_{32} = 0.80 \pm 0.21$, similar to that of NGC 5713.

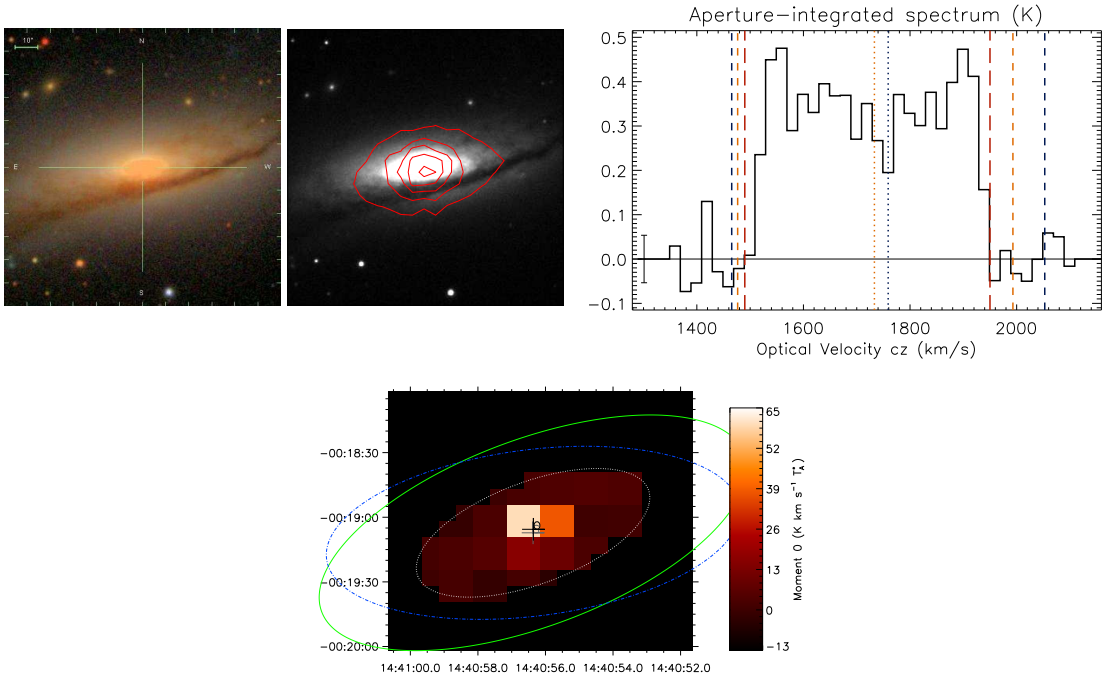

Figure D.3: NGC 5719. Top: SDSS image, 250 μm contours, and aperture-integrated spectra from HARP. Blue lines = H I line width from HIPASS; orange = CO line width from literature; red = CO width integrated over for moment maps. Below: rebinned moment map. 'O' marks the optical centroid and 'S' the SPIRE centroid; the green line is the SPIRE Kron ellipse and blue is the B-band D_{25} isophote. The white line marks the aperture within which the total flux was integrated.

NGC 5719: This source was only observed with HARP, and we obtained an excellent detection with clearly extended emission, a good signal-to-noise map and an obvious rotation curve. Most of the emission is within the central $a = 20''$ aperture (as is most of the FIR/sub-mm emission), although there appears to be extended emission out to $a = 55''$, coincident with extended low-surface-brightness emission in the SPIRE images and a dark dust ring visible in the optical. NGC 5719 is classified as an early-type spiral (SABa) but is peculiar due to the strong, warped dust ring that is clearly visible in the SDSS image. The galaxy is known to have a counter-rotating disk of ionized gas and stars, likely as a result of an interaction with NGC 5713 (Vergani *et al.* 2007; Coccato *et al.* 2011). The rotation curve of the molecular gas matches that of the counter-rotating disk, rather than that of the main stellar component. The gas and dust probably accreted onto NGC 5719 during the interaction and the presence of dense molecular gas suggests that this is fuelling star-formation in the counter-rotating disk.

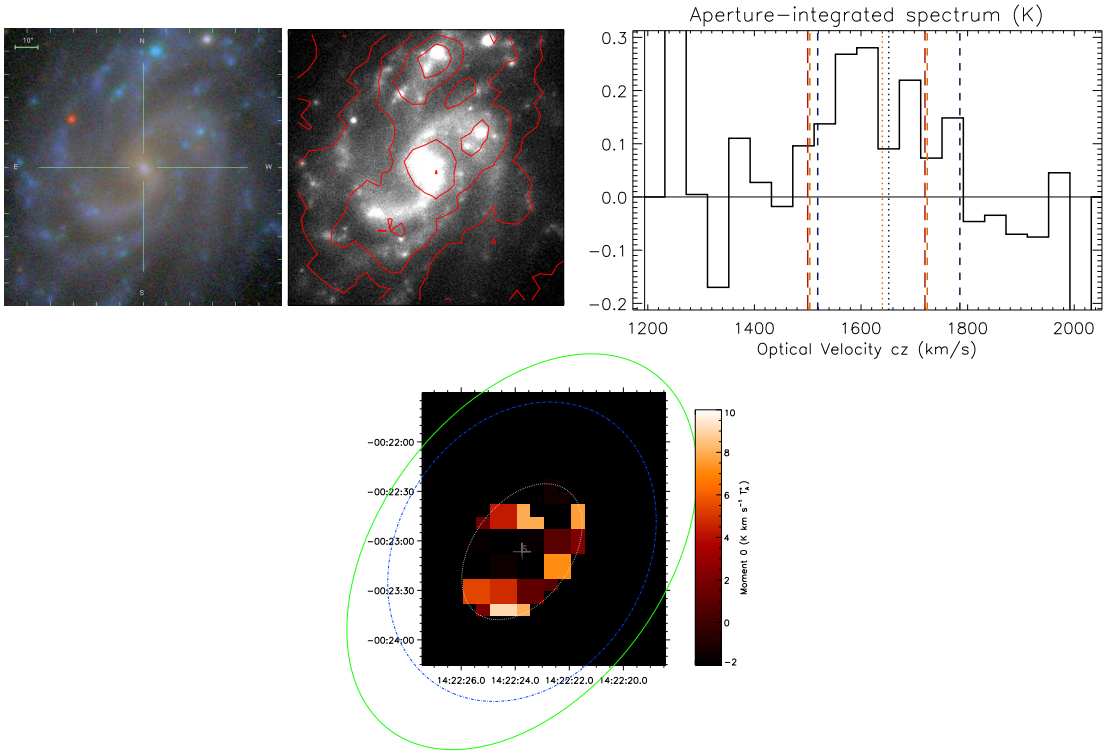

Figure D.4: NGC 5584. Top: SDSS image, 250 μm contours, and aperture-integrated spectra from HARP. Blue lines = H I line width from HIPASS; orange = CO line width from literature; red = CO width integrated over for moment maps. Below: rebinned moment map. 'O' marks the optical centroid and 'S' the SPIRE centroid; the green line is the SPIRE Kron ellipse and blue is the B-band D_{25} isophote. The white line marks the aperture within which the total flux was integrated.

NGC 5584: This galaxy is an isolated, face-on, late-type spiral (SABcd in NED) and is extended over about 2 arcminutes, hence has low surface brightness and requires a large map. Nevertheless, the dust surface brightness is high so one would expect to detect CO across the galaxy. We used two overlapping HARP pointings to cover the full galaxy and to achieve double coverage in the centre. However, despite repeated observations on different nights, some of the data suffered from ripples in the baselines, high system temperatures and spikes. Noisy receptors were masked and baselines were fitted to various different spectral ranges with 1st and 2nd order polynomials in order to achieve flat spectra; however residual baselines remained in many pixels. A large aperture is required to obtain any detection; in fact no significant emission is detected within the central $a \sim 30''$ aperture. A larger aperture does collect significant emission, showing that dense gas in this galaxy is distributed within the outer spiral arms and is very clumpy (consistent with the blue star-forming regions visible in the SDSS image).

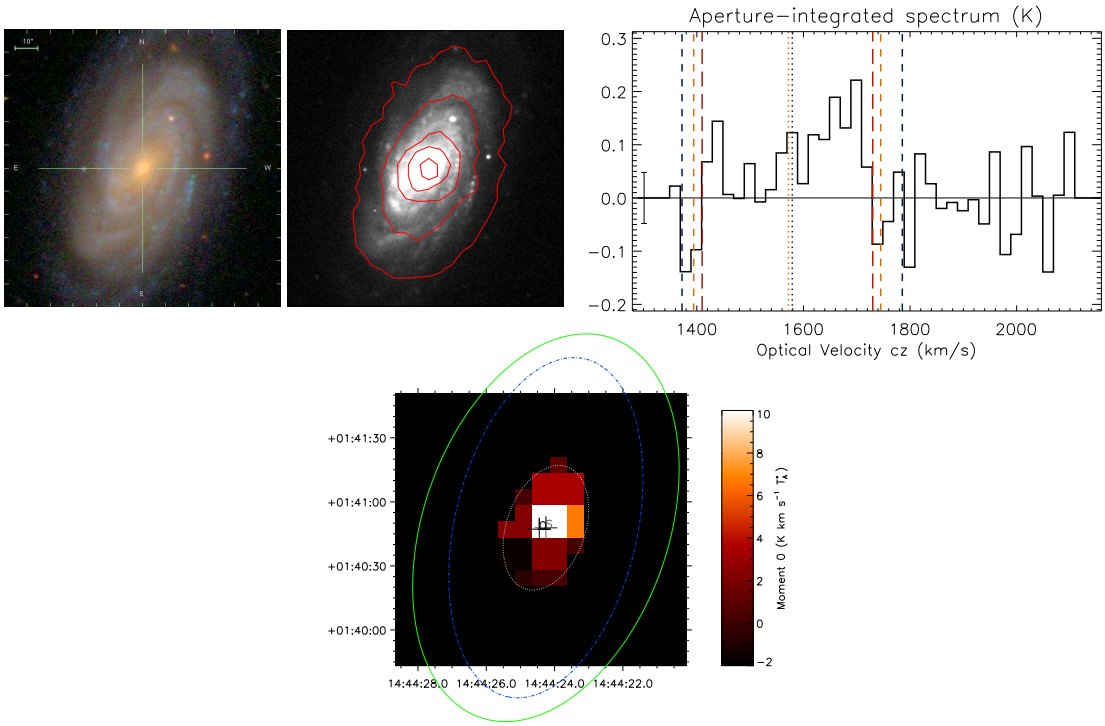

Figure D.5: NGC 5740. Top: SDSS image, 250 μm contours, and aperture-integrated spectra from HARP. Blue lines = H I line width from HIPASS; orange = CO line width from literature; red = CO width integrated over for moment maps. Below: rebinned moment map. 'O' marks the optical centroid and 'S' the SPIRE centroid; the green line is the SPIRE Kron ellipse and blue is the B-band D_{25} isophote. The white line marks the aperture within which the total flux was integrated.

NGC 5740: This is another galaxy observed only with HARP. A good detection of the total intensity was obtained within $a = 30''$, consistent with the extent of the SPIRE emission, and a rotation curve was evident in the cube. It is an extended SABb-type spiral in a pair with NGC 5746, with a projected separation of about 120 kpc (18.3′), offset in radial velocity by about 150 $\mathrm{km\,s^{-1}}$.

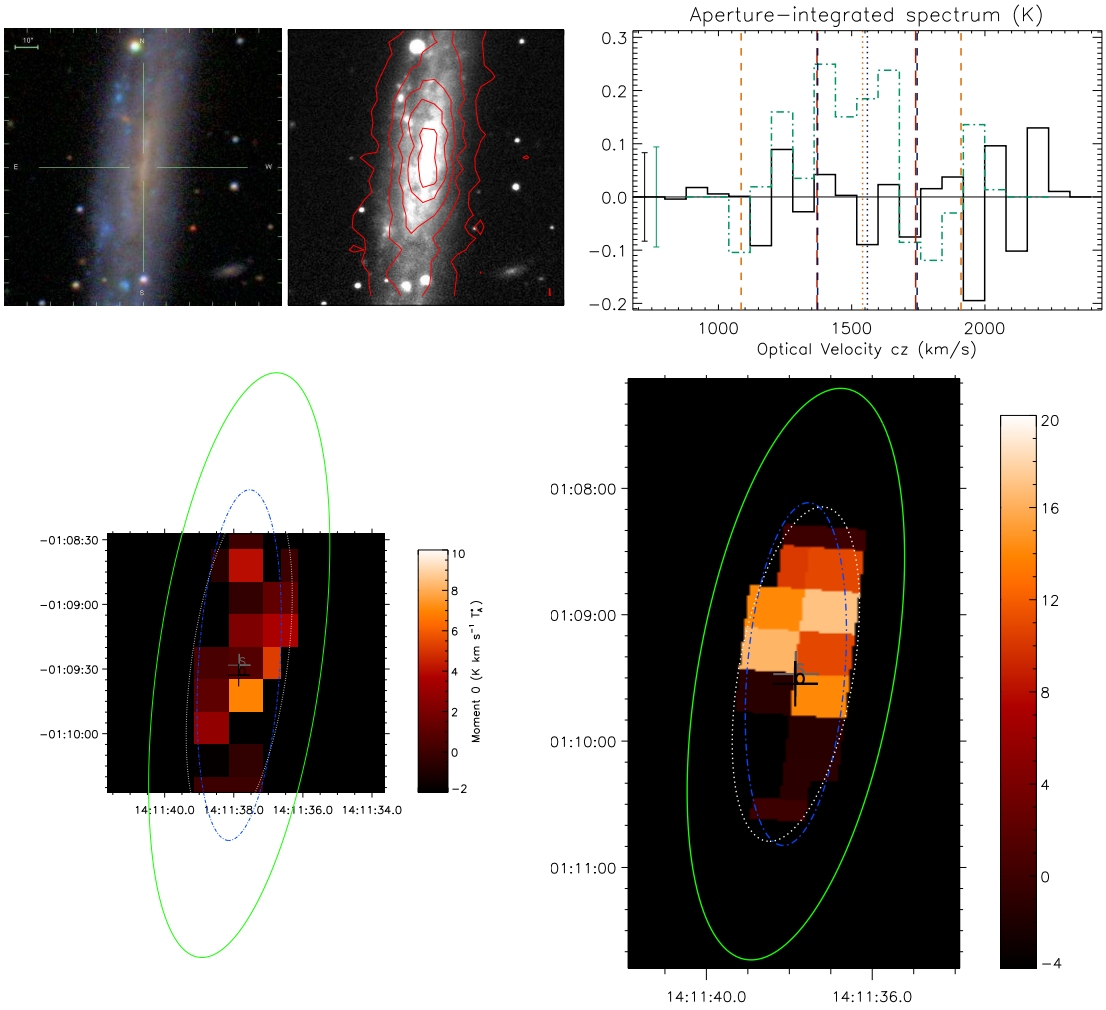

Figure D.6: NGC 5496. Top: SDSS image, 250 μm contours, and aperture-integrated spectra in HARP (black) and RxA (green). Blue lines = H I line width from HIPASS; orange = CO line width from literature; red = CO width integrated over for moment maps. Below: rebinned moment maps in HARP (left) and RxA (right). 'O' marks the optical centroid and 'S' the SPIRE centroid; the green line is the SPIRE Kron ellipse and blue is the B-band D_{25} isophote. The white line marks the aperture within which the total flux was integrated.

NGC 5496: This is an extended, low-surface-brightness, edge-on disk galaxy, with a blue colour similar to NGC 5584. The HARP map may contain some emission in the central $a = 20''$ aperture, but this has $< 2\sigma$ significance. In larger apertures the noise worsens and signal does not increase significantly, so an upper limit was measured in an aperture equal to the full optical size. The RxA map is also noisy, with only a 2.6σ detection within the $80''$ aperture; however the curve of growth does not grow smoothly indicating that this detection may be unreliable due to residual baselines. In the moment map the emission appears to originate from the central and northern parts of the image, which is consistent with the distribution of SPIRE emission.

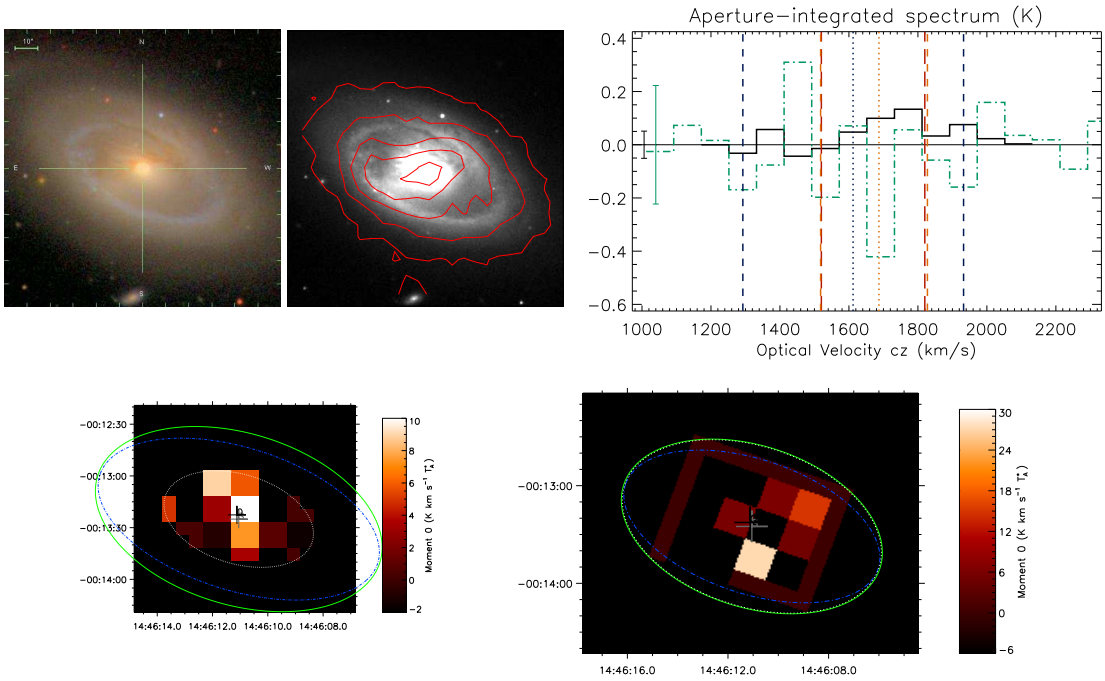

Figure D.7: NGC 5750. Top: SDSS image, 250 μm contours, and aperture-integrated spectra in HARP (black) and RxA (green). Blue lines = H I line width from HIPASS; orange = CO line width from literature; red = CO width integrated over for moment maps. Below: rebinned moment maps in HARP (left) and RxA (right). 'O' marks the optical centroid and 'S' the SPIRE centroid; the green line is the SPIRE Kron ellipse and blue is the B-band D_{25} isophote. The white line marks the aperture within which the total flux was integrated.

NGC 5750: The RxA and HARP cubes for this galaxy had some bad baselines which meant that some pixels had to be masked in both maps, but a clean cube was obtained from the HARP data with a good curve of growth and a detection within an aperture similar to the SPIRE size ($a = 42''$). The rise in the curve of growth at $60''$ is not significant, and appears to be due to a residual baseline. An upper limit was measured from the RxA cube, although the fluctuating curve of growth indicates that some residual baselines may remain. NGC 5750 is an early-type galaxy (SB0/a) similar to NGC 5719, SDP 4, SDP 15 and SDP 18, and is therefore unusual compared with the rest of the flux-limited sample. It also has a blue star-forming ring clearly visible in the SDSS image, which is consistent with the extended SPIRE and CO emission, though unfortunately the signal-to-noise in the HARP and RxA cubes is not good enough to map this. The peak in the CO(2–1) spectrum at around 1450 $\mathrm{km\,s^{-1}}$ may be genuine emission associated with the blue (star-forming) ring, although it is not significant in CO(2–1) and is absent in CO(3–2) so was not included in the integrated intensity.

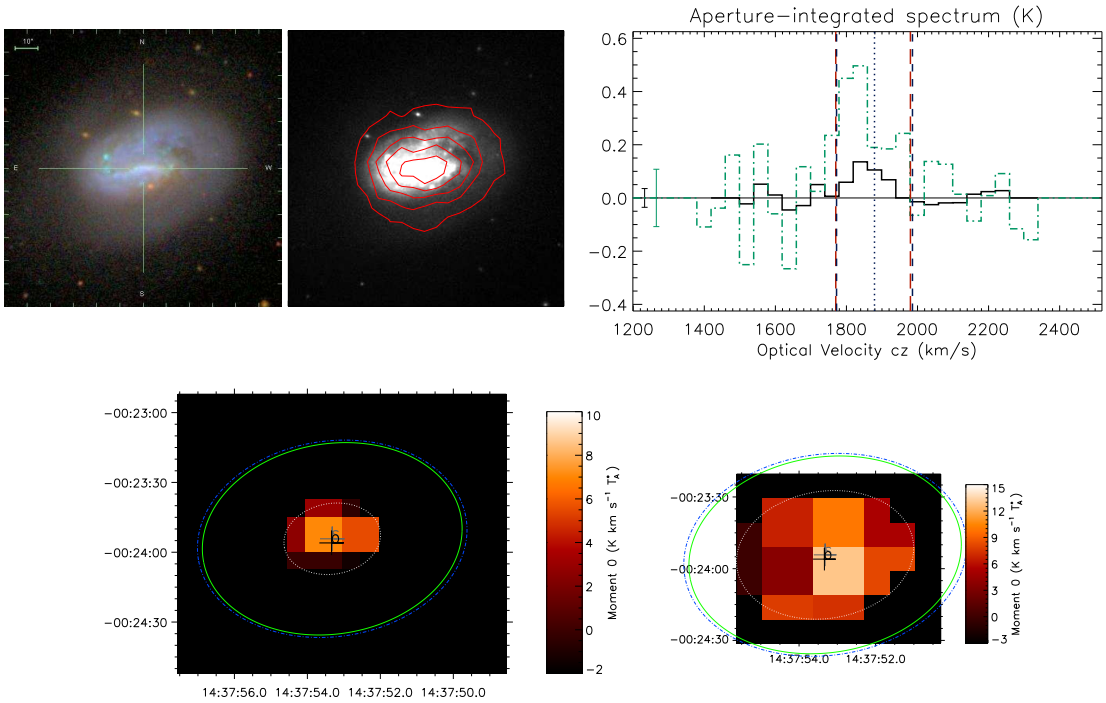

Figure D.8: NGC 5691. Top: SDSS image, 250 μm contours, and aperture-integrated spectra in HARP (black) and RxA (green). Blue lines = H I line width from HIPASS; red = CO width integrated over for moment maps. Below: rebinned moment maps in HARP (left) and RxA (right). 'O' marks the optical centroid and 'S' the SPIRE centroid; the green line is the SPIRE Kron ellipse and blue is the B-band D_{25} isophote. The white line marks the aperture within which the total flux was integrated.

NGC 5691: This galaxy was observed with both HARP and RxA. Problematic baselines were encountered in one of the HARP receptors on the outside of the array, but after masking this there were no further problems. Detections were then obtained in both HARP and RxA maps. The HARP flux is fully contained within about $20''$, but the RxA continues to grow out to about $35''$. This galaxy is another early-type spiral (SABa), but it appears to have a tidal tail in the SDSS image, and is much bluer overall than the other early types (NGC 5750 and NGC 5719) so it may well have undergone an interaction. The CO(3–2) emission appears to be confined mostly to the nucleus and has a narrow line width (consistent with the H I), although CO(2–1) emission appears to extend further out.

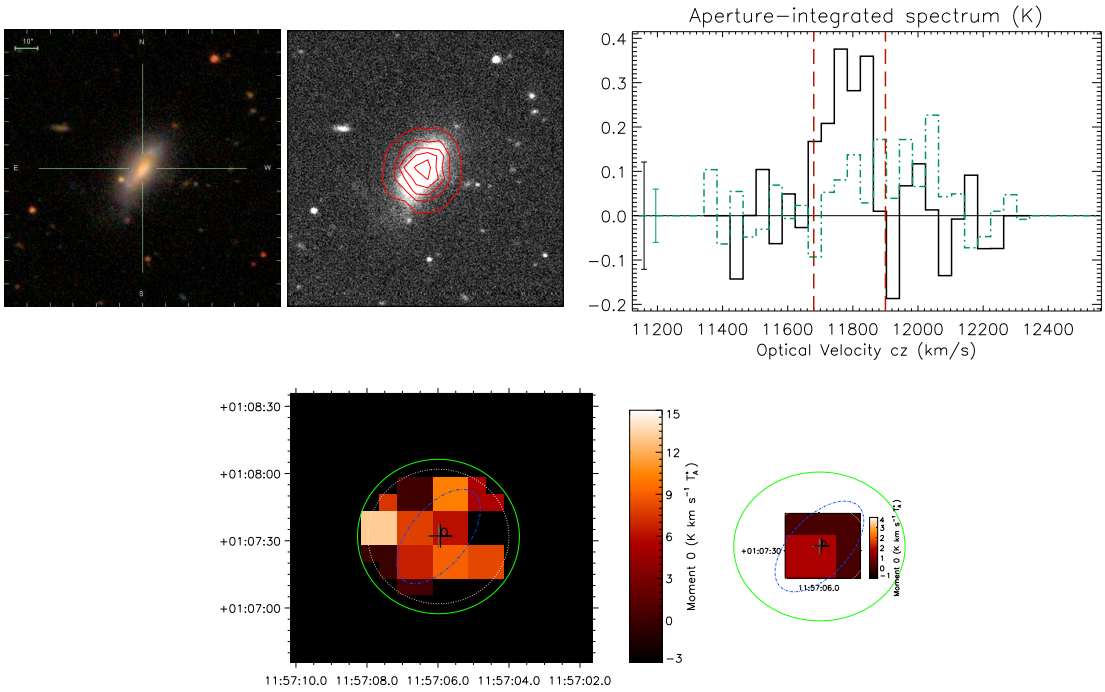

Figure D.9: CGCG 013-010. Top: SDSS image, 250 μm contours, and aperture-integrated spectra in HARP (black) and RxA (green). Red lines = CO width integrated over for moment maps. Below: rebinned moment maps in HARP (left) and RxA (right). 'O' marks the optical centroid and 'S' the SPIRE centroid; the green line is the SPIRE Kron ellipse and blue is the B-band D_{25} isophote. The white line marks the aperture within which the total flux was integrated.

CGCG 013-010: This galaxy is classified as an early-type spiral (Sab) and has the spectral classification of an H II emitter or LINER on NED. A detection was obtained in the HARP cube in a $30''$ aperture and a marginal detection in the RxA cube in $20''$ (which encloses the whole cube). It is possible that the CO(2–1) flux is slightly underestimated since the full aperture used in HARP is not covered by the RxA cube.

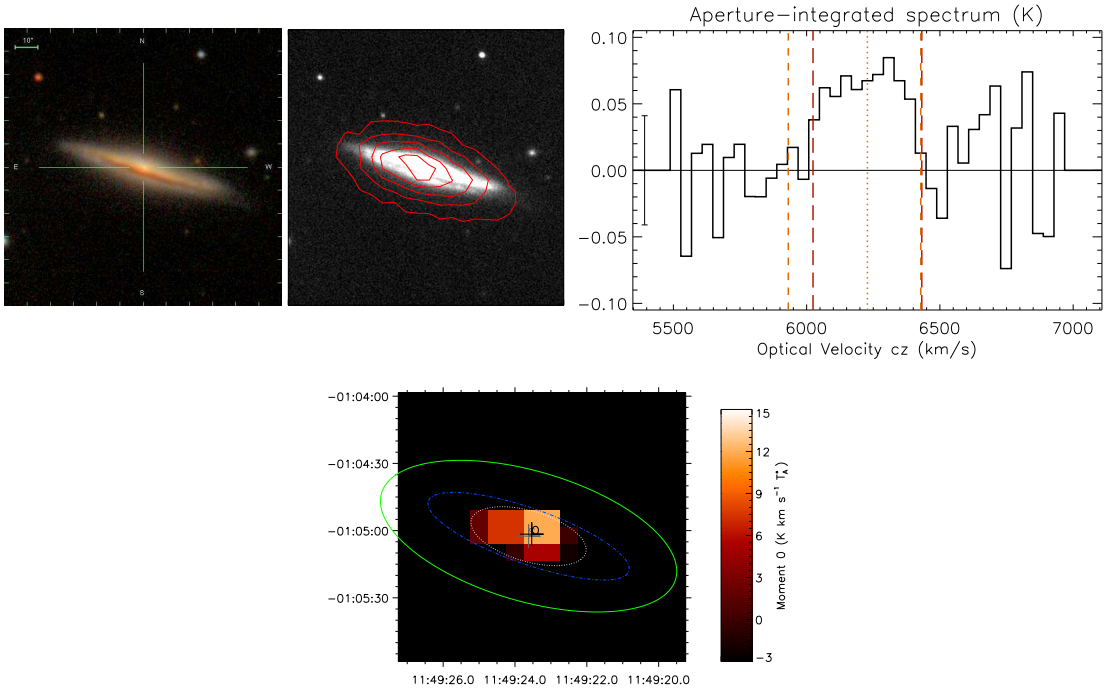

Figure D.10: NGC 3907B. Top: SDSS image, 250 μm contours, and aperture-integrated spectra from HARP. Orange lines = CO line width from literature; red = CO width integrated over for moment maps. Below: rebinned moment map. 'O' marks the optical centroid and 'S' the SPIRE centroid; the green line is the SPIRE Kron ellipse and blue is the B-band D_{25} isophote. The white line marks the aperture within which the total flux was integrated.

NGC 3907B: This was only observed with HARP, and a good detection was obtained. The spectrum is significantly noisier in the wings than in the centre due to the co-addition of two observations with different bandwidths (hence the central velocities have greater integration time). The noise is measured from the part of the spectrum outside the line, and is therefore likely to be over-estimated, and the signal-to-noise of the detection is likely to be better than what is quoted. This galaxy is an edge-on spiral (Sb) with a prominent dust lane, and exists in a pair with NGC 3907 (not in this sample).

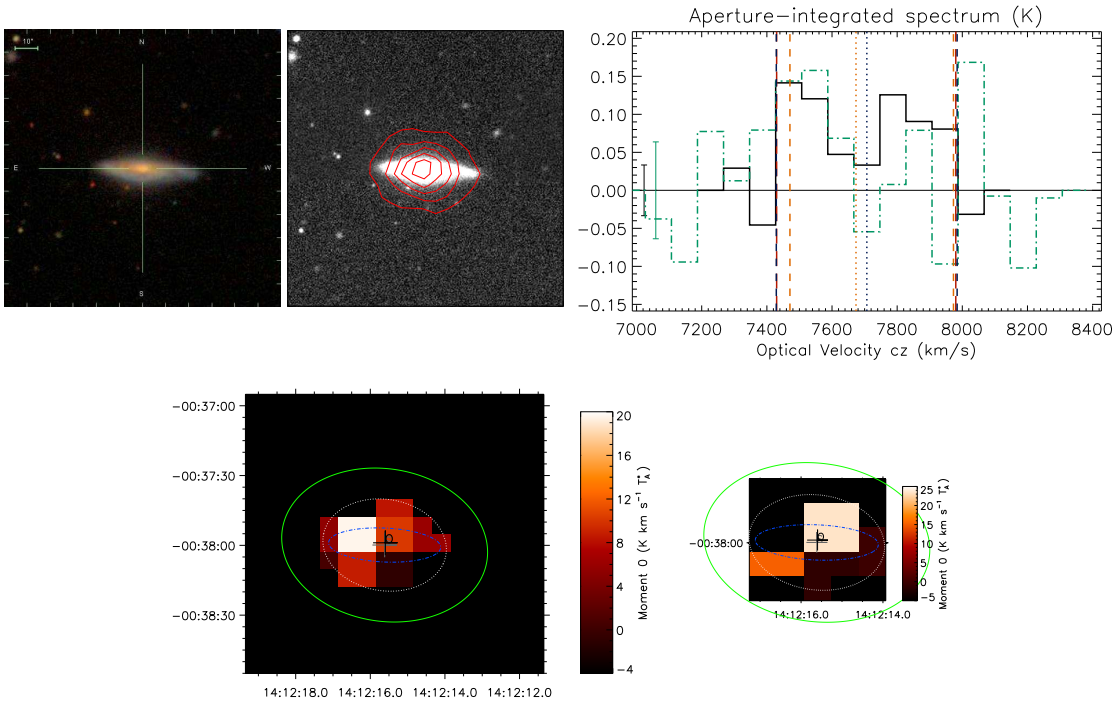

Figure D.11: CGCG 018-077. Top: SDSS image, 250 μm contours, and aperture-integrated spectra in HARP (black) and RxA (green). Blue lines = H I line width from HIPASS; orange = CO line width from literature; red = CO width integrated over for moment maps. Below: rebinned moment maps in HARP (left) and RxA (right). 'O' marks the optical centroid and 'S' the SPIRE centroid; the green line is the SPIRE Kron ellipse and blue is the B-band D_{25} isophote. The white line marks the aperture within which the total flux was integrated.

CGCG 018-077: The RxA spectra for this source suffered from bad baselines and due to the broad line width it was necessary to clip fewer channels from the ends (compared with other spectra), in order to successfully fit and subtract the noisy baselines. Even after doing this, no significant detection was obtained in CO(2–1). A better detection was obtained in the HARP cube within the extent of the optical emission ($a = 22''$), although the curve of growth appears to continue growing beyond this, probably as a result of residual baselines in the noisy outer pixels of the map.

The galaxy is an edge-on spiral (classified as Sc in HyperLEDA) and is more distant (hence smaller) than the NGC galaxies. The broad CO(3–2) line width agrees well with H I.

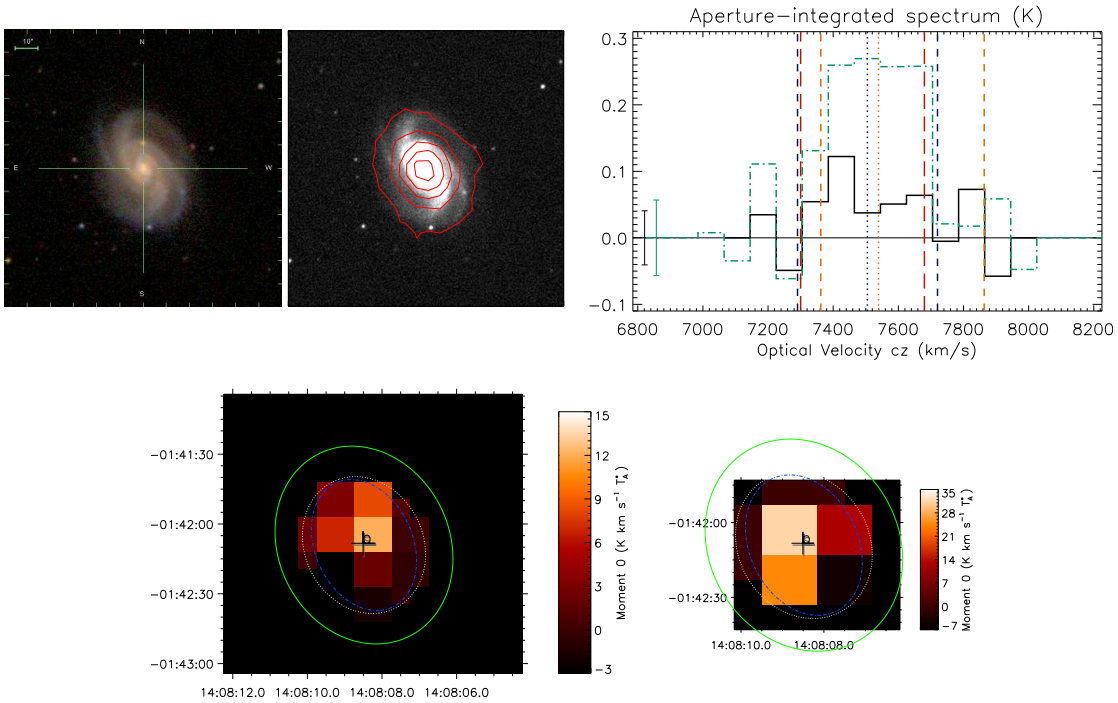

Figure D.12: NGC 5478. Top: SDSS image, 250 μm contours, and aperture-integrated spectra in HARP (black) and RxA (green). Blue lines = H I line width from HIPASS; orange = CO line width from literature; red = CO width integrated over for moment maps. Below: rebinned moment maps in HARP (left) and RxA (right). 'O' marks the optical centroid and 'S' the SPIRE centroid; the green line is the SPIRE Kron ellipse and blue is the B-band D_{25} isophote. The white line marks the aperture within which the total flux was integrated.

NGC 5478: A good detection is obtained in the RxA map and a reasonable one in the HARP map, both within a $30''$ aperture equal to the optical size. The galaxy is an intermediate-type spiral (SABbc) with a red optical colour.

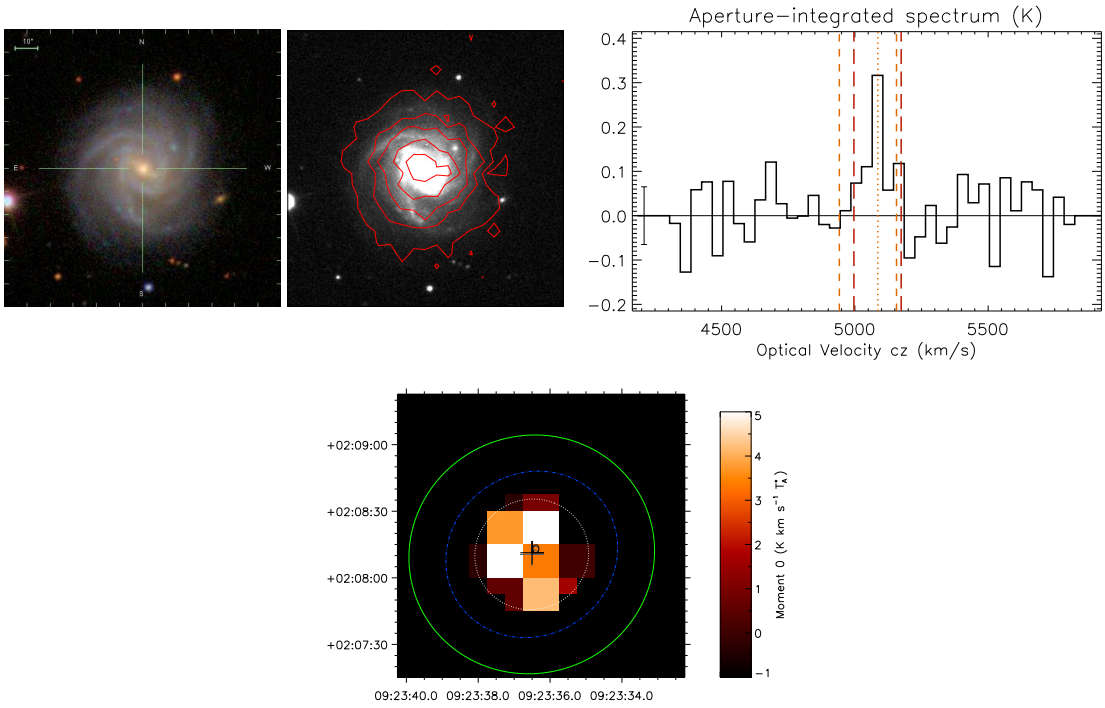

Figure D.13: NGC 2861. Top: SDSS image, 250 μm contours, and aperture-integrated spectra from HARP. Orange lines = CO line width from literature; red = CO width integrated over for moment maps. Below: rebinned moment map. 'O' marks the optical centroid and 'S' the SPIRE centroid; the green line is the SPIRE Kron ellipse and blue is the B-band D_{25} isophote. The white line marks the aperture within which the total flux was integrated.

NGC 2861: This was only observed with HARP. Most of the emission is contained within $20''$ (similar to the SPIRE profile), although there is marginal growth up to the optical extent at $40''$, though this is not significant. An aperture $a = 25''$ was chosen as a compromise. Both CO and H I lines are narrow, as the galaxy is seen face-on. This is a barred spiral (SBbc) that exists in a triplet with CGCG 006-040 and CGCG 006-041 (not in this sample).

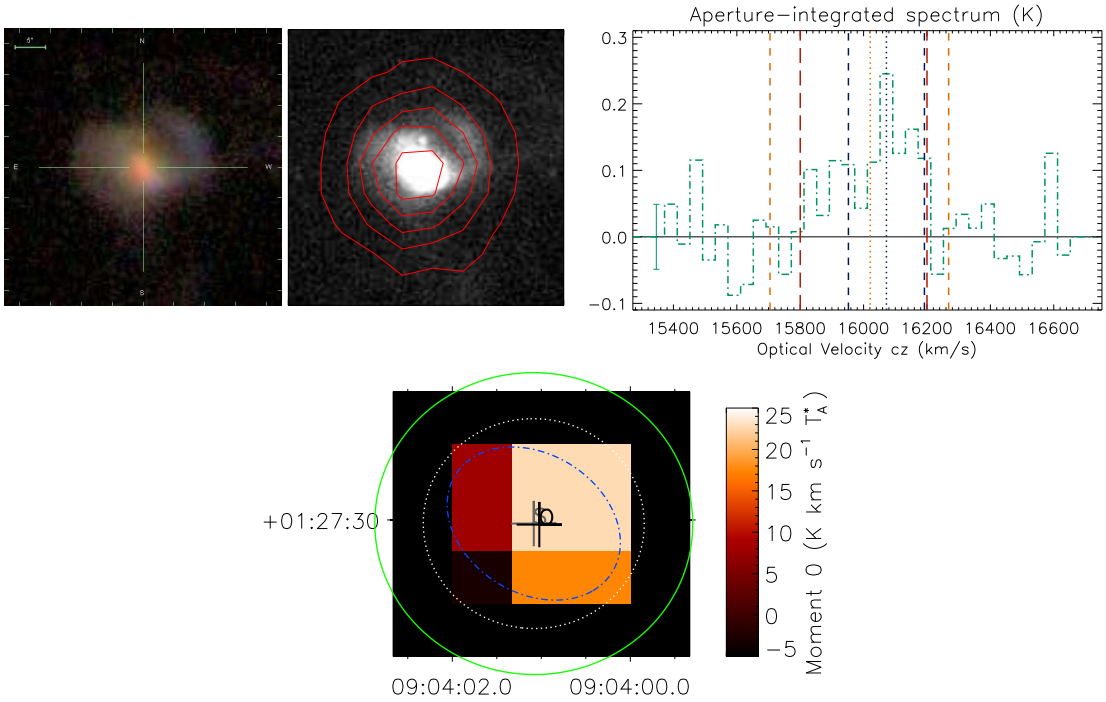

Figure D.14: SDP 1. Top: SDSS image, 250 μm contours, and aperture-integrated spectra from RxA. Blue lines = H I line width from HIPASS; orange = CO line width from literature; red = CO width integrated over for moment maps. Below: rebinned moment map. 'O' marks the optical centroid and 'S' the SPIRE centroid; the green line is the SPIRE Kron ellipse and blue is the B-band D_{25} isophote. The white line marks the aperture within which the total flux was integrated. These images are shown at a higher scale (45″ on a side while the others are 2′) to reveal the structure in the SDSS image.

SDP 1: This was only observed with RxA. A broader line-width was assumed relative to the H I line, based on the observed RxA spectrum, which was consistent with the CO(1–0) line measured in NRO data (see Table 4.4). This is an unresolved source (as it is in SPIRE), and a 20″ aperture contains all the flux. The SDSS image indicates a tidally disturbed or merger morphology, which could account for the existence of molecular gas in a different velocity range from the H I. The spectral classification from SDSS is a narrow-line AGN (with high NII/Hα and OIII/Hβ ratios), and the bright red nucleus is consistent with an optically luminous AGN with strong dust obscuration.

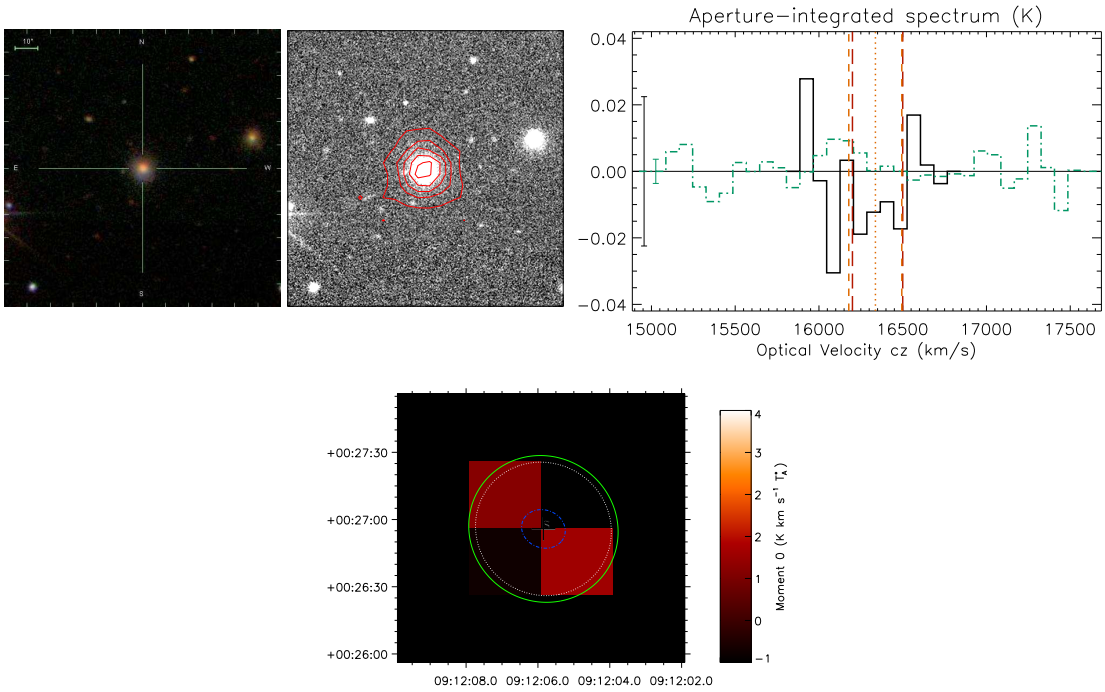

Figure D.15: SDP 15. Top: SDSS image, 250 μm contours, and aperture-integrated spectra from HARP. Orange lines = CO line width from literature; red = CO width integrated over for moment maps. Below: rebinned moment map. 'O' marks the optical centroid and 'S' the SPIRE centroid; the green line is the SPIRE Kron ellipse and blue is the B-band D_{25} isophote. The white line marks the aperture within which the total flux was integrated.

SDP 15: This was observed with HARP as a single pointing, but there is no sign of a detection within the central four pixels that cover the source. It is possible that emission has been missed in this single-pointing HARP map, which does not provide Nyquist sampling of the sky (unlike the jiggle mode used for the other HARP observations). No detection was obtained in the single-pointing observation with RxA either. SDP 15 is an early-type galaxy with a much lower SPIRE flux than the rest of the sample, so this is not surprising.

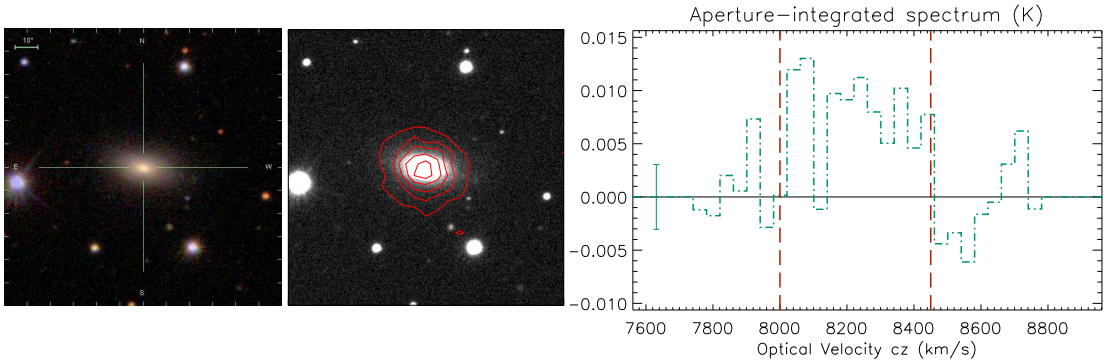

Figure D.16: SDP 4. SDSS image, 250 μm contours, and aperture-integrated spectra from HARP. Orange lines = CO line width from literature; red = CO width integrated over for moment maps.

SDP 4: Like SDP 15, SDP 4 was included in the sample because it was one of the brightest early-type galaxies detected in the H-ATLAS SDP (Rowlands *et al.* 2012). It was observed with RxA and a good detection was obtained, indicating the presence of molecular gas as well as dust in this unusual galaxy. It is classified as S0/a and is an H II emitter.

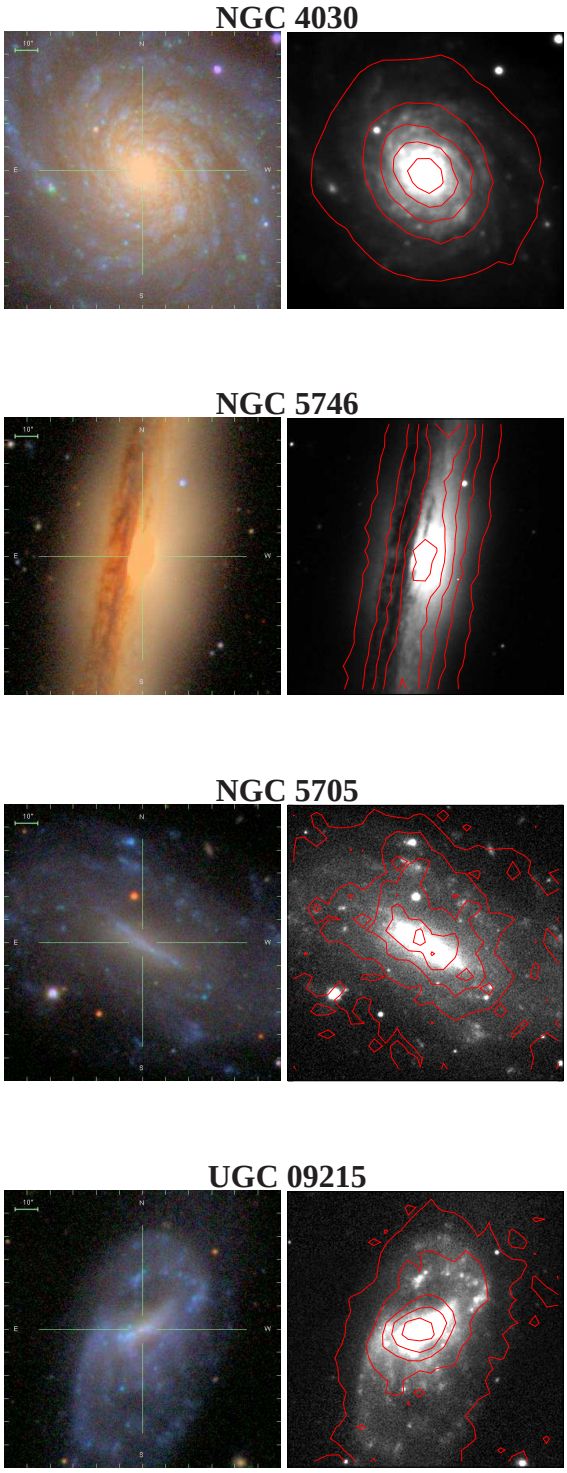

Figure D.17: SDSS images and 250 μm contours for galaxies not observed in CO.

Bibliography

Aaronson M., Olszewski E. W., 1984. *Nature*, **309**, 414. 1.3.2

Abdo A. A. *et al.*, 2010. *ApJ*, **710**, 133. 4.1.1

Adelman-McCarthy J. K. *et al.*, 2008. *ApJS*, **175**, 297. 3.2.1

Afonso J., Hopkins A., Mobasher B., Almeida C., 2003. *ApJ*, **597**, 269. 1.4

Aihara H. *et al.*, 2011. *ApJS*, **193**, 29. 1.5

Albrecht M., Krügel E., Chini R., 2007. *A&A*, **462**, 575. 4.4, D

Allamandola L. J., Hudgins D. M., Sandford S. A., 1999. *ApJ*, **511**, L115. 1.3.4

Alonso-Herrero A. *et al.*, 2006. *ApJ*, **640**, 167. 2.5.1

Alpher R. A., Herman R. C., 1948. *Physical Review*, **74**, 1737. 1.1.1

Alpher R. A., Bethe H., Gamow G., 1948. *Physical Review*, **73**, 803. 1.1.1

Amblard A. *et al.*, 2010. *A&A*, **518**, L9. 2.5.3, 4.2.1

Anderson L. *et al.*, 2012. *ArXiv:1203.6594*. 1.1.1

Angus G. W., Shan H. Y., Zhao H. S., Famaey B., 2007. *ApJ Letters*, **654**, L13. 1.1.1

Appleton P. N. *et al.*, 2004. *ApJS*, **154**, 147. 2.1.2, 2.5.5

Appleton P. *et al.*, 2009. In: *astro2010: The A&A Decadal Survey*, 2. 1.1.2

Ashby M. L. N. *et al.*, 2011. *PASP*, **123**, 1011. 1.2.2

Atek H. *et al.*, 2010. *ApJ*, **723**, 104. 1.2.1

Auger M. W., Treu T., Bolton A. S., Gavazzi R., Koopmans L. V. E., Marshall P. J., Bundy K., Moustakas L. A., 2009. *ApJ*, **705**, 1099. 3.4.2

Babcock H. W., 1939. *Lick Obs. Bull.*, **19**, 41. 1.1.1

Baldry I. K., Glazebrook K., Brinkmann J., Ivezi ., Lupton R. H., Nichol R. C., Szalay A. S., 2004. *ApJ*, **600**, 681. 3.2.2

Baldry I. K. *et al.*, 2010. *MNRAS*, **404**, 86. 3.2.1, 1, 3.4.3

Baldwin J. A., Phillips M. M., Terlevich R., 1981. *PASP*, **93**, 5. 1.2.1

Barger A. J., Cowie L. L., Richards E. A., 2000. *AJ*, **119**, 2092. 1.4

Barger A. J., Cowie L. L., Sanders D. B., Fulton E., Taniguchi Y., Sato Y., Kawara K., Okuda H., 1998. *Nature*, **394**, 248. 1.4, 1.4

Barger A. J., Cowie L. L., Smail I., Ivison R. J., Blain A. W., Kneib J.-P., 1999. *AJ*, **117**, 2656. 1.4

Barlow M. J. *et al.*, 2010. *A&A*, **518**, L138. 1.3.1

Barnes D. G. *et al.*, 2001. *MNRAS*, **322**, 486. 4.4.1, 4.4.1, 4.4.3

Bastian N., Covey K. R., Meyer M. R., 2010. *ARA&A*, **48**, 339. 1.2.1

Bauer A. E., Drory N., Hill G. J., Feulner G., 2005. *ApJ*, **621**, L89. 1.1.2, 2.5.4

Baugh C. M., Cole S., Frenk C. S., 1996. *MNRAS*, **283**, 1361. 1.1.2

Baugh C. M., 2006. *Reports on Progress in Physics*, **69**, 3101. 1.3, 1.1.2

Bell E. F. *et al.*, 2004. *ApJ*, **608**, 752. 3.2.2

Bell E. F., 2003. *ApJ*, **586**, 794. 1.2.2, 1.4, 2.1.1, 2.5, 2.5.4, 2.5.5, 2.13, 2.6

Bendo G. J. *et al.*, 2010. *A&A*, **518**, L65. 3.5.4

Bendo G. J. *et al.*, 2012. *MNRAS*, **419**, 1833. 1.4, 4.5.3, 4.6, 5.1.5

Benson A. J., Lacey C. G., Baugh C. M., Cole S., Frenk C. S., 2002. *MNRAS*, **333**, 156. 1.1.2

Benson A. J., Bower R. G., Frenk C. S., Lacey C. G., Baugh C. M., Cole S., 2003. *ApJ*, **599**, 38. 1.1.2, 1.6

Bertin E., Arnouts S., 1996. *A&AS*, **117**, 393. 4.3.3

Bertone G., 2010. *Nature*, **468**, 389. 1.1.1

Béthermin M., Dole H., Cousin M., Bavouzet N., 2010. *A&A*, **516**, A43. 3.4.3

Bianchi S., Davies J. I., Alton P. B., 1999. *A&A*, **344**, L1. 1.3.3

Bigiel F. *et al.*, 2011. *ApJ Letters*, **730**, L13. 4.1.2

Blain A. W., Barnard V. E., Chapman S. C., 2003. *MNRAS*, **338**, 733. 3.4.4

Blain A. W., Smail I., Ivison R. J., Kneib J.-P., 1999. *MNRAS*, **302**, 632. 3.5.1

Blain A. W., Smail I., Ivison R. J., Kneib J.-P., Frayer D. T., 2002. *Physics Reports*, **369**, 111. 1.4

Blain A. W., Combes F., Draine B. T., Pfenniger D., Revaz Y., 2004. *The Cold Universe: Saas-Fee Advanced Course 32, 2002. Swiss Society for Astrophysics and Astronomy*, Springer, Heidelberg, Germany. 1.3.1, 1.5, 4.1.1

Blain A. W., 1996. *MNRAS*, **283**, 1340. 3.4.2

Blake C. *et al.*, 2011. *MNRAS*, **418**, 1707. 1.1.1

Blanton M. R., Roweis S., 2007. *AJ*, **133**, 734. 3.2.1

Blanton M. R. *et al.*, 2003. *ApJ*, **594**, 186. 3.2.2

Böker T., Lisenfeld U., Schinnerer E., 2003. *A&A*, **406**, 87. 4.4

Bondi M. *et al.*, 2007. *A&A*, **463**, 519. 2.5.1

Boquien M. *et al.*, 2011. *AJ*, **142**, 111. 1.4, 4.5.3, 4.6, 5.1.5

Boselli A. *et al.*, 2010a. *PASP*, **122**, 261. 3.5.3

Boselli A. *et al.*, 2010b. *A&A*, **518**, L61. 1.4, 3.5.4, 4.2.1

Boselli A. *et al.*, 2012. *A&A*, **540**, A54. 4.5.3, 4.6, 5.1.5

Bosma A., 1978. *PhD thesis*, Groningen University. 1.1.1

Bothwell M. S. *et al.*, 2012. *ArXiv:1205.1511*. 4.5.1

Bouché N. *et al.*, 2007. *ApJ*, **671**, 303. 4.1.2

Boulanger F., Abergel A., Bernard J., Burton W. B., Desert F., Hartmann D., Lagache G., Puget J., 1996. *A&A*, **312**, 256. 1.3.3

Bourne N., Dunne L., Ivison R. J., Maddox S. J., Dickinson M., Frayer D. T., 2011. *MNRAS*, **410**, 1155. 1.4, 1.5, 2.1.2, 3.1, 3.4.3, 5.1.2

Bourne N. *et al.*, 2012. *MNRAS*, **421**, 3027. 1.3.1, 1.5, 5.1.3

Bower R. G., Benson A. J., Malbon R., Helly J. C., Frenk C. S., Baugh C. M., Cole S., Lacey C. G., 2006. *MNRAS*, **370**, 645. 1.1.2

Braine J., Combes F., Casoli F., Dupraz C., Gerin M., Klein U., Wielebinski R., Brouillet N., 1993. *A&AS*, **97**, 887. 4.5.3

Brammer G. B., van Dokkum P. G., Coppi P., 2008. *ApJ*, **686**, 1503. 2.2.1

Braun R., 2012. *ApJ*, **749**, 87. 4.4.3

Brinchmann J., Ellis R. S., 2000. *ApJ*, **536**, L77. 2.5.4

Browne I. W. A. *et al.*, 2003. *MNRAS*, **341**, 13. 3.4.2

Bruzual G., Charlot S., 2003. *MNRAS*, **344**, 1000. 2.2.1, 3.2.1

Bruzual A. G., 1983. *ApJ*, **273**, 105. 3.4.5

Buat V., Burgarella D., 1998. *A&A*, **334**, 772. 1.3.2

Buat V., Xu C., 1996. *A&A*, **306**, 61. 1.4

Buat V. *et al.*, 2005. *ApJ Letters*, **619**, L51. 1.3.2

Buat V., Takeuchi T. T., Burgarella D., Giovannoli E., Murata K. L., 2009. *A&A*, **507**, 693. 1.4

Buat V. *et al.*, 2010. *MNRAS*, **409**, L1. 1.4, 3.5.4

Bullock J. S., Kravtsov A. V., Weinberg D. H., 2000. *ApJ*, **539**, 517. 1.1.2

Bundy K., Ellis R. S., Conselice C. J., 2005. *ApJ*, **625**, 621. 1.1.2

Bundy K. *et al.*, 2006. *ApJ*, **651**, 120. 1.1.2, 1.4

Burbidge G. R., 1956. *ApJ*, **124**, 416. 2.1.1

Burton M. G., Hollenbach D. J., Tielens A. G. G., 1992. *ApJ*, **399**, 563. 4.1.1

Butcher H., Oemler A., 1978. *ApJ*, **226**, 559. 1.1.3

Butcher H., Oemler A., 1984. *ApJ*, **285**, 426. 1.1.3

Calzetti D. *et al.*, 2007. *ApJ*, **666**, 870. 1.4, 2.1.1

Calzetti D. *et al.*, 2010. *ApJ*, **714**, 1256. 1.4, 2.1.1

Calzetti D., Kinney A. L., Storchi-Bergmann T., 1994. *ApJ*, **429**, 582. 1.3.2, 1.3.2

Calzetti D., 2001. *PASP*, **113**, 1449. 1.4

Cameron E., 2011. *PASA*, **28**, 128. 3.4.2

Cappellari M. *et al.*, 2011. *MNRAS*, **416**, 1680. 1.1.3

Cappellari M. *et al.*, 2012. *Nature*, **484**, 485. 1.2.1

Caputi K. I., Dole H., Lagache G., McLure R. J., Dunlop J. S., Puget J.-L., Le Floc'h E., Prez-Gonzlez P. G., 2006. *A&A*, **454**, 143. 1.4

Carilli C. L. *et al.*, 2008. *ApJ*, **689**, 883. 1.2.2, 2.2.2

Carroll B., Ostlie D., 1996. *An Introduction to Modern Astrophysics*, Addison-Wesley, USA. 1.2.1, 1.2.2, 1.3.1

Casey C. M., 2012. *ArXiv:1206.1595*. 1.4

Catinella B. *et al.*, 2010. *MNRAS*, **403**, 683. 4.4.3

Catinella B. *et al.*, 2012. *A&A*, **544**, A65. 4.5.5, 4.6

Chabrier G., 2003. *PASP*, **115**, 763. 3.2.1, 3.4.5.2

Chapman S. C., Richards E. A., Lewis G. F., Wilson G., Barger A. J., 2001. *ApJ*, **548**, L147. 1.4

Chapman S. C., Scott D., Borys C., Fahlman G. G., 2002. *MNRAS*, **330**, 92. 1.4

Chapman S. C., Blain A. W., Ivison R. J., Smail I. R., 2003a. *Nature*, **422**, 695. 1.4

Chapman S. C. *et al.*, 2003b. *ApJ*, **585**, 57. 1.4

Chapman S. C., Blain A. W., Smail I., Ivison R. J., 2005. *ApJ*, **622**, 772. 1.4, 2.5.3

Charlot S., Fall S. M., 2000. *ApJ*, **539**, 718. 1.3.2

Chary R., Elbaz D., 2001. *ApJ*, **556**, 562. 2.4.3, 2.5.5, 3.5.1.1, 8, 3.14

Chary R.-R., Pope A., 2010. *ArXiv:1003.1731*. 3.4.3

Chavez M., Bertone E., 2011. *Ap&SS*, **335**, 193. 3.5.4

Chen Y.-M., Wild V., Kauffmann G., Blaizot J., Davis M., Noeske K., Wang J.-M., Willmer C., 2009. *MNRAS*, **393**, 406. 1.1.2

Cherchneff I., 2010. In: *Hot and Cool: Bridging Gaps in Massive Star Evolution*, 237, eds Leitherer C., Bennett P. D., Morris P. W., Van Loon J. T. 1.3.1

Chi X., Wolfendale A. W., 1990. *MNRAS*, **245**, 101. 2.1.1

Clements D. L. *et al.*, 2008. *MNRAS*, **387**, 247. 1.4

Clowe D., Brada M., Gonzalez A. H., Markevitch M., Randall S. W., Jones C., Zaritsky D., 2006. *ApJ*, **648**, L109. 1.1.1

Coccato L., Morelli L., Corsini E. M., Buson L., Pizzella A., Vergani D., Bertola F., 2011. *MNRAS*, **412**, L113. D

Cohen A. S., Röttgering H. J. A., Jarvis M. J., Kassim N. E., Lazio T. J. W., 2004. *ApJS*, **150**, 417. 2.5.1

Colberg J. M. *et al.*, 2000. *MNRAS*, **319**, 209. 1.1.2

Cole S., Aragon-Salamanca A., Frenk C. S., Navarro J. F., Zepf S. E., 1994. *MNRAS*, **271**, 781. 1.1.2, 1.1.2

Cole S., Lacey C. G., Baugh C. M., Frenk C. S., 2000. *MNRAS*, **319**, 168. 1.1.2

Cole S. *et al.*, 2001. *MNRAS*, **326**, 255. 1.6

Cole S. *et al.*, 2005. *MNRAS*, **362**, 505. 1.1.1

Condon J. J., Cotton W. D., Broderick J. J., 2002. *AJ*, **124**, 675. 1.12

Condon J. J., Condon M. A., Gisler G., Puschell J. J., 1982. *ApJ*, **252**, 102. 1.1.3

Condon J. J., 1983. *ApJS*, **53**, 459. 2.4.1

Condon J. J., 1992. *ARA&A*, **30**, 575. 1.2.2, 2.1.1, 2.4.1

Connolly A. J., Szalay A. S., Dickinson M., Subbarao M. U., Brunner R. J., 1997. *ApJ Letters*, **486**, L11. 1.12

Connolly A. J. *et al.*, 2002. *ApJ*, **579**, 42. A.2

Conselice C. J. *et al.*, 2007. *MNRAS*, **381**, 962. 1.1.2, 2.2.1

Coppin K. *et al.*, 2010. *ApJ*, **713**, 503. 2.5.1

Corbelli E. *et al.*, 2012. *A&A*, **542**, A32. 4.1.3, 4.5.1, 4.5.3, 4.5.5, 4.6, 5.1.4

Cortese L., Hughes T. M., 2009. *MNRAS*, **400**, 1225. 3.2.2

Cortese L. *et al.*, 2006. *ApJ*, **637**, 242. 1.3.2, 3.1

Cortese L., Boselli A., Franzetti P., Decarli R., Gavazzi G., Boissier S., Buat V., 2008. *MNRAS*, **386**, 1157. 1.3.2, 1.4

Covey K. R., Bastian N., Meyer M. R., 2011. In: *Stellar Clusters & Associations: A RIA Workshop on Gaia*, p. 65. 1.2.1

Cowie L. L., Songaila A., Hu E. M., Cohen J. G., 1996. *AJ*, **112**, 839. 1.1.2, 2.5.4

Cowie L. L., Songaila A., Barger A. J., 1999. *AJ*, **118**, 603. 1.12

Cox P. *et al.*, 2011. *ApJ*, **740**, 63. 4.2.1

Cox P., Kruegel E., Mezger P. G., 1986. *A&A*, **155**, 380. 4.1.1

Croton D. J. *et al.*, 2006. *MNRAS*, **365**, 11. 1.4, 1.1.2

Cucciati O. *et al.*, 2012. *A&A*, **539**, A31. 1.4

da Cunha E., Charlot S., Elbaz D., 2008. *MNRAS*, **388**, 1595. 1.11, 5.2

da Cunha E., Eminian C., Charlot S., Blaizot J., 2010. *MNRAS*, **403**, 1894. 3.5.3.1

Dabringhausen J., Kroupa P., Pflamm-Altenburg J., Mieske S., 2012. *ApJ*, **747**, 72. 1.2.1

Daddi E. *et al.*, 2005. *ApJ*, **631**, L13. 2.5.3

Daddi E. *et al.*, 2007a. *ApJ*, **670**, 156. 2.2.1

Daddi E. *et al.*, 2007b. *ApJ*, **670**, 173. 1.2.2, 1.4, 2.1.1

Daddi E. *et al.*, 2010a. *ApJ*, **713**, 686. 4.2, 4.1.3

Daddi E. *et al.*, 2010b. *ApJL*, **714**, L118. 4.1.2, 4.1.2

Dale D. A., Helou G., 2002. *ApJ*, **576**, 159. 1.3.2, 2.5.3, 3.5.2

Dale D. A., Helou G., Contursi A., Silbermann N. A., Kolhatkar S., 2001. *ApJ*, **549**, 215. 2.5.3

Dale D. A. *et al.*, 2005. *ApJ*, **633**, 857. 2.1.1

Damen M., Förster Schreiber N. M., Franx M., Labbé I., Toft S., van Dokkum P. G., Wuyts S., 2009a. *ApJ*, **705**, 617. 3.5.1

Damen M., Labbé I., Franx M., van Dokkum P. G., Taylor E. N., Gawiser E. J., 2009b. *ApJ*, **690**, 937. 2.2.1, 2.2.2, 2.5.3, 2.5.4, 2.5.4, 3.5.1

Damen M. *et al.*, 2011. *ApJ*, **727**, 1. 2.2.1

Dariush A. *et al.*, 2011. *MNRAS*, **418**, 64. 3.1, 3.4.1

Davis M., Efstathiou G., Frenk C. S., White S. D. M., 1985. *ApJ*, **292**, 371. 1.1.2

De Breuck C., van Breugel W., Rttgering H. J. A., Miley G., 2000. *A&AS*, **143**, 303. 2.5.1

de Grijp M. H. K., Miley G. K., Lub J., de Jong T., 1985. *Nature*, **314**, 240. 1.3.4

de Jong T., Clegg P. E., Rowan-Robinson M., Soifer B. T., Habing H. J., Houck J. R., Aumann H. H., Raimond E., 1984. *ApJ*, **278**, L67. 1.3.2

de Lucia G., Springel V., White S. D. M., Croton D., Kauffmann G., 2006. *MNRAS*, **366**, 499. 1.1.2, 1.1.2

de Ravel L. *et al.*, 2011. *ArXiv:1104.5470*. 1.1.3

de Vaucouleurs G., de Vaucouleurs A., Corwin H. G., Buta R. J., Paturel G., Fouqué P., 1991. *Third Reference Catalogue of Bright Galaxies*, Springer, New York, NY. 4.4.3

de Vaucouleurs G., 1959. *Handbuch der Physik*, **53**, 275. 1.1.3

de Vaucouleurs G., 1977. In: *Evolution of Galaxies and Stellar Populations*, p. 43, eds Tinsley B. M., Larson, D. Campbell R. B. G. 1.1.3

Deo R. P., Richards G. T., Crenshaw D. M., Kraemer S. B., 2009. *ApJ*, **705**, 14. 1.3.4

Descartes R., 1636. *The World*. 1.1.1

Desert F.-X., Boulanger F., Puget J. L., 1990. *A&A*, **237**, 215. 1.3.2, 2.5.5

Devereux N. A., Eales S. A., 1989. *ApJ*, **340**, 708. 2.1.1

Devereux N. A., Young J. S., 1992. *AJ*, **103**, 1536. 1.4

Devlin M. J. *et al.*, 2009. *Nature*, **458**, 737. 2.5.3

Di Matteo T., Springel V., Hernquist L., 2005. *Nat*, **433**, 604. 1.1.2

Dicke R. H., Peebles P. J. E., Roll P. G., Wilkinson D. T., 1965. *ApJ*, **142**, 414. 1.1.1, 1.1

Dickinson M., FIDEL team, 2007. In: *American Astronomical Society Meeting Abstracts*, 822. 2.2.1

Dickinson M., Papovich C., Ferguson H. C., Budavri T., 2003. *ApJ*, **587**, 25. 1.1.2, 1.4

Dickman R. L., Snell R. L., Schloerb F. P., 1986. *ApJ*, **309**, 326. 4.1.1

Djorgovski S., Davis M., 1987. *ApJ*, **313**, 59. 1.1.3

Dole H. *et al.*, 2006. *A&A*, **451**, 417. 2.2.2, 3.4.3

Donley J. L., Rieke G. H., Pérez-González P. G., Rigby J. R., Alonso-Herrero A., 2007. *ApJ*, **660**, 167. 2.5.1

Donley J. L., Rieke G. H., Pérez-González P. G., Barro G., 2008. *ApJ*, **687**, 111. 2.5.1

Draine B. T., Anderson N., 1985. *ApJ*, **292**, 494. 4.5.3

Draine B. T., Lee H. M., 1984. *ApJ*, **285**, 89. 1.3.2

Draine B. T., Li A., 2007. *ApJ*, **657**, 810. 1.3.1, 1.3.2, 2.5.3

Draine B. T., Salpeter E. E., 1979. *ApJ*, **231**, 438. 1.3.1, 3.5.3.1

Draine B. T. *et al.*, 2007. *ApJ*, **663**, 866. 1.3.1, 1.3.3, 4.5.5, 5.1.5

Draine B. T., 1990. In: *The Evolution of the Interstellar Medium*, p. 193, ed. Blitz L. 3.5.3.1

Draine B. T., 2011. *Physics of the Interstellar and Intergalactic Medium*, Princeton University Press, Princeton, New Jersey. 1.10, 1.3.2, 1.3.3, 1.3.4, 4.1.1

Draper A. R., Ballantyne D. R., 2012. *A Tale of Two Populations: The Contribution of Merger and Secular Processes to the Evolution of Active Galactic Nuclei*. 1.1.3

Dressler A., Lynden-Bell D., Burstein D., Davies R. L., Faber S. M., Terlevich R., Wegner G., 1987. *ApJ*, **313**, 42. 1.1.3

Dressler A. *et al.*, 1997. *ApJ*, **490**, 577. 1.1.3

Dressler A., 1980. *ApJ*, **236**, 351. 1.1.3

Driver S. P. *et al.*, 2006. *MNRAS*, **368**, 414. 3.1

Driver S. P., Popescu C. C., Tuffs R. J., Liske J., Graham A. W., Allen P. D., de Propris R., 2007. *MNRAS*, **379**, 1022. 3.1

Driver S. P. *et al.*, 2009. *Astronomy and Geophysics*, **50**, 12. 3.2.1

Driver S. P. *et al.*, 2011. *MNRAS*, **413**, 971. 3.2.1

Driver S. P. *et al.*, 2012. *MNRAS*, **427**, 3244. 3.5.2, 5.1.3

Dunne L., Eales S. A., 2001. *MNRAS*, **327**, 697. 1.3.3, 3.1, 3.4.4, 3.5.3, 4.5.4, 5.1.5

Dunne L., Eales S. A., Edmunds M. G., 2003. *MNRAS*, **341**, 589. 3.5.3.1

Dunne L., Eales S., Edmunds M., Ivison R., Alexander P., Clements D. L., 2000. *MNRAS*, **315**, 115. 4.1.1, 4.1.3, 4.5.1, 4.5.4

Dunne L. *et al.*, 2009a. *MNRAS*, **394**, 1307. 1.2.2, 1.3.1, 3.5.3.1

Dunne L. *et al.*, 2009b. *MNRAS*, **394**, 3. 2.2.2, 2.2.2, 2.12, 2.5.4, 2.5.5, 3.5.1

Dunne L. *et al.*, 2011. *MNRAS*, **417**, 1510. 3.1, 3.4.1, 3.5.1.1, 3.5.1, 3.5.3, 3.15, 3.16, 3.5.3.1, B

Dwek E., Scalo J. M., 1980. *ApJ*, **239**, 193. 3.5.3.1

Dye S., Eales S. A., Ashby M. L. N., Huang J.-S., Egami E., Brodwin M., Lilly S., Webb T., 2007. *MNRAS*, **375**, 725. 1.3.3

Dye S. *et al.*, 2009. *ApJ*, **703**, 285. 2.5.3, 3.4.4

Dye S. *et al.*, 2010. *A&A*, **518**, L10. 3.1, 3.4.4, 3.5.1

Eales S., Lilly S., Gear W., Dunne L., Bond J. R., Hammer F., Le Févre O., Crampton D., 1999. *ApJ*, **515**, 518. 1.4, 1.4

Eales S., Lilly S., Webb T., Dunne L., Gear W., Clements D., Yun M., 2000. *AJ*, **120**, 2244. 1.4

Eales S. *et al.*, 2009. *ApJ*, **707**, 1779. 3.1, 3.5.1, 3.5.3.1

Eales S. *et al.*, 2010a. *PASP*, **122**, 499. 1.4

Eales S. A. *et al.*, 2010b. *A&A*, **518**, L23. 3.1, 3.5.1, 3.5.3.1

Eddington A. S. ., 1916. *MNRAS*, **76**, 525. 1.1.1

Edelson R. A., Malkan M. A., 1986. *ApJ*, **308**, 59. 1.3.4

Edmunds M. G., 2001. *MNRAS*, **328**, 223. 3.5.3.1

Efstathiou G., Sutherland W. J., Maddox S. J., 1990. *Nature*, **348**, 705. 1.1.1

Einstein A., 1916. *Annalen der Physik*, **354**, 769. 1.1.1

Einstein A., 1917. *Sitzungsberichte der Königlich Preußischen Akademie der Wissenschaften (Berlin)*, **1**, 142. 1.1.1

Eisenstein D. J. *et al.*, 2005. *ApJ*, **633**, 560. 1.1.1

Elbaz D. *et al.*, 2010. *A&A*, **518**, L29. 1.4

Engel H. *et al.*, 2010. *ApJ*, **724**, 233. 4.2, 4.1.2, 4.5.1, 4.6

Erb D. K., Steidel C. C., Shapley A. E., Pettini M., Reddy N. A., Adelberger K. L., 2006. *ApJ*, **647**, 128. 1.1.2, 1.2.1

Evrard A. E. *et al.*, 2002. *ApJ*, **573**, 7. 1.1.2

Faber S. M., Jackson R. E., 1976. *ApJ*, **204**, 668. 1.1.3

Faber S. M. *et al.*, 2007. *ApJ*, **665**, 265. 3.2.2

Fadda D. *et al.*, 2006. *AJ*, **131**, 2859. 2.3.2

Fallest D. W., Nozawa T., Nomoto K., Umeda H., Maeda K., Kozasa T., Lazzati D., 2011. *MNRAS*, **418**, 571. 1.3.1

Fasano G., Poggianti B. M., Couch W. J., Bettoni D., Kjrgaard P., Moles M., 2000. *ApJ*, **542**, 673. 1.1.3

Faure C. *et al.*, 2008. *ApJS*, **176**, 19. 3.4.2

Fazio G. G. *et al.*, 2004. *ApJS*, **154**, 10. 2.2.1

Feldmann R., Gnedin N. Y., Kravtsov A. V., 2012. *ApJ*, **758**, 127. 4.1.2

Ferreras I., La Barbera F., de la Rosa I. G., Vazdekis A., de Carvalho R. R., Falcón-Barroso J., Ricciardelli E., 2012. *MNRAS*. 1.2.1

Feulner G., Goranova Y., Drory N., Hopp U., Bender R., 2005. *MNRAS*, **358**, L1. 1.1.2, 2.5.4

Fitt A. J., Alexander P., Cox M. J., 1988. *MNRAS*, **233**, 907. 2.1.1

Fixsen D. J., Dwek E., Mather J. C., Bennett C. L., Shafer R. A., 1998. *ApJ*, **508**, 123. 3.4.3, 3.2

Flores H. *et al.*, 1999. *A&A*, **343**, 389. 1.12

Fontanot F., De Lucia G., Monaco P., Somerville R. S., Santini P., 2009. *MNRAS*, **397**, 1776. 1.1.2

Forman W., Kellogg E., Gursky H., Tananbaum H., Giacconi R., 1972. *ApJ*, **178**, 309. 1.1.1

Frayer D. T. *et al.*, 2006. *AJ*, **131**, 250. 2.1.2

Frayer D. T. *et al.*, 2011. *ApJ*, **726**, L22. 4.2.1

Fu J., Kauffmann G., Li C., Guo Q., 2012. *MNRAS*, **424**, 2701. 4.2.1

Fukugita M., Hogan C. J., Peebles P. J. E., 1998. *ApJ*, **503**, 518. 1.1.3

Fullmer L., Lonsdale C. J., 1989. *JPL D-1932, Version 2, part no 3, 0 (1989).* 1.4

Gall C., Hjorth J., Andersen A. C., 2011. *A&AR*, **19**, 43. 1.3.1

Gallazzi A., Charlot S., Brinchmann J., White S. D. M., Tremonti C. A., 2005. *MNRAS*, **362**, 41. 1.1.2

Gallimore J. F. *et al.*, 2010. *ApJS*, **187**, 172. 4.5.3

Gao Y., Solomon P. M., 2004a. *ApJS*, **152**, 63. 4.1.3

Gao Y., Solomon P. M., 2004b. *ApJ*, **606**, 271. 4.1.2, 4.2, 4.1.3, 4.5.3, 4.5.4

Gardner J. P., 1995. *ApJ*, **452**, 538. 2.2.1

Garn T., Green D. A., Riley J. M., Alexander P., 2009. *MNRAS*, **397**, 1101. 2.1.2, 2.6

Gawiser E. *et al.*, 2006. *ApJS*, **162**, 1. 2.2.1

Geach J. E., Papadopoulos P. P., 2012. *ApJ*, **757**, 156. 4.1.1

Gebhardt K. *et al.*, 2000. *ApJ*, **539**, L13. 1.1.3

Genzel R. *et al.*, 1998. *ApJ*, **498**, 579. 1.4

Genzel R. *et al.*, 2010. *MNRAS*, **407**, 2091. 4.1.2, 4.2, 4.1.2, 4.1.3, 4.5.4

Genzel R. *et al.*, 2012. *ApJ*, **746**, 69. 4.1.1

Gioia I. M., Gregorini L., Klein U., 1982. *A&A*, **116**, 164. 2.4.1

Giovanelli R. *et al.*, 2005. *AJ*, **130**, 2598. 4.4.3

Giovannoli E., Buat V., Noll S., Burgarella D., Magnelli B., 2011. *A&A*, **525**, A150. 2.5.3

Glazebrook K., Peacock J. A., Miller L., Collins C. A., 1995. *MNRAS*, **275**, 169. 2.2.1

Glenn J. *et al.*, 2010. *MNRAS*, **409**, 109. 3.4.3, B

Gomez H. L. *et al.*, 2009. *MNRAS*, **397**, 1621. 1.3.1

Gomez H. L. *et al.*, 2012a. *MNRAS*, **420**, 3557. 1.3.1

Gomez H. L. *et al.*, 2012b. *MNRAS*, **420**, 3557. 3.5.3.1

González J. E., Lacey C. G., Baugh C. M., Frenk C. S., 2011. *MNRAS*, **413**, 749. 1.4

González-Nuevo J. *et al.*, 2012. *ApJ*, **749**, 65. 3.4.2, 3.1, 4.2.1, 5.1.1

Goto T. *et al.*, 2011. *MNRAS*, **414**, 1903. 3.5.1

Gott J. R., Vogeley M. S., Podariu S., Ratra B., 2001. *ApJ*, **549**, 1. 2.2.2, 2.3.3, 2.3.3, 2.10, 2.12, 3.3.3, 3.4.5, C.1

Gould R. J., Salpeter E. E., 1963. *ApJ*, **138**, 393. 4.1.1

Graciá-Carpio J., García-Burillo S., Planesas P., Fuente A., Usero A., 2008. *A&A*, **479**, 703. 4.2

Grenier I. A., Casandjian J.-M., Terrier R., 2005. *Science*, **307**, 1292. 4.1.1

Greve T. R. *et al.*, 2005. *MNRAS*, **359**, 1165. 4.2, 4.5.1

Greve T. R. *et al.*, 2010. *ApJ*, **719**, 483. 2.1.1, 3.1

Griffin M. *et al.*, 2007. *Advances in Space Research*, **40**, 612. 1.4

Griffith R. L., Stern D., 2010. *AJ*, **140**, 533. 2.2.2

Groves B. *et al.*, 2012. *MNRAS*, **426**, 892. 4.5.3

Gruppioni C. *et al.*, 2010. *A&A*, **518**, L27. 3.5.1, 3.5.3.1

Guilloteau S. *et al.*, 1992. *A&A*, **262**, 624. 1.4

Gunn J. E., Gott J. R., 1972. *ApJ*, **176**, 1. 1.1.3

Gursky H., Solinger A., Kellogg E. M., Murray S., Tananbaum H., Giacconi R., Cavaliere A., 1972. *ApJ*, **173**, L99. 1.1.1

Guth A. H., 1981. *Phys. Rev. D*, **23**, 347. 1.2

Haarsma D. B., Partridge R. B., Windhorst R. A., Richards E. A., 2000. *ApJ*, **544**, 641. 1.12

Harayama Y., Eisenhauer F., Martins F., 2008. *ApJ*, **675**, 1319. 3.5.3.1

Harris A. I. *et al.*, 2012. *ApJ*, **752**, 152. 4.2.1

Hatziminaoglou E. *et al.*, 2010. *A&A*, **518**, L33. 4.5.3

Haynes M. P., Giovanelli R., 1984. *AJ*, **89**, 758. 4.4.1, 4.4.3, 4.4.3

Hayward C. C., Kereš D., Jonsson P., Narayanan D., Cox T. J., Hernquist L., 2011. *ApJ*, **743**, 159. 1.4

Heavens A., Panter B., Jimenez R., Dunlop J., 2004. *Nature*, **428**, 625. 1.1.2

Heidmann J., Heidmann N., de Vaucouleurs G., 1972. *Memoirs of the Royal Astronomical Society*, **75**, 85. 4.4.3

Helou G., Bicay M. D., 1993. *ApJ*, **415**, 93. 2.1.1

Helou G., Soifer B. T., Rowan-Robinson M., 1985. *ApJ*, **298**, L7. 2.1.1, 2.5.5

Helou G., 1986. *ApJ*, **311**, L33. 1.3.2, 1.4

HerMES Collaboration *et al.*, 2012. *MNRAS*, **424**, 1614. 1.4

Hickox R. C. *et al.*, 2012. *MNRAS*, **421**, 284. 1.4

Hill T., Thompson M. A., Burton M. G., Walsh A. J., Minier V., Cunningham M. R., Pierce-Price D., 2006. *MNRAS*, **368**, 1223. 3.4.4, 4.1.1

Hill D. T. *et al.*, 2011. *MNRAS*, **412**, 765. 3.2.1, 3.4.3, 3.2

Ho P. T. P., Moran J. M., Lo K. Y., 2004. *ApJ*, **616**, L1. 1.4

Holland W. S. *et al.*, 1999. *MNRAS*, **303**, 659. 1.4

Hollenbach D. J., Tielens A. G. G. M., 1997. *ARA&A*, **35**, 179. 4.1

Holwerda B. W., Keel W. C., Williams B., Dalcanton J. J., de Jong R. S., 2009. *AJ*, **137**, 3000. 3.5.1

Hopkins A. M., Connolly A. J., Haarsma D. B., Cram L. E., 2001. *AJ*, **122**, 288. 1.4

Hopkins P. F., Younger J. D., Hayward C. C., Narayanan D., Hernquist L., 2010. *MNRAS*, **402**, 1693. 3.5.1

Houck J. R., Schneider D. P., Danielson G. E., Neugebauer G., Soifer B. T., Beichman C. A., Lonsdale C. J., 1985. *ApJ Letters*, **290**, L5. 1.3.2, 1.4

Hoyle F., Tayler R. J., 1964. *Nature*, **203**, 1108. 1.1.1

Hu W., 1999. *ApJ*, **522**, L21. 3.4.2

Huang J., Glazebrook K., Cowie L. L., Tinney C., 2003. *ApJ*, **584**, 203. 1.6

Hubble E., Humason M. L., 1931. *ApJ*, **74**, 43. 1.1.1

Hubble E. P., 1925. *The Observatory*, **48**, 139. 1.1.1

Hubble E. P., 1926. *ApJ*, **64**, 321. 1.1.3

Hubble E., 1929. *Proceedings of the National Academy of Sciences of the United States of America*, **15**, 168. 1.1.1

Hubble E. P., 1936. *Realm of the Nebulae*, Yale University Press, New Haven, USA. 1.1.3

Hughes D. H. *et al.*, 1998. *Nature*, **394**, 241. 1.4, 1.4

Huynh M. T., Gawiser E., Marchesini D., Brammer G., Guaita L., 2010. *ApJ*, **723**, 1110. 2.1.2, 2.5.5

Huynh M. T., Jackson C. A., Norris R. P., 2007. *AJ*, **133**, 1331. 1.4, 2.5.1

Hwang H. S., Elbaz D., Lee J. C., Jeong W.-S., Park C., Lee M. G., Lee H. M., 2010a. *A&A*, **522**, A33. 1.4

Hwang H. S. *et al.*, 2010b. *MNRAS*, **409**, 75. 3.4.4

Ibar E. *et al.*, 2008. *MNRAS*, **386**, 953. 2.1.2, 2.5.5, 2.6

Ibar E., Ivison R. J., Best P. N., Coppin K., Pope A., Smail I., Dunlop J. S., 2010. *MNRAS*, **401**, L53. 1.2.2, 2.4.1

Iglesias-Paramo J., Buat V., Donas J., Boselli A., Milliard B., 2004. *A&A*, **419**, 109. 1.3.2

Ikeda M., Oka T., Tatematsu K., Sekimoto Y., Yamamoto S., 2002. *ApJS*, **139**, 467. 4.1.1

Iono D. *et al.*, 2009. *ApJ*, **695**, 1537. 4.5.1, 4.5.3, 4.5.4, 4.6, 5.1.4

Irwin M., 2010. *UKIRT Newsletter*, **26**, 14. 3.3.1

Israel F. P. *et al.*, 1984. *A&A*, **134**, 396. 4.5.3

Issa M. R., MacLaren I., Wolfendale A. W., 1990. *A&A*, **236**, 237. 4.1.1, 4.5.5

Ivison R. J., Smail I., Le Borgne J.-F., Blain A. W., Kneib J.-P., Bezecourt J., Kerr T. H., Davies J. K., 1998. *MNRAS*, **298**, 583. 1.4

Ivison R. J., Smail I., Barger A. J., Kneib J.-P., Blain A. W., Owen F. N., Kerr T. H., Cowie L. L., 2000. *MNRAS*, **315**, 209. 1.4

Ivison R. J. *et al.*, 2002. *MNRAS*, **337**, 1. 1.4

Ivison R. J. *et al.*, 2004. *ApJS*, **154**, 124. 2.5.1

Ivison R. J. *et al.*, 2007. *ApJ*, **660**, L77. 1.2.2, 2.2.2

Ivison R. J. *et al.*, 2010a. *MNRAS*, **402**, 245. 2.1.2, 2.2.1, 2.2.2, 2.4.1, 2.5.5, 2.6, 5.1.2

Ivison R. J. *et al.*, 2010b. *A&A*, **518**, L31. 2.1.2, 2.5.5, 2.6, 5.1.2

James A., Dunne L., Eales S., Edmunds M. G., 2002. *MNRAS*, **335**, 753. 3.4.4, 4.1.1

Jansen R. A., Franx M., Fabricant D., 2001. *ApJ*, **551**, 825. 1.2.1

Jarosik N. *et al.*, 2011. *ApJS*, **192**, 14. 1.1

Jarvis M. J. *et al.*, 2010. *MNRAS*, **409**, 92. 2.1.2, 2.5.2, 2.5.5, 2.6

Jones T. W., Leung C. M., Gould R. J., Stein W. A., 1977. *ApJ*, **212**, 52. 1.3.4

Juneau S., Narayanan D. T., Moustakas J., Shirley Y. L., Bussmann R. S., Kennicutt, Jr. R. C., Vanden Bout P. A., 2009. *ApJ*, **707**, 1217. 4.1.2

Kant I., 1755. *Allgemeine Naturgeschichte und Theorie des Himmels, Part I,* J.F. Peterson, Königsberg and Leipzig. 1.1.1

Karim A. *et al.*, 2011. *ApJ*, **730**, 61. 1.2.2, 3.5.1

Kauffmann G. *et al.*, 2003. *MNRAS*, **341**, 33. 1.4, 3.2.2

Kauffmann G., Guiderdoni B., White S. D. M., 1994. *MNRAS*, **267**, 981. 1.1.2

Keel W. C., Kennicutt R. C., Hummel E., van der Hulst J. M., 1985. *AJ*, **90**, 708. 1.1.3

Kellogg E., Murray S., Giacconi R., Tananbaum T., Gursky H., 1973. *ApJ Letters*, **185**, L13. 1.1.1

Kennicutt R. C., Kent S. M., 1983. *AJ*, **88**, 1094. 1.1.3

Kennicutt R. C. *et al.*, 2009. *ApJ*, **703**, 1672. 1.4

Kennicutt, Jr. R. C., 1989. *ApJ*, **344**, 685. 4.1.1

Kennicutt R. C., 1992. *ApJ*, **388**, 310. 1.7

Kennicutt R. C., 1998a. *ARA&A*, **36**, 189. 1.7, 1.1.3, 1.2.1, 1.4, 2.1.1, 3.5.1, 4.5.4

Kennicutt R. C., 1998b. *ApJ*, **498**, 541. 1.1.3, 3.5.1, 4.1.1, 4.1.2, 4.1.2, 4.2

Kessler M. F. *et al.*, 1996. *A&A*, **315**, L27. 1.4

Kewley L. J., Geller M. J., Jansen R. A., 2004. *AJ*, **127**, 2002. 1.2.1

Klaas U. *et al.*, 2001. *A&A*, **379**, 823. 1.3.4

Kochanek C. S. *et al.*, 2001. *ApJ*, **560**, 566. 1.6

Kodama T. *et al.*, 2004. *MNRAS*, **350**, 1005. 1.1.2

Komatsu E. *et al.*, 2011. *ApJS*, **192**, 18. 1.1.1

Komugi S. *et al.*, 2011. *PASJ*, **63**, 1139. 4.5.3

Kong X., Charlot S., Brinchmann J., Fall S. M., 2004. *MNRAS*, **349**, 769. 1.3.2

Koribalski B. S. *et al.*, 2004. *AJ*, **128**, 16. 4.4, 4.4.1

Kormendy J., Bender R., 1996. *ApJ Letters*, **464**, L119. 1.1.3

Kormendy J., Bender R., 2012. *ApJS*, **198**, 2. 1.1.3

Koyama Y., Kodama T., Shimasaku K., Hayashi M., Okamura S., Tanaka I., Tokoku C., 2010. *MNRAS*, **403**, 1611. 1.2.1

Kreysa E. *et al.*, 1998. In: *Society of Photo-Optical Instrumentation Engineers (SPIE) Conference Series*, p. 319, ed. Phillips T. G. 1.4

Kroupa P., Weidner C., Pflamm-Altenburg J., Thies I., Dabringhausen J., Marks M., Maschberger T., 2011. *arXiv:1112.3340*. 1.2.1

Kroupa P., 2001. *MNRAS*, **322**, 231. 2.2.1, 2.2.2, 2.5.4

Krumholz M. R., Thompson T. A., 2007. *ApJ*, **669**, 289. 4.1.2

Krumholz M. R., Dekel A., McKee C. F., 2012. *ApJ*, **745**, 69. 4.1.2

Kuhlen M., Diemand J., Madau P., Zemp M., 2008. *Journal of Physics Conference Series*, **125**, 2008. 1.1.2

Kuno N. *et al.*, 2007. *PASJ*, **59**, 117. 4.2

Kurczynski P., Gawiser E., 2010. *AJ*, **139**, 1592. A.1

Kurczynski P. *et al.*, 2010. *ArXiv:1010.0290*. 1.2.2

Lacki B. C., Thompson T. A., 2010. *ApJ*, **717**, 196. 2.5.1, 2.6, 5.1.2

Lacki B. C., Thompson T. A., Quataert E., 2010. *ApJ*, **717**, 1. 2.1.1

Lacy M. *et al.*, 2004. *ApJS*, **154**, 166. 2.5.1

Lada C. J., Lombardi M., Alves J. F., 2010. *ApJ*, **724**, 687. 4.1.2

Lakićević M., van Loon J. T., Patat F., Staveley-Smith L., Zanardo G., 2011. *A&A*, **532**, L8. 1.3.1

Landy S. D., Szalay A. S., 1993. *ApJ*, **412**, 64. 2.3.1, 2.3.1, A.2

Lang R. H. *et al.*, 2003. *MNRAS*, **342**, 738. 4.4.3

Lapi A. *et al.*, 2011. *ApJ*, **742**, 24. 3.4.2, 3.1, 4.2.1, 5.1.1, B

Larson R. B., Tinsley B. M., 1978. *ApJ*, **219**, 46. 1.1.3

Larson R. B., Tinsley B. M., Caldwell C. N., 1980. *ApJ*, **237**, 692. 1.1.3

Law K.-H., Gordon K. D., Misselt K. A., 2011. *ApJ*, **738**, 124. 3.5.4

Lawrence A. *et al.*, 2007. *MNRAS*, **379**, 1599. 3.2.1

Le Floc'h E. *et al.*, 2005. *ApJ*, **632**, 169. 1.4, 1.12, 3.5.1

Lee H.-H., Bettens R. P. A., Herbst E., 1996. *A&AS*, **119**, 111. 4.1.1

Leeuw L. L., Sansom A. E., Robson E. I., Haas M., Kuno N., 2004. *ApJ*, **612**, 837. 3.1, 3.4.4, 3.5.3

Leger A., Puget J. L., 1984. *A&A*, **137**, L5. 1.3.4

Lehmer B. D., Alexander D. M., Bauer F. E., Brandt W. N., Goulding A. D., Jenkins L. P., Ptak A., Roberts T. P., 2010. *ApJ*, **724**, 559. 1.2.2

Lemaître G., 1931. *MNRAS*, **91**, 483. 1.1.1

Leroy A. K., Walter F., Brinks E., Bigiel F., de Blok W. J. G., Madore B., Thornley M. D., 2008. *AJ*, **136**, 2782. 4.2

Leroy A. K. *et al.*, 2009. *AJ*, **137**, 4670. 4.1.2, 4.2

Lewis I. *et al.*, 2002. *MNRAS*, **334**, 673. 1.1.3

Lilly S. J., Le Févre O., Hammer F., Crampton D., 1996. *ApJ*, **460**, L1. 1.4, 2.5.3, 3.4.1

Longair M. S., 1994. *High energy astrophysics: Stars, the Galaxy and the interstellar medium*, Cambridge University Press, Cambridge, UK. 1.1.1

Lonsdale C. J. *et al.*, 2003. *PASP*, **115**, 897. 1.4

Lonsdale Persson C. J., Helou G., 1987. *ApJ*, **314**, 513. 1.3.2, 1.4, 1.4

Lupu R. E. *et al.*, 2012. *ApJ*, **757**, 135. 4.2.1

Lutz D., Spoon H. W. W., Rigopoulou D., Moorwood A. F. M., Genzel R., 1998. *ApJ*, **505**, L103. 1.3.4, 1.4

Lutz D. *et al.*, 2011. *A&A*, **532**, A90. 1.4

Ly C. *et al.*, 2007. *ApJ*, **657**, 738. 1.2.1

Machalski J., Godlowski W., 2000. *A&A*, **360**, 463. 1.12

Madau P., Ferguson H. C., Dickinson M. E., Giavalisco M., Steidel C. C., Fruchter A., 1996. *MNRAS*, **283**, 1388. 1.4, 2.5.3, 3.4.1

Madau P., Pozzetti L., Dickinson M., 1998. *ApJ*, **498**, 106. 2.5.4

Madau P., 1995. *ApJ*, **441**, 18. 1.4

Magdis G. E. *et al.*, 2011. *ApJ*, **740**, L15. 4.5.1

Magnelli B., Elbaz D., Chary R. R., Dickinson M., Le Borgne D., Frayer D. T., Willmer C. N. A., 2009. *A&A*, **496**, 57. 2.5.3, 2.5.5, 3.5.1

Magnelli B. *et al.*, 2010. *A&A*, **518**, L28. 1.4

Magnelli B. *et al.*, 2012. *A&A*, **539**, A155. 1.4

Magorrian J. *et al.*, 1998. *AJ*, **115**, 2285. 1.1.3

Maiolino R. *et al.*, 2008. *A&A*, **488**, 463. 1.1.2

Malmquist K. G., 1922. *Lund Medd. Ser. I*, **100**, 1. 2, 2.2.2

Maloney P., Black J. H., 1988. *ApJ*, **325**, 389. 4.1.1

Mamon G. A., 1992. *ApJ Letters*, **401**, L3. 1.1.3

Mannucci F., Cresci G., Maiolino R., Marconi A., Gnerucci A., 2010. *MNRAS*, **408**, 2115. 1.1.3

Mao R.-Q., Schulz A., Henkel C., Mauersberger R., Muders D., Dinh-V-Trung, 2010. *ApJ*, **724**, 1336. 4.5.4, 4.6, 5.1.4

Mao M. Y., Huynh M. T., Norris R. P., Dickinson M., Frayer D., Helou G., Monkiewicz J. A., 2011. *ApJ*, **731**, 79. 2.1.2, 2.5.5, 2.6

Marks M., Kroupa P., Dabringhausen J., Pawlowski M. S., 2012. *MNRAS*, **422**, 2246. 1.2.1

Marsden G. *et al.*, 2009. *ApJ*, **707**, 1729. 3.1, 3.4.3

Martin D. C. *et al.*, 2007. *ApJS*, **173**, 342. 3.2.2

Masjedi M. *et al.*, 2006. *ApJ*, **644**, 54. 2.3.1

Matsuura M. *et al.*, 2011. *Science*, **333**, 1258. 1.3.1, 3.5.3.1

Matteucci F., 1994. *A&A*, **288**, 57. 1.1.2

McGaugh S., Bothun G., van der Hulst J. M., Schombert J., 1991. In: *Bulletin of the American Astronomical Society*, 1444. 4.5.5

Meurer G. R., Heckman T. M., Calzetti D., 1999. *ApJ*, **521**, 64. 1.3.2

Meyer M. J. *et al.*, 2004. *MNRAS*, **350**, 1195. 4.4.1, 4.4.2

Michalowski M. J., Murphy E. J., Hjorth J., Watson D., Gall C., Dunlop J. S., 2011. In: *Galaxy Evolution: Infrared to Millimeter Wavelength Perspective*, 387, eds Wang W., Lu J., Luo Z., Yang Z., Hua H., Chen Z. 1.3.1

Miley G. K., Neugebauer G., Soifer B. T., 1985. *ApJ Letters*, **293**, L11. 1.3.4

Milgrom M., 1983. *ApJ*, **270**, 365. 1.1.1

Miller N. A., Fomalont E. B., Kellermann K. I., Mainieri V., Norman C., Padovani P., Rosati P., Tozzi P., 2008. *ApJS*, **179**, 114. 2.2.1

Mo H., van den Bosch F., White S., 2010. *Galaxy Formation and Evolution*, Cambridge University Press, Cambridge, UK. 1.1.1, 1.1.2, 1.8

Moore B., Ghigna S., Governato F., Lake G., Quinn T., Stadel J., Tozzi P., 1999. *ApJ Letters*, **524**, L19. 1.1.2

Moran S. M., Ellis R. S., Treu T., Smith G. P., Rich R. M., Smail I., 2007. *ApJ*, **671**, 1503. 1.1.3

Morgan H. L., Edmunds M. G., 2003. *MNRAS*, **343**, 427. 3.5.3.1

Morgan W. W., 1958. *PASP*, **70**, 364. 1.1.3

Morrissey P. *et al.*, 2005. *ApJ*, **619**, L7. 3.2.1

Moshir M., Kopman G., Conrow T. A. O., 1992. *IRAS Faint Source Survey, Explanatory supplement version 2*, Infrared Processing and Analysis Center, California Institute of Technology, Pasadena, CA. 4.2.2, 4.2.2

Murphy E. J. *et al.*, 2006. *ApJ*, **651**, L111. 2.1.1

Murphy E. J. *et al.*, 2011. *ApJ*, **737**, 67. 1.2.2, 1.4

Muzzin A., van Dokkum P., Kriek M., Labbé I., Cury I., Marchesini D., Franx M., 2010. *ApJ*, **725**, 742. 2.5.3

Narayanan D., Cox T. J., Shirley Y., Davé R., Hernquist L., Walker C. K., 2008. *ApJ*, **684**, 996. 4.1.2

Narayanan D., Krumholz M. R., Ostriker E. C., Hernquist L., 2012. *MNRAS*, **421**, 3127. 4.1.1, 4.1.2

Navarro J. F., White S. D. M., 1994. *MNRAS*, **267**, 401. 1.1.2

Negrello M., González-Nuevo J., Magliocchetti M., Moscardini L., De Zotti G., Toffolatti L., Danese L., 2005. *MNRAS*, **358**, 869. 3.4.3

Negrello M., Perrotta F., González-Nuevo J., Silva L., de Zotti G., Granato G. L., Baccigalupi C., Danese L., 2007. *MNRAS*, **377**, 1557. 3.4.2

Negrello M. *et al.*, 2010. *Science*, **330**, 800. 3.4.2, 4.2.1

Nelson E. J. *et al.*, 2012. *ApJ*, **747**, L28. 1.2.1

Neugebauer G. *et al.*, 1984. *ApJ Letters*, **278**, L1. 1.4

Niklas S., Beck R., 1997. *A&A*, **320**, 54. 2.1.1

Noeske K. G. *et al.*, 2007. *ApJ*, **660**, L43. 4.1.2

Nordon R. *et al.*, 2012. *ApJ*, **745**, 182. 1.4

Nozawa T., Maeda K., Kozasa T., Tanaka M., Nomoto K., Umeda H., 2011. *ApJ*, **736**, 45. 1.3.1

Oguri M. *et al.*, 2006. *AJ*, **132**, 999. 3.4.2

Ojha R., Stark A. A., Hsieh H. H., Lane A. P., Chamberlin R. A., Bania T. M., Bolatto A. D., Jackson J. M., Wright G. A., 2001. *ApJ*, **548**, 253. 4.1.1

Oliver S. J. *et al.*, 2010a. *MNRAS*, **405**, 2279. 2.5.4, 3.1, 3.5.1

Oliver S. J. *et al.*, 2010b. *A&A*, **518**, L21. 3.4.3

Omont A. *et al.*, 2011. *A&A*, **530**, L3. 4.2.1

Oort J. H., van de Hulst H. C., 1946. *Bulletin of the Astronomical Institutes of the Netherlands*, **10**, 187. 1.3.1

Oort J. H., 1932. *Bulletin of the Astronomical Institutes of the Netherlands*, **6**, 249. 1.1.1

Ostriker J. P., Peebles P. J. E., 1973. *ApJ*, **186**, 467. 1.1.1

Ostriker J. P., Steinhardt P. J., 1995. *Nature*, **377**, 600. 1.1.1

Padovani P., Miller N., Kellermann K. I., Mainieri V., Rosati P., Tozzi P., 2011. *ApJ*, **740**, 20. 1.2.2

Pannella M. *et al.*, 2009. *ApJ*, **698**, L116. 2.5.5, 3.5.1

Panter B., Jimenez R., Heavens A. F., Charlot S., 2007. *MNRAS*, **378**, 1550. 1.1.2

Papadopoulos P. P., van der Werf P. P., Xilouris E. M., Isaak K. G., Gao Y., Mühle S., 2012. *MNRAS*, **426**, 2601. D

Papadopoulos P. P., Thi W.-F., Viti S., 2002. *ApJ*, **579**, 270. 4.1.1, 4.1.1

Papadopoulos P. P., Thi W.-F., Viti S., 2004. *MNRAS*, **351**, 147. 4.1.1

Papovich C. *et al.*, 2007. *ApJ*, **668**, 45. 2.1.1, 2.2.2

Paradis D., Bernard J.-P., Mény C., 2009. *A&A*, **506**, 745. 1.3.3, 3.4.4, 5, 4.1.1

Pascale E. *et al.*, 2009. *ApJ*, **707**, 1740. 1.3.3

Pascale E. *et al.*, 2011. *MNRAS*, **415**, 911. 3.3.1, 3.3.3

Paturel G., Petit C., Prugniel P., Theureau G., Rousseau J., Brouty M., Dubois P., Cambrésy L., 2003. *A&A*, **412**, 45. 4.2.2

Pearson E. *et al.*, 2012. *in preparation*. 4.2.1

Pedani M., 2003. *New Astronomy*, **8**, 805. 2.5.1

Peebles P. J. E., 1982. *ApJ Letters*, **263**, L1. 1.1.1

Pelupessy F. I., Papadopoulos P. P., 2009. *ApJ*, **707**, 954. 4.1.1

Penzias A. A., Wilson R. W., 1965. *ApJ*, **142**, 419. 1.1.1, 1.1

Perez J., Tissera P., Padilla N., Alonso M. S., Lambas D. G., 2009. *MNRAS*, **399**, 1157. 1.1.3

Pérez-González P. G., Zamorano J., Gallego J., Aragon-Salamanca A., Gil de Paz A., 2003. *ApJ*, **591**, 827. 1.12

Pérez-González P. G. *et al.*, 2008. *ApJ*, **675**, 234. 1.1.2, 2.5.3, 2.5.4

Perlmutter S. *et al.*, 1999. *ApJ*, **517**, 565. 1.1.1, 1.1.1

Persic M., Rephaeli Y., 2002. *A&A*, **382**, 843. 1.2.2

Persic M., Rephaeli Y., Braito V., Cappi M., Della Ceca R., Franceschini A., Gruber D. E., 2004. *A&A*, **419**, 849. 1.2.2

Petropoulou V., Vilchez J., Iglesias-Paramo J., 2012. *ApJ*, **749**, 133. 1.1.3

Pierce C. M. *et al.*, 2010. *MNRAS*, **405**, 718. 2.2.2, 2.5.1

Pimbblet K. A., Smail I., Kodama T., Couch W. J., Edge A. C., Zabludoff A. I., O'Hely E., 2002. *MNRAS*, **331**, 333. 1.1.3

Pirzkal N. *et al.*, 2004. *ApJS*, **154**, 501. 1.2.1

Planck Collaboration *et al.*, 2011a. *A&A*, **536**, A1. 1.3.3

Planck Collaboration *et al.*, 2011b. *A&A*, **536**, A16. 3.4.4

Planck Collaboration *et al.*, 2011c. *A&A*, **536**, A18. 1.1.1

Planck Collaboration *et al.*, 2011d. *A&A*, **536**, A19. 4.1.1

Planck Collaboration *et al.*, 2011e. *A&A*, **536**, A21. 1.3.3, 3.4.4, 4.1.1

Planck Collaboration *et al.*, 2011f. *A&A*, **536**, A24. 1.3.3, 4.1.1

Planck Collaboration *et al.*, 2011g. *A&A*, **536**, A25. 1.3.3, 4.1.1

Poglitsch A. *et al.*, 2006. In: *36th COSPAR Scientific Assembly*, 215. 1.4

Poglitsch A. *et al.*, 2010. *A&A*, **518**, L2. 1.4

Pope A. *et al.*, 2006. *MNRAS*, **370**, 1185. 1, 2.5.3

Pope A. *et al.*, 2008. *ApJ*, **675**, 1171. 2.5.1, 2.5.3

Popescu C. C., Tuffs R. J., Voelk H. J., Pierini D., Madore B. F., 2002. *ApJ*, **567**, 221. 3.1, 3.4.4, 3.5.3

Popescu C. C., Tuffs R. J., Dopita M. A., Fischera J., Kylafis N. D., Madore B. F., 2011. *A&A*, **527**, 109. 3.5.4

Postman M., Geller M. J., 1984. *ApJ*, **281**, 95. 1.1.3

Pozzi F. *et al.*, 2004. *ApJ*, **609**, 122. 1.12, 3.5.1

Press W. H., Schechter P., 1974. *ApJ*, **187**, 425. 1.1.2

Price R., Duric N., 1992. *ApJ*, **401**, 81. 2.1.1

Puech M., Hammer F., Hopkins P. F., Athanassoula E., Flores H., Rodrigues M., Wang J. L., Yang Y. B., 2012. *ApJ*, **753**, 128. 1.1.2

Puget J.-L., Abergel A., Bernard J.-P., Boulanger F., Burton W. B., Desert F.-X., Hartmann D., 1996. *A&A*, **308**, L5. 3.4.3

Ranalli P., Comastri A., Setti G., 2003. *A&A*, **399**, 39. 1.2.2

Reach W. T. *et al.*, 1995. *ApJ*, **451**, 188. 1.3.3

Reddy N. A., Steidel C. C., 2004. *ApJ Letters*, **603**, L13. 1.2.2

Refregier A., 2003. *ARA&A*, **41**, 645. 1.1.1

Rho J. *et al.*, 2008. *ApJ*, **673**, 271. 1.3.1, 3.5.3.1

Rickard L. J., Harvey P. M., 1984. *AJ*, **89**, 1520. 2.1.1

Rieke G. H. *et al.*, 2004. *ApJS*, **154**, 25. 2.3.2

Rieke G. H., Alonso-Herrero A., Weiner B. J., Pérez-González P. G., Blaylock M., Donley J. L., Marcillac D., 2009. *ApJ*, **692**, 556. 2.1.1

Rieke G. H., 1978. *ApJ*, **226**, 550. 1.3.4

Riess A. G. *et al.*, 1998. *AJ*, **116**, 1009. 1.1.1, 1.1.1

Rigby E. E. *et al.*, 2011. *MNRAS*, **415**, 2336. 3.3.3

Roberts M. S., Haynes M. P., 1994. *ARA&A*, **32**, 115. 1.1.3

Roberts M. S., 1963. *ARA&A*, **1**, 149. 1.1.3

Roche P. F., Aitken D. K., Smith C. H., Ward M. J., 1991. *MNRAS*, **248**, 606. 1.3.4

Rodighiero G. *et al.*, 2010a. *A&A*, **515**, A8. 3.5.1, 3.5.3.1

Rodighiero G. *et al.*, 2010b. *A&A*, **518**, L25. 2.5.5

Rohlfs K., Wilson T. L., 2006. *Tools of Radio Astronomy*, Springer, Heidelberg, Germany. 4.5.1

Roseboom I. G. *et al.*, 2012. *MNRAS*, **419**, 2758. 2.6

Rovilos E., Georgakakis A., Georgantopoulos I., Afonso J., Koekemoer A. M., Mobasher B., Goudis C., 2007. *A&A*, **466**, 119. 2.2.2

Rowan-Robinson M., Crawford J., 1989. *MNRAS*, **238**, 523. 1.3.2

Rowan-Robinson M. *et al.*, 2008. *MNRAS*, **386**, 697. 3.5.1

Rowan-Robinson M., 2004. *Cosmology*, Oxford University Press, Oxford, UK. 1.1.2

Rowlands K. *et al.*, 2012. *MNRAS*, **419**, 2545. 1.3.1, 3.5.3, 4.2.1, D

Roychowdhury S., Chengalur J. N., 2012. *MNRAS*, **423**, L127. 2.1.2

Rubin V. C., Ford W. K. J., Thonnard N., 1980. *ApJ*, **238**, 471. 1.1.1

Sadler E. M. *et al.*, 2002. *MNRAS*, **329**, 227. 1.12

Saintonge A. *et al.*, 2011. *MNRAS*, **415**, 61. 4.5.5, 4.6

Sajina A., Scott D., Dennefeld M., Dole H., Lacy M., Lagache G., 2006. *MNRAS*, **369**, 939. 1.3.3

Sakamoto S., Hasegawa T., Hayashi M., Handa T., Oka T., 1995. *ApJS*, **100**, 125. 4.5.3

Salpeter E. E., 1955. *ApJ*, **121**, 161. 2.5.4

Sandage A., 1986. *A&A*, **161**, 89. 1.1.3

Sanders D. B., Mirabel I. F., 1996. *ARA&A*, **34**, 749. 1.4, 4.1.2

Sanders D. B., Phinney E. S., Neugebauer G., Soifer B. T., Matthews K., 1989. *ApJ*, **347**, 29. 1.3.4

Sanders D. B., Mazzarella J. M., Kim D.-C., Surace J. A., Soifer B. T., 2003. *AJ*, **126**, 1607. 4.2.2, 4.2.2

Santini P. *et al.*, 2010. *A&A*, **518**, L154. 3.5.3.1

Sargent M. T. *et al.*, 2010a. *ApJS*, **186**, 341. 2.1.2, 2.2.1, 2.5.5, 6, 2.6

Sargent M. T. *et al.*, 2010b. *ApJ*, **714**, L190. 2.1.2, 2.5.5, 6

Saunders W., Rowan-Robinson M., Lawrence A., Efstathiou G., Kaiser N., Ellis R. S., Frenk C. S., 1990. *MNRAS*, **242**, 318. 3.5.1

Sauty S. *et al.*, 2003. *A&A*, **411**, 381. 4.4

Sauvage M., Tuffs R. J., Popescu C. C., 2005. *Space Sci. Rev.*, **119**, 313. 1.3.3, 5.1.5

Savage B. D., Mathis J. S., 1979. *ARA&A*, **17**, 73. 1.3.4

Savaglio S. *et al.*, 2005. *ApJ*, **635**, 260. 1.1.2

Savoy J., Welch G. A., Fich M., 2009. *ApJ*, **706**, 21. 3.1, 3.5.3

Schaye J., Dalla Vecchia C., 2008. *MNRAS*, **383**, 1210. 4.1.1

Schiminovich D. *et al.*, 2007. *ApJS*, **173**, 315. 3.2.2

Schlegel D. J., Finkbeiner D. P., Davis M., 1998. *ApJ*, **500**, 525. 3.2.1

Schmidt B. P. *et al.*, 1998. *ApJ*, **507**, 46. 1.1.1, 1.1.1

Schmidt M., 1959. *ApJ*, **129**, 243. 1.1.3, 4.1.2

Schmidt M., 1968. *ApJ*, **151**, 393. 2, 3.2.2

Schruba A. *et al.*, 2011. *AJ*, **142**, 37. 4.1.2

Schruba A. *et al.*, 2012. *AJ*, **143**, 138. 4.5.5, 4.6

Schweitzer M. *et al.*, 2006. *ApJ*, **649**, 79. 4.5.3

Scoville N. Z., Sanders D. B., 1987. In: *Interstellar Processes*, p. 21, eds Hollenbach D. J., Thronson, Jr. H. A., D. Reidel Pub. Co. 4.1.1

Sedgwick C. *et al.*, 2011. *MNRAS*, **416**, 1862. 3.5.1

Serjeant S., Harrison D., 2005. *MNRAS*, **356**, 192. 3.5.2, 5.1.3

Serjeant S. *et al.*, 2004. *ApJS*, **154**, 118. 2.2.2

Serjeant S. *et al.*, 2008. *MNRAS*, **386**, 1907. 2.2.1, 2.3.1, 3.1, 3.4.3

Serjeant S., Gruppioni C., Oliver S., 2002. *MNRAS*, **330**, 621. 1.12

Serjeant S., 2010. In: *American Institute of Physics Conference Series*, p. 29, eds Debattista V. P., Popescu C. C. 3.4.3

Seymour N. *et al.*, 2008. *MNRAS*, **386**, 1695. 1.2.2

Seymour N., Huynh M., Dwelly T., Symeonidis M., Hopkins A., McHardy I. M., Page M. J., Rieke G., 2009. *MNRAS*, **398**, 1573. 1.2.2, 1.4, 2.1.2, 2.5.5, 2.6, 5.1.2

Seymour N., Symeonidis M., Page M. J., Huynh M., Dwelly T., McHardy I. M., Rieke G., 2010. *MNRAS*, **402**, 2666. 2.5.3

Silva L., Granato G. L., Bressan A., Danese L., 1998. *ApJ*, **509**, 103. 1.3.2, 2, 3, 2.4.3, 3.5.3.1

Siringo G. *et al.*, 2009. *A&A*, **497**, 945. 2.5.3

Smail I., Ivison R. J., Owen F. N., Blain A. W., Kneib J.-P., 2000. *ApJ*, **528**, 612. 1.4

Smail I., Ivison R. J., Blain A. W., Kneib J.-P., 2002. *MNRAS*, **331**, 495. 1.4

Smail I., Swinbank A. M., Ivison R. J., Ibar E., 2011. *MNRAS*, **414**, L95. 4.2

Smail I., Ivison R. J., Blain A. W., 1997. *ApJ*, **490**, L5. 1.4

Smith D. J. B. *et al.*, 2011. *MNRAS*, **416**, 857. 3.2.1, B

Smith D. J. B. *et al.*, 2012a. *MNRAS*, **427**, 703. 3.4.4, 3.5.1.1, 3.14, 3.5.3.1, 10, 4.2.1, 5.2

Smith M. W. L. *et al.*, 2012b. *ApJ*, **748**, 123. 1.3.1, 3.5.3, 5.1.5

Smith M. W. L. *et al.*, 2012c. *ApJ*, **756**, 40. 4.5.3

Sobral D., Best P. N., Matsuda Y., Smail I., Geach J. E., Cirasuolo M., 2012. *MNRAS*, **420**, 1926. 1.2.1

Sodroski T. J., Odegard N., Arendt R. G., Dwek E., Weiland J. L., Hauser M. G., Kelsall T., 1997. *ApJ*, **480**, 173. 1.3.3

Soifer B. T. *et al.*, 1984. *ApJ Letters*, **283**, L1. 1.3.2

Soifer B. T., Sanders D. B., Madore B. F., Neugebauer G., Danielson G. E., Elias J. H., Lonsdale C. J., Rice W. L., 1987. *ApJ*, **320**, 238. 1.1.3, 1.4

Soifer B. T., Boehmer L., Neugebauer G., Sanders D. B., 1989. *AJ*, **98**, 766. 4.2.2

Soifer B. T., Neugebauer G., Houck J. R., 1987. *ARA&A*, **25**, 187. 1.4

Somerville R. S., 2002. *ApJ Letters*, **572**, L23. 1.1.2

Springel V. *et al.*, 2005. *Nature*, **435**, 629. 1.1.2, 1.4

Springel V. *et al.*, 2008. *MNRAS*, **391**, 1685. 1.1.2

Steidel C. C., Hamilton D., 1993. *AJ*, **105**, 2017. 1.4

Steidel C. C., Giavalisco M., Pettini M., Dickinson M., Adelberger K. L., 1996. *ApJ*, **462**, L17. 1.4

Steinmetz M., Navarro J. F., 2002. *New Astronomy*, **7**, 155. 1.1.2

Stern D. *et al.*, 2005. *ApJ*, **631**, 163. 2.5.1

Stetson P. B., 1987. *PASP*, **99**, 191. 3.3.1

Stevens J. A., Amure M., Gear W. K., 2005. *MNRAS*, **357**, 361. 3.1, 3.5.3

Stickel M., Klaas U., Lemke D., 2007. *A&A*, **466**, 831. 1.3.1, 3.1, 3.5.3

Strateva I. *et al.*, 2001. *AJ*, **122**, 1861. 3.2.2

Stromgren B., 1939. *ApJ*, **89**, 526. 1.2.1

Sullivan M., Mobasher B., Chan B., Cram L., Ellis R., Treyer M., Hopkins A., 2001. *ApJ*, **558**, 72. 1.12

Symeonidis M., Page M. J., Seymour N., Dwelly T., Coppin K., McHardy I., Rieke G. H., Huynh M., 2009. *MNRAS*, **397**, 1728. 1.4, 2.5.3

Symeonidis M. *et al.*, 2011. *MNRAS*, **417**, 2239. 1.2.2

Tacconi L. J. *et al.*, 2010. *Nature*, **463**, 781. 4.2

Takagi T. *et al.*, 2007. *MNRAS*, **381**, 1154. 2.2.2, 3.1

Taylor E. N. *et al.*, 2011. *MNRAS*, **418**, 1587. 3.2.1, 2, 3.4.5.2, 3.5.3.1

Tegmark M. *et al.*, 2004. *ApJ*, **606**, 702. 1.1.1

Temi P., Brighenti F., Mathews W. G., 2009. *ApJ*, **707**, 890. 3.1

Temi P., Brighenti F., Mathews W. G., Bregman J. D., 2004. *ApJS*, **151**, 237. 3.5.3

Temim T., Sonneborn G., Dwek E., Arendt R. G., Gehrz R. D., Slane P., Roellig T. L., 2012. *ApJ*, **753**, 72. 1.3.1

Thomas D., Maraston C., Bender R., Mendes de Oliveira C., 2005. *ApJ*, **621**, 673. 1.1.2

Thompson T. A., Quataert E., Waxman E., Murray N., Martin C. L., 2006. *ApJ*, **645**, 186. 2.1.1, 2.6

Tielens A. G. G. M., Allamandola L. J., 1987a. In: *NATO ASIC Proc. 210: Physical Processes in Interstellar Clouds*, p. 333, eds Morfill G. E., Scholer M. 1.3.1

Tielens A. G. G. M., Allamandola L. J., 1987b. In: *Interstellar Processes*, p. 397, eds Hollenbach D. J., Thronson, Jr. H. A. 1.3.3

Tojeiro R., Percival W. J., Heavens A. F., Jimenez R., 2011. *MNRAS*, **413**, 434. 3.5.4

Tonnesen S., Cen R., 2012. *MNRAS*, **425**, 2313. 1.1.3

Toomre A., 1977. In: *Evolution of Galaxies and Stellar Populations*, 401, eds Tinsley B. M., Larson, D. Campbell R. B. G., Yale University Observatory, New Haven, CT. 1.1.2, 1.1.2, 4.1.1

Totani T., Takeuchi T. T., Nagashima M., Kobayashi M. A. R., Makiya R., 2011. *PASJ*, **63**, 1181. 1.4, 4.5.3, 5.1.5

Tremonti C. A. *et al.*, 2004. *ApJ*, **613**, 898. 1.1.3

Tresse L., Maddox S. J., 1998. *ApJ*, **495**, 691. 1.12

Tresse L., Maddox S., Loveday J., Singleton C., 1999. *MNRAS*, **310**, 262. 3.2.2

Tresse L., Maddox S. J., Le Févre O., Cuby J., 2002. *MNRAS*, **337**, 369. 1.12

Treu T., 2010. *ARA&A*, **48**, 87. 4.2.1

Treyer M. A., Ellis R. S., Milliard B., Donas J., Bridges T. J., 1998. *MNRAS*, **300**, 303. 1.12

Trumpler R. J., 1930. *Lick Observatory Bulletin*, **14**, 154. 1.3.1

Tuffs R. J. *et al.*, 2002. *ApJS*, **139**, 37. 3.1

Tully R. B., Fisher J. R., 1977. *A&A*, **54**, 661. 1.1.3

van de Hulst H. C., 1946. *Recherches Astronomiques de l'Observatoire d'Utrecht*, **11**, 2. 1.3.1

van den Bergh S., 1976. *ApJ*, **206**, 883. 1.1.3

van der Kruit P. C., 1973. *A&A*, **29**, 263. 1.2.2, 2.1.1

van Dokkum P. G., Conroy C., 2010. *Nature*, **468**, 940. 1.2.1

Vega O., Clemens M. S., Bressan A., Granato G. L., Silva L., Panuzzo P., 2008. *A&A*, **484**, 631. 4, 2.4.3

Veilleux S., Osterbrock D. E., 1987. *ApJS*, **63**, 295. 1.2.1

Vergani D., Pizzella A., Corsini E. M., van Driel W., Buson L. M., Dettmar R.-J., Bertola F., 2007. *A&A*, **463**, 883. D

Viero M. P. *et al.*, 2012. *MNRAS*, **421**, 2161. 3.1

Virani S. N., Treister E., Urry C. M., Gawiser E., 2006. *AJ*, **131**, 2373. 2.2.1, 2.5.1

Vlahakis C., Dunne L., Eales S., 2005. *MNRAS*, **364**, 1253. 1.3.1, 3.1, 3.5.3, 4.1.3

Vlahakis C., Eales S., Dunne L., 2007. *MNRAS*, **379**, 1042. 2.1.1

Voelk H. J., 1989. *A&A*, **218**, 67. 2.1.1

Wagoner R. V., Fowler W. A., Hoyle F., 1967. *ApJ*, **148**, 3. 1.1.1

Wall J. V., Jackson C. A., Shaver P. A., Hook I. M., Kellermann K. I., 2005. *A&A*, **434**, 133. 2.5.1

Walter F., Brinks E., de Blok W. J. G., Bigiel F., Kennicutt R. C., Thornley M. D., Leroy A., 2008. *AJ*, **136**, 2563. 4.4.3

Walterbos R. A. M., Greenawalt B., 1996. *ApJ*, **460**, 696. 1.4, 4.5.3

Walterbos R. A. M., Schwering P. B. W., 1987. *A&A*, **180**, 27. 4.5.3

Webb T. M. A. *et al.*, 2006. *ApJ*, **636**, L17. 2.1.1

Werner M. W. *et al.*, 2004. *ApJS*, **154**, 1. 1.4

White S. D. M., Frenk C. S., 1991. *ApJ*, **379**, 52. 1.1.2

White S. D. M., Rees M. J., 1978. *MNRAS*, **183**, 341. 1.1.2, 1.1.3

White R. L., Helfand D. J., Becker R. H., Glikman E., de Vries W., 2007. *ApJ*, **654**, 99. 2.2.2, 2.2.2, 3.3.2

Whittet D., 2003. *Dust in the Galactic Environment*, IOP Publishing, Bristol, UK. 1.3.1, 1.3.3, 1.3.3, 1.3.3, 1.3.3, 1.3.4

Wijesinghe D. B. *et al.*, 2011. *MNRAS*, **415**, 1002. 3.5.4, 3.5.4

Williams R. J., Quadri R. F., Franx M., van Dokkum P., Labbé I., 2009. *ApJ*, **691**, 1879. 2.2.1, 3.4.5

Wilson G., Cowie L. L., Barger A. J., Burke D. J., 2002. *AJ*, **124**, 1258. 1.12

Wilson C. D. *et al.*, 2009. *ApJ*, **693**, 1736. 4.1.3, 4.2.1, 4.5.3

Wilson C. D. *et al.*, 2012. *MNRAS*, **424**, 3050. 4.1.3, 4.5.1, 4.5.3, 4.5.4

Wilson C. D., 1995. *ApJL*, **448**, L97. 4.1.1

Wilson C. D., 1997. *ApJL*, **487**, L49. 4.1.1

Wolf C. *et al.*, 2004. *A&A*, **421**, 913. 2.2.1

Wong O. I. *et al.*, 2006. *MNRAS*, **371**, 1855. 4.4.1

Worthey G., Faber S. M., Gonzalez J. J., 1992. *ApJ*, **398**, 69. 1.1.2

Wright T., 1750. *An Original Theory or New Hypothesis of the Universe*. 1.1.1

Wyder T. K. *et al.*, 2007. *ApJS*, **173**, 293. 3.2.2, 3.2.2, 3.2.2

Xu C., Helou G., 1994. *ApJ*, **426**, 109. 4.5.3

Yamamura I. *et al.*, 2009. In: *American Institute of Physics Conference Series*, p. 169, eds Usuda T., Tamura M., Ishii M. 4.2.2

Yao L., Seaquist E. R., Kuno N., Dunne L., 2003. *ApJ*, **588**, 771. 4.1.3, 4.2.1, 4.4, 4.5.1, 4.5.4, 4.5.5, 4.6, 5.1.4

Yi S. K. *et al.*, 2005. *ApJ*, **619**, L111. 3.2.2, 3.2.2, 3.2.2

Young J. S., Scoville N. Z., 1991. *ARA&A*, **29**, 581. 4.1.1

Young L. M., Bendo G. J., Lucero D. M., 2009. *AJ*, **137**, 3053. 2.1.1

Young J. S. *et al.*, 1995. *ApJS*, **98**, 219. 4.4

Younger J. D. *et al.*, 2009. *MNRAS*, **394**, 1685. 2.6

Yun M. S., Reddy N. A., Condon J. J., 2001. *ApJ*, **554**, 803. 2.1.1, 2.1

Zehavi I. *et al.*, 2011. *ApJ*, **736**, 59. 3.4.1, A.2

Zheng X. Z., Bell E. F., Rix H.-W., Papovich C., Le Floc'h E., Rieke G. H., Pérez-González P. G., 2006. *ApJ*, **640**, 784. 3.1

Zhu G. *et al.*, 2011. *ApJ*, **726**, 110. 3.5.4

Zwicky F., 1933. *Helvetica Physica Acta*, **6**, 110. 1.1.1

'Twas in an ancient galaxy
Light from a star new born
But ere it had escaped to see
Our telescopes forlorn

A molecule of dust, a mote
Of obfuscating smoke
Belaid this ray while yet remote
Mere light-years since invoked

But wait, the villain we can see
Thanks Herschel, Spitzer, Maxwell: Lo!
And launching lofty galleries
To infrared we go!

– Nathan Bourne